Multiscale simulation of atomic displacements induced by radiations into materials employed in microelectronic applications

Thomas Jarrin

THÈSE

En vue de l'obtention du
DOCTORAT DE L'UNIVERSITÉ DE TOULOUSE

Délivré par l'Université Toulouse 3 - Paul Sabatier

Présentée et soutenue par

Thomas JARRIN

Le 20 octobre 2021

Modélisation des effets de déplacements atomiques induits par irradiation dans les matériaux pour la microélectronique

---

Ecole doctorale : **GEETS - Génie Electrique Electronique,Télécommunications et Santé : du système au nanosystème**

Spécialité : **MicroNano Systèmes**

Unité de recherche :
LAAS - Laboratoire d'Analyse et d'Architecture des Systèmes

Thèse dirigée par
Anne HEMERYCK et Nicolas RICHARD

Jury

Mme Lourdes PELAZ, Rapporteure
M. Laurent PIZZAGALLI, Rapporteur
M. Christophe DOMAIN, Examinateur
M. Christophe INGUIMBERT, Examinateur
M. Alfredo CORREA, Examinateur
M. Kai NORDLUND, Examinateur
Mme Anne HEMERYCK, Directrice de thèse
M. Nicolas RICHARD, Co-directeur de thèse

Multiscale simulation of atomic displacements induced by radiations into materials employed in microelectronic applications

Thomas Jarrin

Abstract

The development and usage of dedicated opto and microelectronic devices is an essential aspect of space and nuclear engineering. However, in space and nuclear environments, devices are subject to intense flux of energetic particles jeopardizing their correct working by inducing the formation of free charges via ionization of materials as well as the creation of crystalline defects following atomic displacements. The latter mechanism is the subject of the present PhD thesis. Atomic displacements are quite well known from a technological point of view. For example, it is acknowledged they are responsible for a drastic increase of dark current observed in image sensors, or for the loss of maximum output power of solar cells. Nonetheless, the fundamental physical origins of experimentally measured effects are still subject to debate. The difficulties encountered in the establishment of a clear link between the effects observed in technologies and the fundamental mechanisms are partly due to the very short (of the order of the femtosecond to the picosecond for an atomic collision for example) characteristic timescales of the dynamic process at stake. Indeed, experiments cannot cover dynamic process of so small characteristic times. This is the reason why, in this PhD thesis, we resort to numerical modelling to understand the links between basic physical mechanisms and deleterious effects witnessed in technologies and thus predict the response to atomic displacements effects of materials used in microelectronic applications. Aiming at this ultimate purpose, a multiscale simulation approach has been developed, allowing simulating the entire process of atomic displacements: particle-matter interactions with Monte Carlo techniques, collision cascades propagation using Molecular Dynamics, healing of the damaged structures with a kinetic- Monte Carlo code and finally the electronic characterization of defects thought to be responsible for devices degradation with ab initio methods. All the mentioned steps of this approach, except the last one, have been addressed in this thesis. In more details, lots of efforts have been undertaken to improve the models and methodologies employed in the second molecular dynamics step, regarding the stochastic aspects of cascades as well as the inclusion of electronic effects. Concerning this last aspect, a method based on ab initio Time-Dependent Density Function Theory calculations of electronic stopping power is employed. The results of the studies carried out with the objective of improving the second step of Molecular Dynamics are presented in this thesis. In addition, the three first steps of the global simulation approach are applied to Si, Ge and Si-Ge alloys, and obtained results are presented and discussed in the manuscript.

Contents

Acknowledgments/Remerciements

First, I would like to thank members of the jury, Pr. Lourdes Pelaz and Pr. Laurent Pizzagalli for accepting to review the manuscript, Pr. Kai Nordlund for chairing the defense, Dr. Christophe Domain, Dr. Alfredo Correa and Dr. Christophe Inguimbert for accepting to attend to the defense. For the rest of this acknowledgments section, please apologize me for switching to french as I feel more confident to express the rest of my thanks in my mother tongue.

Je tiens tout d'abord à remercier mes encadrants de thèse, Anne et Nicolas, pour leur accompagnement, leurs encouragements et leur confiance durant ces trois années de thèse, mais aussi pour le temps consacré à le relecture attentive de ce manuscrit lors des derniers mois.

Merci aussi à Antoine, qui m'a largement facilité la tâche en débroussaillant le sujet avant que ma thèse ne débute et qui, s'il n'a pas encadré cette thèse, a suivi de près mon travail, a contribué à l'orientation des travaux et a été le moteur de nombreuses discussions scientifiques entourant mes travaux.

Le mois de mars 2020 a été marqué par le début de longues semaines de confinements dans de très nombreux pays, mais aussi par le début de ma collaboration distancielle, qui a finalement perduré jusqu'à la fin de ma thèse, avec Fabiana et Jos. Merci à vous deux pour toutes les fructueuses discussions que nous avons eues, pour votre enthousiasme et votre bonne humeur.

Durant ces trois ans de thèse, j'ai eu la chance d'encadrer deux stagiaires, Aymeric et Juan. Merci à vous pour votre travail, votre sérieux, votre curiosité et pour cette expérience d'encadrement qui était nouvelle pour moi.

D'une façon plus générale, je veux remercier tous les membres des MAMMASMIAS, et plus particulièrement ceux que j'ai eu la chance de côtoyer le plus souvent : Antoine, Nicolas Richard, Anne (encore eux), Nicolas Salles, Layla, Miha, Ruggero, Pilou ainsi que Gabriela et Chloé qui avec Nicolas Richard et moi forment ou ont formé le contingent CEA des MAMMASMIAS.

Mentionner les MAMMASMIAS sans parler des différents workshops et séminaires passés ensemble ne serait pas rendre justice à la bonne ambiance qui règne dans le groupe, je pense en particulier au GDR MODMAT à Istres avec Antoine, Anne et Gabriela, et au workshop COST à Rethymnon avec Gabriela, Miha, Ruggero et Layla. J'ai toujours dans un coin de ma tête l'idée de retourner à notre "cantine" de la place de la mairie de Rethymnon et d'aller déguster un ou plusieurs racomelo dans les ruelles de Rethymnon ...

Merci aussi à tout le labo du CEA, pour les pauses cafés, déjeuners et autres réjouissements

passés ensemble, ainsi que pour l'atmosphère détendue qui règne au CEA et dans laquelle il a été très plaisant d'évoluer pendant trois ans.

Cette thèse s'est déroulée au CEA à Bruyères-le-Châtel, mais j'ai eu l'opportunité d'aller régulièrement à Toulouse, et ainsi de passer un peu de temps dans le train. Il me tient donc à coeur d'encourager la SNCF à mener à bien le projet de LGV Bordeaux-Toulouse, mais surtout de remercier tous les membres du labo du LAAS.

De quoi sont faits trois ans de thèse ? De toute évidence, pour ma part, de beaucoup de temps passé devant un terminal linux, de simulations mal paramétrées (ce n'est pas le cas des résultats de ce manuscrit), d'articles lus, oubliés, et donc relus ($\times$ 10), de questionnements sans fin sur les résultats, de scripts python, de rédactions d'articles, de préparations de présentations, de réunions ZOOM ... Cependant, et fort heureusement, au temps passé à travailler viennent aussi se mêler des soirées libres, des weekends et des jours de congés. Je tiens donc à remercier les auteurs de livres, réalisateurs et acteurs de films et séries qui m'ont permis d'occuper tous ces moments libres. De plus, et afin de nuancer un peu le tableau du doctorant solitaire, je veux aussi bien-sûr remercier les êtres humains qui ont animé ma vie durant trois ans : ma famille, Capucine, et mes amis, que je pourrais vulgairement classer (ce que je me permets de faire, en réalité) en "amis de Rueil", "amis de prépa", "amis de Nancy", "amis de Londres", "amis d'un des amis de Londres qui sont maintenant mes amis aussi", "amis des Balkans (ou de Colombes/Asnières)", avec quelques éléments cumulant plusieurs casquettes.

Acronyms

arc-dpa Athermal Recombination Corrected Displacements Per Atom.

ARTn Activation-Relaxation Technique nouveau.

BCA Binary Collision Approximation.

BT Bipolar Transistor.

CCD Charge Coupled Device.

CIS Complementary Metal Oxide Semiconductor Image Sensor.

CMOS Complementary Metal Oxide Semiconductor.

DC Dark Current.

DC-RTS Dark Current Random Telegraph Signal.

DD Displacement Damage.

DDD Displacement Damage Dose.

DFT Density Functional Theory.

ED Ehrenfest Dynamics.

EPH Electron-PHonon.

ETRS Enforced Time-Reversal Symmetry.

GGA Generalized Gradient Approximation.

I Interstitial.

kART Kinetic Activation-Relaxation Technique.

kMC Kinetic Monte Carlo.

LDA Local Density Approximation.

LLFP Long Lived Fission Products.

LOCOS LOCal Oxidation of Silicon.

LR-TDDFT Linear Response Time-Dependent Density Functional Theory.

LSS Lindhard Scharff Schiott.

MC Monte Carlo.

MD Molecular Dynamics.

MD-EPH Molecular Dynamics Electron PHonon.

MLFP Medium Lived Fission Products.

MOS Metal Oxide Semiconductor.

MOSFET Metal Oxide Semiconductor Field-Effect Transistor.

MRM Mean Rate Method.

NIEL Non-Ionizing Energy Loss.

NRT Norgett Torrens Robinson.

ODE Ordinary Differential Equation.

PBE Perdew Burke Ernzerhof.

PKA Primary Knock-on Atom.

RT-TDDFT Real Time Time-Dependent Density Functional Theory.

RTS Random Telegraph Signal.

SEE Single Event Effect.

SEM Standard Error of the Mean.

SHI Swift Heavy Ion.

SIA Single Interstitial Atom.

SKA Secondary Knock-on Atom.

SOI Silicon on Insulator.

SPE Solar Particle Event.

SRH Shockley-Read-Hall.

SRIM Stopping and Range of Ions in Matter.

STI Shallow Trench Isolation.

SV Single Vacancy.

SW Stillinger-Weber.

TDDFT Time-Dependent Density Functional Theory.

TEM Transmission Electron Microscopy.

TID Total Ionizing Dose.

TKA Tertiary Knock-on Atom.

TTM Two-Temperature Model.

V Vacancy.

ZBL Ziegler Biersack Littmark.

Introduction

Microelectronic devices are essential components of an always increasing broad panel of human activities. The most obvious example of this certainly is the irresistible growth of personal computers and smartphones, which have become in the past decade daily tools of both the working and personal life of billions of people. This development was allowed by the permanent and steady progress of transistors technologies already predicted in 1965 by the well known Moore's law[1].

Nonetheless, the prominent role of microelectronic devices in today's society does not only result from the vast use of personal devices, but also from the significance of microelectronics in various fields of science and engineering.

For the past decades, energy production and space discovery have constituted the driving forces of a very large picture of engineering and scientific programs. This is expected to hold true in the years to come, as attest the major investments made for the ITER[2] project, whose ultimate purpose is the experimental validation of an energy positive fusion nuclear reactor, and for the missions planned by space agencies from all over the world[3,4] on Mars and Venus, both good candidates for the discovery of signs of life or former life[5,6]. The proper working of such nuclear energy projects and space missions requires employing microelectronic components, for different kinds of sensors and cameras in nuclear reactors, nuclear waste burial sites, spacecrafts and rovers, but also for energy production with solar panels for satellites or rovers. The common point of space and nuclear environments is that they both are highly radiative, thus needing the development of radiation hardened (resistant to radiations) microelectronic devices. Making microelectronic devices resistant to radiation is nontrivial and actually probably is the main microelectronic related concern in recent and yet to come nuclear energy programs and space missions.

When penetrating into matter, an energetic particle loses its kinetic energy following two types of mechanisms: electronic and nuclear. In the former, electrons of the atoms of the target material are excited, and sometimes even ripped off from their bonding with the nuclei following inelastic interactions with an energetic charged incident particle, thus creating free charges in the

[1] G. E. Moore, "Cramming more components onto integrated circuits", Electronics 38 (1965)

[2] ITER project website, (2021) https://www.iter.org/.

[3] Past and current NASA missions, (2021) https://www.jpl.nasa.gov/missions.

[4] Past, current and future ESA missions, (2021) https://www.esa.int/ESA/Our_Missions.

[5] D. S. Mckay, E. K. Gibson, K. L. Thomas-Keprta, et al., "Search for Past Life on Mars: Possible Relic Biogenic Activity in Martian Meteorite ALH84001", Science 273, 924–930 (1996)

[6] J. S. Greaves, A. M. S. Richards, W. Bains, et al., "Phosphine gas in the cloud decks of Venus", Nat. Astron., 10.1038/s41550-020-1174-4 (2020).

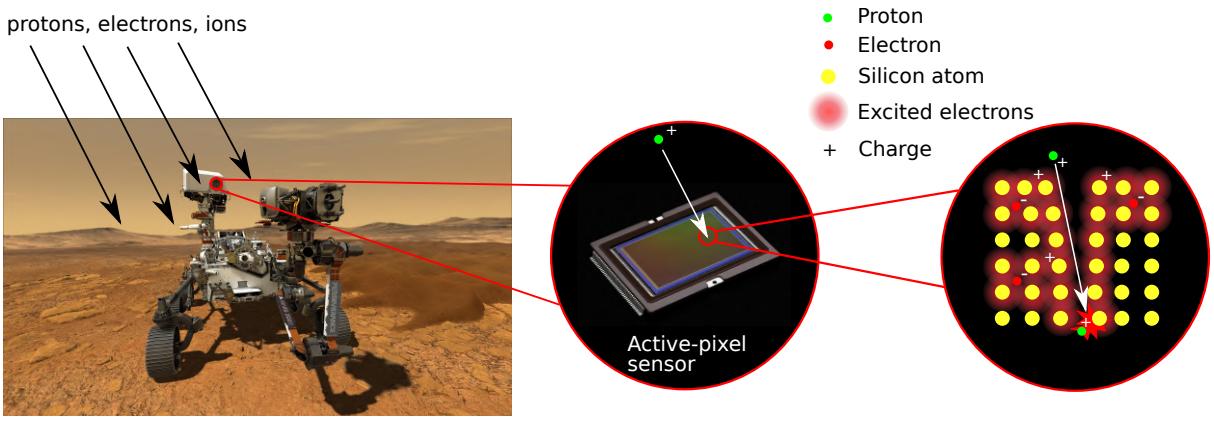

Figure 0.1: *Schematic representation of the ionizing and non-ionizing devices degradation mechanism that may lead to Dark Current or Random Telegraph Signal in space image sensors. The rover appearing in the figure is the NASA Perseverance rover that landed on Mars in 2021.*

device. In nuclear processes, an incident charged or neutral particle, collides with atomic nuclei of the device thus ejecting them from their equilibrium position and creating crystalline defects in the matter. The electronic energy loss mechanism is responsible for what is called ionizing degradation of devices, whereas the nuclear energy loss mechanism is responsible for non-ionizing degradation of devices. From a technological standpoint, the effects of radiations on devices are quite well known. For example, in image sensors, the appearance of hot and blinking pixels due to the Dark Current and Dark Current-Random Telegraph Signal[7] phenomena caused by non-ionizing radiations have been acknowledged for a long time and are regularly observed in space image sensors. However, a complete understanding of radiation degradation processes, from the mechanisms occurring at the atomic scale to the observed deterioration of the microelectronic devices in technologies has not been reached yet. The physics associated with radiation damage in semiconducting materials used in microelectronics is very complex and involves dynamical processes occurring on very short timescales. The excitation of an electron by an incident ion or the ejection of an atom from its equilibrium position following a collision can both occur in less than 10^{-15} s. Experimental methods are able to characterize the state of the material or the device which underwent a radiation event at best a few seconds after the event. Experiments are therefore completely blind to the early stages of radiation degradation in a device. Hopefully, there exists a large variety of simulation techniques of different nature and size scales, which are able to access the physics of the early stages of material deterioration by radiation.

The study of microelectronic materials degradation of all kinds induced by radiations being a far too wide topic for a single manuscript, this thesis focuses on the non-ionizing mechanisms. During a non-ionizing irradiation event, an incident energetic particle, for example a neutron or a proton, collides with an atom of the matter and thus transmits to this atom part of its kinetic energy. The collided atom is ejected from its equilibrium position, and will itself collide other atoms on its path, knocking them out of their equilibrium site. The incident particle also continues to travel inside the matter and keeps colliding with other atoms and creating defects until its energy is not sufficient to knock atoms out of their position. This succession of collisions is called a collision cascade, and the resulting damage caused to the crystalline structure of the material, now containing defects under the form of vacancies, interstitial atoms

[7] C. Durnez, V. Goiffon, C. Virmontois, J. M. Belloir, P. Magnan, and L. Rubaldo, "In-Depth Analysis on Radiation Induced Multi-Level Dark Current Random Telegraph Signal in Silicon Solid State Image Sensors", IEEE Trans. Nucl. Sc. 64, 19–26 (2017).

and clusters of defects is named displacement damage. The purpose of this thesis is to improve and employ a multiscale simulation approach dedicated to the modeling of atomic displacements damage induced by irradiation in materials used in microelectronic devices, from the interaction between the incident energetic particle to the electronic activity of the resulting defects created in the semiconducting materials. The techniques we employ are very diverse in time and size scales, starting with Monte Carlo for particle-matter interactions, passing by Molecular Dynamics for collision cascades propagation and kinetic Monte Carlo for healing of the damaged structures, and ending with *ab initio* methods for the electronic characterization of defects. The semiconducting materials we investigate within the context of our multiscale approach are Si, Ge and Si-Ge alloys. There are two main reasons for the choice of those materials. The first one is technological. Indeed, Si still is today the major semiconducting component of opto and microelectronic devices, but the better charge carriers mobilities of Ge and Si-Ge alloys makes them good candidates to replace Si in future applications. Moreover, Si-Ge alloys offer the opportunity to tune the bandgap of the material with the composition of the alloy. It is therefore relevant to study those materials as they constitute the present and future of a wide range of opto and microelectronic applications. The second reason is more fundamental. Si and Ge have the same atomic structure, but their response to non-ionizing irradiation has been found to be very unalike. It is therefore of great interest to study both materials, and also Si-Ge alloys for which the content of Ge (or Si) certainly induces changes in the response of the material.

To provide a complete overview of devices deterioration induced by radiations, the first chapter of this manuscript presents the different radiation environments in which microelectronic components can be found, the particle-matter interaction mechanisms of interest for us and the types of degradation devices may undergo, with an enhanced attention given to the non-ionizing mechanisms.

The second chapter deals with the theory of collision cascades and displacement damage, presenting already developed models for the nuclear and electronic stopping powers as well as existing empirical predictive models for assessing the level of damage created by a collision cascade. Finally, our multiscale simulation approach in itself as well as objectives and improvements it aims to fulfill are detailed, in light of the existing models and theories introduced in the same chapter.

The theory and most of all the reasons behind the use and combinations of the simulation methods we employ in our multiscale approach is covered in the third chapter, with a focus on the methodology we adopt for molecular dynamics simulations of collision cascades. Indeed, the very nature of collision cascades, far from the standard applications of molecular dynamics simulations, makes their accurate simulation a challenge. Capabilities and limitations of each techniques will be clearly presented.

The fourth chapter is dedicated to accurate definition of the vocabulary used for characterizing collision cascades, the existing methods for counting defects in molecular dynamics simulations and, aiming at quantitatively evaluating the level of stochasticity of molecular dynamics simulations of collision cascades, a convergence study on the output results of collision cascades generated in Si with respect to the number of simulations performed.

In the fifth chapter are compared two methods we have tested for the inclusion of electronic effects into molecular dynamics simulations of collision cascades in Si and Ge: namely the Two-Temperature Model and the EPH model. The methodology for the Time Dependent Density Functional Theory calculations of electronic stopping power, needed for generating input data necessary to the EPH model will also be covered in detail, as well as the results obtained with this technique.

The final and sixth chapter consists in the presentation and discussion of the results obtained with the Monte Carlo, Molecular Dynamics and kinetic-Activation-Relaxation techniques steps of our multiscale simulation approach, in Si, Ge and Si-Ge alloys. We therefore cover in this chapter the results related to particle-matter interaction as well as cascades propagation and damaged structures healing.

Overview of radiation effects in microelectronic devices

1

Contents

Introduction

The mechanisms by which microelectronic devices are deteriorated by radiations are diverse. The types of degradations can be classified according to the nature of the interactions between the incident particles and the matter. Therefore, as the radiation environments dictate the nature of the particles interacting with the devices, good knowledge of the radiation environments in which devices operate are essential to correctly apprehend radiation effects in microelectronic devices. Consequently, in this chapter are presented the most common radiation environments where microelectronic devices degradation has been observed (Section 1.1), the possible particle-matter interaction mechanisms in those environments (Section 1.2) and the resulting devices and materials degradation mechanisms (Section 1.3). The origin of the radiations in each environment as well as the particles types, energies and flux to be expected are detailed in each case. The various particle-matter interactions are classified and the existing degradation mechanisms, namely single-events, ionizing and non-ionizing effects are introduced, focusing on non-ionizing degradations, which are the subject of my thesis work.

1.1 Radiation environments

1.1.1 Space

Radiations jeopardizing the proper working of microelectronic devices in space mainly originate from events occurring in the sun or at the surface of it: solar wind and solar flares. However, devices can also suffer from a low flux of high energy particles coming from outside the solar system, which constitutes the galactic cosmic rays. Moreover, the earth electromagnetic field, which protects us from most part of radiations coming from space (99.9% of incoming particles are deflected by the earth magnetic field) also induces the formation of zones of high particles density around the earth, which are known under the name of Van Allen belts [1]. We do here a brief review of all those aspects of space radiations.

1.1.1.1 Solar flares

Solar flares are single events occurring when an intense magnetic field formed locally and confined to a specific zone of the solar atmosphere is suddenly able to escape and thus releases its energy. In the vast majority of solar flares, radiations are emitted under the form of soft X-rays in the very first stage of the event, followed by hard X-rays and gamma rays. However, some bigger solar flares might lead to Solar Particle Event (SPEs) [2] during which mainly protons with energies up to tens of GeV but also alpha particles, electrons and heavy ions with energies up to 170 MeV/nucleon (*e.g.* Fe ions) are emitted [3]. Protons can be emitted with a flux up to 5.10^4 particles/cm^2/s in the biggest solar flares events like the Carrington event of 1859 and the solar flares of August 1972 [4]. Some SPE can last up to a few days, during which energetic particles are continuously emitted [2]. The high flux and high energies associated with strong solar flares make them a real threat to microelectronic devices in space.

1.1.1.2 Solar wind

Solar wind, contrary to solar flares which are single events, describes the continual emission by the sun of protons, electrons and alpha particles of energies ranging from 0.5 keV to 10 keV [5]. This continual emission results in the creation of a plasma of light charged particles in the entire solar system, called the heliosphere. The flux associated with the solar wind is of about 10^8 particles/cm^2/s to 10^{10} particles/cm^2/s [6]. The low energy associated with solar wind does not make it a direct issue for space missions.

1.1.1.3 Galactic cosmic rays

Galactic cosmic rays are constituted by protons (83%) and alpha particles (13%) but also electrons (3%) and heavy ions (1%) [5], thought to be resulting from events occurring in the vicinity of giant black holes and supergiant stars located outside our solar system, and even outside our galaxy. Fig. 1.1 shows the relative flux of particles constituting the cosmic rays, with respect to their nuclear charge Z. The entire periodic table is spanned, with an overall trend being that the lower Z, the higher the flux [7, 8]. However, a flux peak for the emission of Fe ions can be spotted, which makes this heavy ion a significant issue for devices in spaces. The particle flux in the cosmic rays also decreases with the energy of the particle. It ranges from 10^{-4} particles/cm^2/s for particles in the TeV range to 1 particles/cm^2/s for the lowest energies attained (about 100 MeV) [6]. Even if the flux of cosmic rays particles is some orders of magnitude lower than the flux of particles coming from the sun, due the very high energies of some particles and the fact that heavy ions are involved, cosmic rays particles can be the source of serious issues for space missions, as even shielding might not be enough to protect the devices.

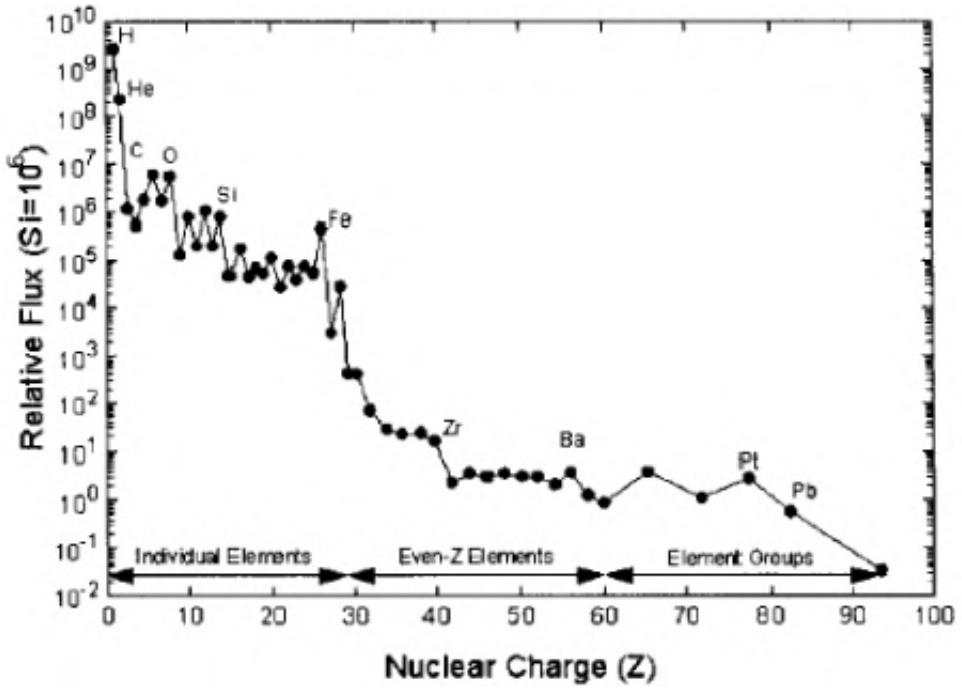

Figure 1.1: *Relative particle flux constituting the cosmic rays with respect to their nuclear charge Z [9].*

1.1.1.4 Van Allen belts

Van Allen belts correspond to two regions shaped like torus in the vicinity of earth and made of electrons and protons coming from the solar wind, solar flares or galactic cosmic rays, trapped by the earth magnetosphere. An artist view of the Van Allen belts is shown in Fig. 1.2. The first region is located between 700 km and 10 000 km [10] above the earth surface and is mainly made of a 10^{-2} particles/cm^2/s to 10^7 particles/cm^2/s flux of protons ranging from 1 keV to 100 MeV [5]. The second one is further from the earth (between 13 000 km and 65 000 km) and is made of a 10 particles/cm^2/s to 10^6 particles/cm^2/s flux of electrons ranging from 1 keV to 30 MeV [2, 5]. Some heavy ions can also find themselves trapped in those belts. The particles trapped in the Van Allen belts originating from solar events and cosmic rays, the energies and flux of the particles vary greatly with the intensity of solar flares, cosmic rays and the solar wind. Those belts are mainly a threat to satellites, but their known location and predictable intensity do not make them a major problem for space missions.

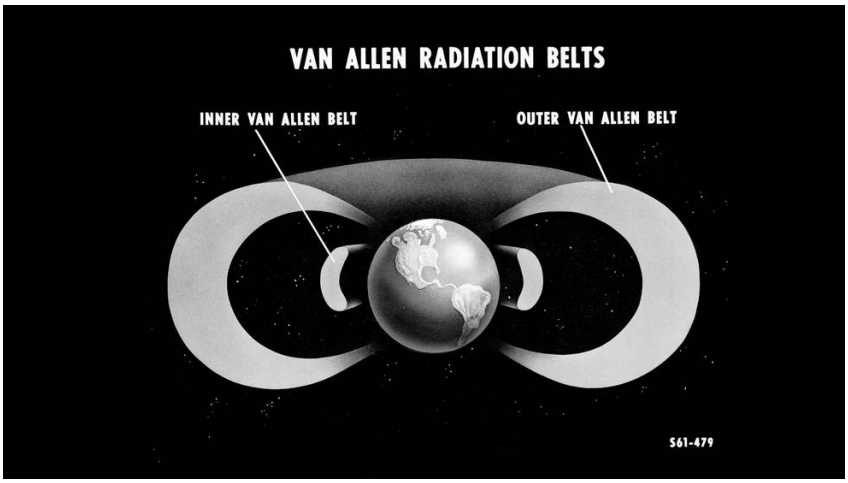

Figure 1.2: *First artist view of the Van Allen radiation belts by the NASA after their discovery in 1958 [11].*

Overall, particles found in space are in the vast majority protons and electrons, but also light ions and more rarely heavy ions. The range of energies covered is very broad, going from less than 1 keV for particles coming from the solar wind to few TeV for particles that constitute galactic cosmic rays. It is interesting to note that despite the nuclear reactions permanently taking place in stars, no neutrons are found in space. The reason for this is that outside the nucleus, the neutrons are unstable and have a mean lifetime of about 880 s. A free neutron in space thus undergoes the so-called beta decay of the neutron or the free neutron decay which leads to the disintegration of the neutron n^0 into a proton p^+, an electron e^- and an electron antineutrino $\bar{\nu}_e$ following the equation below:

$$n^0 \rightarrow p^+ + e^- + \bar{\nu}_e \tag{1.1}$$

There exists another, indirect, source of radiation in space that we have not mentioned, coming from the interaction between primary particles originating from solar and galactic events and matter (satellites, atmosphere). Most of these radiations are made of X-rays created during Bremsstrahlung processes.

1.1.2 Terrestrial radiations

Close to the earth surface, almost all the particles coming from solar events and galactic cosmic rays are either deflected by the earth magnetic field (99.9 % of them) or trapped in Van Allen belts. However, some radiations can still pass through the earth magnetosphere and thus interact with the earth atmosphere. The interactions between the incoming particles and atoms of the atmosphere create "shower" of secondary particles, among them neutrons, protons, pions and muons, usually called a cosmic shower [7]. The created neutrons, named atmospheric neutrons, might lead to the creations of heavy energetic ions by triggering nuclear reactions and are thus an issue for terrestrial applications. The energy of those atmospheric neutrons can go up to a few hundreds of MeV. Their flux decreases with the energy E, approximately following a $1/E$ relation [6]. Also, the flux diminishes with the decrease of the altitude above the sea level and the latitude (the atmospheric protection is less effective near the poles). A standard airliner, flying at an altitude of about 12 km, is subject to a flux of neutron 10^3 times greater than what it is at the sea level, as can be seen on Fig. 1.3. The atmospheric neutrons are therefore to be accounted for in the engineering process of microelectronics for terrestrial applications.

The radiations on earth do not only come from space, but also from the fissile elements which can naturally be found everywhere on earth in trace amounts. For example, Uranium and

Thorium are not unusual in the earth crust. The radioactive decay of those heavy elements lead to the emission of energetic particles (neutrons and alpha particles for example) which can trigger devices degradation.

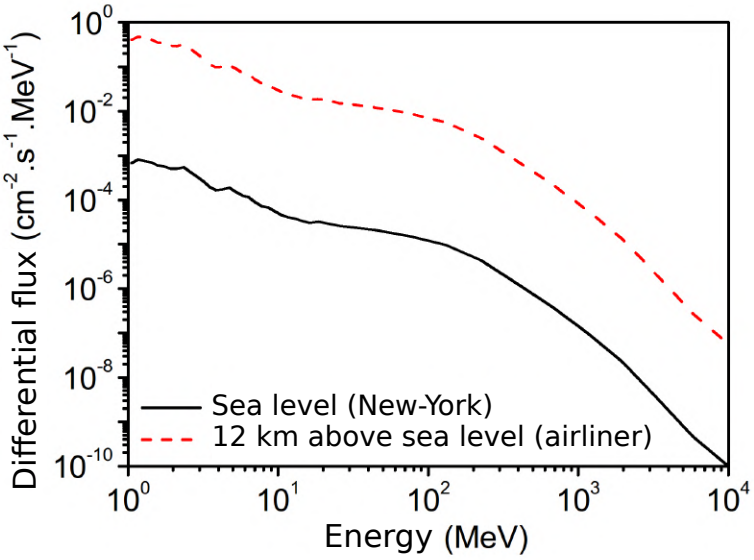

Figure 1.3: *Neutrons flux on earth as a function of the neutron energy, for two different altitudes [6, 12].*

1.1.3 Nuclear energy related environments

Nuclear reactions taking place in civil and experimental nuclear plants emit a large number of neutrons, necessary to sustain the chain of nuclear reactions and thus the energy production in fission reactors. However, depending on the kind of nuclear facility at stake, typical energies of emitted particles are different. In most of the current civil nuclear fission reactors employed for energy production, the nuclear fuel is made of ^{238}U enriched with 3% to 5% of (fissile) ^{235}U. The fission of ^{235}U gives on average 2.47 neutrons, each with an average energy of 1.943 MeV. A fusion reaction between a deuterium atom and a tritium atom like the ones artificially made at ITER or for the Laser Mégajoule project [13] triggers the creation of a neutron of 14.1 MeV and of an Helium ion of 3.5 MeV. Depending on the nature of the nuclear reaction taking place in the core of the nuclear facility, neutrons of different energies are produced, and the microelectronic devices thus have to be adapted.

In the case of fission reactors, the question of the disposal and storage of nuclear wastes also needs appropriate radiation hard microelectronic devices, for handling of the nuclear wastes and monitoring of the storage facilities. In a standard Pressurized Water Reactor, the nuclear wastes mainly consist of spent Uranium fuel (about 94% in mass of ^{238}U and 1% of ^{235}U), which is now recycled in many countries. Initially non present transuranic elements ($Z > 92$) are also produced following the capture of neutrons, among them the ^{236}U isotope can be found in non-negligible quantities (about 0.5%), as well as Pu, under various isotopic forms (about 1%). The other radioactive transuranic elements created are Np, Am and Cm, in very small quantities (about 0.01% in total). Finally, fission products, among them Medium Lived Fission Products (MLFP) like ^{137}Cs and ^{90}Sr, and Long Lived Fission Products (LLFP) like ^{99}Tc, ^{93}Zr and ^{129}I are produced. Those fission products count for about 3.5% of the total mass of generated nuclear wastes. MLFP Cs and Sr have high specific activities of 3.2 TBq/g for ^{137}Cs, and 5.1 TBq/g for ^{90}Sr but a relatively low half-life of about 30 years. On the contrary, LLFP are characterized by lower specific activities (629 MBq/g for ^{99}Tc, 93 MBq/g for ^{93}Zr and 6.5 MBq/g for ^{129}I) but very long half-lives (2.1×10^5 years for ^{99}Tc, 1.5×10^6 years for ^{93}Zr and 1.6×10^7 years for

^{129}I). Both MLFP and LLFP radiates following beta or gamma decays. The facilities for nuclear wastes storage thus have to be equipped with microelectronic devices hardened to those types of radiations. Among the transuranic elements produced, ^{239}Pu has a medium to long half-life of 24 000 years and a relatively high specific activity of 2.3 GBq, which makes it a dangerous nuclear waste component. As a response to this, in addition to recycling the spent Uranium fuels for re-enrichment and use in nuclear reactors again, some countries (France, Japan, United-Kingdom and Russia) develop a fuel from Pu wastes called Mixed Oxide Fuel (MOX). For the countries recycling Pu and U, nuclear wastes are mainly composed of MLFP and LLFP.

1.2 Particle-matter interactions

Energetic particles and photons that constitute the environments presented in the previous section interact with microelectronic devices in various ways, thus initiating undesired phenomena in devices. The energy losses of charged particles or neutrons impacting a material can be divided into two categories: ionizing energy loss and non-ionizing energy loss. The former corresponds to the amount of energy lost via interactions with the electrons of the target material, conducting to ionizations and/or electrons excitations, whereas the latter describes the amount of energy lost via direct collisions with the nuclei of the target material, leading to atomic displacements and Displacement Damage (DD). Another energy loss mechanism can be considered, named radiative energy loss, that corresponds to the interaction of very high energy charged particles leading to radiative emissions (Bremsstrahlung process for example). This last aspect not being of interest in the scope of this thesis, we do not consider it.

In this section, we cover the particle-matter interactions which are at the basis of ionizing and non-ionizing energy loss, induced by photons, neutrons and charged particles. Even if the photons are not as important for space, nuclear and terrestrial microelectronic applications as ions, protons, electrons and neutrons (nuclear and terrestrial), they are used in laboratories to predict the ionizing effects of charged particles. Their interaction mechanisms are therefore presented here.

1.2.1 Photon interactions

The photon interactions with matter result in the ionization of the atoms and the excitation of the electrons. There are three photon interaction mechanisms with matter leading to a free electron production: photoelectric effect, Compton scattering and electron-positron pair production [14]. The relative probability of each of those mechanisms depends on the energy of the incident photon and on the mass of the target atoms. Fig. 1.4, taken from [14], shows the dominant mechanisms depending on the Z number of the target material and the energy of the incident photon. The photons can also interact with the atoms through Rayleigh Scattering, which describes the scattering of a photon by an electron without the absorption of the photon energy. This mechanism does not induce the creation of free charges and is therefore not of interest here.

The photoelectric effect depicts the absorption of an incident photon energy by an atom leading to the release of an electron. The energy of the photon is entirely absorbed and has to be higher than the binding energy U_i of the ejected electron. The emitted electron has an energy equal to the energy of the photon minus U_i. This is the dominant mechanism at low energies [14, 15].

Compton scattering, which becomes dominant over the photoelectric effect at higher energies (see Fig. 1.4), corresponds to the absorption of part of the energy of an incident photon by an atom, leading to the release of an electron. Following its interaction with an atom, the photon is

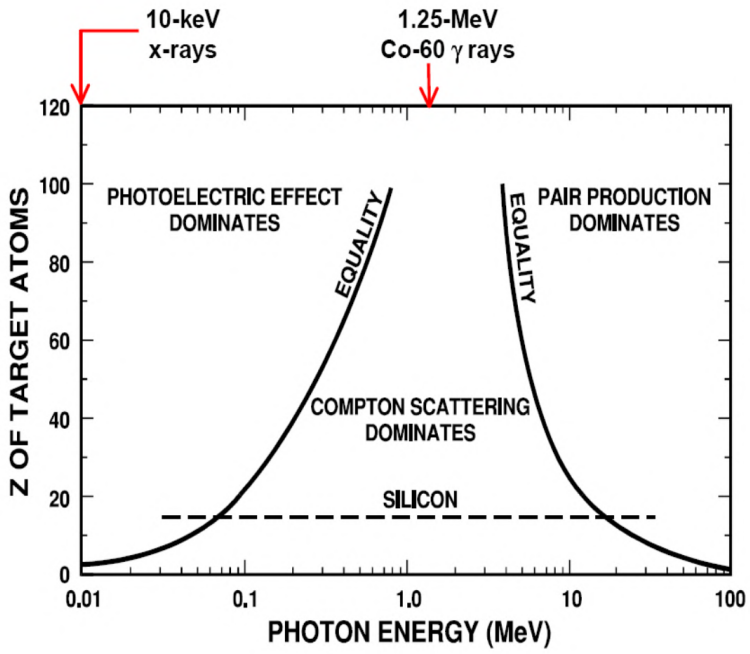

Figure 1.4: *Main photon interactions mechanisms with matter depending on the Z number of the material and the energy of the incident photon [14].*

scattered and deprived of the energy it gave for the ejection of the electron. This is the dominant mechanism at medium energies [14, 15].

Electron-positron pair production can occur when the energy of the incoming photon is greater than 1.022 MeV, the rest mass energies of an electron and a positron. The photon energy is transformed into particle mass, leading to the emission of an electron and a positron (anti-particle of the electron). This is the dominant mechanism at high energies [14, 15].

1.2.2 Charged particle interactions

Due to their charge, the main interaction mechanisms of electrons, protons and ions are electrostatic. Charged particles can interact both with the electrons of the target material and with the nuclei. The interactions with the electrons occur inelastically via the Coulomb force, leading to the excitation of the electrons or the ionization of the atoms. This specific interaction is at the basis of the electronic stopping power concept, describing the amount of energy lost per unit of distance by a charged particle in Coulomb interactions with the electrons of the target material. For charged particles, the ionizing energy loss and the electronic stopping power describe the same interaction mechanisms. Those interactions are characterized by small amounts of energy transferred after each collision, but large cross sections (*i.e.* large interaction probabilities) [15].

When charged particles interact with the nuclei, meaning they manage to overcome the screening of the electron cloud, it leads to the deflection of the incoming charged particle and in some cases to the ejection from its equilibrium position of the collided nuclei, due to elastic Coulomb interactions (also called Rutherford scattering or nuclear Coulomb interactions). It is one of the mechanisms by which DD appears, as the atomic displacements are triggered, and is an underlying mechanism of the non-ionizing energy loss for charged particles [15]. More specifically, it is the mechanism at the basis of the nuclear stopping power, which describes the amount of energy lost per unit of distance by a charged particle due to nuclear Coulomb interactions. Following

such an interaction, new atomic displacements will originate from the initially displaced ions, thus creating a cascade of collisions. It is interesting to note that following a charged particle Coulomb interaction with a nuclei, the atoms (quickly becoming ions) are displaced, thus generating the DD by colliding with other nuclei again, but also exciting and/or ionizing electrons by interacting with them due to their charge. This ionization process by secondary particles is called indirect ionization.

The Coulomb interactions of the charged particles with the electrons or with the nuclei is an essential component of many radiation induced phenomena. A specific nomenclature was therefore defined with the notion of nuclear and electronic stopping power. In many works, the total energy loss per unit of distance $\frac{dE}{dx}$ of a charged particle via Coulomb interactions is written in terms of a sum of electronic stopping power $\frac{dE}{dx}\Big|_{electronic}$ and nuclear stopping power $\frac{dE}{dx}\Big|_{nuclear}$:

$$\frac{dE}{dx} = \frac{dE}{dx}\Big|_{nuclear} + \frac{dE}{dx}\Big|_{electronic} \tag{1.2}$$

As attests (1.2), a stopping power is equivalent to a force (energy per distance unit) and not an actual power (energy per time unit). Consequently, it is starting to be logically replaced by the notation stopping force. However, the term stopping power is still the most widely employed and we are going to use it throughout this manuscript for continuity with published literature on the subject.

Additionally to Coulomb interactions, the high energy ions and protons can also interact via the strong force, directly with the nuclei of atoms and in radiative processes. The latter is characterized neither by ionization nor atomic displacements but by emission of photons, which can induce the ionization by the photon interaction mechanisms described in Section 1.2.1. Contrary to radiative processes, the strong nuclear interaction of charged particles can lead to DD and thus non ionizing energy loss. Charged particles have to overcome the strong repulsion from the positively charged nuclei to be able to interact in such a way. Therefore, their energy must be very high. Actually, there exists a minimum energy below which protons and ions are not able to interact via the strong force with an atom. This energy threshold is of about 2-3 MeV for protons, and increases with the Z number of the considered ion [16]. The energy transmitted to an atom via a nuclear interaction is greater than the energy transmitted via a Coulomb collision, but such an interaction is by far rarer. Nuclear interactions between an atom and charged particles via the strong force, which can be elastic or inelastic (nuclear reaction), lead to atomic displacements and indirect ionization. Even if such interactions could be viewed as being part of the nuclear stopping power, most of the published work on the nuclear stopping power restricts it to nuclear Coulomb interactions, as we have defined it, by symmetry with the electronic stopping power also being due to Coulomb interactions. In the following, we pay attention to use the term nuclear stopping power when only the Rutherford scattering is involved, and non-ionizing energy loss when all kinds of nuclear (Coulomb or not) interactions are involved.

1.2.3 Neutron interactions

A neutron, which is a neutral particle, cannot interact Coulombically with the nuclei and the electrons of the material. Thus, a neutron is only subject to the non-ionizing energy loss, by elastically or inelastically interacting with the nuclei via the strong force [15] similarly to what was just described for the charged particles. The only difference is that there is no energy threshold for neutrons. In an elastic interaction, the incident neutrons transmit part of their kinetic energy to an atom of the matter, thus ejecting this atom from its lattice site and generating an atomic displacement. The neutron energy is now its initial energy minus the kinetic energy it

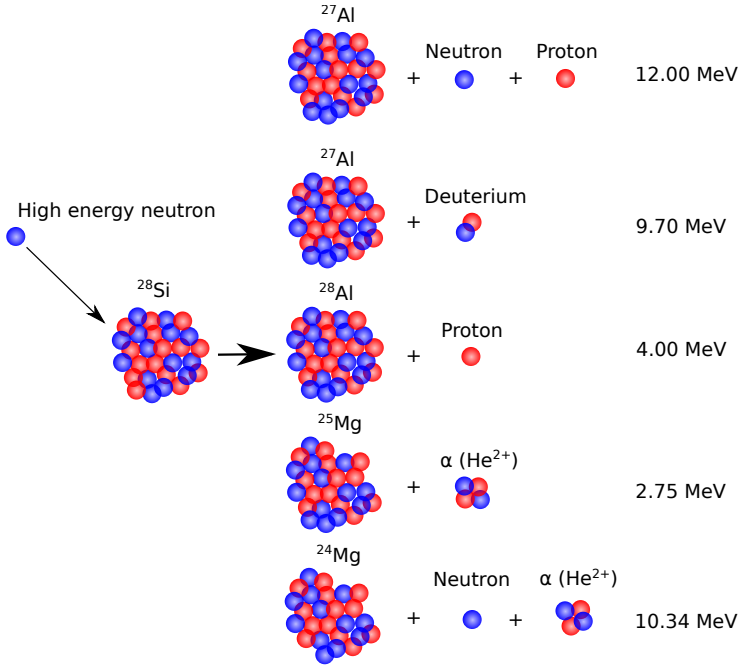

Figure 1.5: *Example of spallation scenarios following the interaction of a neutron with an Si atom. The indicated energies correspond to the threshold energies for the reactions to occur.*

transmitted to the atom. If the collision is inelastic, it means that a nuclear reaction occurred: a neutron of high energy transmitted enough energy to the nuclei of the target atom (via strong force interactions) to split this nuclei into different parts. In Si irradiated by neutrons with an energy greater than 2 MeV, it is not rare to observe spallation reactions leading to Mg or Al ions as well as various other particles. The highest the energy of the neutron, the greater the probability to have an inelastic interaction. Fig. 1.5 depicts common spallation reactions. After a nuclear (or spallation) reaction, particles are emitted with high energies, thus also leading to atomic displacements and indirect ionization. The ions ejected by neutrons in elastic interactions and charged particles emitted after an inelastic interactions will contribute both to DD and indirect excitation and/or ionization via the processes described in Section 1.2.2.

1.3 Degradation mechanisms of materials and devices

From the particle-matter interactions described in the previous section, it appears that the photons interactions and the electronic stopping power related phenomena involving charged particles have in common that they conduct to the excitation of the electrons and/or the ionization of the atoms of the matter, respectively via diverse absorption mechanisms and Coulomb interactions. Those interactions induce the ejection of energetic electrons traveling inside the device which interact with the electrons of the target atom and either ionize the atoms or promote the electrons to higher levels of energy. Electron-hole pairs are thus created in the material. Among all the degradation mechanisms resulting from the formation of electron-hole pairs, some can be induced only by a substantial flux of incident charged particles or photons on a device. In this case, the degradation is said to be cumulative and is referred to as Total Ionizing Dose (TID) effects (Section 1.3.2), the radiation dose being the amount of the energy absorbed by the material per unit of mass of that material. However, it can happen that a flux of incident particles is not even necessary to trigger degradation. The devices can be sensitive to a single energetic particle impacting them on a sensitive spot. The effects resulting from those kinds of events are called Single Event Effects (SEEs) (Section 1.3.3). Contrarily, the interactions at the

root of the non-ionizing energy loss (Coulomb and strong force interactions directly with the nuclei of the atoms) are not related to the electronic excitations but to the atomic displacements. As for the TID effects, the significance of the effects evolves with the flux of incident particles. The non-ionizing dose effects are thus cumulative and referred to as non-ionizing dose effects or Displacement Damage Dose (DDD) effects (Section 1.3.4). There is no equivalent of SEE for the atomic displacements: no case where a single particle would lead to the degradation mechanisms different from the one observed for a flux of particles has been reported. TID and DDD effects as well as SEE can occur in all kinds of radiation environments, space, nuclear or terrestrial. For sake of conciseness and practicality, for each degradation type, the mechanisms are detailed in the case of a Metal Oxide Semiconductor (MOS) device. For TID effects and SEE, we look at a MOS Field Effect Transistor (MOSFET), whereas for DDD effects, we take the example of a Complementary MOS (CMOS) image sensor, whose a basic microelectronic element is a CMOS photodiode. The basic workings of a MOSFET and a CMOS photodiode are explained in Section 1.3.1.

1.3.1 Basic workings of MOS devices

Before being able to understand the design and working of a MOSFET and a CMOS photodiode, it is necessary to study the basic microelectronic elements those devices are made of, namely the PN junction for the CMOS photodiode, which simply describes a n-type semiconductor in contact with a p-type semiconductor, and the MOS structure for the MOSFET, corresponding to a layer of oxide stacked between a metallic layer and a semiconductor layer. Indeed, as it is displayed in Fig. 1.6 and Fig. 1.7, respectively showing cross section views of a MOSFET and a CMOS photodiode, those basic structures are the ones at the heart of the working of such devices.

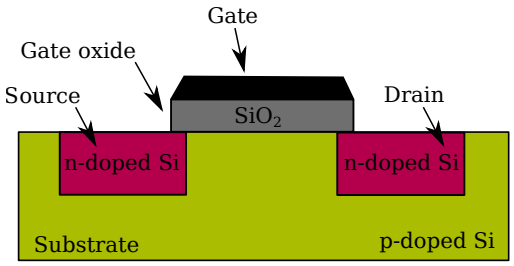

Figure 1.6: *Cross-section view of a MOSFET.*

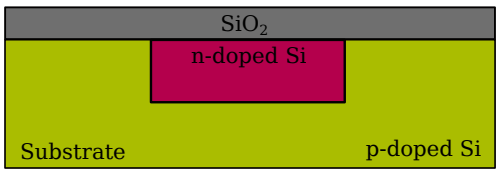

Figure 1.7: *Cross-section view of a CMOS photodiode.*

1.3.1.1 PN junction

In a PN junction, a n-doped semiconductor is in contact with a p-doped semiconductor. We consider the semiconducting material is Si here. In p-doped Si, the concentration of the holes is greater than the concentration of the electrons due to the presence of acceptor dopant atoms, creating energy states close to the valence band. The material is globally neutral, but there are lots of holes in the valence band and few electrons in the conduction band. In a p-type semiconductor, a hole is said to be a majority carrier and an electron a minority carrier. The Fermi level is located between the valence band and the acceptor states, thus very close to the valence band. Indeed, the Fermi level corresponds to the energy level for which the probability

of being occupied by an electron and the one of being occupied by a hole are both equal to 1/2. In a non-doped semiconductor, it lies exactly at the middle of the band gap. In n-doped Si, the situation is reverse compared to the p-doped semiconductor: the concentration of the electrons is greater than the concentration of the holes due to donor dopant atoms creating energy states close to the conduction band. Again, the material is globally neutral, but there are lots of electrons in the conduction band and few electrons in the valence band. In a n-type semiconductor, an electron is said to be a majority carrier and a hole a minority carrier. Also, this time, the Fermi level is close to the conduction band. Therefore, when p-doped and n-doped Si are put in contact, the PN junction is out of equilibrium as the Fermi levels are different in each part.

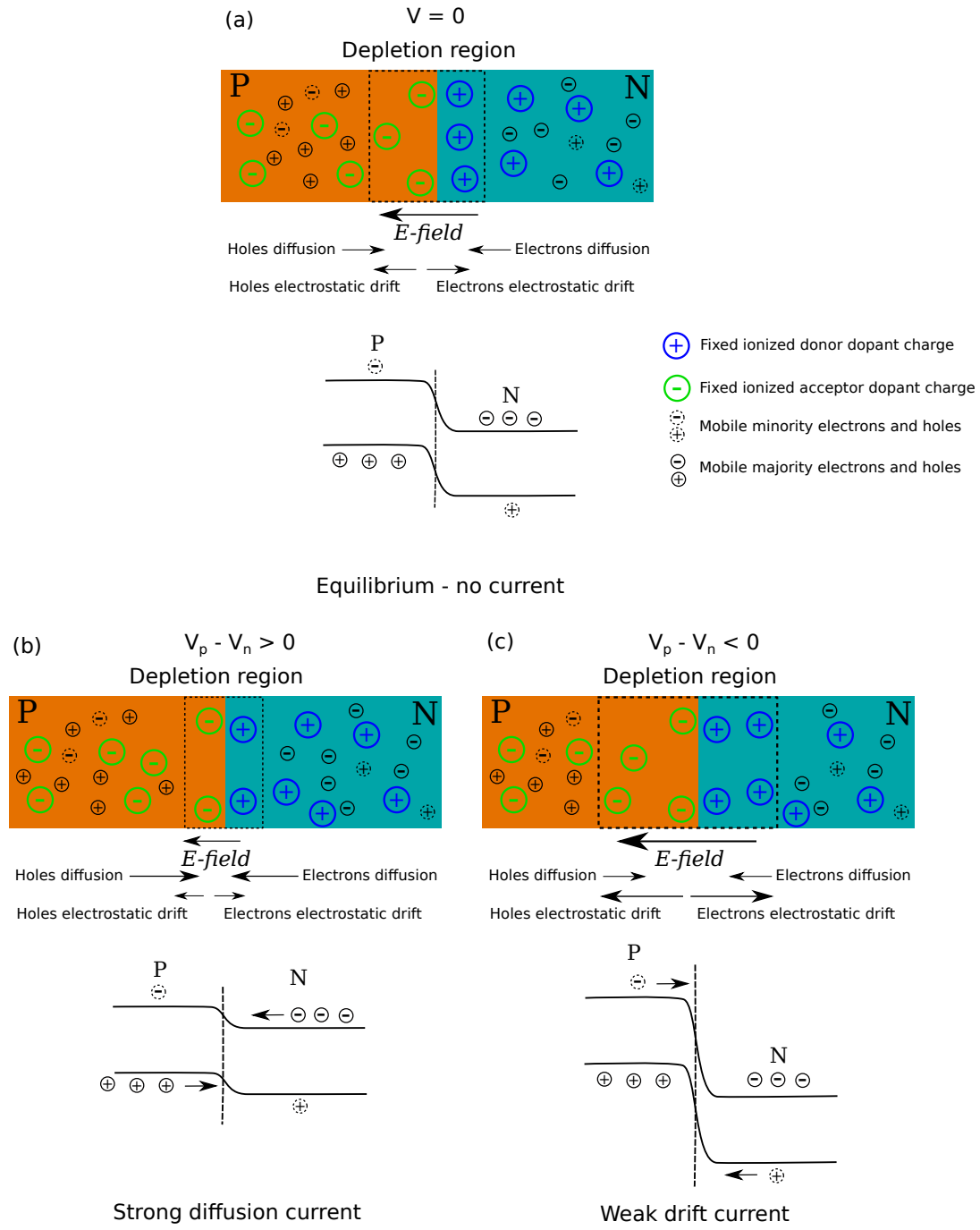

Figure 1.8: *Scheme of a PN junction (a) in the absence of polarization, (b) in direct polarization and (c) in inverse polarization.*

To reach equilibrium (constant Fermi level in the entire junction), the semiconductors need to exchange particles: holes flow from the p-side to the n-side and electrons from the n-side to the p-side. This process can also be understood as particles diffusing towards regions of lower concentration. When enough particles have been exchanged, the Fermi level is constant in the junction and the structure is at equilibrium. Due to the diffusion of holes from the p-side to the n-side, and to the recombination of holes in the p-side with electrons coming from the n-side, there is now a lack of holes in the p-side near the junction interface. Thus, the charges of the ionized acceptor dopant are not compensated, and the region is rich in fixed negative charges. For the same reasons, the region near the junction interface on the n-side is lacking electrons. This region is thus rich in fixed positive charges coming from the donor dopant atoms. The combination of those two regions is called the depletion region or space charge region. Outside of the depletion region, the material is neutral: the mobile charges (holes in the valence and electrons in the conduction) compensate the charges due to dopant atoms. Mobile charges inserted by the dopants are present but also charges created by naturally occurring thermal generation. Consequently to the fixed charges in the depletion region, an electric field appears, which bends the bands in the conduction band: a potential barrier blocks the diffusion of holes from the p-side to the n-side, and inversely for the electrons. At equilibrium, the force deriving from this electric field exactly compensates the diffusion of charge carriers induced by the concentration gradients of holes and electrons. At this stage, no electrical current can be measured. Fig. 1.8(a) depicts the situation described in the above paragraph.

The equilibrium situation results from the compensation of competitive effects. The application of a voltage between the p and n-regions of the junction breaks this equilibrium. When a positive bias is applied (electric potential in the p-region greater than the one in the n-region), both the height of the potential barrier in the depletion region and the width of the depletion region decreases. The electrons are now able to diffuse from the n-region to the p-region, and inversely for the holes. A strong electrical diffusion current can thus be measured. This situation is depicted in Fig. 1.8(b). However, when a negative bias is applied (electric potential in the p-region lower than the one in the n-region), the height of the barrier increases, the depletion region gets wider and the diffusion of carriers remains impossible. This regime is called the reverse polarization. However, due to the electric field applied, the minority carriers might flow in the junction (holes from the n-region to the p-region and electrons from the p-region to the n-region), and a very small drift current appears. This situation is depicted in the bottom right (c) part of Fig. 1.8.

1.3.1.2 MOS structure

In a MOS structure, the situations can be diverse depending on the respective work functions of the metal and the semiconductor. We are not going to review all the possible cases here and we choose to focus on a MOS structure where the metallic layer actually is an heavily doped polycrystalline Si, the oxide layer is made of SiO_2 and the semiconductor layer of p-doped Si. In this case, the work function of the semiconductor layer is greater than the one of the metal layer. Similarly to the case of a PN junction, the structure reaches equilibrium when the Fermi levels of the semiconductor and the metal are at the same level. In order to reach this equilibrium, the holes are going to accumulate at the oxide-semiconductor interface, and the electrons at the metal-oxide interface. As a consequence, the valence and conduction bands of the semiconductor near the oxide are going to bend downwards. To make the bands flat, a negative electrical potential difference needs to be applied between the metal and the semiconductor, called the flats bands electric potential difference V_{fb}. Depending on the voltage applied with respect to V_{fb}, different regimes are possible. We are interested in the one where the applied voltage is greater than V_{fb}, called the depletion regime. In this regime, the applied voltage repels the holes from the oxide-semiconductor interface, the electrons are thus in excess

close to the interface. As the voltage keeps increasing, the electrons become majority carriers in the p-doped semiconductor, which locally turns into a n-type semiconductor. The voltage from which this inversion occurs is called the threshold voltage V_{th}. It is a fundamental characteristic of the MOS structure. When $V > V_{th}$, the electrons tend to accumulate at the interface and a channel of electrons form. An electrical current can flow in this channel of electrons.

1.3.1.3 MOSFET

The working of a MOSFET is in many ways similar to the one of a MOS structure. The motivation to go from a MOS to a MOSFET structure is that in a simple MOS, the electron channel can take several minutes to form, as electrons are minority carriers. It is therefore not adapted to be used in applications. To overcome this issue, two regions of the semiconductor called drain and source are heavily n-doped, thus acting as reservoirs of electrons. They allow the creation of the inversion channel to be formed much more rapidly, and the current to flow between the drain and the source when $V > V_{th}$. The working of a MOSFET is schematized in Fig. 1.9.

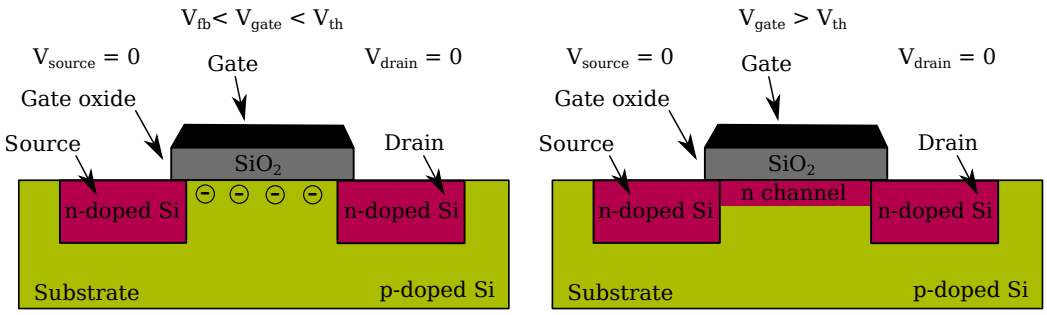

Figure 1.9: *Working scheme of a MOSFET depending on the gate voltage V_{gate} applied.*

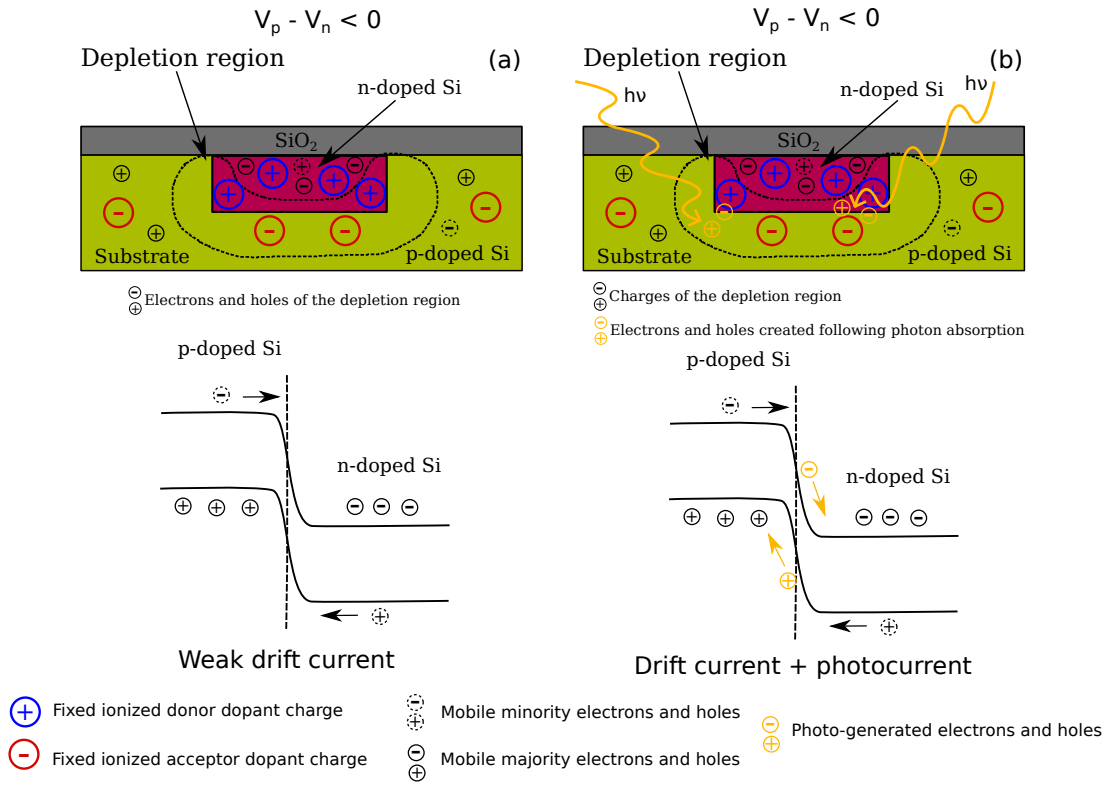

Figure 1.10: *Working scheme of a CMOS photodiode, (a) in the absence of photons and (b) in the presence of photons.*

1.3.1.4 CMOS photodiode

The purpose of a CMOS photodiode is to convert photons into an electrical current. It relies on the reverse polarization of a PN junction. The photons absorbed in the depletion region will promote the electrons in the conduction band and the holes in the valence band via the photoelectric effect. The voltage applied in the reverse polarization regime creates an electric field which then contributes to make the electrons drift to the n-region and the holes to the p-region. Thus, to the very small drift current normally occurring with a reverse polarization, a photocurrent resulting from the creation of charges by the photons and their separation by the applied electric field appears. In other words, the photons are successfully collected and separated to create an electrical current. The working of a CMOS photodiode is schematized in Fig. 1.10.

1.3.2 Total Ionizing Dose effects

The interactions with high energy photons and primary or secondary (following atomic displacements for example) charged particles lead to the creation of free secondary electrons, which will excite the electrons of the target material and induce the creation of the holes in the valence band and the electrons in the conduction band (electron-hole pairs). To quantify the effects of ionizing radiations, the TID, describing the amount of energy per unit of mass of matter absorbed in photon absorption and electronic stopping power processes (typically expressed in MeV/g), is used to calculate the density N of electron-hole pairs generated (typically in cm^{-3}):

$$N = \frac{\mathrm{TID} \times \rho}{E_p} \tag{1.3}$$

where ρ is the density of the material and E_p the minimum energy necessary to create an electron-hole pair in a material (3.6 eV in Si and 17.0 eV in SiO_2). For photons, the TID can be expressed with the incident energy fluence (energy per surface unit) of photons ϕ and the mass absorption coefficient of photons in the material μ/ρ:

$$\mathrm{TID} = \phi \times \mu/\rho \tag{1.4}$$

For charged particles, the TID can be expressed from the fluence $\phi(E)$ (integrated flux, typically expressed in cm^{-2}) of particle of energy E and the electronic stopping power $\frac{dE}{dx}\Big|_{elec}$:

$$\mathrm{TID} = \frac{1}{\rho} \times \frac{dE}{dx}\Big|_{elec} \times \phi(E) \tag{1.5}$$

The quantity $1/\rho \times (dE/dx)_{elec}$ is sometimes called the Ionizing Energy Loss (IEL). If the electronic stopping power for the application of interest is considered constant with E, the evaluation of the TID is straightforward. However, in many realistic cases, this is not the case, and the TID calculation is a bit more involved. General ideas about a more complex theoretical development can be adapted from the development made for the DDD later in this chapter (see Section 1.3.4). The TID presented above allows quantifying the ionizing radiations a device received and to study, as a function of the TID, the degradation of a device. It has important implications in the experimental testing of devices. For more information about this, interested readers can refer to [17].

If the quantification of the cumulative ionizing effects is made easier by the TID, the different device designs and applications involving different degradation mechanisms, the TID effects must be compared in equivalent devices where the same degradation mechanisms are at stake. We choose here to restrict ourselves to degradation mechanisms occurring in a MOSFET.

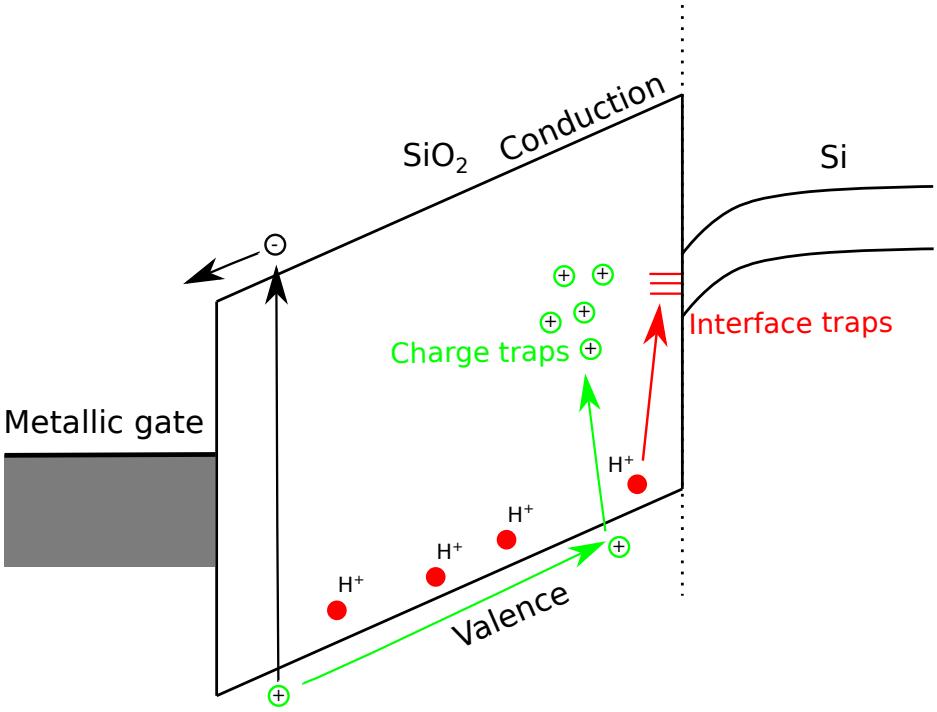

Figure 1.11: *Band gap diagram showing the basic mechanisms of a bulk MOS device degradation.*

Ionizing radiations (photons and charged particles) trigger the creation of electron-hole pairs in the device. The higher the TID, the greater the number of pairs are produced following (1.3). The electron-hole pairs created in the Si substrate only induce the formation of a transient parasitic current, whereas the charges created in the oxide might get trapped. Indeed, in the oxide, part of those electrons and holes will recombine, but some might be separated too quickly to be able to recombine, depending on the band gap engineering and the strength of the electric field present in the device, the former often inducing poorer recombination rates. The unrecombined electrons and holes are the source of deleterious effects in bulk MOS devices, which are schematically represented in Fig. 1.11 and explained in the following.

The first step in the degradation of a bulk MOS is the formation of electron-hole pairs in the oxide layer. Due to the positive applied gate bias, the electrons are transported to the gate and swept away from the oxide, whereas the holes tend to accumulate in deep level sites created both by Oxygen vacancies generated during the manufacturing process and lattice mismatch between Si and SiO_2 [18]. The holes then create positive charges preferentially trapped at the SiO_2/Si interface [19], called holes oxide traps. The diffusion of the holes to the interface via hopping between discrete energy level states distorts the lattice and may favor the release of Hydrogen impurity ions [19]. The released ions can in turn diffuse to the interface and react to form interface traps [19, 20]. Those charged interface traps induce modifications of V_{th} (see Section 1.3.1.3) and of the shape of the current versus gate voltage characteristic of the device. As the size of the oxide layer decreased with progress made in microelectronic devices manufacturing, it was observed that the shift of the threshold voltage due to hole interface traps also decreased [21].

If the development of smaller devices over the years induced a profitable decrease of the gate oxide thickness, the isolation oxides employed in some transistor technologies like LOCal Oxidation of Silicon (LOCOS) transistors or Shallow Trench Isolation (STI) transistors could not be shrinked

in size like the gate oxides were. Those thick oxides are therefore subject to the appearance of interface traps following ionizing radiations, which lead to the presence of a deleterious leakage current inside the device, affecting the current versus gate voltage characteristic of the transistor [22].

In the more recent Silicon on Insulator (SOI) transistors, the same observations as in bulk MOS devices can be made for the gate oxide and isolating oxides. However, the presence of another buried layer of oxide triggers the formation of another leakage current phenomenon following ionizing radiations, again inducing changes in the current versus gate voltage characteristic of the transistor [23].

The devices mentioned in this paragraph being known for some time, mitigation techniques were found. However, the mentioned technologies only cover a part of the devices subject to TID effects. For example, the development of more complex technologies like Fin Field-Effect Transistor (FinFET) triggered the appearance of new degradation mechanisms for which solutions have to be found.

1.3.3 Single Event Effects

Contrary to TID effects, which build-up and strengthen as more and more oxide and interface traps are produced, and thus depend on the flux of incident particles, SEEs originate from the electron-hole pairs created by single incident particles. The most obvious cause of SEEs in a device is the direct and indirect ionization by single charged particles: the incident particle ionizes the material, thus excites and ejects electrons which will create electron-hole pairs, and also collides with the nuclei. This induces atomic displacements or nuclear reactions that conduct to the creation of charged particles which will ionize the material and create electron-hole pairs as well. This indirect mechanism by which secondary ions ionize the material actually is the preferential mechanism for SEEs generated by protons. Indeed, the protons are not heavy enough to create a sufficient amount of charges on their own to induce SEEs. Also, the indirect ionization by a single neutron, via the ions it displaced and the nuclear reactions it triggered, can conduct to SEEs.

The origin of TID effects were to be looked for into the oxide layer of a MOS transistor. In the case of SEEs, observed performance degradation originates from the creation of charges in the Si layer. In inverse-biased PN junctions (constituents of MOS transistors), the depletion region is sensitive to SEEs. An incident particle directly or indirectly creates charges in the depletion region, which will be collected by the electrodes of the device. The charge collection mechanism can be divided into three stages, depicted in Fig. 1.12.

The first stage Fig. 1.12(a) simply is the creation of charges and electron-hole pairs along the projectile path. It is followed by the second stage Fig. 1.12(b) of distortion of the electric field and rapid collection of charges and finally the last stage Fig. 1.12(c) of slower charges collection by diffusion. A SEE occurs whenever the extra charge collected is greater than the electric charge normally collected by the device [25]. In the case of a single MOSFET for example, a transient current pulse appears. The transient current shape resulting from the collected charge is presented in Fig. 1.13.

Depending on the device in which this single MOSFET is implemented and the area where the particle hits the component, the consequences can be non-destructive or destructive for the device. Among the destructive SEE in MOS transistors, we can cite Single Event Latchup (SEL), Single Event Gate Rupture (SEGR) and Single Event Burnout (SEB). A non-destructive SEE is called a Single Event Transient (SET). In this case, if the hit transistor is located in a

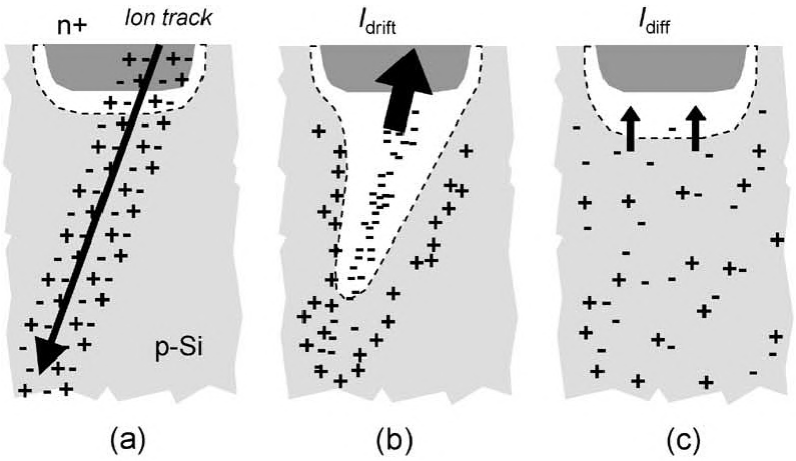

Figure 1.12: *Different stages of charge collection following the penetration of an incident ion near the source (or drain) of a MOSFET [24].*

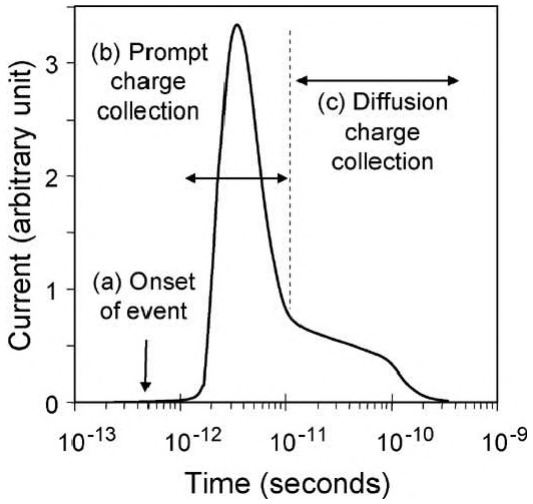

Figure 1.13: *Transient current in a MOSFET resulting from the charges collected following an interaction with a single incident particle. The (a), (b) and (c) steps indicated correspond to the (a), (b) and (c) parts of Fig. 1.12 [24].*

combinational logic element, the transient current induced by the extra collected charge might cause the propagation of errors in the device. There also exists an issue specific to memories, the Single Event Upset (SEU): an incident particle induces flipping of a bit state in the memory. The zoology of existing SEE is only mentioned and not detailed here for conciseness purposes. Interested readers should refer to [25] for more information about SET and SEU, and to [26] for a review article about destructive SEL, SEGR and SEB.

Similarly to TID effects in LOCOS or SOI architectures, the miniaturization of devices makes more probable the appearance of SEEs, even in MOSFET. Indeed, even if the sizes of the sensitive regions where SEEs can occur are reduced, the minimum collected charge to create an SEE decreases with the size of the devices. Thus, as the transistors size gets smaller, particles with lower ionizing power are able to induce SEEs.

1.3.4 Non-ionizing effects

Fundamentally, the non-ionizing interactions take the form of collisions between the incident particles and the atoms of the target material leading to atomic displacements and creation of defects inside the matter. Thus, the causes for the devices degradation due to the non-ionizing effects are to be found in the crystalline semiconducting materials constituting the devices where the defects break the symmetry and the ordering of the matter.

1.3.4.1 Non-Ionizing Energy Loss and Displacement Damage Dose

Similarly to the TID for ionizing effects, a DDD is defined to quantify the amount of energy per unit of mass of matter that was absorbed under the form of non-ionizing events. In simple cases where it can be considered that a particle uniformly deposits damage along its path, DDD can be expressed with the particle fluence ϕ and the Non-Ionizing Energy Loss (NIEL) quantity as follows:

$$\text{DDD} = \text{NIEL} \times \phi \tag{1.6}$$

The NIEL can be understood as the DDD deposited by one single particle per unit of surface exposed to the considered radiation. It depends on the energy of the particle, on the type of particle and on the target material. As a particle inevitably loses energy along its path inside a material (due to electronic and nuclear stopping powers for example), its NIEL is going to change, thus (1.6) does not hold in realistic cases. Accurate DDD calculation need to resort to the following formula:

$$\text{DDD} = \int_{E_{min}}^{E_{max}} \text{NIEL}(E) \frac{d\phi(E)}{dE} dE \tag{1.7}$$

where E_{min} is the minimum particle energy and E_{max} the maximum particle energy.

The evaluation of DDD from (1.7) requires the definition of a non-constant $NIEL(E)$. In the case of charged particles irradiation for which most of the atomic displacements are caused by Coulomb interactions, such a quantity can be derived from the nuclear stopping power $\frac{dE}{dx}\Big|_{nuclear}$. According to [27], in this case, the nuclear stopping power can be written as:

$$\frac{dE}{dx}\Big|_{nuclear} = N \int_{T_{min}}^{T_{max}(E)} T \frac{d\sigma(T)}{dT} dT \tag{1.8}$$

where E is the energy of the incident particle, N the atomic density in the target material, T the energy transmitted during a collision between the incident particle and an atom of the matter, T_{min} and $T_{max}(E)$ respectively the minimum and maximum amount of energy transmitted by a particle of energy E during a collision and $\sigma(T)$ the interaction cross section (*i.e.* sort of probability) of a collision during which an energy T is transmitted. The nuclear stopping power describing the amount of energy lost by a particle per unit of distance in Coulomb elastic collisions, independently from the collision leading to the creation of a Frenkel pair or not, T_{min} should be chosen equal to 0. Along its path, the energy E of the particle decreases, thus the maximum energy $T_{max}(E)$ it can transmit in a collision decreases as well.

From (1.8), the NIEL can be derived as follows [27]:

$$\text{NIEL}(E) = N \int_{T_{min}}^{T_{max}(E)} T \frac{d\sigma(T)}{dT} L(T) dT \tag{1.9}$$

where $L(T)$ is a function giving the fraction of energy lost to non-ionizing processes for a particle of energy T with respect to the total energy lost by the particle (ionizing and non-ionizing processes). The choice of T_{min} for the NIEL expression can be subject to disagreements. Indeed,

if the NIEL is used to quantify only the amount of displacement damage created by a particle, then the integral should start at the threshold displacement energy E_d, which is the minimum required energy to displace an atom. A value of 21 eV is commonly given for the E_d in Si, but the definition of a single E_d value is more complicated than it seems and has important repercussions in NIEL calculations [28]: E_d is crystal direction dependent and very stochastic, the definition of a single value for a material can thus be at best an average value. For more information about E_d see [29–31]. Otherwise, it can be considered that the NIEL quantifies the energy of a particle lost to non-ionizing processes, disrespectfully of if it conducted to damage or not. Indeed, even if a collision occurs between two particles where the transmitted energy is lower than E_d, the energy still is lost for the colliding particle: the energy went to phonons vibrations. In this case, the integral should start at 0.

Although, from (1.8) and (1.9), the nuclear stopping power and the NIEL in the case of a charged particle creating displacements mainly via Coulomb interactions can seem pretty similar, there is a major difference between the two quantities. The nuclear stopping power only provides the energy per unit of distance a single particle of a specific energy loses in non-ionizing processes, whereas the NIEL also takes into account the proportion of the energy transmitted by the incident particle which was employed for DD, via the $L(T)$ coefficient. Schematically, the nuclear stopping power concerns only the primary effect of the incident particle, whereas the NIEL also aims at quantifying the non-ionizing effects of secondary (tertiary, etc ...) particles. Moreover, in the case of neutrons or charged particles high enough in energy to interact with the nuclei via the strong force, the difference between the NIEL and the nuclear stopping power becomes more fundamental as they do not originate from the same basic interaction mechanisms: the NIEL encompasses all possible interactions leading to displacements whereas the nuclear stopping power only deals with nuclear Coulomb interactions. Consequently, the NIEL is the preferential quantity employed for comparing the non-ionizing power of different particles.

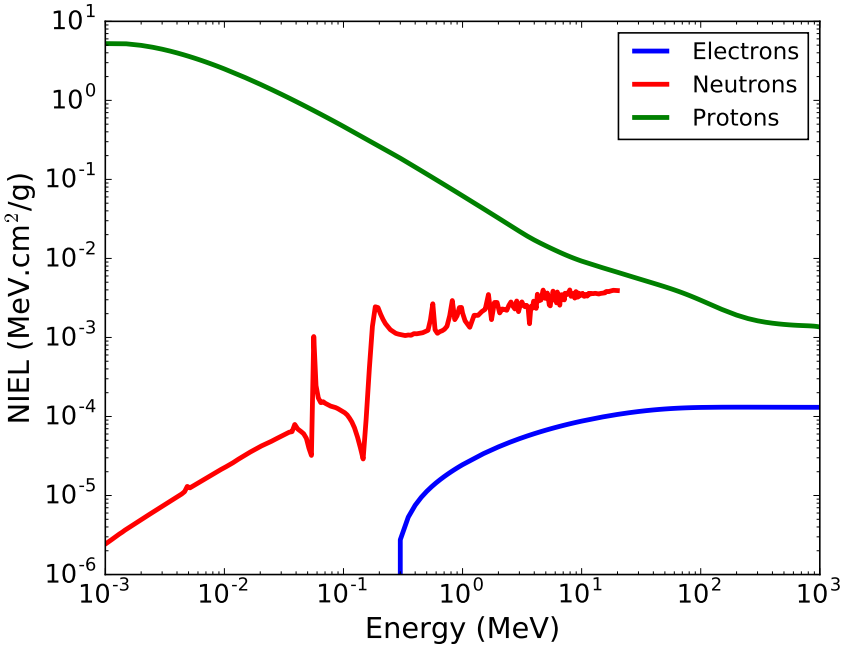

Figure 1.14: *NIEL as a function of the energy for different particles in Si. Obtained with the SR-NIEL online calculator [32].*

Fig. 1.14 shows the NIEL versus energy in Si of electrons, protons and neutrons. At low energies (below 10 MeV), the proton NIEL decreases linearly, due to the similar decrease in the cross

section of Coulomb interactions. However, the proton NIEL is higher than the neutron NIEL. This observation might be misleading but resides in the way the protons and the neutrons interact at low energies. The neutrons are only allowed to interact via strong nuclear collisions, whereas the protons can interact via both Coulomb and strong collisions (above a threshold energy of 2-3 MeV). A neutron will transmit lots of kinetic energy to few ions in matter, via elastic nuclear collisions. On the contrary, a proton will transmit low amounts of energy to many different ions via Coulomb interactions. In the NIEL definition of (1.9), this can explain the differences between the neutrons and the protons at low energy, via the σ term. At energies greater than about 10 MeV, the proton NIEL and the neutron NIEL are equal. At those high energies, the protons almost always interact directly with the nuclei of the atoms via the strong force, they are thus behaving like the neutrons. The NIEL of the electrons is very low compared to the neutron and proton NIEL. This is due to the low mass of the electrons compared to the ones of neutrons and protons.

The DDD and the NIEL that we just defined probably are among the most important quantities in DD theory as they allow to quantify the energy absorbed by a material in non-ionizing processes. However, the understanding of the non-ionizing degradation mechanisms in the microelectronic devices requires examining what happens to the DDD absorbed by a material, *ie* the dynamics of displaced atoms. The keys to understanding DD effects therefore have to be looked for at the atomic scale.

1.3.4.2 Basic mechanisms: collision cascade

At the very basis of non-ionizing effects resides the initial elastic or inelastic collision of an incident energetic particle (neutron, heavy ion, proton or electron) with a nuclei of the matter, via the strong or Coulomb forces, depending on the particle type and energy (see Section 1.2). In an elastic scattering event, the incident particle collides with an atom on its path and transmits a part of its kinetic energy, thus ejecting the atom from its lattice site. This atom is called the Primary Knock-on Atom (PKA) and will also collide, most probably elastically, other atoms on its trajectory. In the case of an inelastic interaction, meaning a nuclear reaction occurred, multiple energetic secondary particles are created. Ions created following a nuclear reaction are named PKAs as well, and will also collide other atoms on their trajectory. The atoms displaced by the PKA are called Secondary Knock-on Atoms (SKAs) and will hit as well other atoms on their path.

This process can keep going on multiple generations of knock-on atoms, until no atom can transmit an energy greater than the threshold displacement energy E_d, the minimum energy necessary to create a Frenkel pair, and thus displace an atom. This succession of collisions is called a collision cascade and conducts to the creation of defects inside the matter, which affect the properties of microelectronic devices (more on this later in this section). Also, at the same time, the primary incident particle generated other PKAs, thus initiating new cascades of collisions. This succession of collisions is highly stochastic, as the outcomes of collided atoms after a collision depend very finely on their velocity, their orientation, but also the ones of the nearby atoms. For a given energy, a slight modification in the direction of the PKA can induce drastic modifications in the cascade of collisions following it. For example, if the PKA finds itself in a direction making him travel between rows of atoms in a crystal in what is called a channeling direction (for instance the <001>, <110> and <111> direction in diamond Si and Ge), it will penetrate deep in the material but will not create many defects compared to a situation where the PKA quickly hits another atom. What we just said for the PKA is also true for every displaced atom having an energy sufficient to displace others. If the trajectory of the PKA, SKAs, and Tertiary KAs (TKAs) could be followed in the matter, it would give more or less the 2D representation of Fig. 1.15.

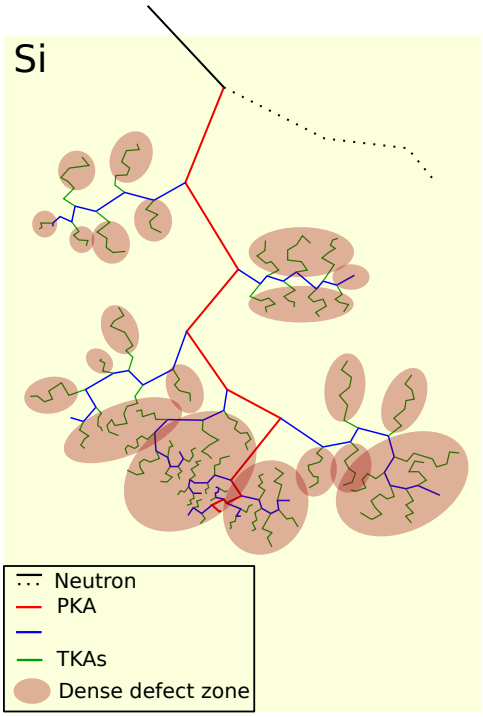

Figure 1.15: *Schematic representation of a succession of collisions initiated by a neutron occurring in a collision cascade event. After its first collision with an atom, the cascades generated by the neutron are not followed.*

The succession of high energy collisions described above, where the energetic atoms lose their energy in displacing other atoms, only corresponds to the first stage of a collision cascade. When the atoms have lower energy, their interaction cross sections for Coulomb elastic interactions with nuclei are greater, and collisions more spatially close. This favorable phase for defects creation is the second main stage of a collision cascade. At the end of this stage, lots of atoms have a kinetic of energy of a few eV, lower than the E_d thus not sufficient to trigger new displacements but enough to heat the material in a process called a heat spike. The heat spikes can lead to melting of some regions of the material. A large majority of those molten regions are going to recrystallize entirely, it may even happen that the heat spikes favor the recombination of defects, but in some cases amorphous clusters are created following a heat spike. The peak level of damage is typically reached during this heat spike process in fractions of picoseconds to few picoseconds after the creation of the PKA, depending on the energy of the PKA initiating the cascade. Following this peak, the number of defects inside the structure decreases. It is said that the structure heals. Basically, it means that nearby interstitial atoms and vacancies are going to diffuse and possibly recombine. The diffusion of defects also triggers a reorganization of the clusters of defects. This healing process can last up to month after the irradiation and consists in the third and last stage of a collision cascade.

So far, we have only considered cascade as depending of the non-ionizing energy loss, as the collisions with nuclei are responsible for the atomic displacements. However, apart from the interaction with an incident particle which can be a neutron, all the collisions involve charged particles. As we know, energetic primary or secondary charged particles undergo both nuclear stopping and electronic stopping powers, thus triggering both displacements and ionizing damage. We neglect here possible nuclear interactions via the strong force. It is thus essential to quantify the portion of the energy going to DD and the one going to ionizing effects. Fig. 1.16 shows the relative energy lost into electronic stopping power (Coulomb interactions with elec-

trons) and nuclear stopping power (Coulomb interactions with nuclei) for an Si ion, an Fe ion and a proton (H^+) into bulk Si, for energies ranging from 1 to 10^5 keV, obtained from the Stopping and Range of Ions in Matter code (SRIM) [33].

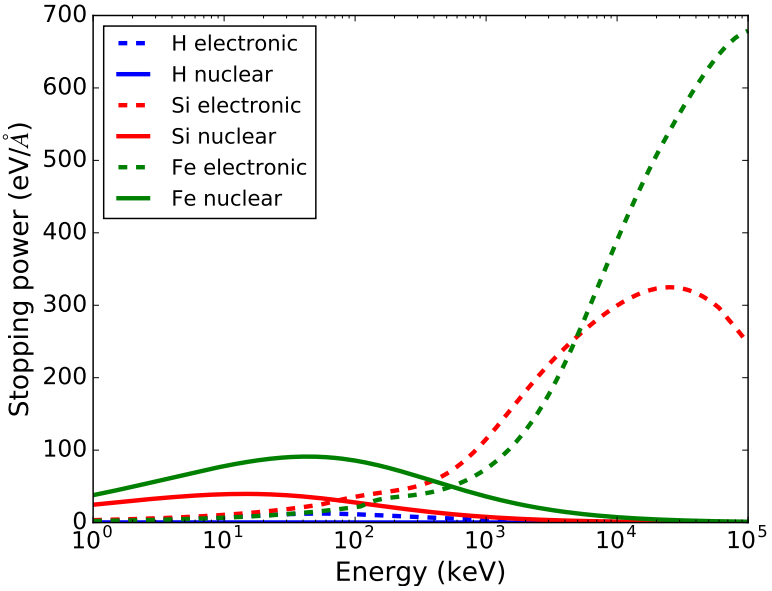

Figure 1.16: *Electronic and nuclear stopping for a Fe ion, a Si ion and a proton into Si bulk, obtained with the SRIM code [33].*

The protons lose very few energy to nuclear processes, even at low energies. Indeed, the nuclear stopping of proton at 1 keV is about 10 times less than its electronic stopping. For all the projectiles, at high energies, the electronic stopping clearly dominates. The maximum electronic stopping value is by far greater than the maximum nuclear stopping value, for all charged projectiles. However, as the energy of the charged projectile and recoils decrease, the contribution of the nuclear stopping power increases and the one of the electronic stopping power decreases. Finally, there comes a point for Fe and Si, when the projectile reaches about 80 keV in Si and about 540 keV in Fe, where displacement damage (nuclear stopping) is dominant over ionizing damage (electronic stopping). This is at those typical energies that charged particles create the great majority of atomic displacements, and thus damage in materials.

The damage done to crystalline structures which underwent a non-ionizing radiation event can take the form of point defects (interstitials (I) and vacancies (V)), or extended defects (dislocations). Extended defects, as they are responsible for elastic and plastic properties of materials, mainly are a threat to materials used for their structural properties in the nuclear or space industry. However, the point defects directly affect the electronic properties of semiconducting materials used in microelectronic applications. The defects created by atomic displacements in the semiconductors can be Single Interstitial Atoms (SIAs) and Single Vacancies (SVs), but also ensembles constituted by more than one defect and called clusters. The size and composition of the formed clusters can vary greatly. A very common defects cluster in semiconductors is the divacancy. It is also possible for defects to combine with dopant atoms of the device. A dopant or impurity atom (As, Sb, P) trapped next to a vacancy is also a common defect in Si and is called an E-center. Also, it was demonstrated both by experiments and simulations that amorphous clusters form in Si and Ge [34, 35], if the particle initial energy is high enough. More than covering a large panel of size inside a given material, the distribution of defects in clusters and the size of clusters of defects formed vary greatly with the material at stake and the initial particle generating the collision cascade. Global trends are that the denser the material and the

heavier and/or the bigger the particle initiating the recoil is, the bigger the created clusters are. For good review articles covering both metals and semiconducting materials, see [31, 36].

This diversity in the created defects is an essential component of DD. Indeed, the degradation of devices is directly related to the electronic activity of defects induced by atomic displacements, via various mechanisms originating from defects creating energy levels in the band gap of semiconductor materials, thus impacting major characteristics of charge carriers.

1.3.4.3 Device degradation

The defects created by displacement damage jeopardize the proper working of microelectronic devices by generating extra energy levels located inside the band gap of semiconducting materials. Depending on the nature of the defects, the energy levels are created at various levels inside the band gap, thus triggering different deleterious effects. Fig. 1.17 depicts the possible mechanisms induced by so-created defect states, in the Shockley-Read-Hall (SRH) theory [37].

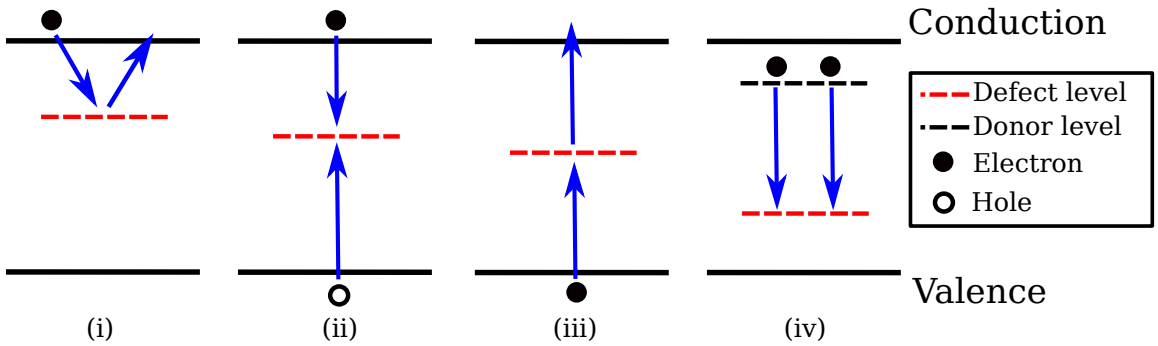

Figure 1.17: *Schematic representation of the different mechanisms allowed by the creation of defect level states inside the band gap of a semiconducting material in the SRH theory: (i) temporary trapping by a shallow level (near band-edges); (ii) recombination of carriers; (iii) thermal generation enhanced by a deep level (near mid-gap); (iv) donors or acceptors (here donors) compensation due to a deep level state*

The temporary trapping by a shallow level (near band-edges) (i) reduces the mobility of both minority and majority charge carriers, depending on the position of the state inside the gap and the doping of the material. The recombination of carriers at a defect level (ii) decreases the concentration of both majority and minority carriers. It decreases the time spent before recombination of a minority carriers, called the recombination lifetime, which is a major parameter of minority carrier devices like bipolar transistors [38]. The thermal generation of electron-hole pairs by a deep level (near mid-gap) (iii) increases the concentration of carriers in the device. This mechanism is in competition with the recombination of carriers at a defect level (ii). Thermal generation dominates when the free carrier concentration is less than the equilibrium concentration of carriers [38]. It is thus the preferential mechanism in the depletion region of devices. The closer to the middle of the gap the level is, the lower in energy is the biggest of the two barriers to cross and thus the more efficient is the thermal generation mechanism. The donors or acceptors compensation (iv) reduces the majority carrier concentration at equilibrium [38].

Additionally to those, most probable, mechanisms can be cited the tunneling of carriers through a potential barrier via a defect level, carrier mobility decrease due to defects acting as scattering centers and type conversion of semiconductor (from n to p and inversely). For more details about those three last mechanisms see [38] and references therein.

In practice, minority carriers device like bipolar transistors as well as optoelectronic devices and solar cells are sensitive to displacement damage via the mechanisms explained above, whereas DD is not an issue for MOS transistors (apart when in image sensors), except at very high particle flux. To be brief on solar cells and bipolar transistors (BTs), which are not our main focus (contrary to MOS devices, see Section 1.3.1), DD introduces leakage currents and gain degradation in BTs, respectively due to thermal generation and recombination whereas it decreases maximum power output and efficiency in solar cells due the reduction of minority carrier lifetime via mechanism (ii) of Fig. 1.17. The effects of DD on BTs [39, 40], light-emitting diodes, optocouplers [41] and solar cells [42] are not detailed here but readers can refer to the cited references for more information. We focus here on the effects of DD in Charge-Coupled Device (CCD) and most of all CMOS Image Sensors (CIS), all being opto-electronic image sensors with applications in space missions and nuclear facilities.

Silicon based image sensor technologies such as CCD and CIS are very sensitive to the thermal generation of carriers. The very basic working of image sensors relies on photon absorption and the subsequent promotion of an electron to the conduction band (also creating a hole in the valence), triggering the creation of a photocurrent (see Section 1.3.1). The presence of an irradiation-induced deep defect level in the depletion region of the sensor makes the promotion of an electron to the conduction band possible via thermal generation. Consequently to this charge flow in the device, an electrical current appears, named Dark Current (DC), as it does not originate from the absorption of a photon. The total current I_{tot} generated by the device therefore has two contributions: the photocurrent I_{ph} coming from the proper working of the device which is proportional to the incident photon flux, and the DC induced by defects I_{DC}. Fig. 1.18 illustrates the mechanisms developed in the above paragraph. We can finally write for the total current I_{tot} collected by the device:

$$I_{tot} = I_{ph} + I_{DC} \tag{1.10}$$

The appearance of DC in a sensor finally ends up in loss of contrast and noise in the image produced by the sensor, but also very large increase of DC for some pixels compared to others (hot pixels), visible in images as very bright dots. The main improvements of CIS compared to (older) CCDs is that each pixel of the array constituting the image sensor can be read independently, thus making possible to investigate DD effects in each pixel. It was then found that due to the irradiation-induced defects, the mean Dark Current in the entire sensor and also the concentration of hot pixels in the array increased with the flux of incident particle. With the healing of the material following irradiation, the DC average level in a sensor was found to slowly decrease with time [43].

More complex than DC in its origin and consequences in technologies, another phenomenon was observed in CIS after irradiation, which can be seen as DC oscillating between different discrete current intensity levels. This phenomena is called the Dark Current Random Telegraph Signal (DC-RTS). Readers should note that RTS is a generic concept of microelectronic describing random oscillations between discrete level of current intensities. Thus, all RTS signals are not related to DC. In the following, we are only interested in DC-RTS. Same as for DC, the presence of defect levels inside the band gap is considered responsible for DC-RTS. The independent study of each pixel of a CIS after irradiation showed various RTS behaviors, with current intensity oscillating between two, three or even more discrete levels. The appearance of RTS following irradiation is thought to be originating from the sudden oscillations of defects between different metastable states. Indeed, it is known that defects creating energy levels in the band gap have different generation rate, measured as the number of electrons promoted to the conduction band per second, as a function of temperature. For instance, the divacancy in Si, generates about 50 e^-/s at 300 K [44]. The generation rate of defect is also very dependent on the electric fields felt by the defects. The higher the generation rate is, the greater the DC level is. It

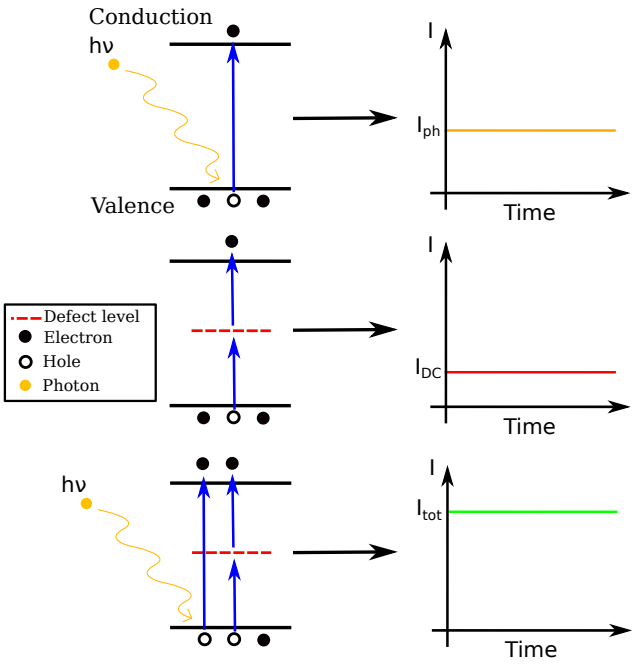

Figure 1.18: *Schematic view of the origin of the current measured in an image sensor.*

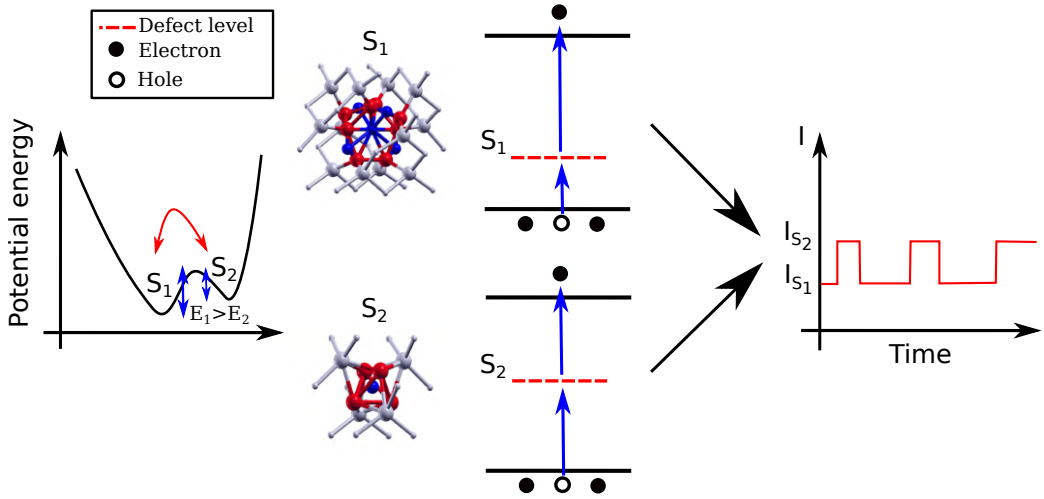

Figure 1.19: *Schematic view of a possible mechanism leading to RTS. A tri-interstitial defect structure in Si (from [45]) oscillates between two metastable states S_1 and S_2. The energy barrier to go from S_1 to S_2 being higher than the reverse one, the defect spends more time in the S_1 state. The defect energy level induced by S_2 being closer to the mid-gap, the S_2 state contributes to RTS with a greater DC value.*

could be possible that different metastable configurations of complex clusters of defects have different generation rates, thus explaining the discrete current levels of RTS signals. Therefore, the specific electronic activity of defects has to be taken into account in order to experimentally understand RTS. The possible mechanism presented above is depicted Fig. 1.19.

Readers might understand from the conditional and cautious tone used in the previous paragraph that basic mechanisms leading to DC-RTS in image sensors are not well understood yet. Actually, it is also important to note that TID in CIS can also induce DC and RTS [46]. As far as DD is concerned, it is certain that both DC and RTS in image sensors originate from defects in the gap, whose concentrations are much more pronounced post-irradiation than pre-irradiation.

However, the link between a specific DC-RTS signal and the structure of the defect present in the material is extremely difficult to achieve experimentally. Just to give some names, among existing techniques employed to characterize defects in semiconducting materials, the most important and employed ones probably are Electronic Paramagnetic Resonance (EPR) and Deep Level Transient Spectroscopy (DLTS). Interested readers can refer to the first chapter of the PhD thesis of Gabriela Herrero Saboya [47] and references therein for more information about experimental characterization of defects. Among the major questions still unanswered concerning DC-RTS, the main one probably is its origin. Although it is acknowledged that DC-RTS comes from defect levels present in the band gap of semiconductors, the nature (divacancy, E-center, amorphous cluster ...) of the defects contributing to DC-RTS is not known. In response to the difficulties faced by experimentalists to access to electronic properties of defects, and to fundamentally understand DC-RTS, capabilities offered by modern simulation techniques and supercomputer infrastructures might be an interesting solution.

Conclusion

This chapter started with an introduction to different radiation environments (space, terrestrial and nuclear facilities) in which microelectronic devices could be harmed by radiations, detailing the particles, associated flux and energies characteristic of each environment. Then, the possible interactions between those particles and material constituents of microelectronic devices were presented. We have seen that there exists a wide variety of possible interactions for neutrons and charged particles, and that all are relevant for the description of devices degradation. Overall, two categories of interactions can still be identified, one leading to the creation of electron-hole pairs and one leading to atomic displacements. The degradation in the devices following those particle-matter interactions were then presented, the ionization of atoms and/or excitation of electrons being responsible of TID effects and SEE effects, whereas atomic displacements conduct to deterioration of devices known as DD effects. Collision cascades, basic phenomena by which DD effects appear in devices are complex in the sense that all the collisions involved are highly stochastic and many different mechanisms and interactions are at stake. Fig. 1.20 summarizes the different steps and mechanisms involved in a collision cascade.

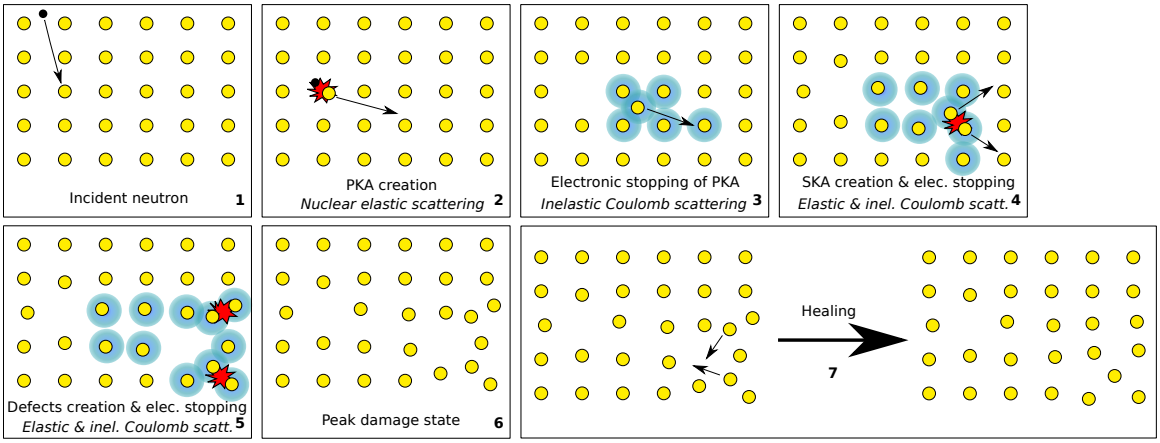

Figure 1.20: *Illustration of the different steps and processes involved in a collision cascade. It is assumed that no inelastic nuclear interactions occurred, and that the ions interact only via elastic Coulomb scattering with other ions.*

Collision cascades are responsible for CCD and CIS degradation via the creation of energy levels inside the band gap of the semiconducting materials, which enhances the thermal generation of carriers in the sensor, resulting in DC and RTS. Both DC and DC-RTS are complex phenomena,

whose fundamental understanding would benefit from accurate simulations of collision cascades, from the interaction with the incident particle, passing by all the processes displayed in Fig. 1.20, to the electronic characteristics of defects created. The global simulation approach we have developed aiming at modeling DD in materials is presented in the next chapter, in the context of an historical review of stopping powers theoretical developments and DD predictive models.

References

[1] J. A. Van Allen and L. A. Frank, "Radiation Around the Earth to a Radial Distance of 107 400 km", Nature **183**, 430–434 (1959).

[2] E. G. Stassinopoulos and J. P. Raymond, "The space radiation environment for electronics", Proc. IEEE **76**, 1423–1442 (1988).

[3] L. I. Miroshnichenko and R. A. Nymmik, "Extreme fluxes in solar energetic particle events: Methodological and physical limitations", Radiat. Meas. **61**, 6–15 (2014).

[4] D. F. Smart, M. A. Shea, and K. G. McCracken, "The Carrington event: Possible solar proton intensity-time profile", Adv. Space Res. **38**, 215–225 (2006).

[5] S. Bourdarie and D. Boscher, *Space Radiation Environment in Space Radiation Environment and its Effects on Spacecraft Components and Systems* (Cépaduès, 2004).

[6] M. Raine, "Etude de l'effet de l'énergie des ions lourds sur la sensibilité des composants microélectroniques", Université Paris-Sud 11, (2011)

[7] J. L. Barth, C. S. Dyer, and E. G. Stassinopoulos, "Space atmospheric and terrestrial radiation environments", IEEE Trans. Nucl. Sc. **50**, 466–482 (2003).

[8] J. S. George et al., "Elemental composition and energy spectra of galactic cosmic rays during solar cycle 23", Astrophys. J. **698**, 1666 (2009).

[9] R. A. Mewaldt, "Galactic cosmic ray composition and energy spectra", Adv. Space Res. **14**, 737–747 (1994).

[10] N. Y. Ganushkina, I. Dandouras, S. Y. Y., and J. Cao, "Locations of boundaries of outer and inner radiation belts as observed by Cluster and Double Star", J. Geophys. Res. **116**, 10.1029/2010JA016376 (2011).

[11] NASA, First created image of the Van Allen radiation belts by the NASA after their discovery in 1958, (2021) https://www.nasa.gov/feature/goddard/2018/studying-the-van-allen-belts-60-years-after-america-s-first-spacecraft.

[12] JEDEC, Measurement and reporting of alpha particle and terrestrial cosmic ray-induces soft errors in semiconductor devices, (2012) https://www.jedec.org/.

[13] CEA, Laser Mégajoule, (2021) http://www-lmj.cea.fr.

[14] F. B. McLean and T. R. Oldham, "Basic mechanisms of radiation effects in electronic materials and devices. Final report September 1986-September 1987", (1987).

[15] A. Lechner, *Particle Interactions with Matter in Proceedings of the CAS-CERN Accelerator School on Beam Injection Extraction and Transfer* (CERN, CH-1211, Geneva 23, Switzerland, 2018).

[16] Insoo Jun, M. A. Xapsos, S. R. Messenger, E. A. Burke, R. J. Walters, G. P. Summers, and T. Jordan, "Proton nonionizing energy loss (NIEL) for device applications", IEEE Trans. Nucl. Sc. **50**, 1924–1928 (2003).

[17] D. M. Fleetwood, P. S. Winokur, and J. R. Schwank, "Using laboratory X-ray and cobalt-60 irradiations to predict CMOS device response in strategic and space environments", IEEE Trans. Nucl. Sc. **35**, 1497–1505 (1988).

[18] R. A. B. Devine, W. L. Warren, J. B. Xu, I. H. Wilson, P. Paillet, and J. L. Leray, "Oxygen gettering and oxide degradation during annealing of Si/SiO2/Si structures", J. App. Phys. **77**, 175 (1995).

[19] F. B. McLean, "A Framework for Understanding Radiation-Induced Interface States in SiO2 MOS Structures", IEEE Trans. Nucl. Sc. **27**, 1651–1657 (1980).

[20] J. R. Schwank, P. S. Winokur, et al., "Radiation-Induced Interface-State Generation in MOS Devices", IEEE Trans. Nucl. Sc. **33**, 1177–1184 (1986).

[21] H. E. Boesch and J. M. McGarrity, "Charge Yield and Dose Effects in MOS Capacitors at 80 K", IEEE Trans. Nucl. Sc. **23**, 1520–1525 (1976).

[22] T. R. Oldham, A. J. Lelis, H. E. Boesch, J. M. Benedetto, F. B. McLean, and J. M. McGarrity, "Post-Irradiation Effects in Field-Oxide Isolation Structures", IEEE Trans. Nucl. Sc. **34**, 1184–1189 (1987).

[23] M. L. Alles, H. L. Hughes, D. R. Ball, P. J. McMarr, and R. D. Schrimpf, "Total-Ionizing-Dose Response of Narrow Long Channel 45 nm PDSOI Transistors", IEEE Trans. Nucl. Sc. **61**, 2945–2950 (2014).

[24] J. Prinzie, J. Steyaert, and M. Leroux, *Radiation Effects in CMOS Technology. In: Radiation Hardened CMOS Integrated Circuits for Time-Based Signal Processing. Analog Circuits and Signal Processing* (Springer, 2018).

[25] R. Gaillard, ""single event effects: mechanisms and classification"", in *Soft errors in modern electronic systems*, edited by M. Nicolaidis (Springer US, Boston, MA, 2011), pp. 27–54.

[26] F. W. Sexton, "Destructive single-event effects in semiconductor devices and ICs", IEEE Trans. Nucl. Sc. **50**, 603–621 (2003).

[27] S. R. Messenger, E. A. Burke, M. A. Xapsos, G. P. Summers, R. J. Walters, Insoo Jun, and T. Jordan, "NIEL for heavy ions: an analytical approach", IEEE Trans. Nucl. Sc. **50**, 1919–1923 (2003).

[28] P. J. Griffin, *Uncertainty in silicon displacement damage metrics due to the displacement threshold treatment* (2016), pp. 1–4.

[29] J. B. Gibson, A. N. Goland, M. Milgram, and G. H. Vineyard, "Dynamics of Radiation Damage", Phys. Rev. Jour. Arch. **120**, 1229–1253 (1960).

[30] K. Nordlund, J. Wallenius, and L. Malerba, "Molecular dynamics simulation of threshold displacement energies in Fe", Nucl. Instr. Meth. Phys. R. B **246**, 322–332 (2006).

[31] K. Nordlund, S. J. Zinkle, S. A. E., F. Granberg, A. R. S., R. E. Stoller, T. Suzudo, L. Malerba, F. Banhart, W. J. Weber, F. Willaime, S. L. Dudarev, and D. Simeone, "Primary radiation damage: A review of current understanding and models", Phys. Rev. B **512**, 450–479 (2018).

[32] M. J. Boschini, P. G. Rancotta, and M. Tacconi, SR-NIEL Calculator: Screened Relativistic (SR) Treatment for Calculating Displacement Damage and Nuclear Stopping Powers for Electrons Protons Light- and Heavy-Ions in Materials (version 7.3.0), `http://www.sr-niel.org/`.

[33] J. F. Ziegler, M. D. Ziegler, and J. P. Biersack, "SRIM - The stopping and range of ions in matter (2010)", Nucl. Instr. Meth. Phys. R. B **268**, 1818–1823 (2010).

[34] J. R. Parsons and C. W. Hoelke, "Observation of Crystal Lattice Planes in Neutron and Ion Bombarded Ge Invited Paper", IEEE Trans. Nucl. Sc. **16**, 37–42 (1969).

[35] J. W. Palko and J. R. Srour, "Amorphous Inclusions in Irradiated Silicon and Their Effects on Material and Device Properties", IEEE Trans. Nucl. Sc. **55**, 2992–2999 (2008).

[36] K. Nordlund, M. Ghaly, R. S. Averback, M. Caturla, T. Diaz de la Rubia, and J. Tarus, "Defect production in collision cascades in elemental semiconductors and fcc metals", Phys. Rev. B **57**, 7556–7570 (1998).

[37] S. M. Sze and K. K. Ng, *Physics of Semiconductor Devices*, 3rd ed. (Wiley, 2006).

[38] J. R. Srour, C. J. Marshall, and P. W. Marshall, "Review of displacement damage effects in silicon devices", IEEE Trans. Nucl. Sc. **50**, 653–670 (2003).

[39] C. W. Gwyn and B. L. Gregory, "Designing Ultrahard Bipolar Transistors", IEEE Trans. Nucl. Sc. **18**, 340–349 (1971).

[40] R. M. Fleming, C. H. Seager, D. V. Lang, and J. M. Campbell, "Annealing neutron damaged silicon bipolar transistors: Relating gain degradation to specific lattice defects", J. App. Phys. **108**, 063716 (2010).

[41] J. L. Gorelick and R. Ladbury, "Proton neutron and gamma degradation of optocouplers", IEEE Trans. Nucl. Sc. **51**, 3730–3735 (2004).

[42] H. Y. Tada, J. R. Carter, B. E. Anspaugh, and R. G. Downing, *Solar Cell Radiation Handbook*, 3rd ed. (JPL Publication, 1982).

[43] J. R. Srour and J. W. Palko, "Displacement Damage Effects in Irradiated Semiconductor Devices", IEEE Trans. Nucl. Sc. **60**, 1740–1766 (2013).

[44] J. Belloir, V. Goiffon, C. Virmontois, P. Paillet, M. Raine, R. Molina, C. Durnez, O. Gilard, and P. Magnan, "Dark Current Spectroscopy in Neutron Proton and Ion Irradiated CMOS Image Sensors: From Point Defects to Clusters", IEEE Trans. Nucl. Sc. **64**, 27–37 (2017).

[45] A. Jay, A. Hémeryck, N. Richard, L. Martin-Samos, M. Raine, A. Le Roch, N. Mousseau, V. Goiffon, P. Paillet, M. Gaillardin, and P. Magnan, "Simulation of Single Particle Displacement Damage in Silicon–Part III: First Principle Characterization of Defect Properties", IEEE Trans. Nucl. Sc. **65**, 724–731 (2018).

[46] C. Virmontois, V. Goiffon, P. Magnan, O. Saint-Pe, S. Girard, S. Petit, G. Rolland, and A. Bardoux, "Total Ionizing Dose Versus Displacement Damage Dose Induced Dark Current Random Telegraph Signals in CMOS Image Sensors", IEEE Trans. Nucl. Sc. **58**, 3085–3094 (2011).

[47] G. H. Saboya, "Defects in silicon: revisiting theoretical frameworks to guide ab initio characterization", Université Toulouse 3 Paul Sabatier, (2020) https://tel.archives-ouvertes.fr/tel-03158564/.

Stopping theory, predictive damage models and development of a multiscale simulation approach

2

Contents

Introduction

The energy loss of a particle inside matter can be divided into ionizing energy loss and non-ionizing energy loss, depending on whether the interactions involve the electrons or the nuclei of the target material. The collisions at stake in a cascade event originate from the interactions responsible for non-ionizing energy losses, which encompasses both nuclear Coulomb interactions and strong nuclear interactions. With the thorough description of collision cascades made in the previous chapter, one can understand that the production of defects inside the matter is mainly due to elastic Coulomb interactions, as this is the mechanism by which the atoms are displaced from their crystalline sites in a collision cascade. Indeed, the energy of displaced atoms during a cascade is, in most cases, not sufficient to make them overcome the electrostatic barrier of the nucleus and interact directly via the strong force. However, strong nuclear interactions are of specific interest to describe the creation of PKAs by an incident energetic particle, a neutron or even a charged particle if its energy is high enough. Still, we focus in this chapter on the mechanisms leading to defects creation inside matter, and therefore choose to restrict ourselves to Coulomb interactions. Thus, we place ourselves in the framework of the stopping power theory, which splits the total stopping power experienced by a charged particle due to Coulomb interactions in nuclear and electronic stopping following the equation below, already seen in the previous chapter:

$$\frac{dE}{dx} = \frac{dE}{dx}\Big|_{nuclear} + \frac{dE}{dx}\Big|_{electronic} \tag{2.1}$$

With the primary purpose of reviewing the theoretical developments at the basis of atomic displacements due to irradiation and therefore nuclear stopping power, we present in Section 2.1.1 the landmark developments of what is known as the nuclear stopping theory (first term on left-hand side of (2.1)), actually describing the collisions between the atoms interacting via nuclear Coulomb interactions. However, in addition to the nuclear stopping, as we have seen in the first chapter of this thesis, the electronic stopping power is not to be omitted for an accurate description of DD and collision cascades, even if it is not responsible for defects production. Indeed, the atoms displaced in matter, depending on the energy which was imparted to them, lose a non-negligible part of their energy to the excitation of electrons. A theoretical description of the electronic stopping power (second term on the left-hand side of (2.1)), focusing on ions, will then be provided in Section 2.1.2. In parallel with the development of the nuclear and electronic stopping theories, analytical models for the prediction of the displacement damage caused to a material by an incoming particle were derived. We are going to present those models, their evolution over time and point out their limitations (Section 2.2). Finally, in light of the theories relevant for the description of DD and predictive models presented, we will detail the strategy we have chosen to adopt to finely study DD in semiconducting materials. The modeling strategy relies on an ambitious multiscale simulation approach covering all the aspects of DD, from the interaction of the material with the incident particle to the electronic properties of defects (Section 2.3).

2.1 Stopping theory

Theoretical work on the subject of the stopping of charged particles in matter due to Coulomb interactions were motivated by the experimental evidence of the existence of rays of electrons and ions, respectively obtained by Thomson in 1897 and Goldstein in 1902, and the progressive unravelling of the radioactivity of atoms, from the works of Becquerel to the ones of Pierre and Marie Curie as well as the studies of Fréderic and Irène Joliot-Curie.

The first theoretical models, developed in the early 1910s, were entirely classical. Thomson derived analytical expressions for the energy transferred by a charged particle hitting another charged particle: his work is considered precursor in the field as it was the first comprehensive

treatment of classical Coulomb scattering between charged particles. However, contrary to Rutherford, he did not derive an expression for the stopping power itself. Moreover, in Thomson model of the atom on which he based his work, there is no nucleus. His views on the stopping power were then outdated by the Rutherford model of the atom and its consequences. Indeed, the Rutherford model incorporates a positively charged and very small nucleus around which the electrons are orbiting like planets around the sun. According to Rutherford, the energy T transmitted by a particle of mass m_1, charge q_1 and velocity v to another particle of charge q_2 and mass m_2 during a collision where the perpendicular distance between the path of the first particle and the position of the second one (impact parameter) is b writes [1]:

$$T = \frac{2q_1^2 q_2^2 k_C^2}{m_2 v^2 b^2} \left(1 + \left(\frac{q_1 q_2}{\mu v^2 b}\right)^2\right)^{-1} \tag{2.2}$$

where $\mu = m_1 m_2/(m_1 + m_2)$ is called the reduced mass and $k_C = 1/4\pi\epsilon_0$ is the Coulomb constant. If we consider that the target does not move and that the projectile particle follows a straight path, (2.2) becomes:

$$T = \frac{2q_1^2 q_2^2 k_C^2}{m_2 v^2 b^2} \tag{2.3}$$

Finally, assuming a particle density n and limiting the integration to b_{min} and b_{max}, respectively the minimum and maximum reachable impact parameters, the stopping power felt by a particle of charge q_1 and mass m_1 in a medium of charged particles of charge q_2, mass m_2 and density n can be written:

$$S_{Rutherford}(v) = n\frac{4\pi q_1^2 q_2^2 k_C^2}{m_2 v^2} \ln\left(\frac{b_{max}}{b_{min}}\right) \tag{2.4}$$

The above equation is valid both for stopping by electrons and stopping by nuclei. It is thus common to nuclear and electronic stopping. An important prediction made by (2.4), which was confirmed by more recent theories and experiments, is the greater significance of the electronic stopping over nuclear stopping at high velocities, and inversely [1]. Indeed, when v is large, the stopping is dominated by the prefactor term, which becomes greater as m_2 decreases [1]. Electrons then contribute more to stopping at large v. The Rutherford stopping model is a landmark in the stopping theory as it was the first model providing an analytical expression for the stopping power, on top of that treating on an equal footing electronic and nuclear stopping. However, at this time, just before the birth of quantum mechanics, atomistic models evolved very quickly, and the Rutherford model of the atom was replaced, just like it itself replaced the Thomson model, by the 1913 Bohr model, who stated that the electrons were confined to discrete orbitals around a nucleus of negative charge. Bohr studies on the stopping theory, contrary to Rutherford views, split the stopping of a charge particle into matter into two contributions, nuclear and electronic, following the equation in the introduction of this chapter. The Bohr stopping model is the last one being entirely classical, all the models that followed were based on the Schrödinger model of the atom and more generally quantum mechanics. It is interesting to note that major breakthroughs in the early stopping theory were strongly correlated with the evolution of atomistic models, which are illustrated in Fig. 2.1. Indeed, Thomson, Rutherford and Bohr all developed their own model of the atom and the subsequent stopping theory based on this model.

After the works of Bohr in 1913 and for many years, distinct theories were developed for nuclear and electronic stoppings using the tools of quantum mechanics. However, the transition between the two regimes was unclear. Fortunately, in the 1960s, splitting of the theory between electronic and nuclear was made obsolete by the famous Lindhard Scharff and Schiott (LSS) stopping theory [2, 3], who developed a unified theory of nuclear and electronic stoppings, showing not a sharp but a smooth and continuous transition between the two regimes. Concerning

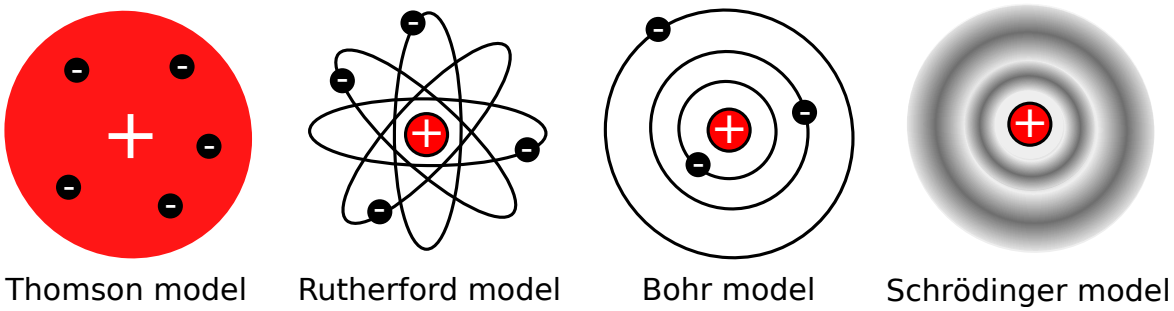

Figure 2.1: *Evolution of the atomistic models from Thomson to Schrödinger.*

nuclear stopping, the LSS theory contributed to the derivation of an accurate analytical expression for the electrostatic potential generated by an atom around itself. This treatment of the nuclear stopping is of main interest for us as it is used into atomistic simulation models. We therefore dedicate Section 2.1.1 to a brief historical and theoretical overview of the conceptual developments that led to the well known Ziegler Biersack Littmark (ZBL) formula for nuclear stopping power [4]. Regarding electronic stopping, a formula for its calculation is developed in the LSS theory, confirming some of the theoretical predictions made by earlier models. In Section 2.1.2, we review the different models of electronic stopping which led to the LSS theory, starting with the Bohr model of stopping in 1913. Those models are highly interesting in the context of atomistic simulations as they are used in many simulation softwares.

2.1.1 Interatomic potential for explicit treatment of nuclear stopping

A few years after Bohr works on the stopping theory, the 1927 Thomas-Fermi atomistic model significantly contributed to improve the theoretical description of the interactions between charged particles and therefore the nuclear stopping. The Thomas-Fermi model is a semiclassical model, whose formalism does not involve the recently introduced electronic wavefunctions of quantum mechanics at the heart of the Schrödinger model of the atom, but only the electronic density $n(r)$ [5]. Initially, this model was derived as an approximation to the distribution of electrons in an atom. Thomas and Fermi showed in their model that the potential $V(r)$ felt by an electron located at a distance r of a nucleus of charge Ze can be written [6]:

$$V(r) = \frac{Ze}{4\pi\epsilon_0 r}\phi\left(\frac{r}{b}\right) \tag{2.5}$$

with

$$b = \frac{1}{4}\left(\frac{9\pi^2}{2Z}\right)^{1/3} a_0 \tag{2.6}$$

where a_0 is the Bohr radius. The potential expression of (2.5) takes the form of a classical Coulomb interaction with a nucleus of charge Ze, screened by the electrons around it, whose effects are included in $\phi(r/b)$. The b quantity is known as the screening length and defines the typical distance of the screening effect of the electrons: when $r << b$, the interaction is nearly not screened, whereas when $r >> b$, the electrons completely screen the interaction. In the Thomas-Fermi model, the screening function ϕ is solution to the following differential equation, known as the Thomas-Fermi equation:

$$\frac{d^2\phi}{dr^2} = \frac{\phi^{3/2}}{\sqrt{r}} \tag{2.7}$$

with the initial condition $\phi(0) = 1$. From (2.5) the potential energy $E_{rep}(r)$ (leading to a repulsive two-body force) originating from the interaction of an incoming particle of atomic

number Z_1 with an atom of the material of atomic number Z_2 can be easily obtained:

$$E_{rep}(r) = \frac{Z_1 Z_2 e^2}{4\pi\epsilon_0 r}\phi\left(\frac{r}{b}\right) \tag{2.8}$$

The potential energy form of (2.8) is the one still in use for the simulation of collision cascades in various simulation techniques. Nonetheless, the Thomas-Fermi equation has no known analytical solution. Thus, in more recent developments, specifically targeting an accurate description of collisions between atoms, and not an atomistic description like Thomas and Fermi, the screening function $\phi(r/b)$ approximates a solution to the Thomas-Fermi equation (2.7), or is obtained by fitting to computational and/or experimental data.

The first expression of an interatomic potential energy describing the elastic Coulomb interactions between a charged particle and an atom, taking as basis (2.5), was obtained from the work of Moliere in 1947 [7]. The cited article is in German, but the mathematical expression of the screening function and its parameters are given in the equations (7.1a) and (7.1b) of the article. Moliere has used a screening corresponding to an empirical fit to the Thomas-Fermi equation under the form of a sum of exponential:

$$\phi(x) = 0.35e^{-0.3x} + 0.55e^{-1.2x} + 0.1e^{-6x} \tag{2.9}$$

with $x = r/a_{moliere}$ and $a_{moliere} = 0.8853a_0(Z_1^{1/2} + Z_2^{1/2})^{-2/3}$.

Later, with the advent of the *ab initio* electronic structure calculations, a "repulsive" interatomic potential energy describing the electrostatic interactions between charged particles and atoms was derived by Ziegler, Biersack and Littmark [4] in 1983. They kept the Thomas-Fermi formalism of (2.8) but chose to fit the screening function with a sum of exponential, just like the Moliere expression, to Hartree-Fock calculations (*ab initio* method) performed on many different couples of atoms. They obtained a mean potential energy for the interaction between two atoms known as the universal ZBL potential. The universal screening function they fit is the following:

$$\phi(x) = 0.18175e^{-0.31998x} + 0.50986e^{-0.94229x} + 0.28022e^{-0.4029x} + 0.02817e^{-0.20162x} \tag{2.10}$$

with $x = r/a_{ZBL}$ and $a_{ZBL} = 0.8853a_0(Z_1^{0.23} + Z_2^{0.23})^{-1}$. The Moliere and ZBL potential energy for Si-Si collisions are plotted in Fig. 2.2.

Still today, this expression for the screening function of the electrostatic potential created by an atom is used in many simulation codes and is considered to be the most advanced universal theoretical development related to nuclear stopping of charged particles by atoms via Coulomb interactions.

2.1.2 Electronic stopping power

If the theoretical developments we choose to present for the nuclear stopping did not follow the path initiated by Rutherford to derive expressions for the stopping power, this is not the case of the existing literature on the electronic stopping. Indeed, the theoretical works on the electronic stopping can be viewed as a gradual improvement of the classical Rutherford stopping formula. All the stopping formulas presented in the following are valid for non-relativistic projectiles. Readers interested in the relativistic extensions of those formulas should look in the cited references.

Following Rutherford formula (2.4), taking as a basis its atomistic model, Bohr developed its own electronic stopping theory [8]. He considered that a charged projectile interacts with classical electrons harmonically bound to their nuclei and orbiting with an angular frequency w_j. The

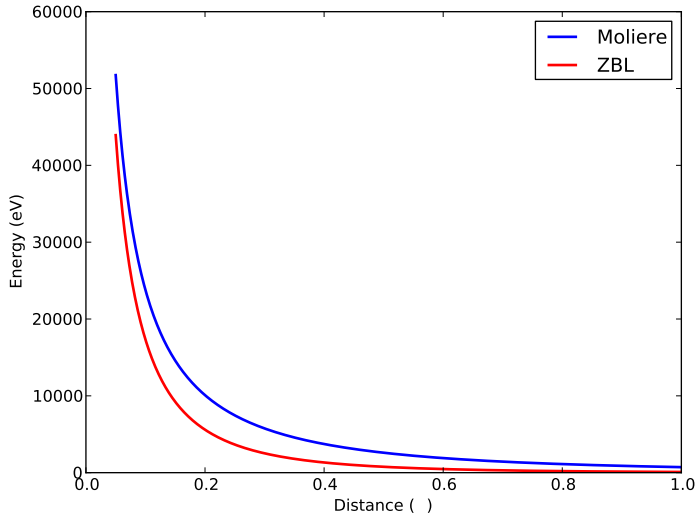

Figure 2.2: *Moliere and ZBL potentials for Si-Si collisions as a function of the interatomic distance.*

magnitude of the Coulomb interaction is considered not to vary during a collision, the path of the projectile is undisturbed and the electrons remain at rest [1]. It led to the following expression for the electronic stopping power $S_{Bohr}(v)$ of a particle of charge Z_1, of velocity v in a medium of electronic density n:

$$S_{Bohr}(v) = n\frac{4\pi Z_1^2 e^4 k_C^2}{m_e v^2}\ln\left(\frac{C m_e v^3}{Z_1 k_C e^2 w_r}\right) \tag{2.11}$$

where C is a dimensionless constant equal to 1.1229, m_e the electron mass and w_r is the resonance frequency of the harmonic oscillator considered for the derivation of the formula. The expression derived by Bohr for the electronic stopping is only valid above a threshold velocity $v_0 = c/137$ (about 700 keV for a Si atom and 1800 keV for a Ge atom) known as the Bohr velocity. It successfully predicted the existence of a Bragg peak for the electronic stopping and the $1/v^2$ decrease of the electronic stopping after the peak. However, before the Bragg peak, the model fails to predict the right velocity dependence of the electronic stopping.

Nearly two decades after the classical treatment of stopping by Bohr, benefiting from the developments of quantum mechanics, Bethe derived the first quantum-based formula for the electronic stopping power. It states that the electronic stopping acting on a particle of charge Z_1 and velocity v in a medium of electronic density n writes [1]:

$$S_{Bethe}(v) = n\frac{4\pi Z_1^2 e^4 k_C^2}{m_e v^2} L_{Bethe} \tag{2.12}$$

with

$$L_{Bethe} = \sum_j f_j \ln\left(\frac{2 m_e v^2}{\hbar w_j}\right) \tag{2.13}$$

where $\hbar w_j$ is the energy associated to the j^{th} excitation of electrons in the target atom and f_j is a generalized oscillator strength [1]. In practice, the j^{th} electronic excitation is hardly reachable. However, it is conceivable to calculate the average excitation energy I defined as:

$$\ln(I) = \sum_j f_j \ln(\hbar w_j) \tag{2.14}$$

with the empirical formula $I = Z_2 \times (10\ eV)$, Z_2 being the charge number of the target atom [1]. Combining (2.12), (2.13) and (2.14), we finally reach the following formula for Bethe stopping:

$$S_{Bethe}(v) = n\frac{4\pi Z_1^2 e^4 k_C^2}{m_e v^2}\ln\left(\frac{2m_e v^2}{I}\right) \tag{2.15}$$

It is interesting that the Bethe formula, derived from a quantum mechanic treatment, is in many ways similar to the classical Bohr formula. Indeed, just like the Bohr formula, the Bethe one is in good agreement with experimental data for velocities greater than the Bragg peak, gives a fairly accurate position for the Bragg peak [1], but fails to provide the correct stopping power behavior for velocities below the Bragg peak. The Bethe formula actually diverges for velocities smaller than $\sqrt{I/2m_e}$, this quantity being its lower velocity limit. Fig. 2.3, illustrates the success and failures of the Bethe and Bohr stopping formulas by displaying the electronic stopping power of Si projectiles into Si calculated with the Bohr formula, the Bethe formula and with the SRIM code [9], with respect to the energy of the incident ion. The accurate description of electronic stopping both by Bohr and Bethe formula at high velocities only can be clearly seen, as well as the consistency of Bohr and Bethe theoretical treatment.

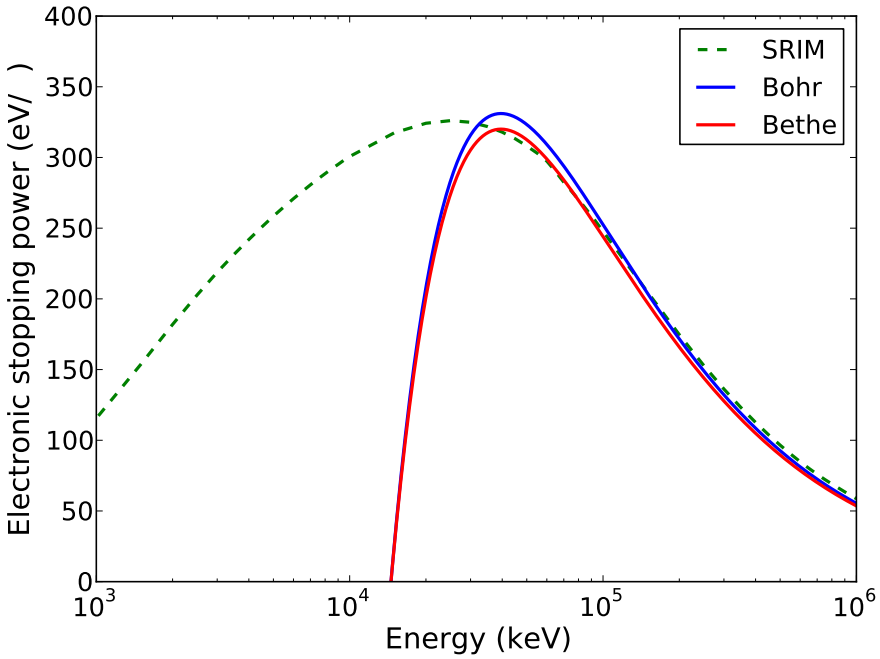

Figure 2.3: *Electronic stopping power of Si projectiles into Si calculated with the Bohr formula, the Bethe formula and with the SRIM code (which can be considered here as the reference data), with respect to the projectile energy $E \propto v^2$. The Bohr and Bethe formula have been treated parametrically respectively as $A/v^2 \times ln(Bv^2)$ and $A'/v^2 \times ln(B'v^3)$, with A, B, A' and B' parameters chosen so that the Bohr and Bethe curves are the closest possible to the SRIM data. This figure is displayed for illustrative and pedagogical purposes only and should not be interpreted or discussed quantitatively.*

Both Bohr and Bethe formulas not being valid for low velocity projectiles, a specific formula describing low velocity projectiles was derived by Fermi and Teller in 1947 [10]. Taking as a basis a free electron gas model, they stated that a particle of charge Z_1 and velocity $v < v_0$ is subject in a free electron gas, with electrons having a Fermi velocity v_F, to the following electronic stopping power:

$$S_{Fermi-Teller}(v) = \frac{2Z_1^2 m_e^2 e^4 k_C^2 v}{3\pi\hbar^3}\ln\left(\frac{\hbar v_F}{k_C e^2}\right) \tag{2.16}$$

The linear evolution of the electronic stopping power with respect to the velocity of the projectile, today a well-known characteristic of electronic stopping of slow projectiles, is made explicit by the formulation of the Fermi-Teller stopping.

Bohr, Bethe and Fermi-Teller electronic stopping formulas are only valid each in their own velocity range. However, in the late 50s and at the beginning of the 60s, with the advent of nuclear power as a source of energy, there was a strong motivation for a global electronic stopping theory which would be valid for all velocities. It is Lindhard who paved the way for such theoretical models [2, 3]. All the models presented so far were built from the interaction between a projectile and a single target atom. This assumption is certainly valid for a dilute stopping medium like a gas, but is not for a solid or liquid target. Indeed, the electronic clouds of the atoms are mutually influenced by each other as well as by the projectile. Lindhard proposed in 1954 to describe electronic stopping by magnetic field equations in order to take into account the response of the medium. In doing so, he introduced a new conception of the dielectric function of a material, which gave birth to the field of the dielectric stopping theory. It was intially developed for an electron gas model, but can be adapted to solids and liquids via the Local Density Approximation (LDA). For more details about this specific aspect interested readers can refer to the PhD thesis of Abdullah Shukri [11]. In Lindhard theory, for an electron gas whose dielectric response ϵ is linear, the electronic stopping formula for a projectile of charge Z_1 and velocity v gives:

$$S_{Lindhard}(v) = \frac{2Z_1^2e^2}{\pi v^2}\int_0^\infty \frac{dk}{k}\int_0^{kv} wdw.\mathrm{Im}\left(\frac{-1}{\epsilon(k,w)}\right) \tag{2.17}$$

where k is the wavevector and w is the frequency. A detailed description of the Lindhard theory of stopping is beyond the scope of this chapter. However, it is interesting to give a bit more details on the outcomes of the Lindhard theory for low velocity projectiles (below the Bohr velocity), which are of main interest for the description of collision cascades. Lindhard and Scharff [12] found, just like Fermi-Teller did a few years earlier, that the stopping power of low velocity projectiles should be proportional to their velocity v following the relation below:

$$S_{Lindhard-Scharff}(v) = n8\pi k_C a_0 e^2 \xi_e \frac{Z_1 Z_2}{Z}\frac{v}{v_0} \tag{2.18}$$

where ξ_e is an empirical fitting factor defined as $Z_1^{1/6}$ by Lindhard and Scharff, $Z = (Z_1^{2/3} + Z_1^{2/3})^{3/2}$ and v_0 is the above-defined Bohr velocity. Almost at the same time but independently, Firsov [13] came up with a formula also giving the electronic stopping as being proportional to the velocity of the projectile:

$$S_{Firsov}(v) = n\frac{C\hbar a_0}{2^{4/3}}(Z_1 + Z_2)v \tag{2.19}$$

with the parameter C being a dimensionless constant to be estimated. In Firsov original work it was chosen equal to 20.4, no matter the values of Z_1 and Z_2. The stopping formula of Firsov as well as the one of Lindhard and Scharff for low velocity ions will be of much use for the development of atomistic models of electronic stopping, as will be shown in the next chapter.

We quickly passed on the history of the theoretical developments related to electronic stopping, but readers interested by all the mentioned theories should refer to the reference books on the penetration of particles into matter by Peter Sigmund [14, 15].

Simply in order to be complete on the subject of the electronic stopping, we can add that the Lindhard stopping formula is still relevant today in the context of the simulations of the penetration of particles into the matter as many simulation softwares, among them the well-known

SRIM code [9] uses it. Within SRIM, the empirical formula used for fitting to experimental data of the electronic stopping of an ion of charge Z_1, of velocity v by a medium constituted by atoms of charge Z_2 is given by the following relation [1]:

$$S(Z_1, Z_2, v) = Z_1^2 \gamma^2 S_{Lindhard}(Z_1 = 1, Z_2, v) \tag{2.20}$$

where $S_{Lindhard}(Z_1 = 1, Z_2, v)$ is the stopping of a proton in the Lindhard theory and γ is a factor, in practice between 1.0 and 1.2, used for fitting to experimental data.

2.2 Analytical predictive models of displacement damage

This section is dedicated to the presentation of the main predictive models of DD in materials. The ultimate purpose of all these models is the calculation of the number of displaced atoms depending on the initial energy E_{PKA} of the PKA. The first and probably most widely known derivation of a predictive model was made by Kinchin and Pease [16]. In this model, as assumed in the introduction of this chapter, all atoms displacements result from Coulomb interactions between the nuclei. Depending on the energy of the moving ions inducing collisions, the Kinchin-Pease model is divided into three regimes: (i) when E_{PKA} is smaller than the threshold displacement energy E_d, no atoms are displaced, (ii) when E_{PKA} is greater than E_d but smaller than $2E_d$, the PKA is able to displace an atom, but the displaced atom energy will not be sufficient to transmit an energy E_d to another atom and therefore displace it: in this case, only one atom is displaced, (iii) when E_{PKA} is greater than $2E_d$, all collisions lead to displacement and Kinchin and Pease derive a formula for the number of displaced atoms $N_d = E_{PKA}/2E_d$. What was just said can be summed up in the following formula:

$$\begin{cases} N_d = 0 & \text{if } E_{PKA} < E_d \\ N_d = 1 & \text{if } E_d \leq E_{PKA} < 2E_d \\ N_d = \frac{E_{PKA}}{2E_d} & \text{if } E_{PKA} \geq 2E_d \end{cases} \tag{2.21}$$

When the Kinchin-Pease model came out in 1955, E_{PKA} was chosen as the total energy of the PKA. However, after the work on the electronic stopping power of Lindhard that we introduced in Section 2.1.2, it was agreed that the part of the energy going into electronic excitations should be subtracted from E_{PKA}. In the following, we call $\bar{E}$ the part of E_{PKA} really going into atomic displacements. Despite its excessive simplicity and proofs of its incapacity in calculating correct number of displaced atoms [17], the Kinchin-Pease model is still in use today in some simulation code, like in the "quick calculation" mode of SRIM.

Nearly two decades later, in the 70s, simulation results which showed that about 20% of the empty sites left by displaced atoms are filled by another atom, encouraged Norgett Torrens and Robinson to review the Kinchin-Pease model and proposed a new formulation of it integrating a recombination factor. Their model is known as the NRT model [18]:

$$\begin{cases} N_d = 0 & \text{if } \bar{E} < E_d \\ N_d = 1 & \text{if } E_d \leq \bar{E} < 2E_d/0.8 \\ N_d = 0.8 \times \frac{\bar{E}}{2E_d} & \text{if } \bar{E} \geq 2E_d/0.8 \end{cases} \tag{2.22}$$

The 0.8 factor now appearing takes into account the defects recombination rate of 20% which was obtained at the time. Even if the NRT model provides results in better agreement with atomistic simulations, it still highly overestimates the number of displaced atoms, and underestimates the number of replaced atoms, as attests the comparison made with experimental data [17]. Very recently, those limitations motivated new research to refresh those theoretical models in light of the modern experiments and simulations it is now possible to carry out.

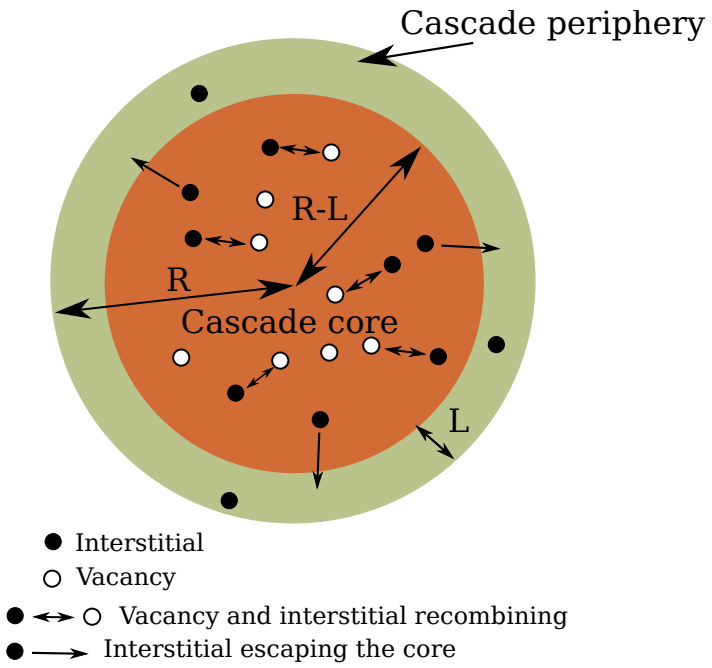

Figure 2.4: *Representation of the assumption and concepts at the basis of the arc-dpa model.*

With the objective of improving the Kinchin-Pease and NRT models, Kai Nordlund and coworkers proposed in 2018 a simple yet interesting improvement targeting the recombination of interstitials and vacancies in collision cascades [19]. Their model is named the athermal recombination corrected displacements per atom (arc-dpa). They assume that a Frenkel pair will not recombine if the vacancy and the interstitial are separated by a distance greater than a distance L, which they name the spontaneous recombination distance. It is also assumed that cascades, when not yet split into subcascades, are spherical of radius R. They state that the defects located in the cascade core, described as a dense defect region, have a great chance of recombining, whereas defects located in the outskirts of the cascade, in the zone between the frontier of the cascade R and the frontier of the cascade core radius $R-L$, will not recombine. The core of the cascade is richer in vacancies as interstitial atoms are transported from the cascade core to the periphery region. The situation is depicted in Fig. 2.4. The fraction of defects which will survive ξ is therefore given by a simple volume ratio:

$$\xi = \frac{V_{outskirt}}{V_{total}} = \frac{4/3\pi R^3 - 4/3\pi(R-L)^3}{4/3\pi R^3} = 3\frac{L}{R}(1-\frac{L}{R}) \tag{2.23}$$

which can be simplified considering that L is very small compared to R in $\xi = 3\frac{L}{R}$. Going further into the refinement of the model, the radius R of the cascade was found for the materials they investigated with SRIM to be related to the energy of the PKA by a power law relation of the form $R = A \times \bar{E}^x$, A being a constant. The number of displaced atoms can thus be written $N_d = 0.4\bar{E}/E_d \times \xi = 0.4\bar{E}/E_d \times 3L/R \propto 1.2L/E_d \times \bar{E}^{1-x}$. The number of defects is thus proportional to $\bar{E}^{1-x}$. Further improvements taking into account the fact that high energy collision cascades might split into subcascades gives the following expression for the number of defects created within the arc-dpa model:

$$\begin{cases} N_d = 0 & \text{if } \bar{E} < E_d \\ N_d = 1 & \text{if } E_d \leq \bar{E} < 2E_d/0.8 \\ N_d = 0.8 \times \frac{\bar{E}}{2E_d} \times \xi_{arcdpa}(\bar{E}) & \text{if } \bar{E} \geq 2E_d/0.8 \end{cases} \tag{2.24}$$

with

$$\xi_{arcdpa}(\bar{E}) = \frac{1 - c_{arcdpa}}{(2E_d/0.8)^{b_{arcdpa}}}\bar{E}^{arcdpa} + c_{arcdpa} \tag{2.25}$$

where b_{arcdpa} and c_{arcdpa} are material constants that need to be determined by experiments or simulations. The arc-dpa model successfully reproduced the number of defects created into experiments in metals [19].

Despite the satisfactory improvements brought by the arc-dpa model, it suffers from some limitations. For example, the assumption stating that cascades are spherical at low energies can be discussed. This is certainly reasonable for some metals [20] and Ge [21], but is hardly valid for Si [22]. Also, the model needs to be parametrized with simulations, which makes the choice of the method for counting defects very important, as the results obtained can be drastically different [20]. Moreover, the timescale associated to simulations can be very different from the characteristic timescale of experiments, making the comparison with experimental data uncertain. Finally, as seen in the previous chapter, the size and shape of the produced clusters of defects are essential in the electronic response of materials to DD. However, the predictive models presented are not able to provide such information. Understanding and predicting DD into materials for microelectronic applications thus have to resort to other means than prediction by analytical models.

2.3 Multiscale simulation approach

In the work we conduct, rather than envisioning DD and collision cascades as being predictable by analytical theoretical models, we aim at simulating the entire process of DD at the atomistic level. Therefore, the theories related to nuclear and electronic stopping are not directly usable as predictive tools to us, but are highly interesting once embedded in the simulation techniques we aim at employing.

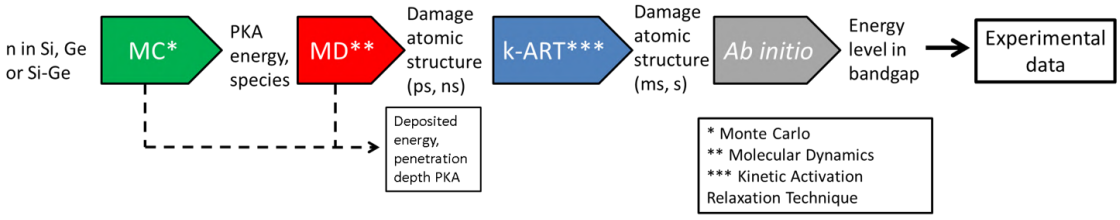

Figure 2.5: *Multiscale simulation approach.*

As we have seen in the previous chapter, the mechanisms at stake in a DD event are quite diverse, going from particle-matter interactions to diffusion of interstitials and vacancies and finally defects having an electronic activity. The global simulation approach we develop thus has to integrate very diverse techniques in their physical basis and working algorithms to be able to cover all aspects of DD. Fig. 2.5 is a schematic representation of our multiscale simulation approach.

The first step of it treats the interaction between the high energy incident particle and the material. We use the Geant4 Monte Carlo (MC) code [23–25] in which the interaction events are considered binary. This step is the only one during which the matter is described as being continuous and not discrete. Its working relies, among other aspects, on the numerical evaluation of interaction cross sections and stopping powers via formulas deriving from the Lindhard theory that we have seen in Section 2.1.2 for electronic stopping. It also makes great use of the interatomic interaction potentials to describe atomic collisions presented in Section 2.1.1. The very low computational cost of MC methods for particle-matter interaction allows obtaining statistical data on millions of events (one event being one particle-matter interaction). We are only interested in the first interaction of the incident particle leading to the creation of a PKA, and follow neither the trajectory of the particle after it interacted to create a PKA nor

the one of the PKA. This is explained by the fact that techniques relying on MC for particle-matter interactions consider those interactions as binary only and are thus not accurate at low energies when collective atomic effects like melting start being important. Therefore, the main information we retrieve from this MC step is an energy spectrum of the created PKAs as a function of the incident energy of the particle and its type. Also, Geant4 incorporates the possibility for spallation reactions to occur. We are therefore interested in the possible spallation products to identify the types of the created PKAs. After having identified the energies and PKAs types of interest, we have to turn to another simulation technique to propagate the collision cascades.

Molecular Dynamics (MD) is a very appropriate tool for the atomistic simulation of collision cascades. We use the well known LAMMPS code [26]. Using the energies identified as representative of the DD case we want to simulate, we initiate simulations by giving to an atom of the simulation box a velocity in the range of the identified energies and an initial direction. This atom will collide others in the box and thus propagate the cascade of collisions. MD simulations are discrete in time, and are based on the solving of the classical equations of motion for every atoms of the simulation box at each timestep of the simulation. At each timestep, the position and velocities of the atoms are updated. The interatomic potential energy expressions describing Coulomb interactions between nuclei presented in Section 2.1.1 are highly interesting for this technique as they can be almost directly used into MD simulations of collision cascades. However, electronic stopping is not as simple to integrate into MD simulations as the technique does not explicitly incorporate electrons in its usual formalism. Consequently, in order to take into account the electronic effects into MD simulations of collision cascades, additional models have to be employed. Those models are based on the Firsov and Lindhard low velocity electronic stopping formulas. They will be derived and discussed in detail in the next chapter.

After a few nanoseconds of MD simulation time, the damaged atomic structures are stable from the MD standpoint as there is not enough energy in the system to make the defects recombine and diffuse. However, experimentally, defects and clusters reordering occur on much longer timescales [27]. To overcome this limitation of MD, we employ the kinetic Activation-Relaxation Technique (kART) implemented in the simulation code of the same name [28]. It consists in the third step of the simulation project, and allows relaxing the damaged structures obtained in MD on timescales up to the second by easing the occurrence of rare reordering events compared to traditional MC codes. It is based on the exploration of the minima of the potential energy surface of the system by efficient numerical methods. Time is not defined explicitly like in MD but is obtained from the energy barriers associated to the events found. Timescales spanned by this technique can be expanded compared to MD because the computational calculation of low energy events (*i.e.* with a very low associated timescale) is accelerated so kART is able to find rarer higher energy events (*i.e.* with a higher associated timescale) in a reasonable computational time. The damaged structures healed with kART are then directly comparable with experimental observations as the respective timescales of the kART method and modern experiments are of the same order of magnitude.

The defects identified with kART as being the more representative are then characterized electronically with *ab initio* methods, namely Density Functional Theory (DFT) and GW calculations, in the fourth and last step of the global simulation approach. Those methods allow to solve, thanks to physical and numerical approximations, the Schrödinger equation of the electrons. In this last step, we are able to identify the different stable structures between which defects oscillate, the reorganization mechanism between each of them, the energy barriers associated and the extra energy levels created in the bandgap (or not) by the defects. After this last step, the ultimate purpose of our approach is to link the technologically observed phenomena like DC and DC-RTS to the electronic properties of the investigated defects. The more global

trends on the total number of defects and their distribution in clusters accessible via the MD and kART step could also allow to give some conclusions on the damage type (single interstitials and vacancies, small clusters, amorphous clusters) at the origin of DC and DC-RTS.

In this thesis, we present results obtained with the three first steps, namely MC, MD and kART. However, as the readers will understand in the next chapters, even if a first version of the entire simulation approach was already performed on Si [29–31], the main focus of this PhD work was on the improvement and testing of the MD step for which the simulation of accurate collision cascades is far from being trivial, due to the high stochasticity of collision cascades and the integration of electronic effects into MD. This last aspect of MD simulations led us to the use of a technique that we have not mentioned so far, the Time Dependent Density Functional Theory (TDDFT), which we have employed, to provide input data to models for the incorporation of electronic effects into MD. Therefore, in the next chapter, we will present in details the MC, MD, kART and TDDFT methods. The last *ab initio* step of the simulation approach is not covered in this manuscript. Other members of our research group are working full time on it. Interested readers on this specific step can refer to the PhD thesis of Gabriela Herrero Saboya [32], or the following article of Antoine Jay *et al.* [31].

Conclusion

Throughout the 20^{th} century, the nuclear and electronic stopping theories have evolved and gained in accuracy and range of applicability with the progress made in the description of atoms. In parallel, benefiting from the nuclear and electronic stopping theories, predictive analytical models were developed aiming at quantifying the number of displaced atoms in collision cascades. Because we are interested in a complete atomistic description of DD, essential for the understanding of observed electronic effects into microelectronic devices, we adopt the strategy to resort to the global simulation approach presented in Section 2.3. The nuclear and electronic stopping theoretical developments presented in Section 2.1 are of direct interest in some of the techniques employed in our multiscale approach. In the next chapter, we will present in detail the simulation techniques employed in our global simulation approach, detailing the theories lying behind them and developing the specific case of their use in the context of our multiscale approach for the simulation of DD in semiconducting materials.

References

[1] C. P. Race, D. R. Mason, M. W. Finnis, W. M. C. Foulkes, A. P. Horsfield, and A. P. Sutton, "The treatment of electronic excitations in atomistic models of radiation damage in metals", Rep. Prog. Phys. **73**, 116501 (2010).

[2] J. Lindhard, M. Sharff, and H. E. Schiott, "Range concepts and heavy ion ranges", Matisk-fysiske Meddelelser det Kongelige Danske Videnskabernes Selskab **33**, 1–44 (1963).

[3] J. Lindhard and A. Winther, "Stopping power of electron gas and equipartition rule", Matisk-fysiske Meddelelser det Kongelige Danske Videnskabernes Selskab **34**, 1–24 (1963).

[4] J. F. Ziegler, J. P. Biersack, and U. Littmark, *The Stopping Range of Ions in Solids*, 1st ed. (Pergamon Press, N. Y, 1983).

[5] L. H. Thomas, "The calculation of atomic fields", Mathematical Proceedings of the Cambridge Philosophical Society **23**, 542–548 (1927).

[6] C. J. Ortiz, L. Luneville, and D. Simeone, "1.19 - Binary Collision Approximation", in *Comprehensive nuclear materials*, edited by R. J. M. Konings and R. E. Stoller, 2nd ed. (Elsevier, Oxford, 2020), pp. 595–619.

[7] G. Moliere, "Theorie der Streuung schneller geladener Teilchen I. Einzelstreuung am abgeschirmten Coulomb-Feld", Zeitschrift für Naturforschung A **2**, 133–145 (1947).

[8] N. Bohr, "On the theory of the decrease of velocity of moving electrified particles on passing through matter", The London, Edinburgh, and Dublin Philosophical Magazine and Journal of Science **25**, 10.1080/14786440108634305 (1913).

[9] J. F. Ziegler, M. D. Ziegler, and J. P. Biersack, "SRIM - The stopping and range of ions in matter (2010)", Nucl. Instr. Meth. Phys. R. B **268**, 1818–1823 (2010).

[10] E. Fermi and E. Teller, "The Capture of Negative Mesotrons in Matter", Phys. Rev. **72**, 399–408 (1947).

[11] A. Shukri, "Ab initio electronic stopping power in materials", Ecole Polytechnique, (2015) https://pastel.archives-ouvertes.fr/tel-01269549/document.

[12] J. Lindhard and M. Scharff, "Energy Dissipation by Ions in the keV Region", Phys. Rev. **124**, 128–130 (1961).

[13] P. Sigmund, "Stopping of Slow Ions", in *Particle penetration and radiation effects volume 2: penetration of atomic and molecular ions* (Springer International Publishing, Cham, 2014), pp. 343–415.

[14] P. Sigmund, *Particle penetration and radiation effects volume 1: penetration of atomic and molecular ions* (Springer International Publishing, Cham, 2014).

[15] P. Sigmund, *Particle penetration and radiation effects volume 2: penetration of atomic and molecular ions* (Springer International Publishing, Cham, 2014).

[16] G. H. Kinchin and R. S. Pease, "The Displacement of Atoms in Solids by Radiation", Rep. Prog. Phys. **18**, 1–51 (1955).

[17] K. Nordlund, S. J. Zinkle, S. A. E., F. Granberg, A. R. S., R. E. Stoller, T. Suzudo, L. Malerba, F. Banhart, W. J. Weber, F. Willaime, S. L. Dudarev, and D. Simeone, "Primary radiation damage: A review of current understanding and models", Phys. Rev. B **512**, 450–479 (2018).

[18] M. J. Norgett, M. T. Robinson, and I. M. Torrens, "A proposed method of calculating displacement dose rates", Nuclear Engineering and Design **33**, 50–54 (1975).

[19] K. Nordlund, S. J. Zinkle, S. A. E., F. Granberg, A. R. S., R. E. Stoller, T. Suzudo, L. Malerba, F. Banhart, W. J. Weber, F. Willaime, S. L. Dudarev, and D. Simeone, "Improving atomic displacement and replacement calculations with physically realistic damage models", Nat. Comm. **9**, 1084 (2018).

[20] K. Nordlund, M. Ghaly, R. S. Averback, M. Caturla, T. Diaz de la Rubia, and J. Tarus, "Defect production in collision cascades in elemental semiconductors and fcc metals", Phys. Rev. B **57**, 7556–7570 (1998).

[21] P. Lopez, L. Pelaz, I. Santos, L. A. Marques, and M. Aboy, "Molecular dynamics simulations of damage production by thermal spikes in Ge", J. App. Phys. **111**, 033519 (2012).

[22] T. Jarrin, A. Jay, A. Hémeryck, and N. Richard, "Parametric study of the Two-Temperature Model for Molecular Dynamics simulations of collision cascades in Si and Ge", Nucl. Instr. Meth. Phys. R. B **485**, 1–9 (2020).

[23] S. Agostinelli et al., "Geant4 a simulation toolkit", Nucl. Instr. Meth. Phys. R. A **506**, 250–303 (2003).

[24] J. Allison et al., "Geant4 developments and applications", IEEE Trans. Nucl. Sc. **53**, 270–278 (2006).

[25] J. Allison et al., "Recent developments in Geant4", Nucl. Instr. Meth. Phys. R. A **835**, 186–225 (2016).

[26] S. Plimton, "Fast Parallel Algorithms for Short-Range Molecular Dynamics", J. Comput. Phys. **117**, 1–19 (1995).

[27] M. Raine, V. Goiffon, P. Paillet, O. Duhamel, S. Girard, M. Gaillardin, C. Virmontois, J. M. Belloir, N. Richard, and P. Magnan, "Exploring the Kinetics of Formation and Annealing of Single Particle Displacement Damage in Microvolumes of Silicon", IEEE Trans. Nucl. Sc. **61**, 2826–2833 (2014).

[28] L. K. Béland, P. Brommer, F. El-Mellouhi, J. F. Joly, and N. Mousseau, "Kinetic activation-relaxation technique", Phys. Rev. E **84**, 046704 (2011).

[29] M. Raine, A. Jay, N. Richard, V. Goiffon, S. Girard, M. Gaillardin, and P. Paillet, "Simulation of Single Particle Displacement Damage in Silicon – Part I: Global Approach and Primary Interaction Simulation", IEEE Trans. Nucl. Sc. **64**, 133–140 (2017).

[30] A. Jay, M. Raine, N. Richard, N. Mousseau, V. Goiffon, A. Hémeryck, and P. Magnan, "Simulation of Single Particle Displacement Damage in Silicon–Part II: Generation and Long-Time Relaxation of Damage Structure", IEEE Trans. Nucl. Sc. **64**, 141–148 (2017).

[31] A. Jay, A. Hémeryck, N. Richard, L. Martin-Samos, M. Raine, A. Le Roch, N. Mousseau, V. Goiffon, P. Paillet, M. Gaillardin, and P. Magnan, "Simulation of Single Particle Displacement Damage in Silicon–Part III: First Principle Characterization of Defect Properties", IEEE Trans. Nucl. Sc. **65**, 724–731 (2018).

[32] G. H. Saboya, "Defects in silicon: revisiting theoretical frameworks to guide ab initio characterization", Université Toulouse 3 Paul Sabatier, (2020) https://tel.archives-ouvertes.fr/tel-03158564/.

Simulation methods

3

Contents

Introduction

The variety of techniques we employ in our multiscale approach (see Fig. 2.5 in the previous chapter) allows us to cover all the aspects of DD in semiconducting materials, in terms of time and size scales. It is the very nature of the methods we use, as well as their intrinsic limitations, which dictates their usage and capabilities in our multiscale approach. For instance, the first MC step of our approach employed for simulating the particle-matter interactions is very affordable computationally, thus allowing the simulation of millions of events in very large simulation boxes on the macroscopic scale. However, the limitations of this method regarding the accuracy of the physical description it gives for low energies does not allow to simulate entire collision cascades. We therefore restrict ourselves, within this first step, to the study of the particle-matter interactions leading to PKAs creation, for which the MC method provides an efficient statistical treatment, and resort to MD for cascades propagation. The latter provides a treatment of collision cascades at the atomic scale, more accurate than MC simulations but heavier computationally speaking. Compared to MC, the systems studied are smaller and far less simulations are carried out. Also, the time scales accessible with this technique can never exceed few nanoseconds at most. This last inner limitation of MD is the reason which explains why we resort to kART simulations. With MD only, it would be impossible to observe complex activated processes like clusters reordering and defects diffusion. The nature of the kART method, designed in such a way that rare but essential reordering events can be sampled in a reasonable computational time, extends the timescale of the simulated process from the nanosecond at the end of the MD step up to few seconds. However, we are again restricted by the inner limitations of the kART method, which does not allow for an extensive study of the electronic properties of the clusters of defects. The clusters studied with kART have to be studied with *ab initio* techniques, namely DFT, GW or even TDDFT. Those techniques are very costly computationally speaking and must therefore be employed on systems made of few hundreds of atoms. Thus, all clusters healed with kART cannot be studied in the last step of our multiscale approach.

In this chapter, we provide detailed presentations of the simulation techniques employed, we highlight their usage, capabilities and clearly mention their limitations in the context of our global simulation approach (see Fig. 2.5 in the previous chapter) . The MC (Section 3.1), MD (Section 3.2) and kART (Section 3.3) methods, which were employed during this PhD work, are presented in detail. In addition, although *ab initio* methods are not employed in this thesis as defects characterization methods (we only treat the three first steps of our global approach), the TDDFT technique is employed in this manuscript to parametrize MD simulations (more on this later). Consequently, we introduce the DFT and TDDFT *ab initio* methods in Section 3.4. More than only giving thorough presentations of the techniques, we spend time throughout this chapter at practically explaining how all the steps of our multiscale approach are connected. Indeed, the transition between the different methods is key to the success of any multiscale approach involving various and very different techniques like ours.

3.1 Monte Carlo (MC) particle-matter interactions methods

The purpose of the first step of our multiscale approach is the simulation of the effects of the incoming energetic particles into the material. A very adequate method in this context is the MC one, which incorporates the generation of random numbers for selecting the events to be simulated. Its low computational cost allows the production of large ensembles of data to be treated statistically. Among the most famous MC codes for particle-matter interactions, we find Geant4 [1–3], which can deal with any type of particle-matter interactions, and SRIM [4], which is dedicated to ion-matter interactions. Both describe matter as being continuous, meaning that

the structure of matter is neglected and that the only discrete particles considered by the code are the projectile and the particles created following interactions with the projectile and matter (and also particles created following interaction of secondary particles with matter and so on). For the first step of our multiscale approach we adopt the Geant4 code as it is able to treat interactions of matter with ions and protons but also with neutrons. Moreover, it integrates the possibility for spallation reactions to occur, contrary to SRIM. The main idea behind Geant4 is that it is for the user to construct its own application, by defining the geometries and materials he wants to investigate and most of all by selecting the allowed physical processes in the simulations. Rather than a simulation code, it is more accurate to present Geant4 as an ensemble of functions and libraries from which the user picks the elements of interest for its specific case of application.

Even if we do not use SRIM specifically for the first step of our global approach, it is employed from time to time throughout this manuscript for illustration and benchmarking purposes. Indeed, it is considered as a reference, including by experimentalists, within the community of ion-solid interactions. SRIM is a Monte Carlo code based on the Binary Collision Approximation (BCA) [5], which is an approximation used by many simulation codes aiming at describing nuclear Coulomb interactions between ions (including protons) and matter. It assumes that nuclear Coulomb interactions are binary processes. Note that the term BCA is restricted to ion-matter interactions via the nuclear Coulomb mechanism only. MARLOWE is another example of famous ion-matter interaction code using the BCA [6]. However, MARLOWE is not a MC code. Actually, there is some confusion in the published literature, which we find useful to clarify here, regarding the denomination of the BCA codes as being MC ones or not. The distinction between the two relies on the way matter is taken into account into the simulation. If matter is described at the atomic scale with defined atomic positions, as this is the case in the MARLOWE code, there is no need for probabilistic evaluation of events via techniques based on the generation of random numbers. Therefore, such codes are not MC ones. However, if matter is not described as discrete but continuous like in SRIM, interactions and events are chosen via MC techniques. SRIM can be classified as a MC-BCA code.

In Geant4, just like in SRIM, all particle-matter interactions are considered binary, *i.e.* encompassing two particles only (projectile and target). To be more precise, the BCA concept is employed within Geant4 to describe nuclear Coulomb collisions and other type of binary formalism are employed for other interactions. Thus, although Geant4 cannot be described as a MC-BCA code like SRIM as it employs the BCA for a specific type of interactions only among the many it can deal with, the BCA is relevant to it as it governs a very important interaction mechanism in the context of DD. From a broader perspective, SRIM and Geant4 have in common the binary interaction concept and the MC one. Therefore, in this section, aiming at covering the theoretical developments behind the Geant4 simulation toolkit but also the SRIM code, we give a detailed presentation of the BCA (Section 3.1.1) and of the MC concept (Section 3.1.2), which are at the heart of those two codes.

3.1.1 Binary Collision Approximation

The very basis of the BCA relies on the assumption that the trajectory of an atom into matter depends only on the nuclear Coulomb binary collisions of this atom with other atoms of the matter. Collective effects or collisions involving more than two atoms are neglected. Within this approximation, between each collision, the moving atoms are not subject to any forces and therefore follow straight trajectories.

In the following, we are going to derive the basic equations of the BCA in the non-relativistic case. The given derivation is largely inspired, with less details, from the one of Eckstein in [7]. We only treat the case of a projectile colliding with an atom at rest. Indeed, this is sufficient as

in the BCA the trajectory of the projectile is viewed as a succession of binary collisions. Fig. 3.1 illustrates the situation we are trying to model.

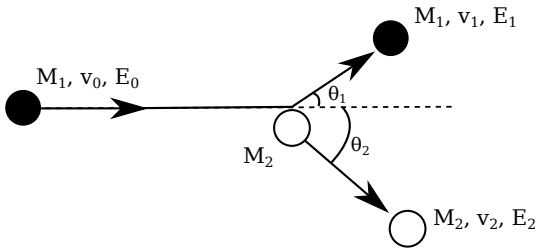

Figure 3.1: *Schematic view of the situation modeled by the BCA in the laboratory system. The projectile atom is the depicted by the black circle and the target atom by the white circle. The signification of all the letters and symbols are given in the text.*

A projectile of mass M_1 and velocity $\vec{v_0}$ (energy E_0) is heading towards a target atom initially at rest of mass M_2. After the collision between the two particles, the projectile velocity is $\vec{v_1}$ (energy E_1), and the one of the target atom $\vec{v_2}$ (energy E_2). The projectile was deflected by an angle θ_1, and the target atom now moves along the direction characterized by θ_2. In this collision, an energy Q was lost into inelastic electronic excitations. Q being very small compared to E_0, E_1 or E_2, the collision is said to be quasi-elastic. Moreover, the energy loss Q is considered to be entirely internal. The conservation of energy applied to the situation depicted gives:

$$E_0 = E_1 + E_2 + Q \tag{3.1}$$

$$\Leftrightarrow \frac{1}{2}M_1 v_0^2 = \frac{1}{2}M_1 v_1^2 + \frac{1}{2}M_2 v_2^2 + Q \tag{3.2}$$

and the conservation of momentum gives:

$$\begin{cases} M_1 v_1 \cos(\theta_1) + M_2 v_2 \cos(\theta_2) = M_1 v_0 \\ M_1 v_1 \sin(\theta_1) + M_2 v_2 \sin(\theta_2) = 0 \end{cases} \tag{3.3}$$

By combining (3.1), (3.2) and (3.3), it is possible to obtain the following expressions for the scattering angles θ_1 and θ_2:

$$\begin{cases} \cos(\theta_1) = \frac{1}{2}\sqrt{\frac{E_1}{E_0}}(1+A) + \frac{1}{2}\sqrt{\frac{E_0}{E_1}}\left(1 - A\left(1 - \frac{Q}{E_0}\right)\right) \\ \\ \cos(\theta_2) = \frac{1}{2}\sqrt{\frac{E_2}{E_0}}\frac{1+A}{\sqrt{A}} + \frac{1}{2}\sqrt{\frac{E_0}{E_2}}\frac{1}{\sqrt{A}}\frac{Q}{E_0} \end{cases} \tag{3.4}$$

with $A = M_2/M_1$. The above equations are valid for what is often called the "laboratory system", *i.e.* for a fixed external observer of the collision. However, in order to go further in the derivation of the equations of the BCA, we also have to apply the energy and momentum conservation in the centre-of-mass system.

In this system, the observer is not anymore fixed in the laboratory but moves with the center of mass of the system constituted by the projectile and the target atom. Therefore, even if the target atom is initially at rest in the laboratory system, it has a velocity $\vec{v_2}$ in the center-of-mass system before the collision as the center-of-mass is moving (the projectile is moving). The situation in the center-of-mass system is depicted in Fig. 3.2. The angle $\bar{\theta}/2$ is defined as the angle between the direction perpendicular to $\vec{v_0}$ (or $\vec{v_1}$) and the segment connecting the position of the two atoms. The projectile has a velocity $\vec{v_1}$ (energy $\bar{E_1}$) before the collision and a velocity $\vec{v_1}'$ (energy $\bar{E_1}'$) after. The target atom has a velocity $\vec{v_2}$ (energy $\bar{E_2}$) before the collision and a

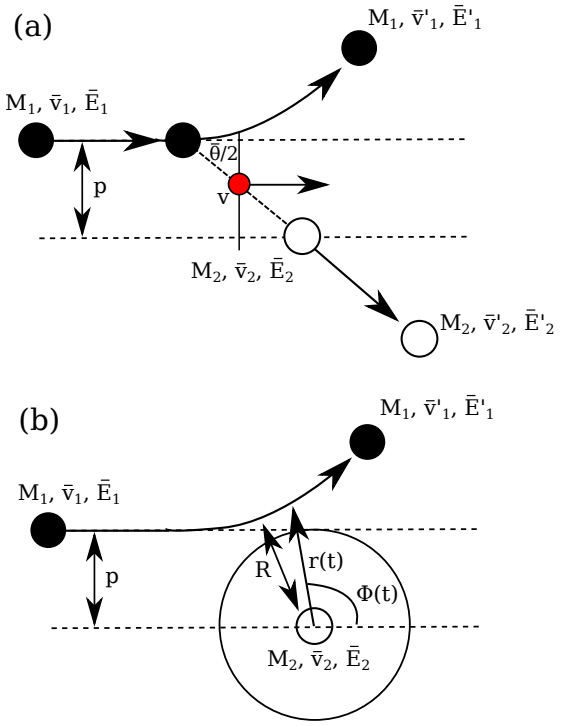

Figure 3.2: *(a) Schematic view of the situation modeled by the BCA in the center-of-mass system. The projectile atom is the depicted by the black circle and the target atom by the white circle. The smaller red circle represents the center-of-mass. In (b) are illustrated the polar coordinates (r, ϕ) used in the derivation of the BCA model. The signification of all the letters and symbols is given in the text.*

velocity $\vec{v_2}'$ (energy $\bar{E_2}'$) after. The velocities are correlated by the following relations, with $\vec{v}$ the velocity of the center-of-mass in the laboratory system:

$$\begin{cases} \vec{v_1} = \vec{v_0} - \vec{v} \\ \vec{v_2} = -\vec{v} \end{cases} \tag{3.5}$$

In this system, energy and momentum conservation respectively give:

$$\bar{E_1} + \bar{E_2} = \bar{E_1}' + \bar{E_2}' + Q \tag{3.6}$$

$$\Leftrightarrow \frac{1}{2}M_1\bar{v_1}^2 + \frac{1}{2}M_2\bar{v_2}^2 = \frac{1}{2}M_1\bar{v_1}'^2 + \frac{1}{2}M_2\bar{v_2}'^2 + Q \tag{3.7}$$

and

$$M_1\vec{v_1} + M_2\vec{v_2} = M_1\vec{v_1}' + M_2\vec{v_2}' = 0 \tag{3.8}$$

It is then possible to obtain the energy $E_r = \bar{E_1} + \bar{E_2}$ of the center-of-mass system from the above equations:

$$E_r = \frac{A}{1+A}E_0 \tag{3.9}$$

Going back to the laboratory system, one can write the energy of the projectile after the collision:

$$\frac{E_2}{E_0} = A\left(\frac{v_2}{v_0}\right)^2 = \frac{A}{(1+A)^2}\left(\cos(\theta_2) \pm \sqrt{f^2 - \sin(\theta_2)^2}\right)^2 \tag{3.10}$$

with $f^2 = 1 - ((1+A)Q)/AE_0$. A similar expression, depending on θ_1, can be obtained for the E_1/E_0 quantity [7]. Using (3.9) and (3.10), the maximum energy transferred (for $f = 1$) to the target atom T_{max} can be written:

$$T_{max} = \frac{4}{1+A}E_r \tag{3.11}$$

Moreover, by using relations between the angles in the laboratory and center-of-mass system derived and given in [7], it is possible to define the ratio E_2/E_0 as a function of the center of mass scattering angle $\bar{\theta}$:

$$\frac{E_2}{E_0} = \frac{A}{(1+A)^2}\left((1-f^2) + 4f\sin^2(\bar{\theta}/2)\right)^2 \tag{3.12}$$

Thus, the transferred energy T can be written, thanks to (3.11):

$$T = T_{max}\left(f\sin^2(\bar{\theta}/2) + \frac{1}{4}(1-f)^2\right) \tag{3.13}$$

The energy transferred after each collision can be obtained following the calculation of the $\bar{\theta}$ angle. The objective of the following is thus to derive an expression for $\bar{\theta}$ which can be calculated. The kinetic energy in the center-of-mass system is:

$$E_{kin} = \frac{1}{2}M_1\bar{v_1}^2 + \frac{1}{2}M_2\bar{v_2}^2 = \frac{1}{2}\frac{M_1M_2}{M_1+M_2}v_0^2 = E_r \tag{3.14}$$

If we write the term v_0^2 in the polar coordinates $(r,\, \phi)$, depicted in Fig. 3.2, the energy conservation gives:

$$E_{kin} + E_{pot} = \frac{\mu}{2}(\dot{r}^2 + r^2\dot{\phi}^2) + V(r) = E_r \tag{3.15}$$

where $\mu = M_1M_2/(M_1+M_2)$ is the reduced mass, $V(r)$ the interaction interatomic potential and dots above r and ϕ indicates differentiation with respect to time. The conservation of angular momentum gives:

$$r^2\dot{\phi} = -v_0p \tag{3.16}$$

with p the impact parameter, defined in Fig. 3.2. Combining (3.15) and (3.16) we obtain $\dot{r}$:

$$\dot{r} = \pm v_0\sqrt{1 - \frac{V(r)}{E_r} - \frac{p^2}{r^2}} \tag{3.17}$$

The minimum distance R between the two colliding atoms is given by:

$$g(R) = 0 \tag{3.18}$$

with

$$g(r) = \sqrt{1 - \frac{V(r)}{E_r} - \frac{p^2}{r^2}} \tag{3.19}$$

From (3.16) and (3.17) it is possible to obtain $d\phi/dr$:

$$\frac{d\phi}{dr} = \frac{\dot{\phi}}{\dot{r}} = \pm\frac{p}{g(r)r^2} \tag{3.20}$$

Finally, from (3.20) and following symmetry considerations clearly exposed in [7], it is possible to derive an expression for the scattering angle $\bar{\theta}$:

$$\int_{\pi}^{\bar{\theta}} d\phi = 2p\int_{\infty}^{R}(r^2g(r))^{-1}dr \tag{3.21}$$

$$\Rightarrow \bar{\theta} = \pi - 2p\int_{R}^{\infty}(r^2g(r))^{-1}dr \tag{3.22}$$

The final expression (3.22) constitutes the main equation of the BCA, from which the scattering angle can be calculated but also the energy transferred following (3.13). In the function $g(r)$

is appearing $V(r)$, a two-body interaction potential. The two-body repulsive nuclear stopping interaction potentials presented in the previous chapter are directly usable for the $V(r)$ expression. In SRIM, the chosen $V(r)$ is the ZBL [8] universal potential presented in the previous chapter.

In all the above, the basic equations of the BCA for a single collision have been derived from simple (but smart) energy and momentum conservation expressions as well as geometric considerations. The whole derivation that we have carried out so far is valid both for the crystalline codes using the BCA and the non-crystalline ones. The differences between the two kinds of codes, in terms of equations and implementations, arises in the way collision partners for the projectile are being searched. In the case of crystalline codes like MARLOWE, the locations of each atom of the matter is known. In view of the fact that the position and direction of the projectile are also known, simple distance and orientation considerations are sufficient to find the next collision partners [9]. The picture is similar to a MD simulation (see Section 3.2) where only forces during collisions are calculated. However, in the case of the non-crystalline codes, the only particles whose positions are known are the projectile and the displaced atoms. Therefore, the search for a collision partner for a projectile or a displaced atom has to resort to other means than simple distance considerations. This is where the Monte Carlo part of the non-crystalline codes, like SRIM and Geant4, resides.

3.1.2 Selection of interaction mechanisms with MC techniques

The generic term of Monte Carlo simulations refers to simulation methods in which probabilities and the generation of random numbers are employed for the calculation of given quantities. In order to introduce the subject, we present a simple case where the Monte Carlo concept can be easily understood. We will come back later to the specific case of the Monte Carlo concept within SRIM and Geant4.

Let's assume we want to calculate an average value $\bar{Q}$ of a given quantity. To do so, we need to find the most probable states of the system and calculate the expectation value of this quantity over the sampled states. The Monte Carlo concept allows to find those states. The potential energy surface of the system is assumed to be dependent on a single position coordinate parameter, and therefore can be plotted on a 2D plot like Fig. 3.3. We assume that the system is in a given state S_1, with an energy E_1. The system has the choice to go down in energy to a state S_2 or to go up in energy up to a state S_3. The situation is depicted Fig. 3.3. If we first look at the possibility to go from S_1 to S_2, the system reduces its energy therefore the step is always accepted, and the system is now in the state S_2. In this case, the situation was simple as we were looking at a situation where the final energy was smaller than the initial energy. However, if before looking at the event S_1 to S_2, we look at the event S_1 to S_3, the situation is different. The step is not automatically accepted as it involves an energy increase. A rule to decide if the step should be accepted or rejected must be determined. We can associate a probability P for the step to occur, given by $P = Ae^{-\Delta E/k_B T}$, A being a constant, $\Delta E = E_3 - E_1$ the energy difference between S_1 and S_3, T the temperature and k_B the Boltzmann constant. We now pick a random number R between 0 and 1. If $R \leq P$, the step is accepted, if $R > P$, the step is rejected. Therefore, the greater the energy difference, the least probable will be for the step to occur. This simple probability comparison to a random number illustrates the Monte Carlo concept. It might happen after some steps that the system is able to overcome the energy barrier ΔE separating S_2 and S_4 and reach the more stable state S_4 depicted in Fig. 3.3. With this method, we sample the possible states of our system, and spend more steps in the most stable ones as the energy barriers to exit from those states are higher and therefore the probability to pick a succession of random numbers allowing us to exit those steps is lower. It is interesting to note that the initial choice of the event to look at is very important. Indeed, the choice of

the initial event dictates the step to be accepted or rejected. This can be done randomly by generating another random number to choose the event to consider among all the possible ones.

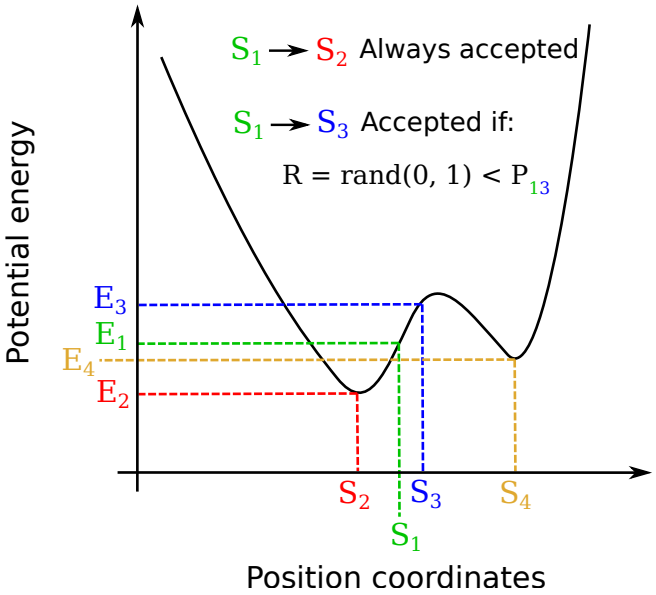

Figure 3.3: *Illustration of the Monte Carlo concept. Different states S_i with respective energies E_i are possible for a system. If from S_1 the system tries to go to the state S_2 of lower energy, the step is always accepted. However, if from S_1 the system tries to go to the state S_3 of higher energy, the step is accepted a posteriori of a comparison of the probability $P_{13}(E_3 - E_1)$ to go from S_1 to S_3 and a random number $z \in [0; 1]$.*

What we have just described constitutes a basic illustration of a Monte Carlo simulation. In Geant4 and SRIM, the situation is of course different but the main idea is the same: probabilistic methods and random numbers are used to determine the interaction mechanism picked among all the possible ones. In Geant4, due to the diversity of possible interaction mechanisms, as we have said in the introduction of this section, the user has to specify which ones have to be incorporated to its application. For each interaction mechanism listed by the user, the corresponding interaction cross sections σ, *i.e.* quantities homogeneous to a surface and giving the interaction probabilities, are selected by Geant4 from its library of pre-incorporated cross sections. Those interaction cross sections σ depend on the particle type Z_1, its energy E and the target atom type Z_2, *i.e.* $\sigma = \sigma(Z_1, Z_2, E)$. The cross sections are employed for computing the mean free path and probability of each interaction mechanism. At each step, an interaction mechanism is picked based on its probability following the MC scheme described a few lines below. All the interactions based on cross sections are thus discrete and binary as at each step only one is picked and applied. However, when the energy of a particle falls below a certain cutoff value, the interactions are not considered discrete anymore but continuous. For example, electronic stopping is described by Coulomb interactions between the projectile and electrons above the energy cutoff and by the Lindhard stopping formula below it. We focus in the following on discrete interactions based on cross sections. In SRIM, cross sections are used for nuclear Coulomb interactions between ions (nuclear stopping power), and Coulomb interactions between ions and electrons are dealt with via the Lindhard formula as explained in the previous chapter. In Geant4, the choice of an interaction event actually involves two steps: (i) the distance traveled by the particle before a collision is calculated and then (ii) the interaction mechanism is picked. In SRIM, only the first step is necessary as the interaction mechanism will always be nuclear Coulomb interactions. We first describe the method employed for determining the distance traveled by the particle before an interaction occurs. The mean free path λ_i of the associated particle to each of the interaction mechanism i is calculated from

the cross sections σ_i and the material density n, also specified as an entry parameter. Then, the total mean free path λ is calculated with:

$$\frac{1}{\lambda} = \sum_i \frac{1}{\lambda_i} \tag{3.23}$$

The probability density $p(x)$ that the considered particle interacts between x and $x+dx$ is given by:

$$p(x) = \frac{1}{\lambda} e^{-\frac{x}{\lambda}} dx \tag{3.24}$$

Thus, the probability that the particle interacts before it reaches a distance L reads:

$$P(x \leq L) = 1 - e^{-\frac{L}{\lambda}} \tag{3.25}$$

It is possible to show that $P(x \leq L) = R$, where R is an uniform random number between 0 and 1 [7]. Therefore, the distance traveled by the particle before interacting gives:

$$L = -\lambda \ln(R) \tag{3.26}$$

The mean value of $\ln(R)$ is -1, thus the mean value of the distance L, which is often called the free path, actually is the mean free path λ, which seems pretty consistent. In practice, the distance traveled by the particle before interacting is obtained by generating a random number R and multiplying $-\ln(R)$ with λ, following (3.26). Within SRIM, the Monte Carlo concept goes no further. Indeed, from this point, the particle is transported of a distance L, the SRIM version of the Lindhard electronic energy loss formula we have seen in the previous chapter is employed and the BCA method presented in Section 3.1.1 is applied for calculating the transferred energy during the collision and scattering angle. Particles (initial one and created one following the interaction) positions and velocities are updated, and we proceed to the next step following the same method. However, within Geant4, an interaction mechanism must be chosen. To do so, probabilities of occurrence p_i for each of the interaction mechanisms i are defined from their cross section σ_i as follows:

$$p_i = \frac{\sigma_i}{\sum_i \sigma_i} \tag{3.27}$$

and the cumulative probabilities P_i can thus be defined:

$$P_i = \sum_{j=1}^{i} p_j \tag{3.28}$$

A new uniform random number R between 0 and 1 is then generated, and the interaction mechanism i is chosen if the following rule is respected:

$$P_{i-1} \leq R < P_i \tag{3.29}$$

It guarantees that the most probable interaction mechanism is picked. Then, the selected interaction is applied, for example with the BCA if the nuclear Coulomb interaction mechanism is picked. The same two MC steps are applied to each of the particles, *i.e.* the initial projectile and the newly created (or displaced) particles following the interaction. When the energy of a particle falls below a predefined energy cutoff, it is not followed anymore and its trajectory is stopped. The trajectory and the interactions of each particle are followed and stored. Thus, it is possible to calculate the trajectory and interactions as a function of time, from the calculation of the time-of-flights between each interaction. However, there is no notion of global system time in Geant4, as each particle is followed independently in the framework of the condensed history or track model concepts: each particle has its own clock. It thus cannot be viewed as a kinetic or dynamic MC program like the one we employ in Section 3.3.

3.1.3 Usage of MC particle-matter interaction simulations results in our multiscale approach

In our global simulation approach, the Geant4 code is used to simulate particle-matter interactions. We are interested in the interaction of neutrons, protons and ions with matter. Therefore, all the possible interactions between those particles and atoms have to be specified. The main data we retrieve from this step are the energies and types of the PKAs created following neutron or proton interactions under the form of statistical data built from millions of simulated incident interactions between incident particles and with matter. Following the PKA creation, the collision cascade is not propagated with Geant4. The reason for this resides in the most important and well known drawbacks of the MC particle-matter interactions codes, being that the approximation of considering the interactions as binary breaks down at low energies. Indeed, at low energies, the most probable mechanism of interaction is the nuclear Coulomb one, dealt with via the BCA, which is not valid at low energies as it does not take into account effects originating from many-body nuclear Coulomb interactions like temperature effects (which starts appearing at low energy). Consequently to this limitation, the BCA fails to predict the melting of some regions of the material following irradiation and thus the formation of amorphous pockets, which constitutes an important degradation mechanism in Si and Ge [10]. Moreover, in Geant4, matter is considered continuous. Therefore, a dynamic atomic description of a collision cascade cannot be simulated with it.
Aiming at simulating the atoms dynamic following an irradiation, we resort to MD for propagating the collision cascade, taking as basis the information obtained on the created PKAs with MC simulations.

3.2 Molecular Dynamics (MD)

Following the first MC step and the simulation of PKAs creation, the MD code LAMMPS is employed to simulate the successions of atom collisions initiated by the PKAs inside the material. We move from a binary continuous description of matter and collisions at the high energies of interest for particle-matter interactions, to an atomic, time explicit and many-body description of matter and collisions.

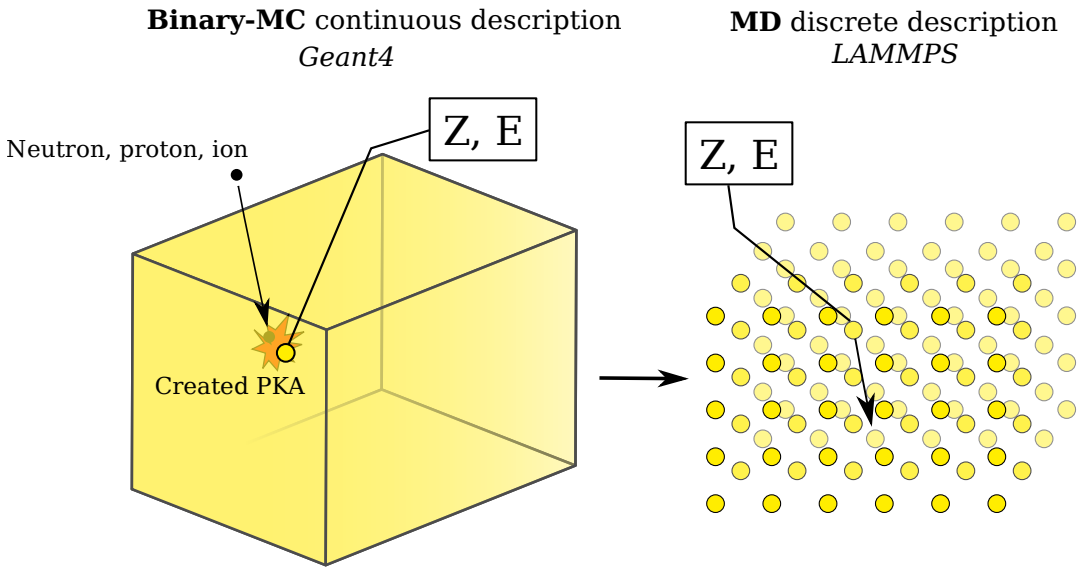

Figure 3.4: *Illustration of the transition from MC to MD in our multiscale approach.*

To transition from the MC to the MD step, the representative characteristics of the PKAs identified in the MC step are used as input to the MD simulations following what is depicted

in Fig. 3.4: an atom of the MD simulation box acting as the PKA is attributed an energy and a velocity to initiate the collision cascade. A single collision cascade per simulation box is performed.

Time is discretized in timesteps Δt in MD, making it possible to simulate the dynamic evolution of the atoms in the simulation box. In order to do so, at each timestep is solved the Newton's equation of motion for each atom i of the simulation box:

$$m_i \frac{d\vec{v_i}}{dt} = \vec{F_i} \tag{3.30}$$

where m_i is the mass of atom i, $\vec{v_i}$ its velocity and $\vec{F_i}$ the force acting on atom i. To be able to update the position and velocity vectors of each atom at every timestep, the forces $\vec{F_i}$ must be known. The quantity $\vec{F_i}$ is derived from what is called an interatomic potential. It simply is an analytical expression of the potential energy of the atoms of the system which enables to calculate the forces acting on a given atom depending on the position of the other atoms of the simulation box. Interatomic potentials define the entirety of the properties of the studied material with MD, from its crystalline structure to its thermal properties, for example. The Moliere [11] and ZBL [8] repulsive potentials that we have seen in the previous chapter are examples of such interatomic potentials, where only the repulsive contributions of pairs of atoms are taken into account. In MD, more complex interatomic potentials have to be used as the crystalline structure of materials as well as their properties have to be reproduced. Therefore, potentials often integrate a repulsive part like the Moliere and ZBL ones and an attractive part, allowing for a material to have a stable structure. There also exists interatomic potentials where triplets or quadruplets of atoms are considered. In the following, we take the example of a many-body interatomic potential with a two-body contribution ϕ_2 but also a three-body (triplets) one ϕ_3. If we consider a system of N atoms, the potential energy V_i of atom i can be written:

$$V_i = \sum_{j \neq i}^{N} \phi_2(r_i, r_j) + \sum_{j \neq i}^{N} \sum_{k>j}^{N} \phi_3(r_i, r_j, r_k) \tag{3.31}$$

where i, j and k are atom indexes and r_i corresponds to the position of atom i. At each timestep the quantity V_i is calculated, and the force F_i deriving from it is calculated with the relation:

$$\vec{F_i} = -\vec{\text{grad}}(V_i) \tag{3.32}$$

where $\vec{\text{grad}}$ is the notation we adopt for gradients. In practice, for MD simulations in periodic systems, all the atoms do not contribute to the potential of a given atom i like it is the case in (3.31): a cutoff radius R_c is chosen so that atoms further than R_c to the atom i are not considered in the calculation. It is assumed that their contribution is so small compared to the one of closer atoms it can be neglected. The entire physics of a MD simulation lies in the derivation and/or choice of an accurate interatomic potential. Consequently, an extensive attention is given in the literature to the derivation of interatomic potentials. We will come back to this point for the specific case of the simulation of collision cascades, as well as other aspects of MD simulations of collision cascades in Section 3.2.2. For now, we focus on the numerical integration of the equations of motions within MD, for any type of applications.

3.2.1 Numerical considerations

3.2.1.1 Timestep

In order to model the dynamic evolution of a system of atoms, (3.30) must be integrated over time. As mentioned earlier, time is discretized in timesteps of duration Δt. Usually, the employed timesteps are in the order of 1 fs.

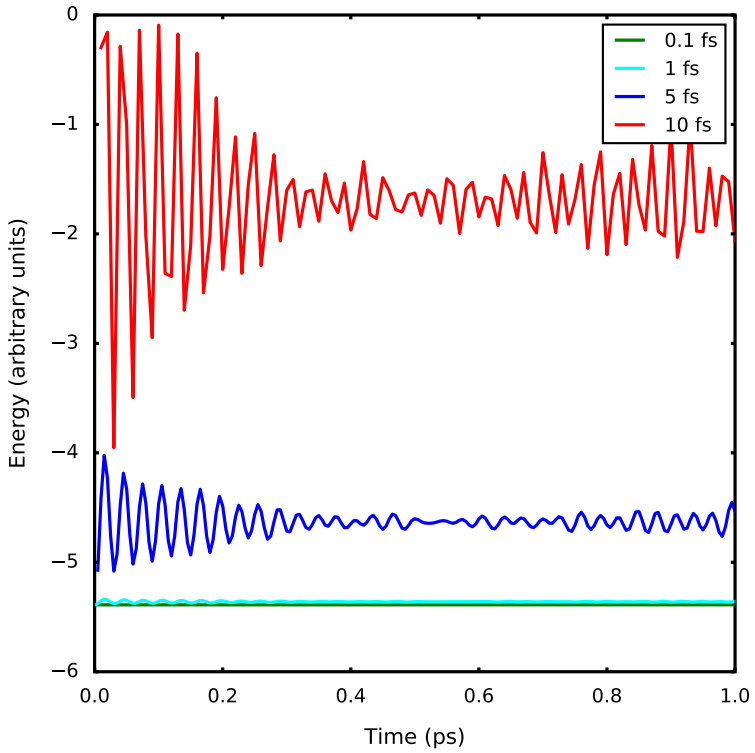

Figure 3.5: *Total energy evolution over 1 ps for diamond Si with respect to the timestep employed, for a given interatomic potential.*

At each timestep, the equation of motion of all the atoms are solved and their positions and velocities are updated accordingly. Therefore, the choice of the timestep is fundamental. Indeed, if the chosen timestep is too big, the changes in velocities and positions of atoms between successive steps are too important and the simulation lacks accuracy. Consequently, it might happen that the energy is not conserved during the simulation, or that there are strong oscillations in the total energy. It is even possible for a simulation to "explode" (*i.e.* diverge very quickly) if the integration timestep is chosen too big. On the contrary, a small timestep provides an accurate simulation but increases the computational time. Indeed, the smaller the timestep, the greater number of steps are necessary to run a simulation for a given amount of time. A compromise thus has to be found. Fig. 3.5 shows the total energy evolution with respect to time for simulations ran on a simple perfectly ordered Si system with a given interatomic pseudopotential at different timesteps. The influence of the timestep on the stability of the simulation is made blatant by Fig. 3.5: the total energy converges to its definite value as the timestep decreases and the smaller the timestep, the smaller the oscillations in total energy. By running longer simulations, it would have been possible to observe total energy drift with the 5 fs and 10 fs timesteps.

3.2.1.2 Integration schemes

The choice of the timestep depends on the interatomic potential employed, but also on the algorithm used for the integration of the equations of motions. Those schemes must allow the choice of relatively big timesteps while conserving the total energy of the simulation. Moreover, they should permit fast simulations, require little memory and be time-reversible (just like the Newton's equation of motion is). There exists diverse adequate algorithms. Here, we detail two integration schemes among the most used ones: the Verlet algorithms.

3.2.1.2.1 Position-Verlet

The position-Verlet algorithm [12] is a very simple yet efficient integration scheme. It is derived by writing the third-order Taylor expansions of the position $\vec{r_i}(t)$ of atom i at $t = t + \Delta t$ and $t = t - \Delta t$:

$$\begin{cases} \vec{r_i}(t+\Delta t) = \vec{r_i}(t) + \frac{d\vec{r_i}(t)}{dt}\Delta t + \frac{1}{2!}\frac{d^2\vec{r_i}(t)}{dt^2}\Delta t^2 + \frac{1}{3!}\frac{d^3\vec{r_i}(t)}{dt^3}\Delta t^3 + O(\Delta t^4) \\ \vec{r_i}(t-\Delta t) = \vec{r_i}(t) - \frac{d\vec{r_i}(t)}{dt}\Delta t + \frac{1}{2!}\frac{d^2\vec{r_i}(t)}{dt^2}\Delta t^2 - \frac{1}{3!}\frac{d^3\vec{r_i}(t)}{dt^3}\Delta t^3 + O(\Delta t^4) \end{cases} \tag{3.33}$$

From (3.33) we can obtain:

$$\vec{r_i}(t+\Delta t) = 2\vec{r_i}(t) - \vec{r_i}(t-\Delta t) + \frac{d^2\vec{r_i}(t)}{dt^2}\Delta t^2 + O(\Delta t^4) \tag{3.34}$$

Considering that we integrate the Newton's equation of motion, we have:

$$\frac{d^2\vec{r_i}(t)}{dt^2} = \frac{\vec{F_i}(\vec{r_i}(t))}{m_i} \tag{3.35}$$

which allows (3.34) to be turned into:

$$\vec{r_i}(t+\Delta t) = 2\vec{r_i}(t) - \vec{r_i}(t-\Delta t) + \frac{\vec{F_i}(\vec{r_i}(t))}{m_i}\Delta t^2 + O(\Delta t^4) \tag{3.36}$$

The position of atom i at $t = t+\Delta t$ can therefore be calculated from the positions at the current and previous timesteps as well as the forces acting on the atom (deriving from the interatomic potential), with an error of the order of $O(\Delta t^4)$. This algorithm is easy, fast, allows the choice of a big timestep and is reversible. However, the first step of the algorithm might be an issue as positions from two previous steps are needed. The algorithm is said to be non-self-starting. Moreover, velocities are not directly calculated and must be obtained, only after the calculation of $\vec{r_i}(t+\Delta t)$, from the subtraction of $\vec{r_i}(t+\Delta t)$ and $\vec{r_i}(t-\Delta t)$, with a global error of the order of $O(\Delta t^2)$:

$$\vec{v_i}(t) = \frac{\vec{r_i}(t+\Delta t) - \vec{r_i}(t-\Delta t)}{2\Delta t} + O(\Delta t^2) \tag{3.37}$$

To overcome the issues related to the accuracy in the velocity calculations and the non self-starting characteristic of the Verlet algorithm, other integration schemes have been developed.

3.2.1.2.2 Velocity-Verlet

The velocity-Verlet algorithm [12] corrects the issues arising in the position-Verlet. This time, one Taylor expansion for the position and one for the velocity are used, instead of two Taylor expansions for the positions:

$$\begin{cases} \vec{r_i}(t+\Delta t) = \vec{r_i}(t) + \frac{d\vec{r_i}(t)}{dt}\Delta t + \frac{1}{2!}\frac{d^2\vec{r_i}(t)}{dt^2}\Delta t^2 + O(\Delta t^3) \\ \vec{v_i}(t+\Delta t) = \vec{v_i}(t) + \frac{1}{2}(\frac{d\vec{v_i}(t)}{dt} + \frac{d\vec{v_i}(t+\Delta t)}{dt})\Delta t + O(\Delta t^3) \end{cases} \tag{3.38}$$

where the lower equation of the system can be obtained by writing the Taylor expansion of $\vec{a_i}(t+\Delta t) = d\vec{v_i}(t+\Delta t)/dt$. Once again, considering that we can calculate the forces at the current timestep via the interatomic potential, (3.38) can be rewritten in the following way:

$$\begin{cases} \vec{r_i}(t+\Delta t) = \vec{r_i}(t) + \vec{v_i}(t)\Delta t + \frac{1}{2m_i}\vec{F_i}(\vec{r_i}(t))\Delta t^2 + O(\Delta t^3) \\ \vec{v_i}(t+\Delta t) = \vec{v_i}(t) + \frac{1}{2m_i}(\vec{F_i}(\vec{r_i}(t)) + \vec{F_i}(\vec{r_i}(t+\Delta t)))\Delta t + O(\Delta t^3) \end{cases} \tag{3.39}$$

This time, the algorithm is self-starting. Indeed, $\vec{r_i}(t+\Delta t)$ can be calculated directly from the upper equation in (3.39). Then , from $\vec{r_i}(t+\Delta t)$ the force term $\vec{F_i}(\vec{r_i}(t+\Delta t)))$ can be obtained, from which $\vec{v_i}(t+\Delta t)$ can be calculated. Finally, we have successfully calculated the positions and velocities for the next step using only information of the current step, and the velocities are calculated with an $O(\Delta t^3)$ accuracy. The velocity-Verlet algorithm is the default one of LAMMPS, and the one we employ in our simulations.

3.2.1.2.3 Integration ensembles

In MD, the equations of motions are always said to be integrated in a given ensemble. It can be viewed as a frame which defines the rules to respect for the global quantities of the system like the temperature, the pressure, the volume or the total energy, which are all calculated from the positions and velocities of the atoms. If we are interested in a closed system of a given volume without temperature or pressure constraint (*i.e.* the temperature or pressure of the system is not influenced by an exterior element), we place ourselves in what we call the *NVE* ensemble (or microcanonical ensemble). The denomination *NVE* states that the number N of atoms (or molecules) in the simulation is conserved during the integration, as well as the volume V and the total energy E. This is the most basic ensemble of integration, which is the default one of the MD integration schemes. Indeed, they are all designed to conserve the energy.

In some cases, it may happen that we want to control the temperature T of our simulation. A good solution to do so is to connect our system to a thermostat of a given temperature. Our system and the thermostat will exchange heat thus maintaining our system at the thermostat temperature. Such an ensemble of integration is called *NVT* ensemble (or canonical ensemble). In this case the total energy of our system is not conserved anymore, but the temperature can be kept constant. Nonetheless, the total energy of the global system made of our system and the thermostat is conserved. There are diverse methods to simulate a thermostat in MD. Among those methods, we can cite the deterministic Nose-Hoover thermostat [13] and the stochastic Langevin thermostat [14]. We describe the latter in the next few lines. The Langevin thermostat aims at maintaining the temperature of the system equal to the desired one by modifying the Newton's equation of motion to be integrated into MD:

$$m_i \frac{d\vec{v_i}}{dt} = \vec{F_i} - \gamma_i \vec{v_i} + \vec{f_i}^{stoch} \tag{3.40}$$

where $\vec{F_i}$ still is the force term deriving from the interatomic potential, γ_i is a friction coefficient and $\vec{f_i}^{stoch}$ a stochastic force term. The random numbers in the stochastic force term are chosen from a Gaussian distribution having a mean equal to zero and a variance $\sigma_i^2 = 2m_i\gamma_i k_B T/\Delta t$. The Langevin thermostat mimics a system in contact with a medium of a given viscosity (thus explaining the friction force). Fictitious collisions between particles of this medium and atoms of our system, depicted by the stochastic force term in (3.40), maintain our system at the desired temperature T. Similar methods are employed for pressure P control in the *NPT* ensemble. Depending on the thermostat or barosthat formalisms employed, the quantities ($\vec{r_i}$ and $\vec{v_i}$ at different steps) to keep in memory or the calculation order for the different quantities at each step might be changed. The integration schemes therefore have to be chosen accordingly. For example, in the case of a Langevin thermostat, velocity-Verlet is more adequate than position-Verlet as the velocity is explicitly needed for the friction force calculation.

3.2.2 The specific case of collision cascades

So far, we have been focusing on general aspects of MD simulations, useful for any type of systems studied. We are now going to detail the specific case of the simulation of collision cascades, and some of the choices we have made in the settings of the simulations. From what

we have seen in the previous chapters, we know that collision cascades are highly stochastic out of equilibrium phenomena involving high energy collisions between atoms. This can make the MD simulations of collision cascades a challenge. Moreover, the inclusion of electronic effects is not to be neglected for accurate MD simulations of collision cascades. However, as one can understand from the theoretical description of MD made, the technique does not explicitly integrate electrons into its formalism. Of course, the electrostatic effects are taken into account via the interatomic potential, but the effects related to electronic excitations cannot be. Therefore, it is necessary to resort to models to be combined to MD to incorporate the electronic effects. In the following, after rapidly presenting general aspects of MD simulations of collision cascades (Section 3.2.2.1), we are going to see how to cope with high energy collisions into MD simulations (Section 3.2.2.2), how to get meaningful results despite the stochasticity of collision cascades (Section 3.2.2.3) as well as how to incorporate electronic effects into the simulations (Section 3.2.2.4).

3.2.2.1 Generalities

The collision cascade is initiated by giving to an atom (the PKA) of the simulation box a certain velocity, as depicted in Fig. 3.4. This atom will thus collide with others and generate the collision cascade. The size of the simulation box needs to be chosen with respect to the energy given to the PKA. Indeed, the greater the energy the longer (and wider) will be the cascade and thus the bigger must be the simulation box to contain the entire cascade. Typically, cascades initiated with 10 keV PKAs in Si must be carried out in boxes made of 1 000 000 to 4 096 000 atoms (*i.e.* 50×50 ×50 to 80×80×80 unit cells or cubes of about 270 Å to 430 Å in length). Moreover, the timestep must be adapted to the velocity of the atoms in the simulation box. Indeed, in the beginning of the simulation, some atoms have high velocities, and the timestep must be adapted so that they do not move too much between each step. It is often advised not to let an atom move more than 0.1 Å during a single step. Modern computational power means allow to easily reduce this distance. For 10 keV Si PKAs, the starting timestep can be chosen between 10^{-3} fs and 10^{-2} fs. It should then be reduced during the simulation, as the system reaches equilibrium. Indeed, keeping such a small timestep is not necessary when there are no high velocity atoms anymore in the simulation box. It would also make deterrent the computational cost of a cascade simulation. Even better than reducing the timestep "manually" during the simulation, an adaptative timestep can be employed. With such a method, the timestep is automatically updated so that no atom in the simulation box move more than a predefined distance.

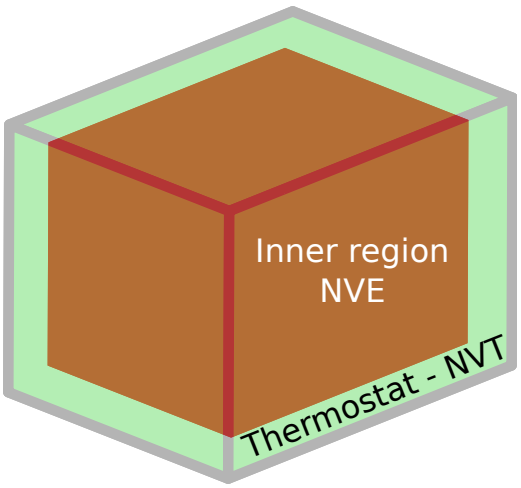

Figure 3.6: *MD simulation box divided in a NVE and a NVT region.*

It is also of prime importance to note that collision cascades simulations need to be carried out in the *NVE* ensemble. Indeed, *NPT* or *NVT* ensembles would induce modification of the

equations of motion (see (3.40)) to maintain a constant temperature which can drastically affect the collisions and defects creation. To allow heat induced by the PKA to be evacuated from the simulation box, the *NVE* region, where the collisions occur can be connected to a *NVT* region of constant temperature. Typically, the inner region is chosen to be *NVE* and the very outer atomic layers are integrated in an *NVT* ensemble or in a *NVE* ensemble with a simple temperature rescaling, as depicted in Fig. 3.6. In this case, an initial equilibration period of some picoseconds must be allowed before launching the cascade so that the *NVT* region and the *NVE* region equilibrates at the desired *NVT* temperature. We followed all the guidelines given above in our simulations. More details will be given when needed in the chapters to come presenting simulation results.

3.2.2.2 Treating atomic collisions with the interatomic potential

The vast majority of interatomic potentials are designed for simulations of systems at or near the equilibrium. The typical interatomic distances in such simulations thus do not vary much around the equilibrium distances. Consequently, poor effort is given to have interatomic potentials accurately describing forces between atoms separated by small interatomic distances compared to the equilibrium ones. Nonetheless, in the case of collision cascades, the high energies involved make it possible for interatomic distances between atoms to become very small. Therefore, an accurate description of forces when the interatomic distances are short must be incorporated into the potential for the simulation of collision cascades with MD. This aspect might only be useful for the first few high energy collisions of the simulation, but still is essential as the cascade evolution is dictated by those high energy collisions. Obviously, for a trustworthy simulation, general properties of the material studied must also be well reproduced by the interatomic potential. Among those properties, we can cite global one like the crystalline structure, lattice parameter, elastic constants, melting temperature and heat conductivity and other properties more specific to collision cascades like the threshold displacement energy and the vacancy formation energy, among others. The potentials usually employed in MD simulations actually are constructed to reproduce correctly those properties (at least the general ones). Therefore, an adequate interatomic potential for the simulation of collision cascades with MD would be a combination of, a repulsive potential designed to correctly account for collisions between atoms at short interatomic distances, and at longer interatomic distances a more commonly employed general-purpose MD potential. This is precisely the strategy that we and many other research groups have chosen to adopt [15, 16]. In our case, we choose to employ for Si, Ge and Si-Ge alloys (all diamond-like crystals) a combination of the Stillinger-Weber (SW) [17] types potentials and of the universal ZBL [8] potential described in the previous chapter for accurate collisions description.

SW potentials are many-body potentials including a two-body and a three-body contribution. The two-body contribution ϕ_2^{SW} dictates the calculation of forces during collisions via the repulsive part of the potential (which we are going to correct with the ZBL potential) and the equilibrium distance via its attractive part. It only depends on the interatomic distance between the couple of considered atoms. The three-body contribution ϕ_3^{SW} is responsible for the orientation of the atoms one with respect to another and therefore the crystalline structure of the studied system. Thus, it integrates an angular dependence and a distance dependence. The potential energy of an atom is given by the sum of the two contributions just like in (3.31). The two-body and three-body terms of the SW potential are defined in the following way:

$$\begin{cases} \phi_2^{SW}(r_{ij}) = A_{ij}\epsilon_{ij}\left(B_{ij}\left(\frac{\sigma_{ij}}{r_{ij}}\right)^{p_{ij}} - \left(\frac{\sigma_{ij}}{r_{ij}}\right)^{q_{ij}}\right)\exp\left(\frac{\sigma_{ij}}{r_{ij}-a_{ij}\sigma_{ij}}\right) \\ \\ \phi_3^{SW}(r_{ij}, r_{ik}, \theta_{ijk}) = \lambda_{ijk}\epsilon_{ijk}(cos\theta_{ijk} - cos\theta_{0ijk})^2 \exp\left(\frac{\gamma_{ij}\sigma_{ij}}{r_{ij}-a_{ij}\sigma_{ij}}\right)\exp\left(\frac{\gamma_{ik}\sigma_{ik}}{r_{ik}-a_{ik}\sigma_{ik}}\right) \end{cases} \tag{3.41}$$

where i, j and k are atom indexes, r_{ij} is the interatomic distance separating atoms i and j, θ_{ijk} is the angle made by the vectors going from atom i to atom j and atom i to atom k. All the other terms are material-dependent parameters of the potential. The summations in (3.41) go over all j and k neighbors of atom i within a cutoff distance $a_{ij}\sigma_{ij}$ or $a_{ik}\sigma_{ik}$. The exponential terms of (3.41) actually act as "smooth cutoff" terms. All the work in the construction of a given potential lies in the derivation of analytical expressions like the ones of (3.41) and the careful fitting of the parameters to reproduce desired materials characteristics. For our Si simulations, we use the parametrization of the original SW potential [17]. In the case, of pure Ge, we use the parameters presented in [18] with the slight correction made in [15] aiming at correctly reproducing the melting temperature. Those parametrizations of the SW potentials for Si and Ge were shown to be the optimal ones for comparing collision cascades results in Si and Ge [10]. More specifically, they reproduce very well the thermal properties of Si and Ge. For Si-Ge alloys, we combine the Si and Ge SW potentials following the rules exposed in [19].

Following the choice of the SW potentials parametrizations, they have to be combined to the repulsive universal ZBL one, described in the previous chapter, but whose expression is recalled to the reader just below:

$$\phi_2^{ZBL}(r) = \frac{Z_1 Z_2 e^2}{4\pi\epsilon_0 r} \times \phi\left(\frac{r}{a_{ZBL}}\right) \tag{3.42}$$

with,

$$\phi\left(\frac{r}{a_{ZBL}}\right) = 0.18175e^{-0.31998x} + 0.50986e^{-0.94229x} + 0.28022e^{-0.4029x} + 0.02817e^{-0.20162x} \tag{3.43}$$

with $x = r/a_{ZBL}$ and $a_{ZBL} = 0.8853a_0(Z_1^{0.23} + Z_2^{0.23})^{-1}$. In order to combine the two potentials, we followed the idea that Gao *et al.* have used in [16] and [20]: they combined a Tersoff [21] type potential with the ZBL potential using a Fermi function $F(r_{ij})$ of the following form:

$$F(r_{ij}) = \frac{1}{1 + e^{-b_{ij}^F(r_{ij} - r_{ij}^F)}} \tag{3.44}$$

where b_{ij}^F and r_{ij}^F are parameters to be determined for every couple of atoms of different types considered. This Fermi function is equal to 0 when r_{ij} is very small and gradually goes to 1 as r_{ij} increases. Therefore, by fitting the b_{ij}^F and r_{ij}^F parameters, it is possible to smoothly transition from a repulsive two-body contribution dominated by the ZBL potential $\phi_2^{ZBL}(r_{ij})$ at small r_{ij} to a two-body contribution entirely described by the $\phi_2^{SW}(r_{ij})$ term of the SW potential using the following relation:

$$\phi_2^{final}(r_{ij}) = (1 - F(r_{ij}))\phi_2^{ZBL}(r_{ij}) + F(r_{ij})\phi_2^{SW}(r_{ij}) \tag{3.45}$$

The two-body contribution of the final potential is thus given by (3.45) whereas the three-body contribution remains the ϕ_3^{SW} term of (3.41). Doing this, we benefit from the assets of both potentials: the ZBL one for collisions and the SW one for general properties of the material. In practice, the b_{ij}^F and r_{ij}^F parameters are chosen so that the potentials and their first derivative (forces) are smooth. All the parameters cited in this section dedicated to the interatomic potentials are detailed in Table 3.1 for pure Si and pure Ge.

Table 3.1: *Parameters employed in the SW+ZBL interatomic potentials used for pure Si and pure Ge. Units are given for the LAMMPS metal units style.*

	ϵ (eV)	σ (Å)	a	λ	γ	$cos(\theta_0)$	A	B	p	q	b^F	r^F
Si	2.1683	2.0951	1.80	21.0	1.20	-1/3	7.04955	0.60222	4.0	0.0	6.8	1.12
Ge	1.58	2.1810	1.80	21.0	1.20	-1/3	7.04955	0.60222	4.0	0.0	9.5	1.15

In order to assess the trustworthiness of our potentials, we checked that the general material properties are unchanged compared to pure SW potentials and that they are close to experimental values. In Table 3.2 are displayed some important material properties obtained with the SW and SW+ZBL potentials, for Si and Ge. We understand from Table 3.2 that the global material properties are not affected by the combination of SW with the ZBL potential. It is the behavior we were looking for as the purpose of the combination with the ZBL potential was only to correct the description of the collisions between atoms. This can be further confirmed by Fig. 3.7 showing the plots of the two-body attractive (long-range) part of the SW and SW+ZBL potentials in the case of Si and Ge with respect to the interatomic distance r. The SW potentials are clearly unchanged for $r > 1.5$ Å.

Table 3.2: *Material properties calculated with the SW and SW+ZBL parameters in Si and Ge. Melting points displayed for the SW potentials are taken from [10] whereas melting points for the SW+ZBL potentials were obtained following the procedure described in [22]. The experimental data are taken from [23].*

		Lattice param. (Å)	Bulk modulus (GPa)	Melting point (K)
Si	SW	5.431	101	1653
	SW+ZBL	5.432	102	1700 ± 30
	Expt.	5.431	100	1683
Ge	SW	5.654	66	1211
	SW+ZBL	5.654	66	1200 ± 30
	Expt.	5.654	65	1211

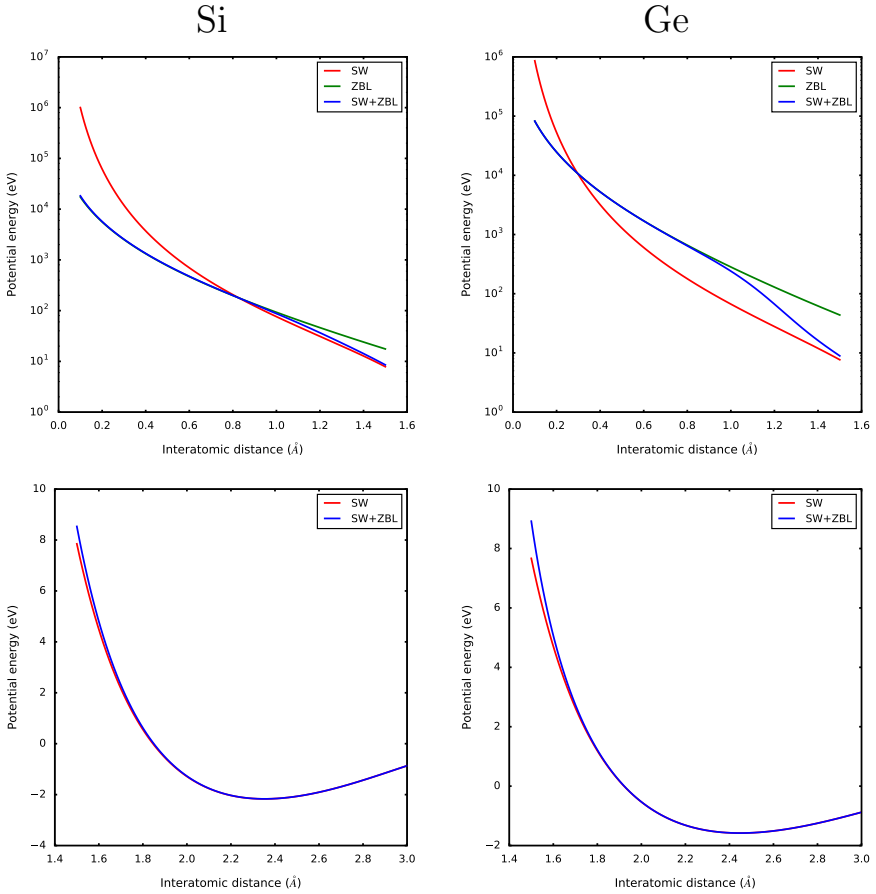

Figure 3.7: *Short-range (top) and long-range (bottom) two-body SW, ZBL (top only) and SW+ZBL potentials for Si (left) and Ge (right).*

The significance of the modifications for the collisional part is shown in Fig. 3.7 showing the repulsive two-body parts of the SW and SW+ZBL potentials for Si and Ge and in Fig. 3.8, which displays in the case of head-on collisions between a Si (Ge) PKA and a Si (Ge) atom, at various energies, the minimum interatomic distance between the two atoms. Although both for Si and Ge, the discrepancies between the ZBL and SW potentials are significant, the transitions between the two in the SW+ZBL potentials are smooth. In the case of Ge, the transition had to be a bit more abrupt compared to the Si transition, due to the larger discrepancy between the SW and the ZBL potentials. To ensure close collisions described by the ZBL and an equilibrium part with no influence of the ZBL potential, we had to make this more abrupt transition. The effects of the modifications in the repulsive two-body part of the SW potential are made blatant in Fig. 3.8. The typical collision distance are greater for Si with the SW+ZBL potential than with the purely SW potential, in agreement with the softening of the potential observed in Fig. 3.7. For Ge, the inverse is observed.

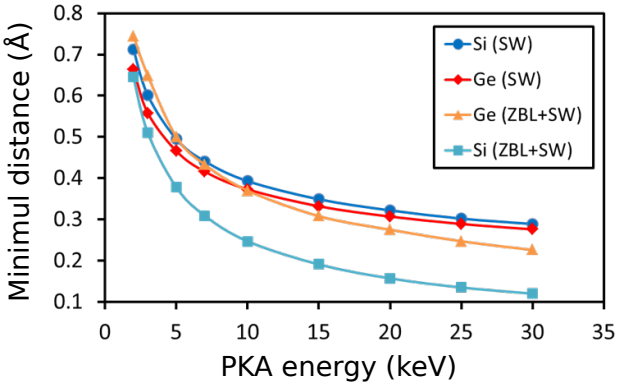

Figure 3.8: *Minimum distance attained in a head on collision between two Si or two Ge atoms depending on the potential employed.*

3.2.2.3 Coping with the stochasticity of the collision cascades

In a collision cascade, every collisions can be viewed as a stochastic event. Indeed, a slight modification of the velocity vectors directions of the atoms, of their respective orientation or their energy can induce drastic changes. For example, Fig. 3.9 shows the final damage state of two cascades simulated with MD in Si with an initial PKA energy of 10 keV. The only difference between the two cascades is the initial direction of the PKA.

Qualitatively speaking, the shape of the two cascades are drastically different. Quantitatively, it results in very different numbers of created defects and clusters as well as different sizes of clusters and PKA penetration depth. The fact that a large diversity of cascades scenarios can be obtained only by slightly changing the initial direction of the PKAs indicates that the stochasticity must be accounted for by running large number of simulations for each case studied, and therefore sampling a large number of possible cascades scenarios. With particle-matter interactions MC codes, it is possible to easily perform very large number of simulations (few millions), due to the very low computational cost of the technique, whereas the computational cost of MD makes it impossible to run that many cascades. However, published MD collision cascades studies all acknowledge the necessity to cope with the stochasticity of collision cascades. This is usually done by running a certain number of simulations with various initial directions for the PKA. Below is a non-exhaustive list of the chosen methods for setting both the initial directions of the PKAs and the size of the statistical ensembles in recent MD collision cascades simulations articles: Trung *et al.* constructed sets of 10 simulations in NiAl [24], He *et al.* based their statistical ensembles on 30 simulations initiated in random directions distinct by a little angle from a defined direction in GaAs [25], Buchan *et al.* chose to construct their mean values

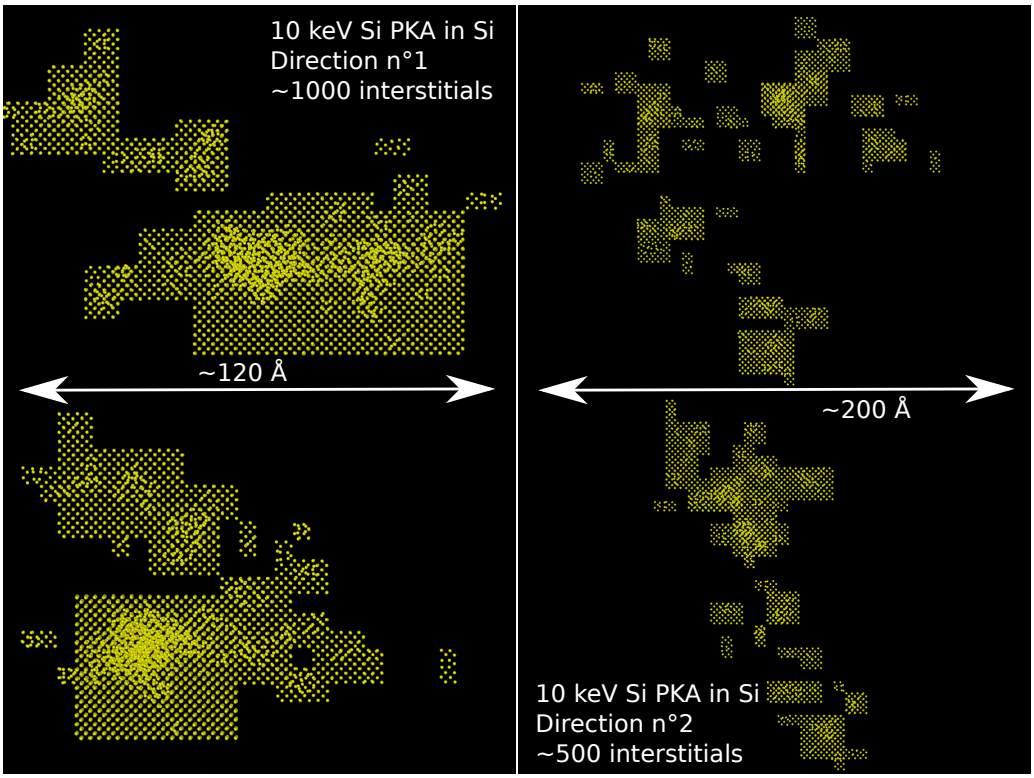

Figure 3.9: *State after 200 ps of cascades initiated in Si with 10 keV PKAs initially having different directions. The top and bottom views are the two same cascades, with different viewpoints. Only the clusters of defects are represented.*

in graphite over 25 simulations in definite directions [26], Zarkadoula *et al.* statistics for Ni and NiFe are based on 12 simulations in random directions [27], Gao *et al.* chose to initiate the cascades with random PKA directions for the 20 simulations performed in GaAs [16] and Christie *et al.* chose to do 20 simulations in well defined directions in graphite [28]. From the mentioned articles, no consensus on a satisfactory number of simulations to perform or on a strategy to employ to have converged results arises. This lack of coherence in the methods employed probably comes from a lack of studies focused on the specific aspect of the stochasticity in MD simulations of collision cascades. To our knowledge, apart from ours [29], there exists only two papers dedicated to this subject:

- In 2015, Warrier *et al.* proved in [30] that for cascades initiated with PKAs of energies in the range of 1 keV to 5 keV, whose initial directions are distinct and randomly chosen, 50-60 simulations are needed to make the number of displaced atoms stabilize in W and 60-80 simulations in Cu.

- More recently, Voskoboinikov studied the influence of the number of simulations performed on the estimated number of defects and clusters created following ion implantation in Ni, Al, Ti and their alloys [31] and provided a minimum number of simulations to be performed to reach the convergence depending on the system of interest, the temperature and the energy of the PKA.

Considering the studies of Warrier *et al.* and Voskoboinokov, we choose to run for each case studied 100 collision cascades simulations initiated by PKAs of different directions. The data obtained from the 100 simulations carried out are then treated in a rigorous statistical framework,

with uncertainties calculations for each mean value given as well as distribution plots under the form of histograms or box plots. With 100 simulations, we make sure to work with converged statistical data. Moreover, similarly to what was done in [26] and [28] but contrary to what Warrier *et al.* did in [30], we take into account the symmetry of the system when setting the initial directions of the PKAs. The method based on symmetry to choose the initial directions of the PKAs was first used by Jay *et al.* in [32] in Si. It is directly applicable to Ge and Si-Ge alloys as all those materials crystallize in a diamond structure.

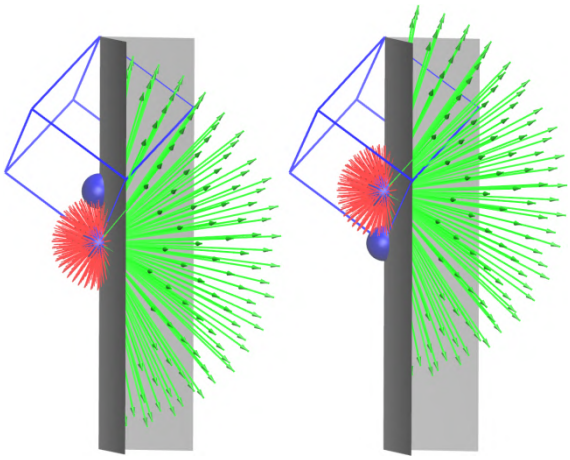

Figure 3.10: *Scheme of the minimal space domain in which 100 inequivalent directions are constructed. The two inequivalent atomic sites of the face-centered cubic diamond primitive unit cell are represented in blue. The inequivalent directions are depicted by long green arrows and the minimal space domain is delimited by the grey boundaries. The red small arrows represent the directions symmetrically equivalent to the green arrows of the minimal space domain. This figure was made by Antoine Jay.*

With this method, a set of distinct unit vectors (*i.e.* directions) uniformly distributed on the surface of a sphere is defined. Only the directions which are in the minimal space domain inequivalent to the others by crystalline symmetries have been kept, as depicted in Fig. 3.10. The unit sphere surrounding an atom is therefore divided into 6 symmetric parts. The minimal space domain is one of these parts. Thus, for each direction in the minimal space domain, there exists 5 others perfectly equivalent in the unit sphere. The weight of all the chosen directions is therefore the same.

In the next chapter, a detailed convergence study of the collision cascades results with respect to the chosen method for setting the initial PKA directions as well as the number of simulations performed will be presented.

3.2.2.4 Incorporation of electronic effects

The inclusion of electronic effects into MD simulations requires to resort to models to be employed in addition to the standard MD framework. The purpose of such models is to describe the exchange of energy between the ions and the electrons. Historically, theoretical works on the subject have been divided between the energy exchanges originating from *electronic stopping* and the ones originating from *electron-phonon coupling*. The former is now familiar to us and describes the excitation of electrons of the target material by high energy projectiles, whereas the latter depicts the energy exchanges between electrons and ions of low velocities (typically having thermal vibration energies). In a collision cascade, electrons quickly acquire an excess of energy compared to the majority of the ions, due to electronic stopping. Thus, the first stage of the electron-phonon coupling process consists in an energy exchange in the great majority from

the electrons to the ions. Then, when the electrons and ions are more or less at equilibrium, the amounts of energy exchanged from and to the electrons are of the same order. Despite the separate treatment by the theory of those two modes of energy exchange, the physics of the energy exchange are the same in both cases [33, 34]. This observation is of prime importance for the models aiming at incorporating the electronic effects into MD simulations. In the following (Paragraph 3.2.2.4.1 and Paragraph 3.2.2.4.2), we are going to see specific characteristics of the electronic stopping and electron-phonon coupling regimes of interest for the integration of electronic effects into MD simulations. Then, we will focus on two models (Paragraph 3.2.2.4.3 and Paragraph 3.2.2.4.4) taking as basis the mentioned electronic stopping and electron-phonon coupling specificities.

3.2.2.4.1 Electronic stopping

We aim at describing the electronic stopping of ions of velocities smaller than the Bohr velocity (about 700 keV for Si). The incorporation of the electronic stopping power can thus be based on the electronic stopping formulas of Lindhard and Firsov, both detailed in the previous chapter, which state that for low energy ions (*i.e.* up to few hundreds of keV, velocities we are interested in for collision cascades simulations), the electronic stopping power S_e is proportional to the velocity v of the ion: $S_e(v) = \lambda v$ where λ is a proportionality constant. The effects of the electronic stopping on a moving atom can therefore be seen as a simple friction force. This is the basic assumption from which electronic stopping is incorporated into MD.

3.2.2.4.2 Electron-phonon coupling

Before covering the basis of the electron-phonon coupling incorporation into models to be combined to MD, we have to say a few words on the existing controversy around the significance of electron-phonon coupling effects. In Swift Heavy Ion (SHI) irradiations experiments, *i.e.* material irradiation with heavy ions having initial energies in the MeV order, cylindrical regions where the atoms are disordered around the ion path are observed [35, 36]. Those regions are named ion tracks. The high velocities employed in SHI irradiations experiments make the probability of nuclear collisions between the projectile ions and target atoms of matter very unlikely. Therefore, the mechanism leading to the creation of the ion tracks must find its origin in the excitation of electrons and ionization of atoms. Some believe that electron-phonon coupling is the responsible mechanism: highly excited electrons by the incident heavy ion transmit sufficient energies to the ions of the lattice under the form of phonons to create disordered molten regions. This mechanism is called the *heat spike* mechanism [37, 38]. In this scenario, electron-phonon coupling is the principal mechanism leading to defects creation in SHI irradiations and is thus of prime importance.

However, many other studies defend a different point of view [39, 40]. According to those studies, the created defects might be due to Coulomb repulsion between ions of the matter, now positively charged because ripped of from the majority of their electrons. In this case, electron-phonon coupling has nothing to do with the production of defects. This mechanism is known as the *Coulomb explosion* model. Those two mechanisms have been presented as competing for many years, but the most complete view on the formation of ion tracks might actually be a combination of both mechanisms as stated in [41]. According to the paper just cited, both mechanisms are at stake, at different times of the formation of the ion track.

Going back to the case of collision cascades, where energies are by far less important than in SHI irradiations, the heat spike and Coulomb explosion mechanisms should not be as significant. In practice, the Coulomb explosion phenomenon is usually not incorporated into MD simulations

of collision cascades. The rate of energy loss by ionization is not sufficient to induce defects production via Coulomb repulsion between ions, or will produce very few disorder compared to the Coulomb collisions between nuclei. However, it can be taken into account into MD simulations of SHI irradiations by the use of a strongly repulsive screened Coulomb potential, like it was done in [41]. Unlike Coulomb explosion, electron-phonon coupling is incorporated into MD models of electronic effects. Although electron-phonon coupling is not suspected to have a major influence on the collision cascades results, it should be taken into account in the simulations. Indeed, it is a mechanism of energy exchange between ions and electrons which can therefore affect the simulation on a greater scale than Coulomb explosion, which actually does not induce exchanges of energy between ions and electrons.

Famous and successful models describing electron-phonon coupling in the heat spike model as well as electronic stopping power via the Lindhard and Firsov theory, both presented above, are named Two Temperature Models (TTMs). They are based on the assumption that following electronic excitation due to electronic stopping, electrons and ions (lattice atoms electrons are subtracted from) are out-of-equilibrium but that ions and electrons are respectively in internal equilibrium. Thus an atomic/ionic temperature T_{ionic} and an electronic temperature T_{elec} can be defined. In all those models, electrons are in many ways treated similarly to a heatbath of non-constant electronic temperature T_{elec} exchanging energy with the ions. The first TTMs developed were not thought to be combined to MD simulations. Initially, they were developed to simulate the dynamics of ions and electrons energy exchange following laser irradiation [42]. In those models, the atomic temperature T_{ionic} and electronic temperature T_{elec} were governed by a heat diffusion equation. Roughly, those models thus describe the energy exchanges between a continuous ionic bath and a continuous electronic bath. An atomistic description of matter was completely absent from those models. However, using as a basis the formalism of a Langevin thermostat, Caro and Victoria [33] paved the way for the combination of TTM with MD. In their model, the MD ionic (the MD system is said to be ionic and not atomic because electrons are considered in another system) system exchanges energy with an homogeneous heatbath of electrons. More recently, their idea was reemployed and adapted by Duffy and Rutherford [43] who improved it by making it possible for the electronic heatbath to be inhomogeneous. The model by Duffy and Rutherford, which is called the MD-TTM, will be presented in the following. Also, we are going to introduce a very recent state-of-the-art model further improving the MD-TTM model of Duffy and Rutherford and developed by Tamm *et al.* [44] and Caro *et al.* [45]. This model is called the MD-Electron-PHonon (MD-EPH) model. Originally, all those models were developed for metals, as the Lindhard and Firsov theory of stopping power were derived for metals. No specific model has been developed for semiconductors. However, it was proven from MD-TTM simulations in Si that bandgap effects of semiconducting materials can be included via correct definition of the parameters of the models [46] and from TDDFT simulations in Si that the electronic stopping in bandgap materials is metal-like above a projectile energy of few keV and nearly metal-like below [47]. We therefore apply those models to semiconducting materials.

3.2.2.4.3 Two-Temperature Model for MD (MD-TTM)

The basic idea of the MD-TTM is to couple the usual MD system of interest to a fictitious electronic system acting as a heatbath, as illustrated in Fig. 3.11. The coupling of the ionic subsystem to the electronic heatbath follows the formalism of a Langevin thermostat that we have seen in Section 3.2.1.

Both the ionic system and the electronic subsystem are divided into small cells, which form two regular grids with the same size. In each cell, an ionic temperature T_{ionic} and an electronic

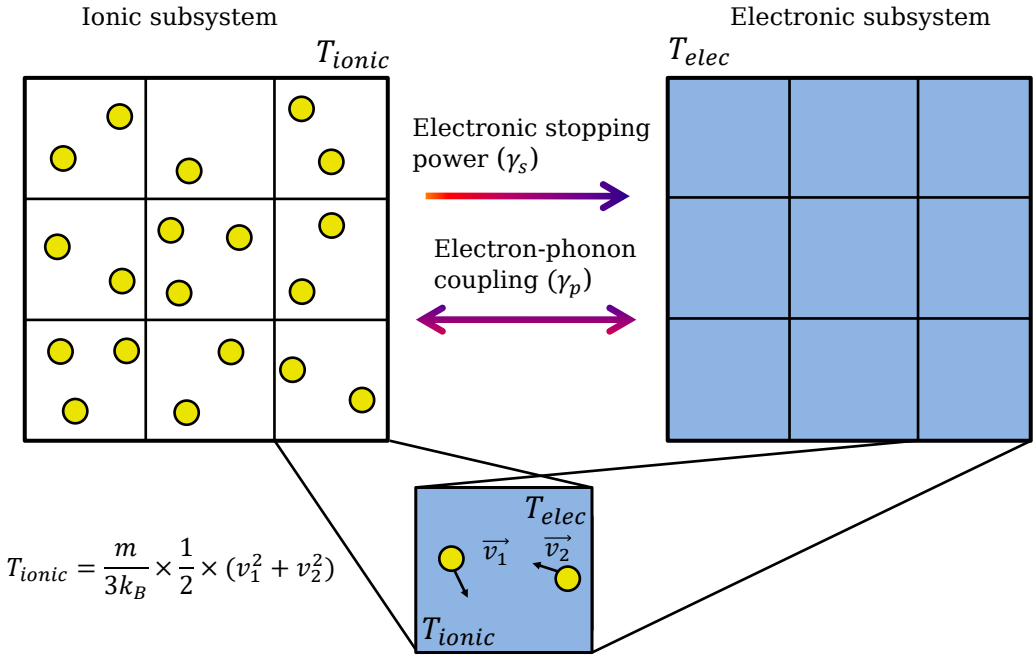

Figure 3.11: *2D illustration of the working principle of the TTM model. All terms appearing in the figure are defined in the text.*

temperature T_{elec} are defined. The electronic heatbath can thus be inhomogeneous, with each cell having its own T_{elec}. However, the electronic density in every cell is the same and thus considered to be constant in the entire simulation box. T_{ionic} is defined in each cell as the usual MD temperature given by:

$$T_{ionic} = \frac{m}{3k_B} \frac{1}{N} \sum_{i=1}^{N} v_i^2 \tag{3.46}$$

where, in the considered example, all ions have the same mass m, N is the number of ions in the cell, v_i is the velocity of the i^{th} ion of the cell. In practice, each cell must contain enough atoms to define a statistically meaningful temperature.

The cells of the ionic and electronic systems which are at the same position exchange energy through the γ_s and γ_p parameters of the model as pictured in Fig. 3.11. The former being the electronic stopping power and the latter the electron-phonon coupling. The ions lose a part of their kinetic energy because of γ_s and γ_p. This energy is transferred to the electronic subsystem, which increases its temperature T_{elec}. It is interesting to note that both parameters play the same role in the kinetic energy loss of moving ions. Part of the energy gained by the electronic subsystem can be fed back to the ionic system through the electron-phonon coupling γ_p. To account for those energy exchanges, the MD ionic equations of motion are rewritten in the framework of a Langevin thermostat, where a friction force acts as the electronic stopping, following the work of Firsov and Lindhard, and a stochastic force term embodies electron-phonon coupling (3.47):

$$m_i \frac{d\vec{v_i}}{dt} = \vec{F_i} - \gamma_i \vec{v_i} + \vec{f_i^{stoch}} \tag{3.47}$$

where, $\vec{v_i}$ is the velocity of the ion i, $\vec{F_i}$ represents the adiabatic forces acting on the ion i deriving from the potential, γ_i is the friction coefficient, and $\vec{f_i^{stoch}}$ represents the stochastic forces acting

on ion i. The latter has zero mean and its magnitude is related to T_{elec} and γ_p following:

$$\begin{cases} < \vec{f}_i^{stoch}(t) >= 0 \\ < \vec{f}_i^{stoch}(t).\vec{f}_i^{stoch}(t') >= 2k_B T_{elec}\gamma_p \delta(t-t') \end{cases} \tag{3.48}$$

where $\delta(t-t')$ equates to 0 except for $t = t'$ for which it equates to 1. Thus, it ensures no temporal correlations between the stochastic force terms. According to the fluctuation-dissipation theorem [48], $< \vec{f}_j^{stoch}(t).\vec{f}_j^{stoch}(t') >$ in (3.48) should actually be equal to $2k_B T_{elec}\gamma_i \delta(t-t')$. However, it is chosen in the TTM, for obvious physical considerations, that the electronic stopping parameter γ_s should not contribute to energy going from the electrons to the ions. This has consequences (that we will see later) on the energy balance between the electronic and ionic subsystems, normally ensured by the fluctuation dissipation theorem.

The γ_i coefficient depends on the velocity of the considered ion. If the velocity of the ion i is below a critical velocity v_0, then $\gamma_i = \gamma_p$, otherwise, $\gamma_i = \gamma_s + \gamma_p$. The friction coefficient γ_i can then be defined like in (3.49):

$$\begin{cases} \gamma_i = \gamma_p \ \text{ if } \ ||\vec{v}_i|| \leq v_0 \\ \gamma_i = \gamma_p + \gamma_s \ \text{ if } \ ||\vec{v}_i|| > v_0 \end{cases} \tag{3.49}$$

From (3.49), it appears that the friction force is defined as a sum of γ_p and γ_s for $||\vec{v}_i|| > v_0$. At high enough velocities, the total electronic energy loss of the ions is viewed as a sum of the electronic stopping power and of the electron-phonon coupling. This is a vision somewhat controversial as electron-phonon coupling is not suspected to have a major role at high velocities. Some models directly derived from the TTM added another velocity threshold above which only electronic-stopping power γ_s was taken into account. Also, even if this is not incorporated in the original derivation of the MD-TTM of Duffy and Rutherford, it is often recommended to let the system evolve for a fraction of ps before including the electron-phonon coupling [49] because during the early stages of the cascade, the atomic temperatures are ill-defined due to the very fast-moving atoms. This option can be added through the definition of a new parameter called t_{eph}.

In addition, the heat diffusion in the electronic subsystem is taken into account via the following relation:

$$C_e \frac{\partial T_{elec}}{\partial t} = \nabla(\kappa_e \nabla T_{elec}) - g_p(T_{elec} - T_{ionic}) + g_s T'_{ionic} \tag{3.50}$$

where C_e is the electronic specific heat, κ_e is the electronic heat conductivity, T_{ionic} is the atomic temperature, T'_{ionic} has the dimension of a temperature and ensures the energy balance between electronic and ionic subsystem. The coefficients g_s and g_p derive from γ_s and γ_p via the following relations:

$$\begin{cases} g_p = \frac{3Nk_B\gamma_p}{\Delta V m} \\ g_s = \frac{3Nk_B\gamma_s}{\Delta V m} \end{cases} \tag{3.51}$$

where ΔV is the volume of the considered regular grid cell. The left hand side and first term of the right hand side of (3.50) govern basic energy diffusion, the second term of (3.50) represents the energy exchange with the ionic system due to the temperature difference between the electronic and ionic cell and the third term is a source term added to ensure energy balance between the two systems in spite of the energy lost by the ions via the γ_s parameter not being compensated by the stochastic force term as highlighted in (3.48). The expression of T'_{ionic} can be obtained by equating at each timestep the total frictional energy loss ΔU_{loss} of a given ionic cell:

$$\Delta U_{loss} = \Delta t \sum_i^N \gamma_i v_i^2 \tag{3.52}$$

with the energy ΔU_{gained} gained by the electronic subsystem of the connected cell:

$$\Delta U_{gained} = g_p \Delta V \Delta t (T_{ionic} + T'_{ionic}) \tag{3.53}$$

We obtain in the end the expressions of (3.51) for g_p and g_s as well as the following expression for T'_{ionic} [43]:

$$T'_{ionic} = \frac{m}{3k_B} \frac{1}{N'} \sum_{i \in S}^{N'} v_i^2 \tag{3.54}$$

where N' is the number of atoms having a velocity higher than v_0 in a given cell and S gathers all the atoms with $v_i > v_0$.

All the employed fundamental parameters (the ones which cannot be defined from a combination of parameters) in the above equations have to be specified by the user of the MD-TTM model. Their physical sense as well as their optimal values or expressions for Si and Ge, according to our careful literature search, are given in the following.

Electronic specific heat (C_e)

The electronic specific heat C_e describes the amount of energy needed to increase by 1 K the temperature of the electronic system. It is electronic temperature dependent. Following (3.50), it governs the temporal rate of energy exchange between the ionic and the electronic subsystem: the greater C_e, the smaller the rate. In metals, C_e is linear at low T_{elec} and constant and equal to the free electron gas value of $3/2k_B$ at high T_{elec}. Simple models can be built to accurately describe the T_{elec} dependence of C_e in the TTM for metals [43]. For semiconductors, C_e is first nearly constant and equal to zero at low T_{elec} due to the band gap, and then starts increasing. Khara *et al.* have calculated C_e for Si [46]: they have estimated the T_{elec} dependence of C_e in Si with DFT calculations. They use a Fermi-Dirac smearing for performing finite electronic temperature calculations. In our case, we consider C_e constant and equal to the free electron gas value of $3/2k_B$ above the Fermi temperature (when the conduction band is populated). Aiming at constructing a simple model, we have modified the C_e model of Duffy and Rutherford [43] to adapt it to semiconductors in a similar manner as what was done by Phillips *et al.* in [50]:

$$C_e(x) = 0.5 \times (A - \epsilon) \times (1 + \tanh(B(x - x_f))) + \epsilon \tag{3.55}$$

where $x = T_{elec}/1000$, $A = 3/2k_B$, and the coefficients B and x_f are fitted to reproduce the experimental measurements [51] at low temperature and the $3/2k_B$ asymptote above the Fermi temperatures. The Fermi temperatures are 6 498 K and 3 829 K for Si and Ge respectively. For Si, we have $B = 2.2$ and $x_f = 2.0$, whereas for Ge it is $B = 1.3$ and $x_f = 3.1$. Due to numerical limitations intrinsic to the TTM implementation of LAMMPS, C_e cannot be set as close to zero as desired. This is the purpose of ϵ in (3.55) that guarantees a minimum small value for C_e ($\epsilon = 10^{-6}$ eV/K). Therefore, C_e does not match perfectly the low temperature experimental points as can be seen in Fig. 3.12 and is set as low as possible, without any consequences on the results.

Electronic thermal conductivity (κ_e)

The electronic thermal conductivity κ_e characterizes the temporal rate at which the different cells forming the electronic subsystem exchange energy one with each other. It is electronic temperature dependent. Note that the ratio of κ_e and C_e gives the electronic diffusivity $D_e = \kappa_e/\rho C_e$, which quantifies the rate at which an electronic cell loses or gains energy via exchange with the nearby cells or via exchange with the ionic subsystem. Within the TTM implementation of LAMMPS, D_e is considered to be constant and must be given as an entry parameter by the user

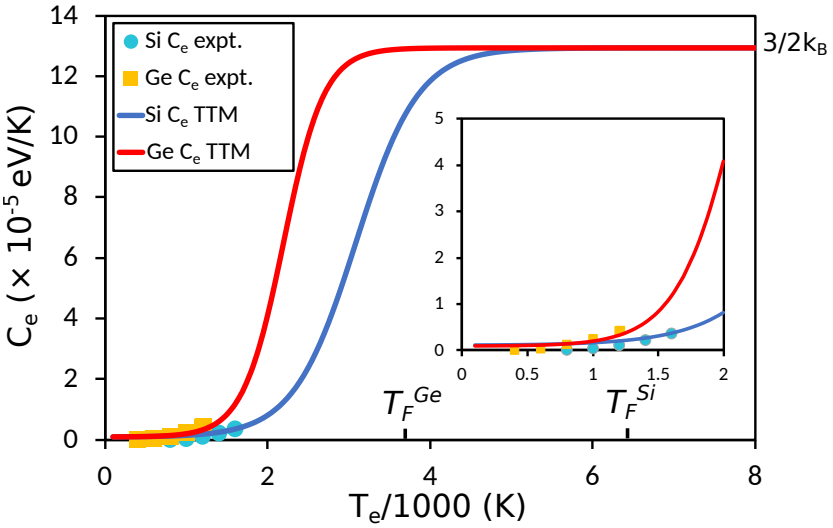

Figure 3.12: *Variation of the electronic specific heat for Si and Ge as a function of the temperature. The Fermi temperatures, written T_F^{Si} and T_F^{Ge}, and the asymptotic value are shown. Variations at low temperatures are given in the insert.*

whereas κ_e is not defined directly by the user but indirectly via $\kappa_e = \rho D_e C_e$, and the definition of the electronic density ρ, C_e and D_e by the user. According to [52], in Si, ρ can be chosen equal to 0.05 $e^-/Å^3$ and D_e to 20000 $Å^2$.

Electronic stopping power (γ_s)

In the MD-TTM framework, the electronic stopping power is a friction coefficient through which fast enough moving atoms lose energy to the electronic subsystem. In practice, calculating the electronic stopping power of an ion moving with a certain velocity can be done with TDDFT [53]. However, the easiest way to quantify it for the TTM remains the use of SRIM tables and the Lindhard and Sharff model [4, 54]. For nearly 0 keV to 100 keV Si ions in Si, the calculation of γ_s with SRIM gives 39.4 g/mol/ps (LAMMPS metal units for γ_s), *i.e.* 4.1×10^{-3} eV.ps/$Å^2$. For nearly 0 keV to 100 keV Ge ions in Ge it gives 31.6 g/mol/ps, *i.e.* 3.3 $\times10^{-3}$ eV.ps/$Å^2$.

Electron-phonon coupling (γ_p)

This parameter has two roles in the MD-TTM. First it is part of the friction coefficient through which the ions lose energy to the electronic subsystem. Second, it drives the amount of energy fed back to the ions from the electronic subsystem, the energy at stake being proportional to the electron-ion coupling. In the TTM model, it is considered to be constant for the entire range of temperature. For some material, the electron-phonon coupling is determined by combining experiments and theoretical models. As noticed by Duffy [43], the range of reported values for the electron-phonon coupling parameter for a given material can be very large. For Si, two values, differing by a factor of 3, have been reported [55, 56]. To us, the value of 24.4 g/mol/ps [55] which was optimized for SHI simulations in Si to provide the best fit with experimental data is the most trustworthy. No data were available for the electron-phonon coupling in Ge at the time this thesis was written, it thus did not seem unreasonable to use the same value as for Si. The values for the two materials are expected to be similar considering the common properties they share. The current hypothesis is that the real Ge value is probably slightly lower than the Si one due to the enhanced size of thermal spikes in Ge compared to Si ones which could make it harder for Ge to support phonons [43].

Velocity threshold for the electronic stopping power (v_0)

The electronic stopping power can be envisioned as acting only on ions whose velocity is not too small [7]. At low energies, only the electron-phonon coupling acts on the ions [57]. The v_0 parameter idea is to incorporate this fact into the TTM model. The choice of a correct value or rule to follow for v_0 is still debated: Zarkadoula *et al.* [27] and Jay *et al.* [32] used a threshold corresponding to twice the cohesive energy of the material whereas Björkas *et al.* [58] employed a threshold velocity corresponding to the cohesive energy and Nordlund *et al.* [59] chose the value of 10 eV. In order to be coherent with our previous studies [32], we choose to set v_0 to twice the cohesive energy of the system. Thus, v_0 is set to 79.8 Å/ps (*i.e.* a cohesive energy of 4.6 eV [23]) in Si and 45.2 Å/ps (*i.e.* a cohesive energy of 3.8 eV [23]) in Ge.

Electron-phonon activation time (t_{eph})

It is recommended to turn on the electron-phonon coupling only after a certain amount of time [49]. Indeed, in the early stages of a cascade, the atomic temperatures T_{ionic} calculated by the MD code are artificially high due to the presence of very fast moving atoms. Thus, the energy exchanges between the electronic and ionic subsystems are biased at the beginning of the cascade. This issue can be overcome by delaying the electron-phonon energy exchanges. We added this option in LAMMPS, thus defining a new parameter called t_{eph}. The electron-phonon coupling γ_p is then:

$$\begin{cases} \gamma_p = 0 \quad t \leq t_{eph} \\ \gamma_p = 24.4 \quad \text{g/mol/ps} \quad t > t_{eph} \end{cases} \tag{3.56}$$

3.2.2.4.4 Electron-Phonon model for MD (MD-EPH)

One of the main limitations of the MD-TTM lies in the electronic density, considered constant in the entire material. With such an approximation, even if the dynamic of the atoms is followed atom by atom in the MD framework, the electronic effects modelled are completely independent of the atoms movements. For example, no distinction is made between the electronic stopping power felt by an ion travelling in a low electronic density channelling direction and an ion sampling regions of higher electronic densities along its trajectory, whereas it was observed via TDDFT simulations [60] and experiments [61] that electronic stopping power in crystalline solids is highly crystal direction (*i.e.* electronic density) dependent. Also, the strength of the electron-phonon coupling is the same in a perfectly crystalline region or in an amorphous pocket, whereas it is well known that amorphous materials hardy support phonons. The MD-EPH model consists in a significant improvement of the MD-TTM by incorporating a non-constant electronic density. The latter now depends on the position of the nuclei in the simulation box and is therefore dynamic. It opens the way for the modelling of complex electronic stopping and electron-phonon density-dependent features.

The MD-EPH formalism is based, just like MD-TTM, on the framework of a Langevin thermostat as well as two regular grids, one for the ionic subsystem and one for the electronic subsystem. The electronic subsystem is also T_{elec} inhomogeneous. However, the equations of the thermostat are complexified in order to incorporate a spatial dependence (via the electronic density, which is spatial dependent) in the electronic stopping and electron-phonon coupling. We move from the scalar description adopted in the MD-TTM to the many-body matrix/tensorial notations described in [44]. In the framework of the EPH model, forces act in a correlated manner over different particles and the equation of motion for ion i is now written:

$$m_i \frac{d\vec{v_i}}{dt} = \vec{F_i} - \sum_j B_{ij}\vec{v}_j + \sum_j W_{ij}\vec{\xi}_j \tag{3.57}$$

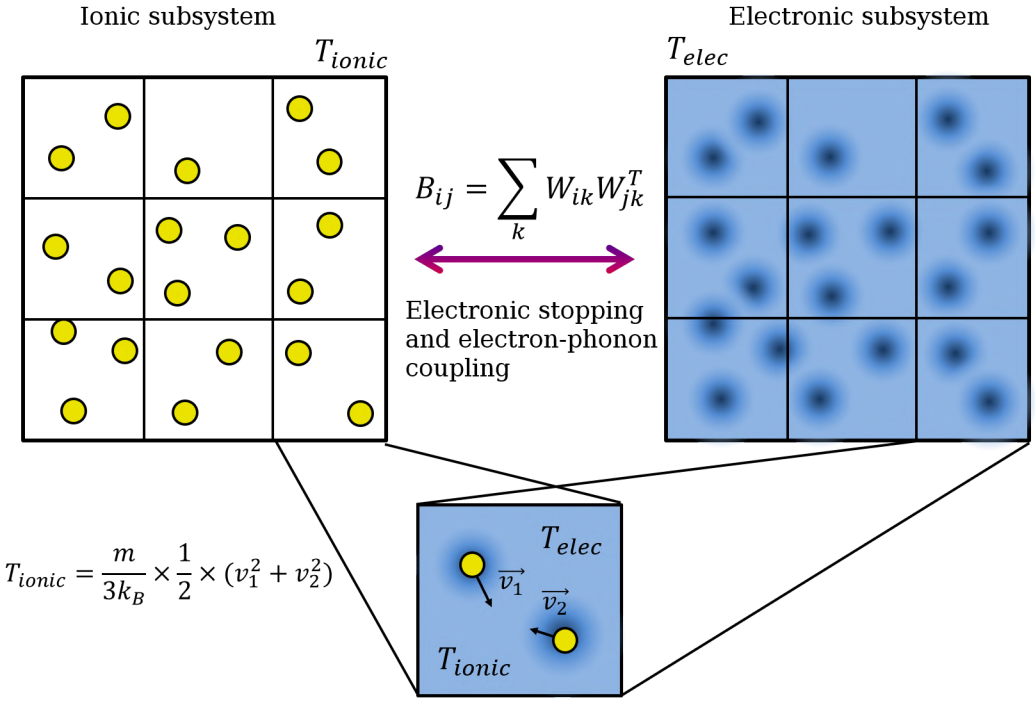

Figure 3.13: *2D illustration of the EPH model. The variation in the color of the electronic subsystem highlights the non-constant electronic density of the model. All terms appearing in the figure are defined in the text.*

where $\vec{F_i}$ are the adiabatic forces deriving from the interatomic potential, $\sum_j B_{ij}\vec{v}_j$ the friction force acting on ion i where B_{ij} are ij components of the B tensor defining the magnitude of the friction force and $\sum_j W_{ij}\vec{\xi}_j$ the stochastic force acting on ion i. In this last term, $\vec{\xi}_j$ are uncorrelated Gaussian random variables with zero mean and normalized to $2k_BT_e$ and W_{ij} are ij components of the W tensor defining the magnitude of electron-phonon coupling. The characteristics of the stochastic forces $\vec{f}_i^{stoch} = \sum_j W_{ij}\vec{\xi}_j$ are as follows:

$$\begin{cases} < \vec{f}_i^{stoch}(t) >= 0 \\ < \vec{f}_i^{stoch}(t).\vec{f}_j^{stoch}(t') >= 2k_BT_{elec}\delta(t-t')\sum_k W_{ik}W_{jk}^T \\ < \vec{\xi}_i(t).\vec{\xi}_j(t') >= 2k_BT_{elec}\delta(t-t')\delta_{ij} \end{cases} \tag{3.58}$$

where $\delta(t-t')$ equates to 1 if $t = t'$ (0 otherwise) and δ_{ij} equates to 1 if $i = j$ (0 otherwise). From (3.58), we understand that $\vec{\xi}_i$ random variables have no time and space correlations, whereas the random forces are not time correlated (just like in the MD-TTM) but are space correlated via the off-diagonal terms of the W matrix. With those off-diagonal terms, the random force acting on particle i is dependent on the random forces acting on other particles. The same observation can be made for the friction force: the electronic stopping of ion i depends on the stopping and velocities of other ions of the simulation box. It is interesting to note that if the W and B matrices are taken diagonal, with $W_{ij} = \gamma_p\delta_{ij}$ and $B_{ij} = \gamma_s\delta_{ij}$, we find back the equations of the MD-TTM. Progressing into the derivation of the model, based on the fluctuation-dissipation theorem [48], it can be shown that friction and random forces need to be related by the following expression:

$$B_{ij} = \sum_k W_{ik}W_{jk}^T \tag{3.59}$$

The magnitude of the friction and random forces are therefore both defined by the W tensor. This strong choice made in the EPH model is based on the works of Caro *et al.* [33] and Koponen [34] of the early 90s, as well as on recent results by Caro *et al.* [62], which states that electronic stopping and electron-phonon coupling are the "opposite limits of the same basic governing equations" (or mechanism) [34]. In other words, based on the same physics of energy exchange, electronic stopping power describes the case of high velocity projectiles sampling regions of various electronic density, whereas electron-phonon coupling corresponds to low velocity ions oscillating around their equilibrium positions of relatively low electronic densities. This aspect is made explicit by the correlations between friction and random forces shown in (3.59). The definition of W must ensure the conservation of angular and linear momentum [44] in order to have a rich electron-phonon mode. Aiming at this, the W_{ij} matrix terms of the W tensor are defined as follows in the MD-EPH model:

$$W_{ij} = \begin{cases} -\alpha_j(\bar{\rho}_j)\frac{\rho_i(r_{ij})}{\bar{\rho}_j}\vec{e}_{ij} \otimes \vec{e}_{ij} & (i \neq j) \\ \alpha_i(\bar{\rho}_i)\sum\limits_{k\neq i}\frac{\rho_k(r_{ik})}{\bar{\rho}_i}\vec{e}_{ik} \otimes \vec{e}_{ik} & (i = j) \end{cases} \tag{3.60}$$

where $\rho_i(r_{ij})$ is the electronic density created by atom i at a distance r_{ij} from itself, $\bar{\rho}_i = \sum_{j\neq i}\rho_j(r_{ij})$, $\vec{e}_{ij}$ are unit vectors of the ij direction and $\alpha_i(\bar{\rho}_i)$ density-dependent parameters homogeneous to the square root of the electronic stopping power divided by a velocity. In (3.60) are appearing two density-dependent terms, the weighting $\rho_i(r_{ij})/\bar{\rho}_j$ and $\sum\limits_{k\neq i}\rho_k(r_{ik})/\bar{\rho}_i$ terms defining the weight of the different contributions to the W_{ij} term and the $\alpha(\rho)$ parameters, controlling the magnitude of the friction and random forces deriving from the W_{ij} matrix terms.

The electronic density in the MD-EPH model is not the real one, as it would require solving of the Schrödinger equation at every step of the simulation. Instead, a similar description of electronic density as in the case of Embedded-Atom-Method (EAM) interatomic potentials is used: the contribution to the total electronic density of an atom is equal to the spherical electronic density of the atom if it was not in a crystal. The electronic density at a given point of the simulation box is thus equal to the sum of the spherical single atom contributions. The single atom spherical electronic densities have to be specified by the user. A solution used by the developers of the EPH model in [45] and [63] is to employ the pseudopotential generation code OPIUM [64] to calculate the spherical electronic densities.

Additionally to the electronic density files, the $\alpha(\rho)$ parameters have to be specified by the users of the MD-EPH model. In practice, they can be obtained by doing Real Time-TDDFT (RT-TDDFT) calculations of electronic stopping in the Ehrenfest Dynamics (ED) formalism, from which it is possible to extract the evolution of the electronic stopping power of a projectile as a function of the local electronic density sampled by the projectile. The RT-TDDFT technique is acknowledged to provide with accurate description of both electronic stopping [65] and electron-phonon coupling [62]. The efforts to be made by the user in order to be able to employ the MD-EPH model are therefore more important than for the MD-TTM, as preparatory ED calculations have to be carried out. However, the electronic effects can be incorporated with better accuracy with this model compared to the MD-TTM one. Fig. 3.14 compares the energy lost to electronic excitations along a given trajectory by a Si PKA in Si with the MD-TTM and with the MD-EPH model. The energy lost to the electrons in the case of a TDDFT simulation, which can be considered as reference, is shown for comparison. The energy loss with MD-TTM is linear, thus unable to follow the complex electronic density dependence revealed by the reference ED data, whereas the energy loss obtained with the MD-EPH model follows closely the reference TDDFT data. A complete theoretical description of TDDFT, RT-TDDFT and ED will be given in Section 3.4. The methodology to extract the $\alpha(\rho)$ parameters from the ED calculations will

be detailed in a chapter dedicated to the simulation of collision cascades with the MD-TTM and MD-EPH model.

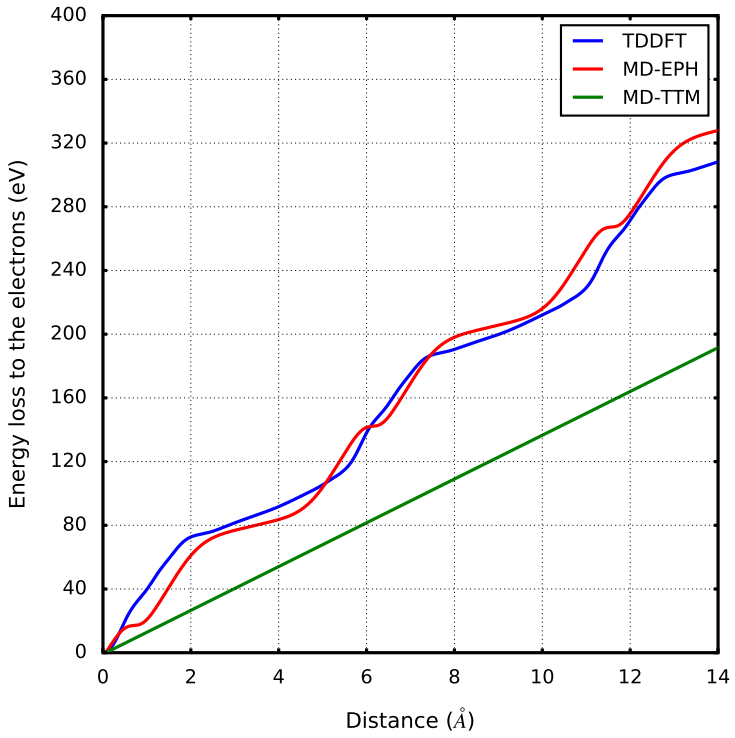

Figure 3.14: *Energy lost to the electrons along a given trajectory by a 100 keV Si PKA in Si with MD-TTM, MD-EPH and TDDFT, with respect to the distance travelled by the PKA.*

We have covered in the above the equations of the MD-EPH model related to the ion dynamics part of the model. The treatment of the electronic heatbath, apart from the electronic density, is actually the same as in the MD-TTM: a 3D regular grid made of cells each defined by their own T_{elec} exchange energy with the corresponding ionic cells, just like in Fig. 3.11. The electronic heat diffusion is also governed by a heat diffusion equation. Therefore, the electronic thermal parameters (C_e, D_e, κ_e) employed in the MD-TTM are also used in the MD-EPH model, with the same signification.

3.2.3 Usage of MD simulations results in our multiscale approach

The out-of-equilibrium and stochastic nature of collision cascades make it a challenge to accurately simulate them with MD. Methods were presented to cope with those issues, relying on wise choice of interatomic potentials to correctly describe collisions as well as statistical treatment of the simulation results. However, to be incorporated in our global simulation approach, the MD step must also account for electronic effects. To do so, it is necessary to resort to models (for instance MD-EPH and MD-TTM) to be used in addition to the standard framework of MD. Considering all those aspects, MD offers a trustworthy picture of the defects production in materials. The major outputs of the MD step of our multiscale approach are the final damaged structures files, from which can be post-processed the number of defects created, their distribution inside clusters, the size of the collision cascades, among other properties. Nonetheless, all the efforts undertook to make our MD simulations of collision cascades trustworthy cannot bypass the major limitation of MD; its timescale. Above few nanoseconds of simulated time, there is not enough energy in the system to make it evolve. Indeed, after few nanoseconds the only possible events are diffusion ones leading to reordering of clusters. Those events are said to

be activated, meaning an energy barrier must be overcome for them to occur. Overall, although few nanoseconds are long enough to describe the collisional phase of the cascade, defects production and immediate healing, it cannot account for defects and clusters reordering occurring on longer timescales [66], which are essential for the identification of typical cluster sizes and comparison with experiments. This is the reason why the damaged structures obtained with MD are further relaxed with the kART code, which we present in detail in the next section.

3.3 Kinetic Activation-Relaxation Technique (kART)

It has been observed in CMOS image sensors that following an irradiation, the DC and DC-RTS levels can vary on timescales of the order of hours after the irradiation, sometimes even more. It means that defects reordering occur inside matter, via activated events, in timescales not accessible with MD simulations. To be able to simulate reordering of defects and clusters by diffusion, we choose to use the kART technique [67, 68]. With this technique, timescales equivalent to experimental ones (seconds or more) are accessible in reasonable computing times. The damaged structures at the end of the kART runs are therefore much more similar to the real damaged material structures on which the DC and DC-RTS measurements are carried out.

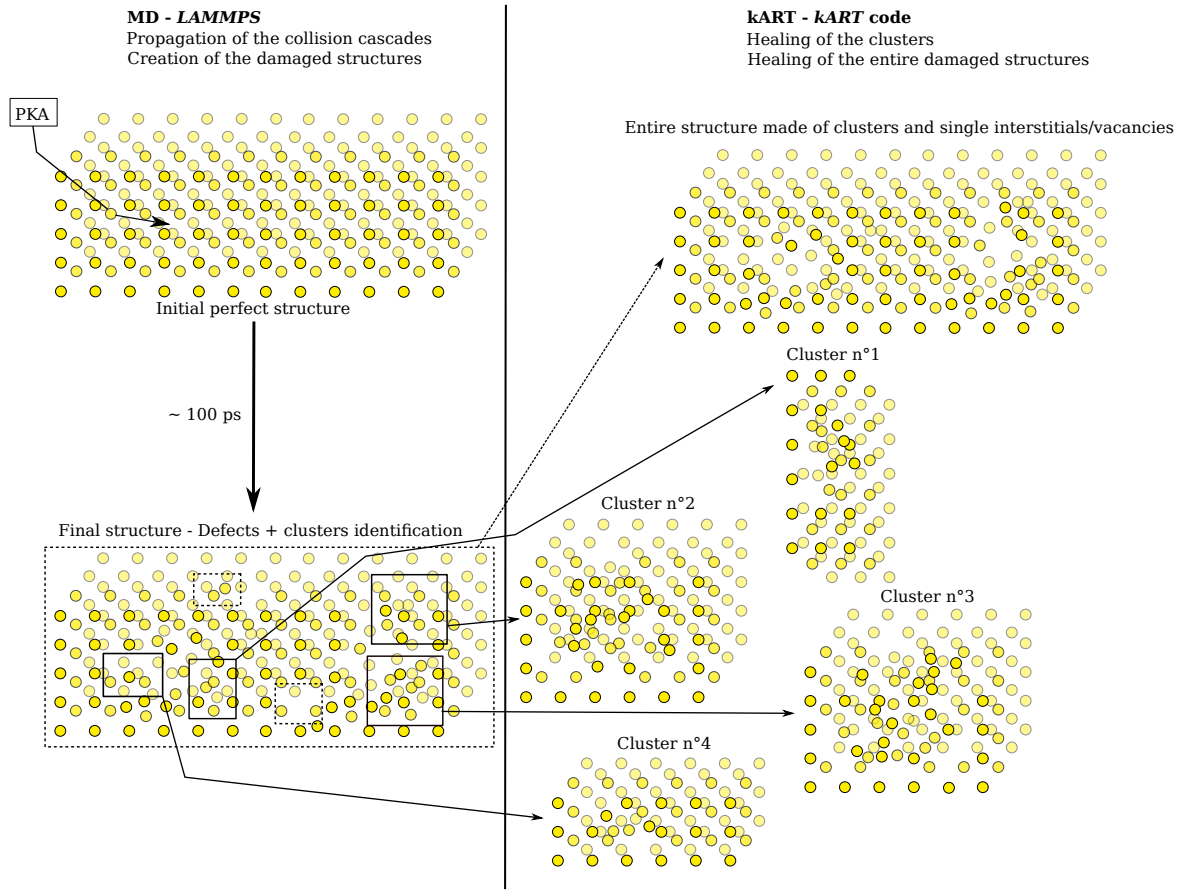

Figure 3.15: *Illustration of the transition from MD to kART in our multiscale approach. In kART the clusters can be studied separately and/or the complete structure made of clusters as well as single interstitials and vacancies can be studied in a single longer simulation.*

In theory, the transition between the 2^{nd} MD step of our multiscale approach and the 3^{rd} kART step is relatively straightforward. Indeed, both techniques are atomistic, and the damaged structures obtained at the end of the MD simulations are directly usable to launch kART calculations. In practice, as a kART simulation on an entire MD cell can be prohibitive in terms of simulation time, it is also possible, to run multiple simulations on clusters of defects extracted from the

complete MD simulation cells. Of course, this should be done when clusters are far enough one from each other so that they do not interact and recombine. This strategy, more than just being faster, can also enable to accelerate simulations on complete MD cells, benefiting from the so-called "self-learning" aspect of the code (more on this later in this section). The transition between the MD and the kART step of our multiscale approach is illustrated Fig. 3.15.

The kART technique combines the kinetic-Monte Carlo (kMC) method for the choice of events to the ART-nouveau (ARTn) technique [69, 70] allowing to search for events on-the-fly. It corrects many of the issues related to standard kMC codes by being off-lattice and in a certain way "self-learning". To give a complete description of the kART technique, we are first going to introduce the kMC concepts, extending what we have seen on simple MC codes, before presenting the kART algorithm in itself and the ARTn event search algorithm.

3.3.1 Kinetic-Monte Carlo

The fundamental difference between standard MC and kMC techniques is the possibility in the latter to study the dynamic evolution of a system by explicit time description. In a standard MC code, the acceptation or not of events is based on the computation of the event probability. In a kMC code, instead of static probabilities, transition rates are employed. Apart from this conceptual difference, the main ideas between MC and kMC are very similar. In particular, the MC algorithms of Geant4 for the selection of interaction mechanism presented in Section 3.1 and the kMC implementation of kART are very much alike. Within kART, the transition rate r from a state S_1 to another state S_2 separated by an energy barrier ΔE_{12} comes from the transition-state theory [71] formula below:

$$r = \tau_0 e^{-\frac{E_{12}}{k_B T}} \tag{3.61}$$

where τ_0 is called the attempt frequency and is considered within kART constant and equal to 10^{13} s^{-1}, for optimization and simplicity purposes. It is a simplification to consider it constant but in Si, the given value was found to be compatible with *ab initio* vacancy diffusion calculations [72]. Also, it has been shown that τ_0 do not vary much with the described event [73]. Based on this formula for the rate, we explain in the following the basic kMC concepts. We consider a system at a time t in a state in which N events are possible. Each event has an associated rate r_i defined following (3.61). The cumulative rates R_i are defined as follows:

$$R_i = \sum_{j=1}^{i} r_j \tag{3.62}$$

A uniform random number z between 0 and 1 is generated. The event i is picked if it obeys to the the rule below:

$$R_{i-1} \leq z R_N < R_i \tag{3.63}$$

This rule makes the probability for an event to be chosen proportional to its rate r_i, which is what we are looking for. Note how (3.63) is similar to (3.29) for selecting interaction mechanisms with Geant4 (Section 3.1). The rule formalized in (3.63) is often illustrated just like in Fig. 3.16, depicting the event as sections of a segment: a random point is selected on the segment, the chosen event is the one corresponding to the segment part where the point is located.

With Fig. 3.16, it clearly appears that the bigger r_i is (*i.e.* the larger the r_i segment section), the greater the probability is for the event to be picked. Note that in the kMC algorithm, contrary to the simple MC algorithm described in Section 3.1, every step leads to the choice of an event. The algorithm is said to be rejection-free. The search for a rejection-free algorithm is one of the reason that led Bortz *et al.* to develop the kMC method [74, 75]. However, as mentioned earlier,

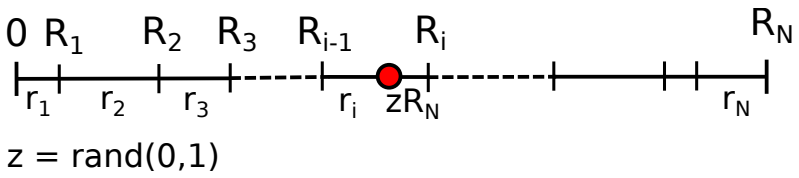

Figure 3.16: *Illustration of the rule for choosing the events depending on their rates in kMC algorithms.*

the main motivation to develop the kMC approach was the explicit treatment of time, allowing to follow dynamical evolution of systems, when standard MC samples the different equilibrium states of a system to compute average observables.

The mean number of events occurring per unit of time is given by R_N. Therefore, the average waiting time $< \Delta t >$ between two events can be defined as $< \Delta t >= 1/R_N$. Nonetheless, at each step of a kMC simulation time is not incremented of this mean quantity $< \Delta t >$. Indeed, it can be proven that waiting times are distributed following a Poisson distribution [75]. To stay true to this time distribution, it can be shown that the waiting time between two successive events should be defined as follows [75]:

$$\Delta t = -\frac{\ln(z)}{R_N} \tag{3.64}$$

where z is a uniform random number comprised between 0 and 1. The average value of $\ln(z)$ being equal to -1, we find back the intuitive result that the average waiting time between successive events is given by $1/R_N$. This formula for the timestep is the same as the one employed for determining the distance a particle travels before it interacts in the SRIM and Geant4 code (see (3.26) in Section 3.1).

The described algorithm can be summed up as follows: (i) Possible event rates r_i are computed from a catalog of events. (ii) A uniform random number z_1 is generated. (iii) An event i is chosen following the rule detailed in (3.63) and Fig. 3.16. (iv) The system is advanced to the chosen state, and the r_i rates are calculated again as they may have changed. (v) Another uniform random number z_2 between 0 and 1 is generated again to increment the time t following $t = t + \Delta t$ with $\Delta t = -\ln(z_2)/R_N$.

It has to be noted that this algorithm is in most cases called the kMC algorithm, just like we did call it, but can be found in the literature under the name of the N-fold way algorithm, the Bortz-Kalos-Liebowitz (BKL) [74] algorithm or the residence-time algorithm.

Within kART, a kMC algorithm is implemented to govern time increment and choice of events. However, one of the main improvements of the kART technique is that, contrary to many kMC codes, it does not require an initial catalog of events, but is able to compute on-the-fly its own events catalog via the ARTn algorithm. To achieve this, kART is coupled to LAMMPS for the calculation of forces with interatomic potentials. The potential energy surface defined by the interatomic potential is sampled following defined rules we present in the following, and among the sample paths, some are chosen with the kMC algorithms we just described.

3.3.2 Activation-Relaxation Technique

The Activation-Relaxation Technique is employed in kART to construct catalog of events. It is combined to a topological classification of atomic configurations via the NAUTY open-access code [76]. Labeling atoms based on their topology and not their geometry eases the classification

and recognition of atoms and events. Moreover, the topological classification of atoms allows to define events not restricted to predefined lattice positions. The code is said to be off-lattice. To label atoms based on their topology, all atoms are considered to be part of a connectivity graph. A truncated graph of a given radius (5.0 Å for Si) is constructed around each atom, and a unique topology key is computed by the NAUTY package for each atom-centered graph. Slight position changes (elastic distortions for example) will not modify the topology of a given atom. It is a very efficient way to identify atoms with similar atomic neighbor configurations.

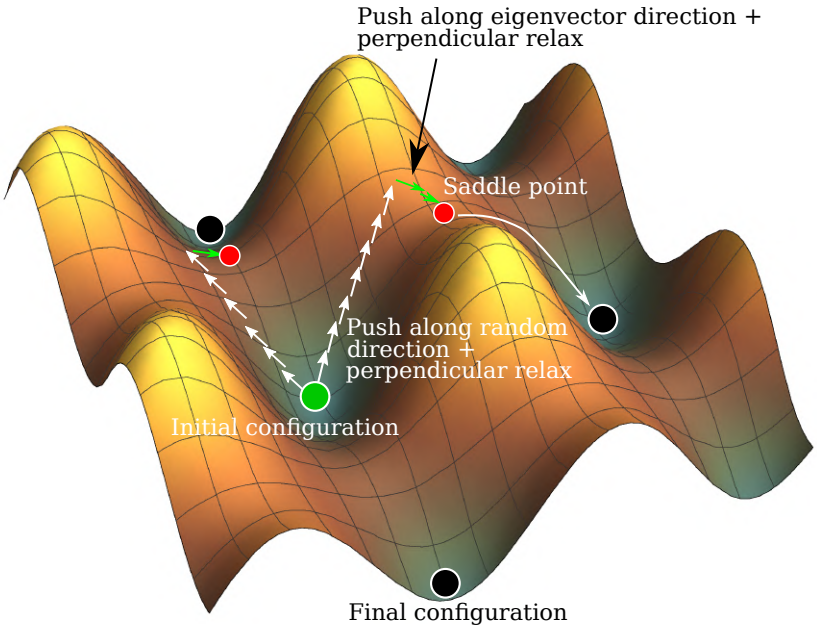

Figure 3.17: *Illustration of the kART event search algorithm on a potential energy surface. The abrupt direction changes of the small arrows (and color change from white to green) depict the crossing of the inflection line and thus the change from a push in the direction of the inital random vector to a push in the direction of the eigenvector.*

The ARTn event search must start in a local energy minimum. Therefore, before the construction of the events catalog can start, the system undergo a minimization. In kART, the interatomic forces can be computed via the same interatomic potentials which are developed for MD simulations. Actually, kART can be coupled to LAMMPS for the calculation of forces (in this case, LAMMPS must be compiled as a library). Therefore, the initial minimization is handled by LAMMPS minimization routines, with the chosen potential. Note that for small systems, forces could also be calculated via *ab initio* methods, like it was done in [77]. Once the system is in a potential energy surface minimum, all atoms of the system of interest are labeled based on their topologies. In the systems we study, part of the atoms are entirely crystalline (*i.e.* the structure of their connectivity graph is crystalline). Those atoms are not of much interest as they cannot be at the origin of events. Indeed, we are interested in defects and clusters reorganizations. Therefore, to speed-up the calculations, the crystalline topology key of the studied structure can be specified, so that those atoms are not considered for the search of events. After the atoms of interest are identified, the event search can start. The event search algorithm, detailed below, is illustrated in Fig. 3.17. For an excellent dynamic description of the event search algorithm, interested readers can refer to the video made by Antoine Jay and published as a supplementary material of [77].

To initiate the event search, a given atom and its neighbors are pushed along a random direction to make the system escape from the harmonic basin (*i.e.* local minimum) it finds itself in following the initial minimization step. Note that forces are still calculated with interatomic

potentials, and the local minimum is defined by the energy surface of the potential we employ. After each push, energy is minimized in the hyperplane perpendicular to the push direction, and the lowest eigenvalue (λ_0) of the Hessian is calculated via the Lanczos algorithm [78]. After a few iterations, λ_0 will become lower than a given negative threshold. It means the inflection line of the potential energy surface has been reached and that the system has successfully escaped the harmonic basin. Then, the Activation part of the algorithm can start. The configuration is pushed to the saddle point following the direction defined by the eigenvector $\vec{e_0}$ corresponding to λ_0. Again, after each push the configuration is relaxed in the hyperplane perpendicular to the push direction. At some point, the total force will fall below a user-specified threshold, which means the saddle point has been reached. After reaching the saddle point, the configuration is further pushed along $\vec{e_0}$ until reaching a new local minimum. The latter actually is the final configuration of the event. The initial configuration, the saddle point configuration and the final configuration fully defines an event. The atoms of the event that moved the most is named the central atom. Each event label is obtained as a combination of the topology of the central atom in the initial, saddle and final configuration. For each event, the initial, saddle and final configurations are stored. Then, low energy ones have a greater probability of being picked, they are more strictly relaxed (initial, saddle and final configuration), so that their associated energies and structures are more accurate. Those relaxed events are named specific, whereas the non-relaxed higher energy ones are named generic. As they have a greater probability of being chosen, low energy events are relaxed in order to describe them more accurately. Specific events are proper to a given initial atomic configuration, whereas the generic ones are proper to an initial topology (slight atom positions change are not accounted for). All the generic events are stored in order to be re-used latter if an already encountered topology appears again, whereas specific ones by definition cannot be re-employed as they are specific to the precise atomic configuration at the current simulation step. After all generic events are stored and some relaxed into specific events, event rates are computed based on the energy difference between the initial configuration and the saddle configuration (see (3.61)), and one event is picked following the kMC procedure described in Section 3.3.1. Time and atomic positions are then updated accordingly. The system is then in a new state, and a new topology searched is launched. For all the already known topologies, events are already stored (generic events), so no event search is launched. The events associated to the given topology are re-used, following a relaxation for the low energy ones to make them specific to the current atomic configuration. In a way, the algorithm is "self-learning". However, if new atom topologies appear in the updated system configuration, a new event search is launched for each topology. The algorithm thus searches for events "on-the-fly". The longest step of the simulation thus is the first one, in which all events have to be constructed. At a certain point in the simulation, all the encountered topologies are known. Thus, all possible events are already listed, the low energy ones are relaxed to be more specific to the actual configuration of the system, and one of them is chosen via the kMC concept. There is no event search with the ARTn algorithm anymore.

For our applications, we are interested in the simulation of rare diffusion events leading to clusters reordering and defects healing. A common issue of usual kMC codes is that, in cases where the system is in a basin of the potential energy surface made of very low energy barriers, surrounded by higher energy barriers, the system easily get trapped in describing only low energy events, and does not expand much the reachable simulation time compared to MD. This situation is illustrated in Fig. 3.18. Indeed, the multitude of low energy possible events results in a very high total rate (R_N in (3.64)). Thus, complex reordering events mostly occurring in escaping the harmonic basins are not sampled in the simulations. In order to circumvent this issue, kART integrates a specific method to handle low-energy barriers. This method is inspired by the Mean Rate Method (MRM) of Puchala *et al.* [79]. It is named the basin-auto-constructing MRM (bac-MRM) and is based on an adjustment of the rates of event leading to a basin exit to enhance the probabilities of basin exit events being picked by the algorithm. In practice, each

event, whose associated energy barrier lies below a user-defined energy-threshold, is suspected to be a low-energy basin state. If one of those suspected basin events is chosen by the kMC step, it is added to a list of basin events, and removed from the list of possible events. Then, the event is executed and new events are searched by kART. As we have executed an event, there are two known states in the basin so far (initial and final state). The MRM procedure described in [79] is applied, *i.e.* rates of events leading to a basin exit are adjusted. If the next chosen step lead to a not yet sampled basin state, it is chosen, added to the list of basin events, removed from the list of possible events and the adjusted rates for leaving the basin are calculated again based on the MRM formalism and the list now made of three basis states. If the chosen step leads to an already sampled basin state, it is rejected and removed from the list of possible events but still added to the basin event list. The adjusted exit rates are calculated based on the updated basin event list. This technique does not respect the dynamics of the system as events in the basins have to be rejected *a posteriori* but it makes much more easy for the system to exit basin states and sample interesting phenomena. Moreover, the distribution of the events permitting to exit the basin is correctly reproduced by the algorithm.

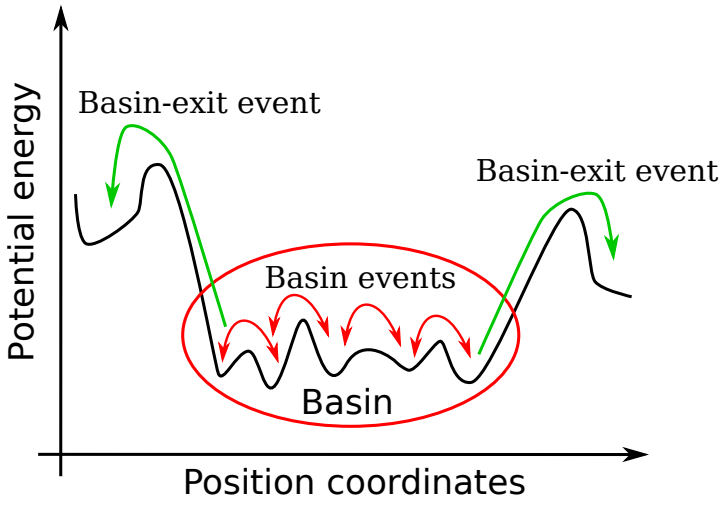

Figure 3.18: *2D representation of a basin in the potential energy surface.*

3.3.3 Usage of kART simulations results in our multiscale approach

We employ the kART code to heal the damaged structures obtained after MD, *i.e.* to observe defects recombination and also clusters reordering. We therefore gain valuable information on the number of defects created few seconds after irradiation, the amount of defects which recombined following the MD step, the clusters reordering dynamics and the size and shape of the clusters. Those information are of prime importance to characterize the response of a material to non-ionizing radiation and its susceptibility to DD effects. However, the observed effects resulting from atomic displacements like DC and DC-RTS are related to the electronic activities of defects inside matter. This is the reason why the last step of our multiscale approach is dedicated to the *ab initio* characterization of the electronic properties of defects identified as common with kART. This last step is not treated in this manuscript, therefore the methods employed will not be presented. However, the TDDFT method we have mentioned earlier in this manuscript is an *ab initio* technique we employ during the MD step of the simulation approach. Indeed, the use of the EPH model to incorporate electronic effects into MD simulations of collision cascades, presented in Paragraph 3.2.2.4.4, requires to calculate electronic stopping powers with TDDFT to feed the model. Consequently, in the next section we review the TDDFT method and therefore give a presentation of the DFT technique, which is one of the *ab initio* techniques which can be employed in the fourth and last step of our multiscale approach. However, the presentation we make of DFT and TDDFT is not centered on electronic characterization of

defects. For a specific description of the methods used in the last step of our global approach and examples of their capabilities in terms of defects characterization, interested readers should refer to the PhD thesis of Gabriela Herrero Saboya [80].

3.4 Density-Functional *ab initio* methods

The TDDFT, which has been employed in this thesis work, is part of the so-called *ab initio* or first-principles techniques. Those methods allow the calculation of electronic properties of materials from the well known Schrödinger equation of quantum mechanics. More specifically, TDDFT is a member of the Density-Functional family of techniques, whose particularity is to base the calculation of every electronic properties on the electronic density of the system. In our case, we want to simulate the electronic excitations induced by the passage of an ion in matter and the subsequent energy loss of this ion, *i.e.* electronic stopping. The ultimate purpose is the parametrization of the EPH model for the inclusion of electronic effects into MD (see Paragraph 3.2.2.4.4). Commonly employed codes in the community of radiation effects on microelectronic devices like SRIM are unable to give the level of information and physical treatment (*i.e.* atomic-scale treatment, explicit electron dynamics propagation) we are aiming at to parametrize the EPH model, which is why we resort to *ab initio* calculations.

Standard DFT is a ground state technique, meaning it allows to calculate the ground state electronic density and properties of a material, but does not enable for electronic excitations to occur. It is therefore not adapted to our problematic, which is why we turn to TDDFT, which allows to model the dynamics of the electrons and therefore their excitations. There exists multiple frameworks of TDDFT. The first-developed and probably most used one is restricted to linear perturbations in the frequency domain. It is named Linear-Response TDDFT (LR-TDDFT) and is intensively used for the calculation of spectroscopic properties of materials. For the simulation of electronic stopping, we need to go further than this and therefore resort to what is called RT-TDDFT, which allows the propagation of the electron dynamics in real time. However, RT-TDDFT in itself only describes the electron dynamics. In order to simulate the electronic stopping of ions into matter, the equations of motion of the nuclei must also be incorporated into the framework. ED, which couples MD for the nuclei dynamics and RT-TDDFT for the nuclei forces calculations and electrons dynamics, is an adequate solution. In this section, we start by introducing the notations and concepts of the density-functional framework via a presentation of the DFT theory (Section 3.4.1). Then, in Section 3.4.2, we extend the DFT framework presented to the TDDFT case, the RT-TDDFT one and finally to the ED formalism.

3.4.1 Density-Functional Theory (DFT)

3.4.1.1 From the many-body Schrödinger equation to the Kohn-Sham equations

As an *ab initio* method, DFT aims at modelling materials without the help of experimental input or empirical parameters. Therefore, it has to resort to quantum mechanics and the Schrödinger equation. However, the complexity of the many-body Schrödinger equation makes it unusable in a numerically feasible scheme from which ground state densities of materials could be obtained. The Schrödinger equation thus has to be adapted in order to be implemented into efficient numerical algorithms. The approximations and concepts employed to turn the Schrödinger equation into a practical form known as the Kohn-Sham equations actually is the core of the DFT. In the following, we detail the different steps, concepts and approximations which are constitutive of the DFT. For reasons of clarity, we neglect the notations related to the spin of the electrons in the equations of this section.

We start by writing the basic stationary Schrödinger equation in the absence of external field for a system made of N electrons and M nuclei:

$$\hat{H}_{tot}(\vec{r}_1,...,\vec{r}_N,\vec{R}_1,...,\vec{R}_M)\psi_{tot}(\vec{r}_1,...,\vec{r}_N,\vec{R}_1,...,\vec{R}_M) = E_{tot}\psi_{tot}(\vec{r}_1,...,\vec{r}_N,\vec{R}_1,...,\vec{R}_M) \quad (3.65)$$

where $\hat{H}_{tot}$ is the Hamiltonian of the entire system of N electrons and M nuclei, $\vec{r}_i$ are space coordinates of electron i, $\vec{R}_I$ are space coordinates of nuclei I, ψ_{tot} is the wavefunction of the entire system and E_{tot} is the total energy of the system. The Hamiltonian $\hat{H}_{tot}$ can be expressed the following way:

$$\begin{aligned}\hat{H}_{tot} = &-\sum_i^N \frac{\hbar^2}{2m}\vec{\nabla}_i^2 - \sum_I^M \frac{\hbar^2}{2M}\vec{\nabla}_I^2 - \sum_i^N\sum_I^M \frac{Z_I e^2}{4\pi\epsilon_0|\vec{r}_i - \vec{R}_I|} + \\ &\sum_i^N\sum_{j>i}^N \frac{e^2}{4\pi\epsilon_0|\vec{r}_i - \vec{r}_j|} + \sum_I^M\sum_{J>I}^M \frac{Z_I Z_J e^2}{4\pi\epsilon_0|\vec{R}_I - \vec{R}_J|}\end{aligned} \quad (3.66)$$

where m is the electron mass, M the nuclei mass, i indexes correspond to electrons, I indexes correspond to nuclei, e is the elementary charge, Z_I is the atomic number of nuclei I and $\vec{\nabla}^2 = \text{div}(\vec{\text{grad}})$. The first term of (3.66) corresponds to the kinetic energy of the electrons, the second one to the kinetic energy of the nuclei, the third term is the electron-nuclei interaction term, the fourth one the electron-electron interaction term and the last one the nuclei-nuclei interaction term. To decrease the level of complexity of (3.66) and thus (3.65), we can take advantage of the fact that nuclei mass are greater than electron mass by about four orders of magnitude. Consequently, the electrons move a lot faster than the nuclei, and it can be considered that they immediately respond to any nuclei movements. The dynamics of electrons and nuclei can thus be decoupled. This is known as the Born-Oppenheimer Approximation (BOA). As a consequence of the BOA, ψ_{tot} appearing in (3.65) can be split into a nuclei contribution ϕ_{nuclei} which depends on the atomic positions only and an electronic contribution ψ_{elec} which depends explicitly on the electronic coordinates and parametrically on the nuclei coordinates:

$$\psi_{tot}(\vec{r}_1,...,\vec{r}_N,\vec{R}_1,...,\vec{R}_M) = \phi_{nuclei}(\vec{R}_1,...,\vec{R}_M) \times \psi_{elec}^{\mathbf{R}}(\vec{r}_1,...,\vec{r}_N) \quad (3.67)$$

where $\mathbf{R}$ describes the entire set of nuclear space coordinates. Considering that electrons react to perturbations much faster than nuclei due to their low mass, the latter can be considered fixed. In this case, we can express the Schrödinger equation and the Hamiltonian $\hat{H}$ for the electrons only based on the definition of the wavefunctions given in (3.67) in the Dirac (or bra-ket) formalism (we got rid of the *elec* notation of (3.67) for simplicity purposes):

$$\hat{H}\left|\psi\right\rangle = E\left|\psi\right\rangle, \quad (3.68)$$

$$\hat{H} = -\sum_i^N \frac{\hbar^2}{2m}\vec{\nabla}_i^2 - \sum_i^N\sum_I^M \frac{Z_I e^2}{4\pi\epsilon_0|\vec{r}_i - \vec{R}_I|} + \sum_i^N\sum_{j>i}^N \frac{e^2}{4\pi\epsilon_0|\vec{r}_i - \vec{r}_j|} = \hat{T} + \hat{V}_{ne} + \hat{V}_{ee} \quad (3.69)$$

The nuclei-electron interaction term $\hat{V}_{ne}$ can be viewed as an external potential in which the electrons are immersed, and can thus be rewritten:

$$\hat{V}_{ne} = \hat{V}_{ext} = \sum_i^N v_{ext}(\vec{r}_i) \quad (3.70)$$

with

$$v_{ext}(\vec{r}_i) = \sum_I^M \frac{Z_I e^2}{4\pi\epsilon_0|\vec{r}_i - \vec{R}_J|} \quad (3.71)$$

The total energy of the system E_{tot} is given by the sum of the electronic energy E appearing in (3.69) and the energy deriving from the purely nuclear nuclei-nuclei interaction term of (3.66) (for fixed nuclei):

$$E_{tot} = E + \sum_{I}^{M} \sum_{J>I}^{M} \frac{Z_I Z_J e^2}{4\pi\epsilon_0 |\vec{R}_I - \vec{R}_J|} \tag{3.72}$$

The purpose of the DFT is to calculate the ground state total energy of a given system. Although the second term of (3.72) can be directly (and easily) calculated, the first term of electronic energy must be obtained by solving the Schrödinger equation for the electrons (3.68). However, this equation cannot be solved as it is written in (3.68). Indeed, to be employed on realistic systems computationally speaking, it is necessary to decrease the level of complexity of the Schrödinger equation. Aiming at this, DFT proposes to use the electronic density $\rho(\vec{r})$ as the basic quantity to describe the electronic system, instead of the wavefunctions. It is much simpler to manipulate as the electronic density $\rho(\vec{r})$ simply is a scalar function of the position $\vec{r}$. The electronic density for a system of N electrons is expressed:

$$\rho(\vec{r}) = N \int ... \int |\psi(\vec{r}, \vec{r}_2, ..., \vec{r}_N)|^2 d\vec{r}_2 ... d\vec{r}_N \tag{3.73}$$

According to the *Hohenberg-Kohn theorem* [81], every properties can be computed from $\rho(\vec{r})$. The Hohenberg-Kohn theorem states that $\hat{V}_{ext}$ is a unique functional of the ground state density $\rho_0(\vec{r})$. In more details, it says that a given external potential defined by a given set of nuclei coordinates $\mathbf{R}$ leads to a unique $\psi(\vec{r}_1, ..., \vec{r}_N)$, via (3.69), which leads to a unique electronic density $\rho(\vec{r})$ via (3.73). Those one-to-one correspondences go both ways. One of the major consequence of this theorem is that, as any observable of the system is a function of the wavefunction ψ, and as there is a unique correspondence between ψ and ρ, any observable $\hat{O}$ of the system is a functional of the density:

$$\langle \psi[\rho(\vec{r})] | \hat{O} | \psi[\rho(\vec{r})] \rangle = \hat{O}[\rho(\vec{r})] \tag{3.74}$$

Thus, the total energy E is a functional of the density and can be written the following way:

$$E = \langle \psi[\rho(\vec{r})] | \hat{T}_{ee} + \hat{V}_{ee} | \psi[\rho(\vec{r})] \rangle + V_{ext}[\rho(\vec{r})] = T_{ee}[\rho] + V_{ee}[\rho] + E_{ext}[\rho] = E[\rho] \tag{3.75}$$

where notations for the energy are as the same as for the operators of the Hamiltonian, and we now write ρ instead of $\rho(\vec{r})$ to make the equations more readable, unless we want to explicitly emphasize the $\vec{r}$ dependence of ρ. Note that the Hohenberg-Kohn theorem is not only valid for the $\hat{V}_{ne}$ external potential but also for the sum of the nuclei-electron interaction potential and potential deriving from an external field applied to the system. It is not restricted to the field-free formalism we have used so far.

The second major theorem at the heart of the derivation of the equations of the DFT is named the *Variational Principle* [82]. It states that a minimization of $E[\psi]$ with respect to ψ yields the exact ground state wavefunction ψ_0. It can be summed up as follows:

$$E_0 = \min_{\phi} \langle \phi | \hat{H} | \phi \rangle = \langle \phi_0 | \hat{H} | \phi_0 \rangle \tag{3.76}$$

If we combine this statement to the Hohenberg-Kohn theorem, it becomes valid for a minimization with respect to ρ the same way it is for ψ. Thus, it is possible to write:

$$E_0 = \min_{\rho}(E[\rho]) = E[\rho_0] \tag{3.77}$$

Another way of writing it is:

$$\left. \frac{\delta E[\rho]}{\delta \rho} \right|_{\rho_0} = 0 \tag{3.78}$$

The ground state electronic density ρ_0 and consequently ground state energy E_0 are found by minimizing the total energy with respect to ρ. However, there does not exist any method/algorithm to calculate $\hat{T}_{ee}$ and $\hat{V}_{ee}$, and thus no way to minimize E. To solve this issue, in 1965, Kohn and Sham had an idea which would drastically simplify the picture [83]. They proposed to turn the system of N interacting electrons into a fictitious system of N non-interacting electrons with the same ground state density $\rho_0(\vec{r})$. In this picture, calculations are a lot easier. This is known as the *Kohn-Sham formulation*. The system of N non-interacting particles can thus be decomposed into single-electron Hamiltonians $\hat{h}_i$, whose sum constitutes the total Hamiltonian for the non-interacting system $\hat{H}_{ni}$:

$$\begin{aligned} \hat{H}_{ni}\phi_{ni}^{\mathbf{R}}(\vec{r}_1,...,\vec{r}_N) =& E_{ni}\phi_{ni}^{\mathbf{R}}(\vec{r}_1,...,\vec{r}_N), \\ \hat{H}_{ni} =& \sum_i^N \hat{h}_i \end{aligned} \tag{3.79}$$

with

$$\hat{h}_i = -\frac{1}{2}\nabla_i^2 + v_i(\vec{r}) \tag{3.80}$$

where ϕ_{ni} are the wavefunctions of the non-interacting system, E_{ni} the energy of the non-interacting system and $v_i(\vec{r})$ is an external potential operator of the electron i. The single-electron wavefunctions ϕ_i and energies e_i of all the electrons of the system obey to the following one-electron Schrödinger equation:

$$\hat{h}_i\phi_i(\vec{r}) = e_i\phi_i(\vec{r}) \tag{3.81}$$

The total non-interacting wavefunction ϕ_{ni} can be exactly written as a Slater determinant of the single-electron wavefunction as follows:

$$\phi_{ni}^{\mathbf{R}}(\vec{r}_1,...,\vec{r}_N) = \frac{1}{\sqrt{N!}}\det[\phi_i(\vec{r}_j)] \tag{3.82}$$

In this picture of N single-electrons, the electronic density reads:

$$\rho(\vec{r}) = \sum_i^N |\psi_i(\vec{r})|^2 \tag{3.83}$$

The equations of the non-interacting system of electrons, described by the equations (3.79) to (3.83), can be solved exactly. However, we completely neglect the electron-electron interaction, which may seem (at least to me) counter-intuitive considering we actually are interested in the properties of a real system of interacting electrons, not a fictitious one of non-interacting electrons. The working and cleverness of the Kohn-Sham picture actually reside in the choice of the v_i terms of (3.80). Indeed, we want to find an expression for the single-electron potential v_i which would yield the same ground-state density as in the interacting case. If such a potential exists, the interacting system can be modelled by single-electron Schrödinger equations, thus drastically simplifying the problem. We do not demonstrate it here, but such a single-electron potential exists and is unique. However, what we need to remember is that the total electronic energy E of the system we want to model reads:

$$E[\rho] = T_{ni}[\rho] + V_{ne}[\rho] + E_H[\rho] + E_{xc}[\rho] \tag{3.84}$$

where T_{ni} is the kinetic energy in the non-interacting picture, E_H is named the Hartree energy and E_{xc} the exchange-correlation energy, which can itself be divided into an exchange energy E_x and a correlation energy E_c following $E_{xc} = E_x + E_c$. The Hartree energy corresponds to

the classical density-density interaction energy, part of $\hat{V}_{ee}$, we know how to calculate as long as we know $\rho(\vec{r})$:

$$E_H[\rho] = \frac{1}{2}\int\int \frac{\rho(\vec{r}_1)\rho(\vec{r}_2)}{4\pi\epsilon_0|\vec{r}_1 - \vec{r}_2|} d\vec{r}_1 d\vec{r}_2 \tag{3.85}$$

We also know how to express E_x and E_c, respectively:

$$E_x[\rho] = \langle\phi_{ni}|\,\hat{V}_{ee}\,|\phi_{ni}\rangle - E_H[\rho] \tag{3.86}$$

and

$$E_c[\rho] = \langle\psi[\rho]|\,\hat{T} + \hat{V}_{ee}\,|\psi[\rho]\rangle = T_c[\rho] + V_c[\rho] \tag{3.87}$$

where

$$T_c[\rho] = \langle\psi[\rho]|\,\hat{T}\,|\psi[\rho]\rangle - \langle\phi_{ni}[\rho]|\,\hat{T}\,|\phi_{ni}[\rho]\rangle \tag{3.88}$$

and

$$V_c[\rho] = \langle\psi[\rho]|\,\hat{V}_{ee}\,|\psi[\rho]\rangle - \langle\phi_{ni}[\rho]|\,\hat{V}_{ee}\,|\phi_{ni}[\rho]\rangle \tag{3.89}$$

$T_c[\rho]$ and $V_c[\rho]$ respectively are the difference between the kinetic and electron-electron interaction energies calculated with the wave functions of the interacting system and the non-interacting one. Then, in minimizing the energy E it can be shown that there exists an expression of the single-electron potential v_i in the non-interacting picture which yields the same electronic density as the interacting picture. Such a potential is called the Kohn-Sham potential v_{KS} and reads:

$$v_i = v_{KS} = v_{ne} + v_H + v_x + v_c \tag{3.90}$$

where

$$v_H = \frac{\delta E_H([\rho],\vec{r})}{\delta\rho} = \int \frac{\rho(\vec{r'})}{4\pi\epsilon_0|\vec{r} - \vec{r'}|} d\vec{r'} \tag{3.91}$$

and

$$v_c = \frac{\delta E_c([\rho],\vec{r})}{\delta\rho} \tag{3.92}$$

and

$$v_x = \frac{\delta E_x([\rho],\vec{r})}{\delta\rho} \tag{3.93}$$

Combining (3.80), (3.81) and (3.90), we finally obtain the Schrödinger-like Kohn-Sham equations:

$$\left(-\frac{1}{2}\nabla_i^2 + v_{KS}([\rho],\vec{r})\right)\phi_i(\vec{r}) = e_i\phi_i(\vec{r}) \tag{3.94}$$

The above equations actually are the core equations of the DFT. As the Kohn-Sham potential depends on the density, they must be solved self-consistently following the procedure displayed in Fig. 3.19:

(i) an initial guess is made for the electronic density ρ,

(ii) the Kohn-Sham potentials are calculated,

(iii) the Kohn-Sham equations are solved,

(iv) ρ is updated,

(v) we come back to (ii) considering this new ρ.

The Kohn-Sham equations are solved again with this new ρ and another electronic density ρ^* is calculated. This process is performed iteratively, when two densities ρ and ρ^* calculated during two successive steps are equal, the ground state is considered to be found.

Readers who would like to dive more into the theory than what has been done here should refer to the PhD thesis of Ivan Maliyov [84], from which the derivation of the DFT equations proposed in this section is inspired from, with less details.

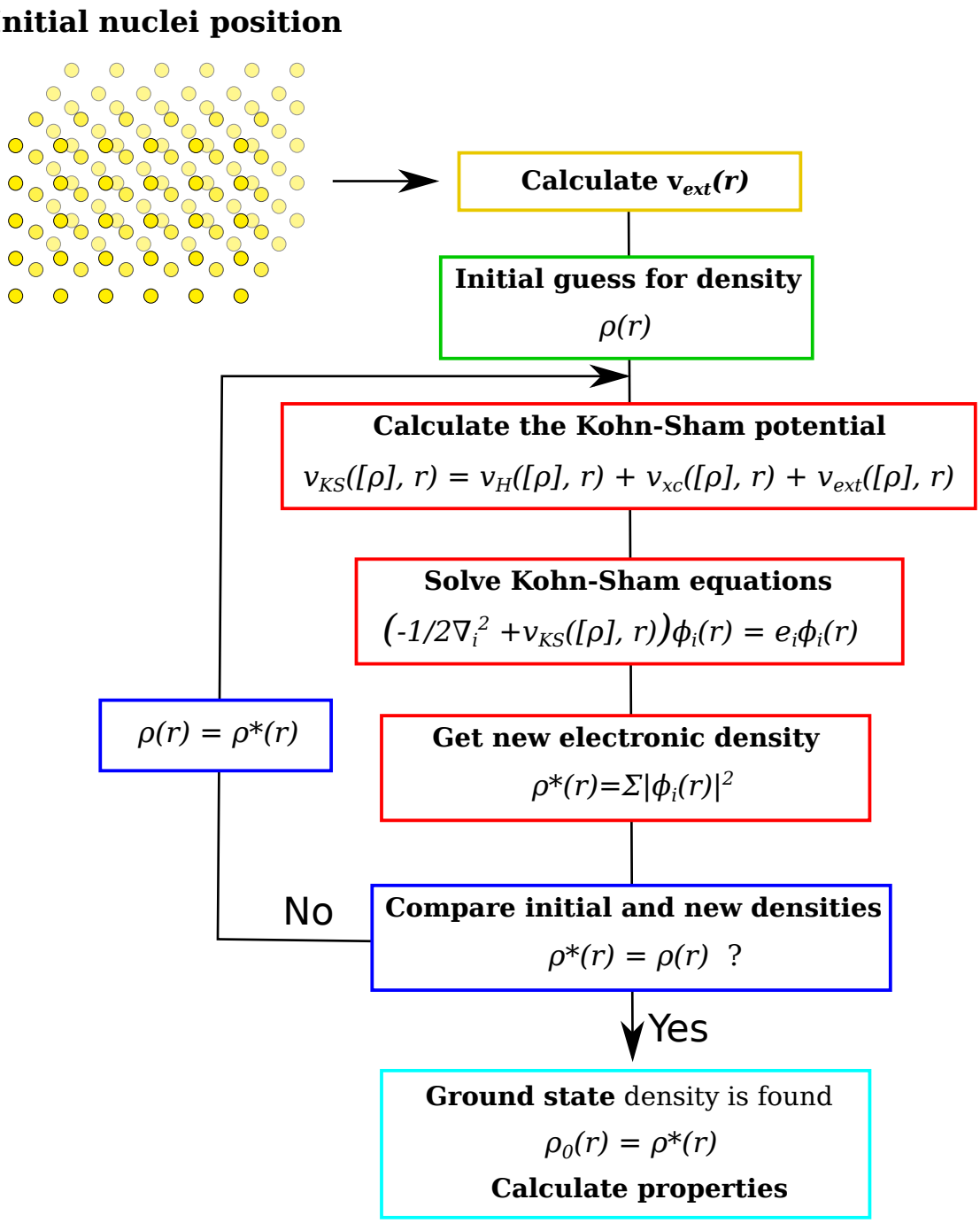

Figure 3.19: *The self-consistent algorithm of the DFT is detailed. At each iteration of the algorithm, the electronic density is calculated based on the updated Kohn-Sham potential. If two successive steps lead to the same electronic density, the ground state is considered to be reached.*

3.4.1.2 Approximating the exchange-correlation functionals

In theory, the DFT formalism is exact. Indeed, we have not used any approximation, except the BOA, to end up to (3.94). However, in practice, it is impossible to find the exact expression of the exchange and correlation terms of the Kohn-Sham potential. Therefore, they have to be approximated in order for the DFT to have a practical utility. The first of those approximations

which was developed is the Local Density Approximation (LDA) [83]. The exchange and correlation energy E_{xc}^{LDA} is defined from the exchange and correlation energy of a single-electron in a free-electron gas model e_{xc}, which we know how to calculate:

$$E_{xc}^{LDA}[\rho(\vec{r})] = \int \rho(\vec{r}) e_{xc}[\rho(\vec{r})] d\vec{r} \tag{3.95}$$

Going further than the simple LDA, approaches where the exchange correlation energy is a functional of the density and of the gradient of the density can be employed. Such approximations are named Generalized Gradient Approximations (GGA):

$$E_{xc}^{GGA}[\rho(\vec{r})] = \int \rho(\vec{r}) f[\rho(\vec{r}), \mathrm{grad}(\rho(\vec{r}))] d\vec{r} \tag{3.96}$$

A widely used example of GGA functionals is the Perdew, Burke and Ernzerhof (PBE) functional [85]. In addition to the choice of exchange-correlation functionals, in practice, single-electron wavefunctions have to be constructed from a basis set of functions. This aspect is fundamental to the practical implementation of DFT methods as it governs many of the parameters used in the simulations. In the following, we review the basis of plane-waves DFT codes, where single-electron wavefunctions are constructed from plane-waves.

3.4.1.3 Density-Functional Theory in the plane-wave formalism

The most used DFT codes for simulations of solids, among them Quantum Espresso [86, 87], abinit [88] and VASP [89, 90], treat the wavefunctions as summation of plane-waves. It is based on the fact that any periodic function can be written as a sum of plane-waves. In a crystal, single-electron wavefunctions are periodic (unit-cell period) and can be defined as follows:

$$\phi(\vec{r}) = \sum_{\vec{G}} C_{\vec{G}} e^{i\vec{G}\vec{r}} \tag{3.97}$$

where $\vec{G}$ are vectors of the reciprocal space and $C_{\vec{G}}$ are plane-waves coefficients. The more $\vec{G}$ vectors are employed, the closer to the real wavefunction will be the plane-waves summation. However, the number of plane-waves should be finite. Therefore, in order to set an upper value to the number of plane waves we define an energy cutoff E_{cut}. Only $\vec{G}$ vectors whose norm is lower than G_{cut} defined, by (3.98), are employed:

$$E_{cut} = \frac{\hbar^2 G_{cut}^2}{2m} \tag{3.98}$$

This rule sets an upper bound on the number of plane-waves. However, it must be ensured that enough plane-waves are employed to have converged calculations.

Another important aspect of plane-waves DFT code is the pseudopotential. Their use are based on the observation that plane-waves are not efficient at describing localized features (sharp features) of wavefunctions: lots of plane-waves are needed to correctly reproduce localized features, thus increasing the computational cost of the calculations. However, the states which are the most localized are the tightly bound ones, the 1s or 2s orbitals in Si for example. Luckily, those states do not participate in electronic bonding, and are therefore not of much interest for us. Therefore, they can be neglected by defining a pseudopotential $v_{pp}(\vec{r})$ to be added to the Kohn-Sham equations as follows:

$$\left(-\frac{1}{2}\nabla_i^2 + v_{KS}([\rho], \vec{r}) + v_{pp}(\vec{r})\right) \phi_i^{pp}(\vec{r}) = e_i^{pp} \phi_i^{pp}(\vec{r}) \tag{3.99}$$

In using (3.99) rather than the standard Kohn-Sham equations (3.94), the calculated energies and wavefunctions are not the standard *all-electron* (when no pseudopotential is used) ones, but the pseudopotential ones e_i^{pp} and ϕ_i^{pp}. However, the pseudopotential must be defined to guarantee $e_i^{pp} = e_i$ and $\phi_i^{pp}(\vec{r}) = \phi_i(\vec{r})$ for $r > R_c$, R_c being a cutoff radius which should defined during the creation of the pseudopotential. Indeed, the localized features of wavefunctions we want to get rid of are found at low r only. With the pseudopotential method, we decrease the number of required plane-waves and therefore increase the computational efficiency of the algorithms. An illustration of the shape of wavefunctions in the standard all-electron formalism and in the pseudopotential one is given in Fig. 3.20.

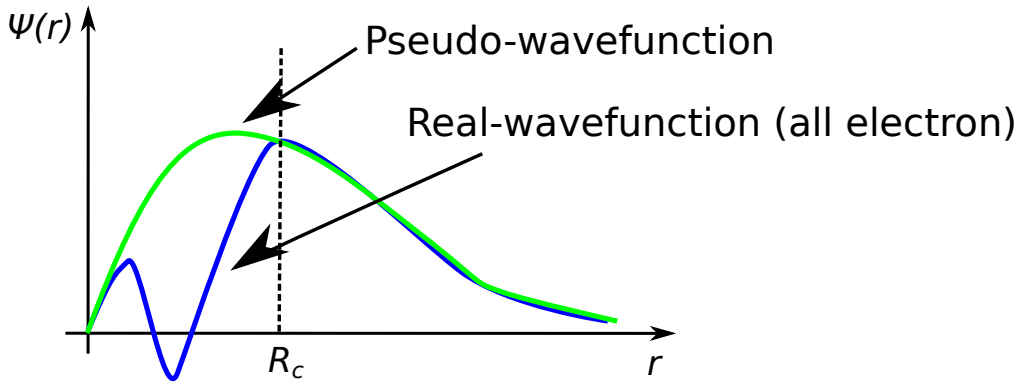

Figure 3.20: *Illustration of the pseudopotential concept. The pseudowavefunction calculated from the Kohn-Sham equations modified to integrate the pseudopotential term is smoother than the real (all electron) wavefucntion below R_c and equal to it above.*

In addition to the energy cutoff and the pseudopotential, another essential aspect of the implementation of plane-waves DFT code is the notion of sampling of the Brillouin zone with so-called $\vec{k}$-points. Very briefly, following the well known Bloch's theorem [23] for periodic systems, the Kohn-Sham equations are solved in reciprocal space (plane-waves space) on a definite set of points, named the $\vec{k}$-points. The theoretical treatment of k-points would require to spend several pages on solid state physics concepts, which is not in the scope of this section. We therefore direct the authors interested in the subject to existing textbooks on the subjects of solid-state physics and plane-waves DFT [23, 91].

3.4.2 Time-Dependent Density-Functional Theory (TDDFT)

3.4.2.1 From the time-dependent many-body Schrödinger equation to the time-dependent Kohn-Sham equations

The TDDFT technique can be envisioned as a time-dependent extension of the DFT. Indeed, the main steps in the derivation of the TDDFT are in many ways similar to the ones followed in the derivation of the DFT. We start by writing the many-body electronic wavefunction, time-dependent this time and not stationary like (3.65) was:

$$i\frac{\partial\psi(\vec{r}_1,...,\vec{r}_N,t)}{\partial t} = \hat{H}_{tot}(\vec{r}_1,...,\vec{r}_N,\vec{R}_1,...,\vec{R}_M,t)\psi_{tot}(\vec{r}_1,...,\vec{r}_N,t) \tag{3.100}$$

As for every first-order differential equation, an initial condition $\psi(\vec{r},t=0) = \psi_0$ is needed for its resolution. Just like for the stationary Schrödinger equation, the time-dependent Hamiltonian can be divided into an electronic kinetic energy term, an electron-electron interaction term and an external potential term (containing the nuclei-electron interaction term and an external time-dependent perturbation):

$$\hat{H}_{tot}(\vec{r}_1,...,\vec{r}_N,\vec{R}_1,...,\vec{R}_M,t) = \hat{T}_{ee} + \hat{V}_{ee} + \hat{V}_{ext} \tag{3.101}$$

The time-dependent density simply reads:

$$\rho(\vec{r},t) = N \int ... \int |\psi(\vec{r},\vec{r}_2,...,\vec{r}_N,t)|^2 d\vec{r}_2 ... d\vec{r}_N \tag{3.102}$$

As it can be understood from our derivation of the equations of the DFT, at this point, it is impossible to solve the Schrödinger equation as we have expressed it so far. Just like for DFT, simplification can be achieved by writing everything as a function of the time-dependent density $\rho(\vec{r},t)$, which we write simply ρ from this point, unless we want to highlight the t and/or $\vec{r}$ dependence of ρ. This simplification is theoretically made possible by the equivalent of the Hohenberg-Kohn theorem for the time-dependent case, *i.e.* the *Runge-Gross theorem* [92]. It states that there is a one-to-one correspondence between the time-dependent external potential felt by each electron $v_{ext}(\vec{r},t)$ and the time-dependent density ρ.

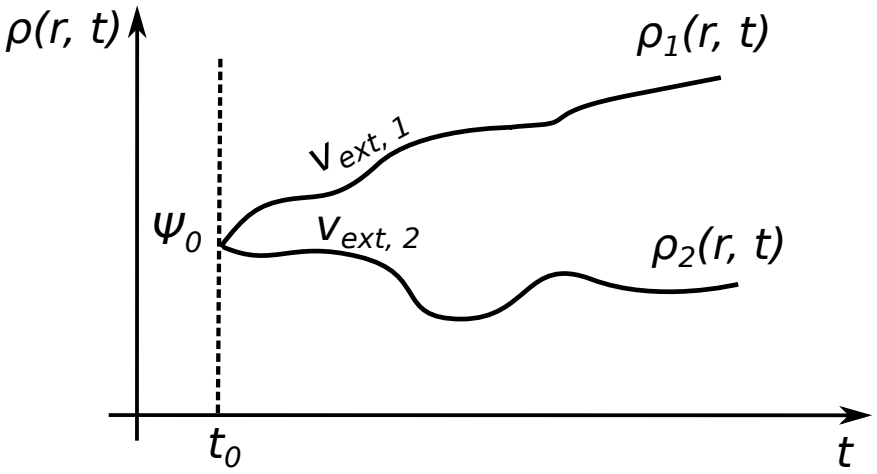

Figure 3.21: *Illustration of the Runge-Gross theorem. If two densities initially in the same initial state are subject to different time-dependent potentials, they will become different right after* t_0.

The situation is often depicted as in Fig. 3.21: if two identical systems have the same initial electronic density $\rho_1(\vec{r},t=0) = \rho_2(\vec{r},t=0)$ (same initial state) but are subject to two potentials $v_{ext,1}(\vec{r},t)$ and $v_{ext,2}(\vec{r},t)$ differing by more than an additive purely time-dependent function, the densities become different immediately after $t = 0$. The Runge-Gross theorem has the same consequences that the Hohenberg-Kohn theorem. Indeed, any expectation value of time-dependent observables $\hat{O}[\rho(t),\psi_0]$ can be written as a function of the time-dependent electronic density and the initial state:

$$\langle \psi[\rho,\psi_0]| \hat{O}[\rho,\psi_0] |\psi[\rho,\psi_0]\rangle = \hat{O}[\rho,\psi_0] \tag{3.103}$$

At this point in the DFT derivation, we were able to apply the variational principle and state that the minimization of the total energy $E[\rho]$ with respect to ρ yields the ground state energy E_0 and that the corresponding minimizing density ρ_0 is the ground-state density. However, in the time-dependent case, there is no variational principle of the energy [93]. Still, it is possible to apply the Kohn-Sham scheme to the time-dependent case in assuming, in addition to the Runge-Gross theorem, which states that the potential generating a given density is unique, that the time-dependent Kohn-Sham potential yielding a given density exists. Note that both the Runge-Gross theorem and the existence of the Kohn-Sham potential (called non-interacting v-Representability) can be demonstrated [93]. Time-dependent Kohn-Sham equations can thus be defined as follows:

$$i\frac{\partial \phi_i(\vec{r},t)}{\partial t} = \left(-\frac{1}{2}\nabla_i^2 + v_{KS}([\rho,\psi_0],\vec{r},t)\right)\phi_i(\vec{r},t) \tag{3.104}$$

with the Kohn-Sham potential expressed in a similar fashion as for DFT:

$$v_{KS}([\rho,\psi_0],\vec{r},t) = \int \frac{\rho(\vec{r'},t)}{4\pi\epsilon_0|\vec{r}-\vec{r'}|}d\vec{r'} + v_{ext}(\vec{r},t) + v_{xc}([\rho,\psi_0],\vec{r},t) \tag{3.105}$$

The potentials are now functionals of the time-dependent density ρ and of the initial state ψ_0. The time-dependent electronic density can be easily calculated from the single-electron time-dependent wavefunctions:

$$\rho(\vec{r},t) = \sum_i^N |\phi_i(\vec{r},t)|^2 \tag{3.106}$$

Just like DFT, TDDFT is an exact theory. However, similarly to DFT, the time-dependent exchange-correlation potential $v_{xc}([\rho,\psi_0],\vec{r},t)$ is not known and has to be approximated. The real functional has "memory" [93], meaning it depends on the history of electronic density at previous times. The approximations employed for the time-dependent exchange-correlation potential assume that the time-dependence of $v_{xc}([\rho,\psi_0],\vec{r},t)$ does not come from the functional itself but only from the time-dependence of the electronic density. It is called the adiabatic approximation. The memory aspect of the functional is thus neglected, and any exchange-correlation functional from standard DFT can be employed. If we write v_{xc}^{DFT} a DFT exchange-correlation functional and v_{xc}^{A} a TDDFT exchange-correlation functional in the adiabatic approximation, we have:

$$v_{xc}^{A}([\rho(\vec{r},t),\phi_0(\vec{r},t=0)],\vec{r},t) = v_{xc}^{DFT}([\rho(\vec{r},t)],\vec{r}) \tag{3.107}$$

The adiabatic extension of LDA for TDDFT is named Adiabatic LDA (ALDA).

3.4.2.2 TDDFT in the plane-wave formalism

Just like it is successfully done in DFT codes, the time-dependent wavefunctions $\psi_i(\vec{r},t)$ can be expressed as sum of plane-waves [94]:

$$\phi_i(\vec{r},t) = \sum_{\vec{G}} C_{\vec{G}}(t)e^{i\vec{G}\vec{r}} \tag{3.108}$$

where $\vec{G}$ are vectors of the reciprocal space, and the $C_{\vec{G}}(t)$ plane-waves coefficients are time-dependent. The plane-waves summation approach to the time-dependent wavefunctions is the approach adopted in the QB@LL [95, 96] code we employ for TDDFT calculations. Similarly to what is done for DFT, a plane-wave energy cut-off is defined and pseudopotential files are used for the simulations. Also, the wavefunctions are solved on a $\vec{k}$-points grid in reciprocal space.

3.4.2.3 Real-Time TDDFT

In spite of their similarities, there are some essential differences between DFT and TDDFT. The most evident one is the fact that excited states of atoms can be sampled via the time-dependent density. Some others naturally arised in the derivation, like the absence of a variational principle or the need for an initial state, but there is another essential difference: due to the absence of variational theorem, the time-dependent Kohn-Sham equations cannot be solved self-consistently like in the case of DFT but must be propagated in time. There exists two classes of methods for time-propagation: propagator methods and Ordinary Differential Equations (ODE) methods [94]. Within the QB@LL code we use, both are available.

The propagator method relies on the search for an approximate expression of a propagator operator $\hat{U}(t,t+\Delta t)$ taking the system from t to $t+\Delta t$. Formally, the action of $\hat{U}(t,t+\Delta t)$ can be written as follows:

$$\phi_i(\vec{r},t+\Delta t) = \hat{U}(t,t+\Delta t)\phi_i(\vec{r},t) \tag{3.109}$$

In practice, operator propagators approximate expressions are obtained by resorting to Dyson series [94]:

$$\hat{U}(t, t+\Delta t) = \hat{1} + \sum_{n=1}^{\infty}(-1)^n \int_t^{t+\Delta t} dt_1 \int_t^{t_1} dt_2 \ldots \int_t^{t_{n-1}} dt_n \hat{H}(t_1)\ldots\hat{H}(t_n) \tag{3.110}$$

Taking advantage of the Dyson series expression of the propagator operator, it is possible to reach expressions of the form of (3.111) for the wavefunctions at a time $t + \Delta t$ [84]:

$$\phi_i(t+\Delta t) = \hat{T}\exp\left(-i\int_t^{t+\Delta t} \hat{H}(\tau)d\tau\right)\phi_i(t) \tag{3.111}$$

where Δt can be viewed as the timestep of the propagation and $\hat{T}$ is the time-ordering operator behaving as follows for two arbitrary operators $\hat{A}$ and $\hat{B}$:

$$\hat{T}(\hat{A}(t_1)\hat{B}(t_2)) = \begin{cases} \hat{A}(t_1)\hat{B}(t_2) & \text{if} \quad t_1 > t_2 \\ \hat{B}(t_2)\hat{A}(t_1) & \text{if} \quad t_1 < t_2 \end{cases} \tag{3.112}$$

Among the most employed time propagator techniques can be cited the Enforced Time Reversal Symmetry (ETRS) method or the Magnus method [97].

Contrary to propagator approaches whose aim is to find approximate expressions for the propagator, ODE methods aim at approximating solutions to the time-dependent Kohn Sham equations, which are envisioned as a system of ODE. Consequently, usual methods for propagating time in a system of ODE can be applied. The Crank-Nicolson and Runge-Kutta [97] methods are the generally adopted ones in TDDFT codes. Although the QB@LL code we employ integrates both propagator techniques (ETRS) and ODE methods (Runge-Kutta), we do not present here a derivation of the ODE methods as we have only employed the ETRS propagator method in our simulations. Conceptually, the working of the Runge-Kutta and Crank-Nicolson methods is similar to the Verlet schemes we have seen in the context of MD in Section 3.2.1. Interested readers on the subject of time-propagator and ODE techniques can refer to [84], [94] and [97].

The time propagation equation of the wavefunctions, as presented in (3.111) for instance, coupled to the time dependent Kohn-Sham equations, constitutes the main equations of the RT-TDDFT, which is employed to simulate the dynamics of the electrons. In order to propagate the dynamics of the electrons and of the nuclei simultaneously, which is needed for electronic stopping power calculations, we have to combine the RT-TDDFT formalism to a scheme for nuclei dynamics integration. This combination is known as the ED method.

3.4.2.4 Ehrenfest Dynamics (ED)

The Ehrenfest's theorem [98] states that Newton's equations are satisfied for mean values in quantum systems. If we assume that the positions of the nuclei correspond to their mean values, the position of a nuclei I at a time t, in the formalism of ED, follows the Newton-like law below [84]:

$$M_I \frac{\partial^2 \vec{R}_I(t)}{\partial t^2} = -\sum_i^N \langle\phi_i(t)|\nabla_{\vec{R}_I}\hat{H}|\phi_i(t)\rangle - \nabla_{\vec{R}_I}\left(\sum_{J\neq I}^{M} \frac{Z_I Z_J}{|\vec{R}_I - \vec{R}_J|}\right) \tag{3.113}$$

where $\hat{H}$ is the Hamiltonian of the electronic time-dependent system. The first term of the right hand-side of (3.113) represents the forces felt by the nuclei coming from the electrons of the system, calculated from the single-electron Kohn-Sham wavefunctions and the second term

corresponds to the forces deriving from the nuclei-nuclei interactions with all the other nuclei. The picture is actually very similar to the MD one. Ehrenfest dynamics can be viewed, for the nuclei motion, as a MD simulation where forces are calculated via TDDFT. Just like for classical MD which we have presented in detail in Section 3.2, the equations of motions of the nuclei must be integrated in time by discretizing time in timesteps of duration Δt. The integration schemes we have presented for classical MD, namely position-Verlet and velocity-Verlet (see Section 3.2.1) are adequate algorithms for propagating (3.113) in time. In parallel to the update of the nuclei coordinates at each timestep, the single-electron wavefunctions solutions of the time-dependent Kohn-Sham equations are propagated in time. Note that the timestep used for the nuclei motion should be the same as the one used for the electron dynamics with (3.111). A general detailed procedure for Ehrenfest dynamics simulations is given in Fig. 3.22:

(*i*) the initial state is obtained via a ground state DFT calculation,

(*ii*) the external time-dependent perturbation is applied,

(*iii*) the time-dependent Kohn-Sham potentials are calculated and the time-dependent Kohn-Sham equations are solved,

(*iv*) electronic wavefunctions and then nuclei positions are propagated to $t + \Delta t$,

(*v*) we come back to (*iii*) with an updated Kohn-Sham potential consequently to the state of the system at $t + \Delta t$.

This procedure ends when t becomes superior to an initially defined maximum simulation time. This coupling of wavefunctions propagation with RT-TDDFT and Verlet (or other similar scheme) integration of the equations of motion of the nuclei (where forces derive from the calculated electronic wavefunctions) is characteristic of the ED method.

3.4.3 Usage of TDDFT simulations results in our multiscale approach

The necessity of the incorporation of electronic effects into MD simulations of collision cascades was already pointed out at the time of the publication of the original article presenting our global approach [99]. We actually employ TDDFT in this context, more precisely as a way of parametrizing the EPH model for the incorporation of electronic effects (see Paragraph 3.2.2.4.4). Intrinsically, we are interested in the calculation of electronic stopping powers of PKAs with TDDFT and the ED formalism. The calculation of electronic stopping powers of PKAs in crystals gives valuable information on the physics of the electron dynamics in a material during an irradiation event. More than serving as a way to parametrize the EPH model, the calculation of electronic stopping powers of PKAs in crystals gives valuable information on the physics of the electron dynamics in a material during an irradiation event. The methodology we follow for extracting the electronic stopping power from TDDFT calculations is exposed in Chapter 5.

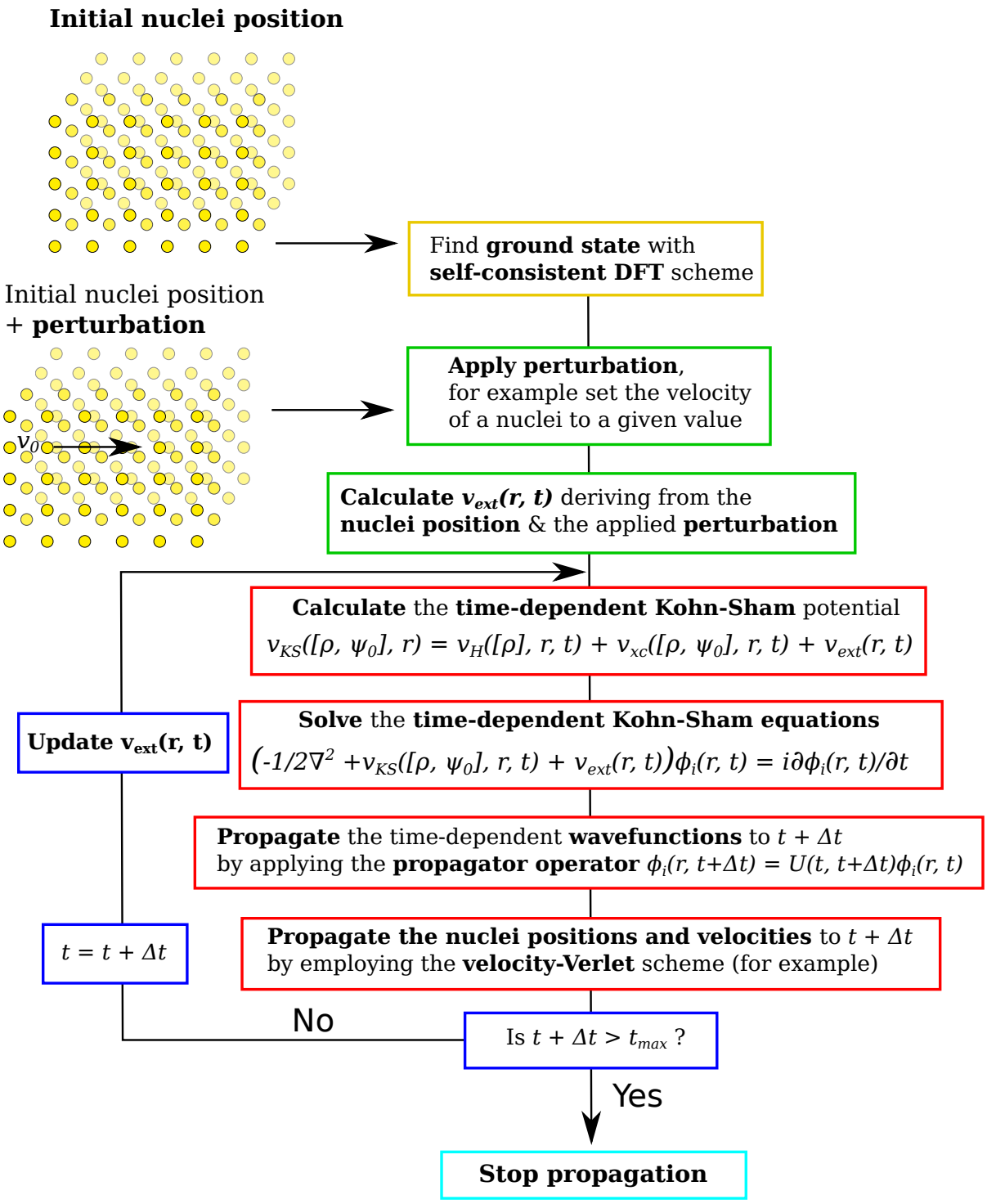

Figure 3.22: *Example of Ehrenfest algorithm procedure. The initial state required to solve the time-dependent Kohn-Sham equations is obtained by performing a self-consistent DFT calculation.*

Conclusion

In this chapter are presented in detail the simulation techniques employed in this PhD work, in the context of their use in our multiscale approach. We have seen the theory lying behind particle-matter MC codes, which are employed to study the creation of PKAs into matter. The usage of the data produced during this first MC step, as input parameter to the MD step of the global approach was also detailed. Concerning the MD step during which cascades are propagated, we spent time explaining the specificities of the usage of MD for the simulation of collision cascades, focusing on the efforts to undertake to have a trustworthy interatomic potential, to cope with the stochasticity and also to incorporate electronic effects. On this last aspect, a lengthy presentation of TDDFT was given, as we use this technique for the parametrization of the EPH model for the incorporation of electronic effects. Finally, the kART technique which we employ to heal the damaged structures obtained at the end of the MD step has been presented in detail.

The next two chapters focus on the improvement and testing of the MD step of our simulation approach. Chapter 4 is dedicated to some vocabulary and methodology definition for MD simulations of collision cascades as well as a convergence study in Si to assess the degree of uncertainty in MD simulations results due to the stochasticity of collision cascades. Chapter 5 is dedicated to the comparison of the EPH and TTM model for the inclusion of electronic effects into MD. It incorporates an extensive study of the TTM influence on the cascades simulations results in Si and Ge as well as cascades simulations results obtained with the EPH model in Si. The TDDFT study performed to parametrize the EPH model is also presented, and the methodologies of the calculation of electronic stopping powers with TDDFT and of the EPH model parametrization detailed. Finally, Chapter 6 focuses on the production of results with our multiscale approach, in Si, Ge and Si-Ge alloys.

References

[1] S. Agostinelli et al., "Geant4 a simulation toolkit", Nucl. Instr. Meth. Phys. R. A **506**, 250–303 (2003).

[2] J. Allison et al., "Geant4 developments and applications", IEEE Trans. Nucl. Sc. **53**, 270–278 (2006).

[3] J. Allison et al., "Recent developments in Geant4", Nucl. Instr. Meth. Phys. R. A **835**, 186–225 (2016).

[4] J. F. Ziegler, M. D. Ziegler, and J. P. Biersack, "SRIM - The stopping and range of ions in matter (2010)", Nucl. Instr. Meth. Phys. R. B **268**, 1818–1823 (2010).

[5] M. T. Robinson, "The binary collision approximation: Background and introduction", Rad. Eff. Def. Sol. **null**, 3–20 (1994).

[6] M. T. Robinson and I. M. Torrens, "Computer simulation of atomic-displacement cascades in solids in the binary-collision approximation", Phys. Rev. B **9**, 5008–5024 (1974).

[7] W. Eckstein, "The Binary Collision Model", in *Computer simulation of ion-solid interactions* (Springer Berlin Heidelberg, Berlin, Heidelberg, 1991), pp. 4–32.

[8] J. F. Ziegler, J. P. Biersack, and U. Littmark, *The Stopping Range of Ions in Solids*, 1st ed. (Pergamon Press, N. Y, 1983).

[9] C. J. Ortiz, L. Luneville, and D. Simeone, "1.19 - Binary Collision Approximation", in *Comprehensive nuclear materials*, edited by R. J. M. Konings and R. E. Stoller, 2nd ed. (Elsevier, Oxford, 2020), pp. 595–619.

[10] P. Lopez, L. Pelaz, I. Santos, L. A. Marques, and M. Aboy, "Molecular dynamics simulations of damage production by thermal spikes in Ge", J. App. Phys. **111**, 033519 (2012).

[11] G. Moliere, "Theorie der Streuung schneller geladener Teilchen I. Einzelstreuung am abgeschirmten Coulomb-Feld", Zeitschrift für Naturforschung A **2**, 133–145 (1947).

[12] L. Verlet, "Computer "Experiments" on Classical Fluids. I. Thermodynamical Properties of Lennard-Jones Molecules", Phys. Rev. Jour. Arch. **159**, 98–103 (1967).

[13] D. J. Evans and B. L. Holian, "The Nose-Hoover thermostat", J. Chem. Phys. **84**, 4069 (1985).

[14] G. E. Uhlenbeck and L. S. Ornstein, "On the Theory of the Brownian Motion", Phys. Rev. **36**, 823–841 (1930).

[15] K. Nordlund, M. Ghaly, R. S. Averback, M. Caturla, T. Diaz de la Rubia, and J. Tarus, "Defect production in collision cascades in elemental semiconductors and fcc metals", Phys. Rev. B **57**, 7556–7570 (1998).

[16] F. Gao, N. Chen, E. Hernandez-Rivera, D. Huang, and P. D. Levan, "Displacement damage and predicted non-ionizing energy loss in GaAs", J. App. Phys. **121**, 095104 (2017).

[17] F. H. Stillinger and T. A. Weber, "Computer simulation of local order in condensed phases of silicon", Phys. Rev. B **31**, 5262–5271 (1985).

[18] K. Ding and H. C. Andersen, "Molecular-dynamics simulation of amorphous germanium", Phys. Rev. B **34**, 6987–6991 (1986).

[19] S. Ethier and L. J. Lewis, "Epitaxial growth of Si1-xGex on Si(100)2 x 1: A molecular-dynamics study", J. Mat. Res. **7**, 2817–2827 (1992).

[20] N. Chen, E. Rasch, D. Huang, E. R. Heller, and F. Gao, "Atomic-Scale Simulation for Pseudometallic Defect-Generation Kinetics and Effective NIEL in GaN", IEEE Trans. Nucl. Sc. **65**, 1108–1118 (2018).

[21] J. Tersoff, "New empirical approach for the structure and energy of covalent systems", Phys. Rev. B **37**, 6991–7000 (1988).

[22] J. R. Morris, C. Z. Wang, K. M. Ho, and C. T. Chan, "Melting line of aluminum from simulations of coexisting phases", Phys. Rev. B **49**, 3109–3115 (1994).

[23] C. Kittel, *Introduction to Solid State Physics*, 8th ed. (John Wiley and Sons, 2004).

[24] N. Trung, H. Phuong, and M. D. Starostenkov, "Molecular dynamics simulation of displacement cascades in B2 NiAl", Lett. Mat. **9**, 168–172 (2019).

[25] H. He, C. He, J. Zhang, W. Liao, H. Zang, Y. Li, and W. Liu, "Primary damage of 10 keV Ga PKA in bulk GaN material under different temperatures", Nucl; Eng. Tech., 10.1016/j.net.2019.12.027 (2019).

[26] J. T. Buchan, M. Robinson, H. J. Christie, D. L. Roach, D. K. Ross, and N. A. Marks, "Molecular dynamics simulation of radiation damage cascades in diamond", J. App. Phys. **117**, 245901 (2015).

[27] E. Zarkadoula, G. Samolyuk, H. Xuen, H. Bei, and W. J. Weberab, "Effects of the two-temperature model on cascade evolution in Ni and NiFe", Scr. Mat. **124**, 6–10 (2016).

[28] H. J. Christie, M. Robinson, D. L. Roach, D. K. Ross, I. Suarez-Martinez, and N. A. Marks, "Simulating radiation damage cascades in graphite", Carbon **81**, 105–114 (2015).

[29] T. Jarrin, A. Jay, N. Richard, and A. Hémeryck, "Coping with the stochasticity of collision cascades in Molecular Dynamics simulations", Nucl. Instr. Meth. Phys. R. B **500-501**, 1–9 (2021).

[30] M. Warrier, U. Bhardwaj, H. Hemani, R. Schneider, A. Mutzke, and M. C. Valsakumar, "Statistical study of defects caused by primary knock-on atoms in fcc Cu and bcc W using molecular dynamics", J. Nucl. Mat. **467**, 457–464 (2015).

[31] R. Voskoboinikov, "Optimal sampling of MD simulations of primary samage formation in collision cascades", Nucl. Instr. Meth. Phys. R. B **479**, 18–22 (2020).

[32] A. Jay, M. Raine, N. Richard, N. Mousseau, V. Goiffon, A. Hémeryck, and P. Magnan, "Simulation of Single Particle Displacement Damage in Silicon–Part II: Generation and Long-Time Relaxation of Damage Structure", IEEE Trans. Nucl. Sc. **64**, 141–148 (2017).

[33] A. Caro and M. Victoria, "Ion-electron interaction in molecular dynamics cascade", Phys. Rev. A **40**, 2287–2291 (1989).

[34] I. Koponen, "Energy transfer between electrons and ions in dense displacement cascades", Phys. Rev. B **47**, 14011–14019 (1993).

[35] D. A. Young, "Etching of Radiation Damage in Lithium Floride", Nature **182**, 375–377 (1958).

[36] N. Itoh, D. M. Duffy, S. Khakshouri, and A. M. Stoneham, "Making tracks: electronic excitation roles in forming swift heavy ion tracks", Journal of Physics: Condensed Matter **21**, 474205 (2009).

[37] A. Kamarou, W. Wesch, E. Wendler, A. Undisz, and M. Rettenmayr, "Swift heavy ion irradiation of InP: Thermal spike modeling of track formation", Phys. Rev. B **73**, 184107 (2006).

[38] M. Lang, R. Devanathan, M. Toulemonde, and C. Trautmann, "Advances in understanding of swift heavy-ion tracks in complex ceramics", Curr. Opin. Solid State Mater. Sci. **19**, 39–48 (2015).

[39] R. L. Fleischer, P. B. Price, R. M. Walker, and E. L. Hubbard, "Criterion for Registration in Dielectric Track Detectors", Phys. Rev. **156**, 353–355 (1967).

[40] Y. Yavlinskii, "Coulomb repulsion of lattice ions under swift heavy ion irradiation", Nucl. Instr. Meth. Phys. R. B **245**, Swift Heavy Ions in Matter, 114–116 (2006).

[41] E. M. Bringa and R. E. Johnson, "Coulomb Explosion and Thermal Spikes", Phys. Rev. Lett. **88**, 165501 (2002).

[42] E. Carpene, "Ultrafast laser irradiation of metals: Beyond the two-temperature model", Phys. Rev. B **74**, 024301 (2006).

[43] D. M. Duffy and A. M. Rutherford, "Including the effects of electronic stopping and electron-ion interactions in radiation damage simulations", J. Phys.: Cond. Matter. **19**, 1–11 (2007).

[44] A. Tamm, M. Caro, A. Caro, G. Samolyuk, M. Klintenberg, and A. A. Correa, "Langevin Dynamics with Spatial Correlations as a Model for Electron-Phonon Coupling", Phys. Rev. Lett. **120**, 185501 (2018).

[45] M. Caro, A. Tamm, A. A. Correa, and A. Caro, "Role of electrons in collisions cascades in solids. 1. Dissipative model", Phys. Rev. B **99**, 174301 (2019).

[46] G. Khara, S. T. Murphy, S. L. Daraszewicz, and D. M. Duffy, "The influence of the electronic specific heat on swift heavy ion irradiation simulations in silicon", J. Phys.: Cond. Matter. **28**, 395201 (2016).

[47] A. Lim, W. M. C. Foulkes, A. P. Horsfield, D. R. Mason, A. Schleife, E. W. Draeger, and A. A. Correa, "Electron Elevator: Excitations across the Band Gap via a Dynamical Gap State", Phys. Rev. Lett. **116**, 043201 (2016).

[48] R. Kubo, "The fluctuation-dissipation theorem", Rep. Prog. Phys. **29**, 255–284 (1966).

[49] E. Zarkadoula, G. Samolyuk, and W. J. Weber, "Effects of the two-temperature model on cascade evolution in Ni and NiFe", J. Nucl. Mat. **490**, 317–322 (2017).

[50] C. L. Phillips, R. J. Magyar, and P. S. Crozier, "A two-temperature model of radiation damage in α-quartz", J. Comput. Phys. **133**, 144711 (2010).

[51] C. J. Glassbrenner and G. A. Slack, "Thermal Conductivity of Silicon and Germanium from 3K to Melting Point", Phys. Rev. A **134**, 1058–1069 (1966).

[52] M. Toulemonde, C. Dufour, A. Meftah, and E. Paumier, "Transient thermal processes in heavy ion irradiation of crystalline inorganic insulators", Nucl. Instr. Meth. Phys. R. B **166-167**, 903–912 (2000).

[53] A. A. Correa, "Calculating electronic stopping power in materials from first principles", Comp. Mat. Sci. **150**, 291–303 (2018).

[54] J. Lindhard and M. Sharff, "Energy loss in matter by fast particles of low charge", Matisk-fysiske Meddelelser det Kongelige Danske Videnskabernes Selskab **27**, 15 (1953).

[55] A. Chettah, H. Kucal, Z. G. Wang, M. Kac, A. Meftah, and M. Toulemonde, "Behavior of crystalline silicon under huge electronic excitations: A transient thermal spike description", Nucl. Instr. Meth. Phys. R. B **267**, 2719–2724 (2009).

[56] O. Osmani, I. Alzaher, T. Peters, B. Ban, A. Cassimi, H. Lebius, I. Monnet, N. Medvedev, B. Rethfled, and M. Scleberger, "Damage in crystalline silicon by swift heavy ion irradiation", Nucl. Instr. Meth. Phys. R. B **282**, 43–47 (2012).

[57] M. W. Finnis, P. Agnew, and A. J. E. Foreman, "Thermal excitation of electrons in energetic displacement cascades", Phys. Rev. B **44**, 567–574 (1991).

[58] C. Bjorkas and K. Nordlund, "Assessment of the relation between ion beam mixing electron-phonon coupling and damage production in Fe", Nucl. Instr. Meth. Phys. R. B **267**, 1830–1836 (2009).

[59] K. Nordlund, L. Wei, Y. Zhong, and R. S. Averback, "Role of electron-phonon coupling on collision cascade development in Ni, Pd and Pt", Phys. Rev. B **57**, R13965–R13968 (1998).

[60] C. Lee, J. A. Stewart, R. Dingreville, S. M. Foiles, and A. Schleife, "Multiscale simulations of electron and ion dynamics in self-irradiated silicon", Phys. Rev. B **102**, 024107 (2020).

[61] S. Lohmann, R. Hole ňák, and D. Primetzhofer, "Trajectory-dependent electronic excitations by light and heavy ions around and below the bohr velocity", Phys. Rev. A **102**, 062803 (2020).

[62] A. Caro, A. A. Correa, A. Tamm, G. D. Samolyuk, and G. M. Stocks, "Adequacy of damped dynamics to represent the electron-phonon interaction in solids", Phys. Rev. B **92**, 144309 (2015).

[63] A. Tamm, M. Caro, A. Caro, and A. A. Correa, "Role of electrons in collision cascades in solids. 2. Molecular dynamics", Phys. Rev. B **99**, 174302 (2019).

[64] J. Yang, "Opium-Pseudopotential Generation Project", http://opium.sourceforge.net (2018).

[65] R. Ullah, E. Artacho, and A. A. Correa, "Core Electrons in the Electronic Stopping of Heavy Ions", Phys. Rev. Lett. **121**, 116401 (2018).

[66] M. Raine, V. Goiffon, P. Paillet, O. Duhamel, S. Girard, M. Gaillardin, C. Virmontois, J. M. Belloir, N. Richard, and P. Magnan, "Exploring the Kinetics of Formation and Annealing of Single Particle Displacement Damage in Microvolumes of Silicon", IEEE Trans. Nucl. Sc. **61**, 2826–2833 (2014).

[67] F. El-Mellouhi, N. Mousseau, and L. J. Lewis, "Kinetic activation-relaxation technique: An off-lattice self-learning kinetic Monte Carlo algorithm", Phys. Rev. B **78**, 153202 (2008).

[68] L. K. Béland, P. Brommer, F. El-Mellouhi, J. F. Joly, and N. Mousseau, "Kinetic activation-relaxation technique", Phys. Rev. E **84**, 046704 (2011).

[69] G. T. Barkema and N. Mousseau, "Event-Based Relaxation of Continuous Disordered Systems", Phys. Rev. Lett. **77**, 4358 (1996).

[70] R. Malek and N. Mousseau, "Dynamics of Lennard-Jones clusters: A characterization of the activation-relaxation technique", Phys. Rev. E **62**, 7723–7728 (2000).

[71] K. J. Laidler and M. C. King, "Development of transition-state theory", J. Phys. Chem. **87**, 2657–2664 (1983).

[72] F. El-Mellouhi, N. Mousseau, and P. Ordejón, "Sampling the diffusion paths of a neutral vacancy in silicon with quantum mechanical calculations", Phys. Rev. B **70**, 205205 (2004).

[73] H. Yildirim, A. Kara, and T. S. Rahman, "Origin of quasi-constant pre-exponential factors for adatom diffusion on Cu and Ag surfaces", Phys. Rev. B **76**, 165421 (2007).

[74] A. B. Bortz, M. H. Kalos, and J. L. Lebowitz, "A new algorithm for Monte Carlo simulation of Ising spin systems", J. Comput. Phys. **17**, 10–18 (1975).

[75] K. A. Fichtorn, "Theoretical foundations of dynamical Monte Carlo simulations", J. Chem. Phys. **95**, 1090 (1991).

[76] B. D. McKay, "Practical graph isomorphism", Congressus Numerantium **30**, 45–87 (1981).

[77] A. Jay, C. Huet, N. Salles, M. Gunde, L. Martin-Samos, N. Richard, G. Landa, V. Goiffon, S. De Gironcoli, A. Hémeryck, and N. Mousseau, "Finding Reaction Pathways and Transition States: r-ARTn and d-ARTn as an Efficient and Versatile Alternative to String Approaches", J. Chem. Theory Comput. **16**, 6726–6734 (2020).

[78] C. Lanczos, "An Iteration Method for the Solution of the Eigenvalue I Problem. of Linear Differential and Integral Operators", Journal of Research of the National Bureau of Standards **45**, 2133 (1950).

[79] B. Puchala, M. L. Falk, and K. Garikipati, "An energy basin finding algorithm for kinetic Monte Carlo acceleration", J. Chem. Phys. **132**, 134104 (2010).

[80] G. H. Saboya, "Defects in silicon: revisiting theoretical frameworks to guide ab initio characterization", Université Toulouse 3 Paul Sabatier, (2020) https://tel.archives-ouvertes.fr/tel-03158564/.

[81] P. Hohenberg and W. Kohn, "Inhomogeneous electron gas", Phys. Rev. **136**, B864 (1964).

[82] J. J. Sakurai and J. Napolitano, *Modern Quantum Mechanics*, 2nd ed. (Cambridge University Press, 2017).

[83] W. Kohn and L. J. Sham, "Self-Consistent Equations Including Exchange and Correlation Effects", Phys. Rev. **140**, A1133 (1965).

[84] I. Maliyov, "Ionic irradiation of materials : real-time dynamics of electronic excitations", Université Paris-Saclay, (2019) https://tel.archives-ouvertes.fr/tel-02495699.

[85] J. P. Perdew and A. Zunger, "Self-interaction correction to density-functional approximations for many-electron systems", Phys. Rev. B **23**, 5048 (1981).

[86] P. Giannozzi et al., "QUANTUM ESPRESSO: a modular and open-source software project for quantum simulations of materials", J. Phys.: Cond. Matter. **21**, 395502 (2009).

[87] P. Giannozzi, O. Baseggio, P. Bonfà, D. Brunato, R. Car, I. Carnimeo, C. Cavazzoni, S. de Gironcoli, P. Delugas, F. Ferrari Ruffino, A. Ferretti, N. Marzari, I. Timrov, A. Urru, and S. Baroni, "Quantum ESPRESSO toward the exascale", J. Chem. Phys. **152**, 154105 (2020).

[88] X. Gonze et al., "The Abinit project: Impact, environment and recent developments", Comput. Phys. Commun. **248**, 107042 (2020).

[89] G. Kresse and J. Hafner, "Ab initio molecular-dynamics simulation of the liquid-metal–amorphous-semiconductor transition in germanium", Phys. Rev. B **49**, 14251–14269 (1994).

[90] G. Kresse and J. Furthmüller, "Efficient iterative schemes for ab initio total-energy calculations using a plane-wave basis set", Phys. Rev. B **54**, 11169–11186 (1996).

[91] D. S. Sholl and J. A. Steckel, *Density-Functional Theory: A Practical Introduction* (Wiley, 2009).

[92] E. Runge and E. K. U. Gross, "Density-Functional Theory for Time-Dependent Systems", Phys. Rev. Lett. **52**, 997–1000 (1984).

[93] M. A. L. Marques, N. T. Maitra, F. M. S. Nogueira, E. K. U. Gross, and A. Rubio, *Fundamentals of Time-Dependent Density Functional Theory* (Springer-Verlag Berlin Heidelberg, 2012).

[94] D. A. Rehn, Y. Shen, M. E. Buchholz, M. Dubey, R. Namburu, and E. J. Reed, "ODE integration schemes for plane-wave real-time time-dependent density functional theory", J. Chem. Phys. **150**, 014101 (2019).

[95] F. Gygi, "Architecture of Qbox: A scalable first-principles molecular dynamics code", IBM Jour. Res. Dev. **52**, 137–144 (2008).

[96] E. W. Draeger, X. Andrade, J. A. Gunnels, A. Bhatele, A. Schleife, and A. A. Correa, "Massively parallel first-principles simulation of electron dynamics in materials", J. Par. Dist. Comp. **106**, 205–214 (2017).

[97] A. A. Gómez Pueyo, M. A. L. Marques, A. Rubio, and A. Castro, "Propagators for the Time-Dependent Kohn–Sham Equations: Multistep, Runge–Kutta, Exponential Runge–Kutta, and Commutator Free Magnus Methods", J. Chem. Theory Comput. **14**, 3040–3052 (2018).

[98] P. Ehrenfest, “Bemerkung über die angenäherte Gültigkeit der klassischen Mechanik innerhalb der Quantenmechanik”, Z. Physik **45**, 455–457 (1927).

[99] M. Raine, A. Jay, N. Richard, V. Goiffon, S. Girard, M. Gaillardin, and P. Paillet, “Simulation of Single Particle Displacement Damage in Silicon – Part I: Global Approach and Primary Interaction Simulation”, IEEE Trans. Nucl. Sc. **64**, 133–140 (2017).

Collision cascades characterization

4

Contents

Introduction

In the previous chapter, we detailed the cautious approach we adopt to simulate collision cascades with MD. In addition to the efforts to undertake in the modeling of physical processes at stake in collision cascades, the characterization of the cascades results should also be performed with great care. Indeed, the possibilities in terms of cascades properties and analysis methods are very diverse. It is thus essential to properly identify and define the properties of interest. Appropriate and clearly defined methods should also be employed so that the results are comparable and reproducible. For example, there exists multiple methods for defining defects and thus counting defects, each yielding different results. A single method should be chosen and unequivocally defined for a given study. Moreover, the stochastic aspect of collision cascades makes mandatory to construct a methodology permitting to cope with the stochasticity of the cascades, and thus to resort to a statistical treatment of the results. This involves the need for clear definitions and interpretations of the statistical quantities used to describe properties of interest as well as the assessment of the correct convergence of the statistical quantities with respect to the number of simulations performed. This chapter's objective is to properly introduce all the necessary definitions and methods for the analysis of MD simulations of collision cascades. Thus, in Section 4.1, we review the cascades properties we are going to encounter in the three last chapters of this manuscript as well as the statistical quantities we are going to employ. In Section 4.2, we present the Lindemann spheres and Weigner-Seitz methods for counting defects, and we apply those methods to the characterization of MD simulations of collision cascades carried out in Si and Ge. Finally, in Section 4.3, we perform a convergence study of the mean values and overall distributions of several cascades properties in Si with respect to the number of simulations performed and to the method employed for choosing the initial directions of the PKAs.

4.1 Vocabulary definition

4.1.1 Cascades properties

To quantify the level of damage created during a collision cascade, the **number of created defects**, their distribution in clusters as well as the extension of the spatial distribution of defects should be quantified. A very important notion is therefore the one of defect. A defect can be either a vacancy or an interstitial atom. In a MD simulation of collision cascade, as there is no loss or addition of atoms during a simulation, the numbers of interstitial atoms and vacancies are always equal. Thus, when we mention a number of defects, we refer to the number of interstitial atoms or vacancies, not the sum of the two. This is sometimes referred to as the number of Frenkel pairs. In this manuscript, we systematically refer to the number of defects when discussing cascades results, as it is an essential feature to assess the level of damage caused to a material. To be able to count the defects, we must be able to identify them in the damaged structures obtained at the end of our MD and/or kART simulations. This is far from being straightforward and the specific aspect of the existing methods for finding defects is treated in Section 4.2.

Once defects are identified, they can be divided into clusters of defects. The **number of clusters** in a simulation as well as the number of defects in each cluster are essential properties of a collision cascade at a given MD simulation time. In this manuscript, we adopt a simple rule for defining the clusters of defects: two defects (vacancy or interstitial atom) are considered to belong to the same cluster if they are separated by a distance shorter than twice the nearest neighbor distance of the crystalline structure. With this simple rule, all defects can be classified into clusters characterized by a number of vacancy and a number of interstitial atom. The number of clusters is a property we systematically look at in our collision cascades analysis.

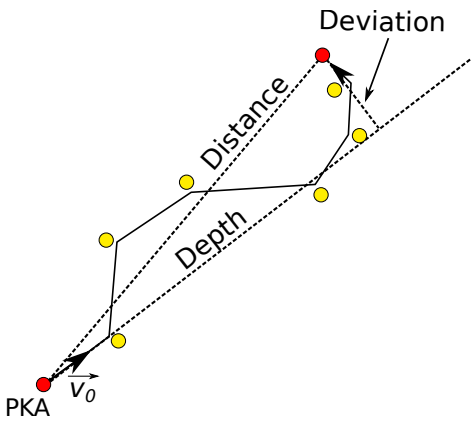

Figure 4.1: *Representation of the distance, penetration depth and deviation quantities. The PKA is in red, yellow circles depict the atoms it shocked. The straight line is the trajectory of the PKA.*

In order to have a complete overview of the density and shape of collision cascades, the spatial extension of the cascades must be quantified. The **distance of the identified defects to the initial position of the PKA** is an interesting characteristic, which we will employ in Chapter 6 of this manuscript. The **distance between the current position of the PKA and its initial position** is also employed from time to time throughout this manuscript. The quantity we systematically employ is the **penetration depth of the PKA**. We define the penetration depth of the PKA as the projection on the initial PKA velocity unit vector of the vector going from the initial position of the PKA to its current position. From the definition of the PKA penetration depth also arises another quantity we call the **PKA deviation length**, defined as the projection on a vector normal to the initial PKA velocity unit vector of the vector going from the initial position of the PKA to its current position. This last quantity will also be used from times to times. The depth quantity is the one we use the most as it is directly comparable to the projected range concept employed in MC codes like SRIM [1], to which we regularly compare our results. In Fig. 4.1 are illustrated on a fictitious 2D example the distance, penetration depth and deviation quantities.

4.1.2 Statistical quantities

In the previous section, we have presented the quantities we look at for each cascade. However, due to the high degree of stochasticity of collision cascades, many simulations depicting as much representative cases as possible have to be carried out to be able to draw conclusions from the obtained results. Consequently, adequate statistical concepts and indicators have to be applied to large ensembles of collision cascades simulations. In the following, we define the statistical indicators we employ for the characterization of MD simulations of collision cascades.

For each cascade property we look at (for example the number of defects, number of clusters and PKA penetration depth), we calculate the **mean value $\boldsymbol{\mu}$** over the set of simulations carried out. However, the mean value in itself is not satisfactory as the stochasticity of cascades can make it subject to large uncertainties and thus unusable for interpretations. Uncertainties on the mean values should always be given, in order to avoid biased results interpretation. The uncertainties on the mean values are defined from the **Standard Error of the Mean (SEM)**, defined as follows for a given set of N measures x_i having a mean equal to μ:

$$\text{SEM} = \frac{1}{\sqrt{n}}\sqrt{\frac{\sum_{i=1}^{N}(x_i-\mu)^2}{n-1}} = \frac{\sigma}{\sqrt{n}} \tag{4.1}$$

where σ is the standard deviation and is unequivocally defined in (4.1). The SEM is a good indicator of the uncertainty on the calculated mean value. We assume that all the properties we look at are normal random variables. Thus, the 95% confidence interval of the calculated mean values is given by [μ - $k(n)$×SEM; μ + $k(n)$×SEM], where $k(n)$ is a coefficient depending on the number n, for us the number of simulations performed, and is equal to 1.96 for large enough ensembles. In other words, there is a 95% probability that the real mean value of the property of interest falls within the confidence interval specified. The **standard deviation σ** which we have defined in (4.1) is also employed from time to time in this manuscript. It does not quantify an uncertainty on a mean value calculation but the dispersion of a dataset around its mean value. The greater σ is, the more dispersed the dataset is.

Going further than the mean values, we also use the **minimum and maximum values** of our simulation sets as well as the first, second and third quartile values. The minimum and maximum values are important quantities as they sample the best and worst case scenarios depending on the property we look at. The **first quartile** value of a dataset is the value below which lies 25% of the entries of the dataset. The **second quartile** value of a dataset, also called **median**, is the value below which lies 50% of the entries of the dataset. The **third quartile** value of a dataset is the value below which lies 75% of the entries of the dataset. The quartile values are very useful for the graphical representation of the properties distribution under the form of box plots (or whiskers plots), as it will be done in Section 4.3. Box plots have the advantage over histograms of being more concise and of making easier the visual comparison between multiple simulation sets. However, we lose a bit of information compared to histograms. Therefore, when it is possible, *i.e.* when we do not have to compare more than two simulation sets, we also resort to histograms for the graphical representation of cascades properties.

All the statistical indicators mentioned above are employed in this manuscript for the statistical evaluation of the cascades properties of interest we identified in Section 4.1.1.

4.2 Methods for finding defects

The theoretical definitions of an interstitial atom and of a vacancy are simple. The former corresponds to an atom in a crystal which is not located on a lattice site and the latter is a lack of an atom on a specific lattice site of a crystalline material. However, defining a method for identifying defects in an atomic structure is not easy. Indeed, atoms vibrate around their crystalline sites, suffer from elastic distortions due to nearby defects, and are therefore not perfectly located on their associated atomic site, though they are crystalline. The numerical definition of interstitial atoms and vacancies is thus blurrier than it seems at first sight. Consequently, different methods exist for counting defects. In this section we introduce the widely employed Lindemann spheres [2] and Wigner-Seitz [3] methods, which we both apply to Si and Ge. Both methods have already been benchmarked on Si by Nordlund *et al.* in [4], who showed that for each cascade studied the ratio of defects found with the Lindemann and the Wigner-Seitz method is nearly constant. Our purpose here is to confirm this statement for Si, verify it stays true for Ge and finally adopt a method for counting defects.

4.2.1 Lindemann spheres

The Lindemann sphere method bases its definition of defects on the notion of crystalline site. With this method, a perfect crystal structure is superimposed to the atomic structure of interest. Around each lattice site of the perfect crystal structure is constructed a sphere of a given radius R_{lin}. If an atom is located within one of the spheres, it is considered crystalline. However, if an atom is not inside any of the spheres, it is labelled as an interstitial atom. Thus, a vacancy is defined as a lattice site whose sphere is empty. The situation is illustrated in 2D in Fig. 4.2.

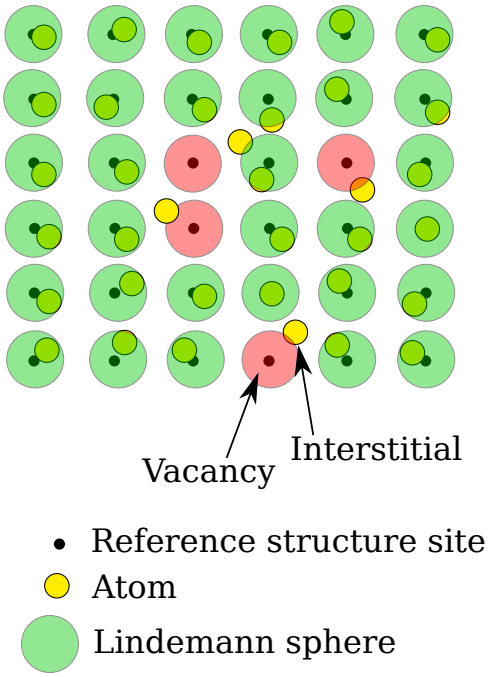

Figure 4.2: *2D illustration of the Lindemann spheres method for counting defects in an atomic structure. The red Lindemann spheres depict the presence of a vacancy.*

The Lindemann method involves the specification of a cutoff radius R_{lin}. In Si, some have chosen to employ half the nearest neighbor distance [4], but this is not the value most authors who employed the Lindemann sphere have agreed on. Following studies of the extent of thermal vibrations of Si atoms at their melting point [5], the value of 0.45 Å for R_{lin} is the commonly accepted one [2, 4]. When we use the Lindemann method, we use R_l^{Si}=0.45 Å for Si and a simple scaling relationship with respect to the lattice parameter for Ge and Si-Ge alloys:

$$R_l^{\mathrm{Ge,Si}_{1-x}\mathrm{Ge}_x} = R_l^{\mathrm{Si}} \times \frac{a_{\mathrm{Ge,Si}_{1-x}\mathrm{Ge}_x}}{a_{\mathrm{Si}}} \tag{4.2}$$

where $R_l^{\mathrm{Ge,Si}_{1-x}\mathrm{Ge}_x}$ is the Lindemann radius value for Ge or Si-Ge alloys, $a_{\mathrm{Ge,Si}_{1-x}\mathrm{Ge}_x}$ is the lattice parameter of Ge or Si-Ge alloys and a_{Si} is the lattice parameter of Si. For Ge, we have $R_l^{\mathrm{Ge}} = 0.468$ Å.

4.2.2 Wigner-Seitz cells

The main idea behind the Wigner-Seitz cells method is different from the one behind the Lindemann spheres method. It also lies on the superimposition of a perfect crystalline structure to the atomic structure of interest, but this time, instead of lattice-sites centered spheres, Wigner-Seitz cells centered on each lattice site are constructed. A Wigner-Seitz cell is the region of space in which every point is closer to the perfect lattice site being the center of the cell than to any other lattice site. The edges of Wigner-Seitz cells are equidistant to the two closest cell centers. Contrary to the Lindemann spheres method, the Wigner-Seitz method does not require the definition of an empirical cutoff radius. After the definition of the cells, to each cell is associated an occupancy number equal to the number of atoms in the cell. A defectless structure should yield all occupancies equal to one. However, a defective structure would show some cells having occupancies greater than one, meaning that one or more interstitials are located in the cells, and cells having occupancies equal to zero, which are identified as vacancies. The idea behind the Wigner-Seitz cell method is illustrated in Fig. 4.3.

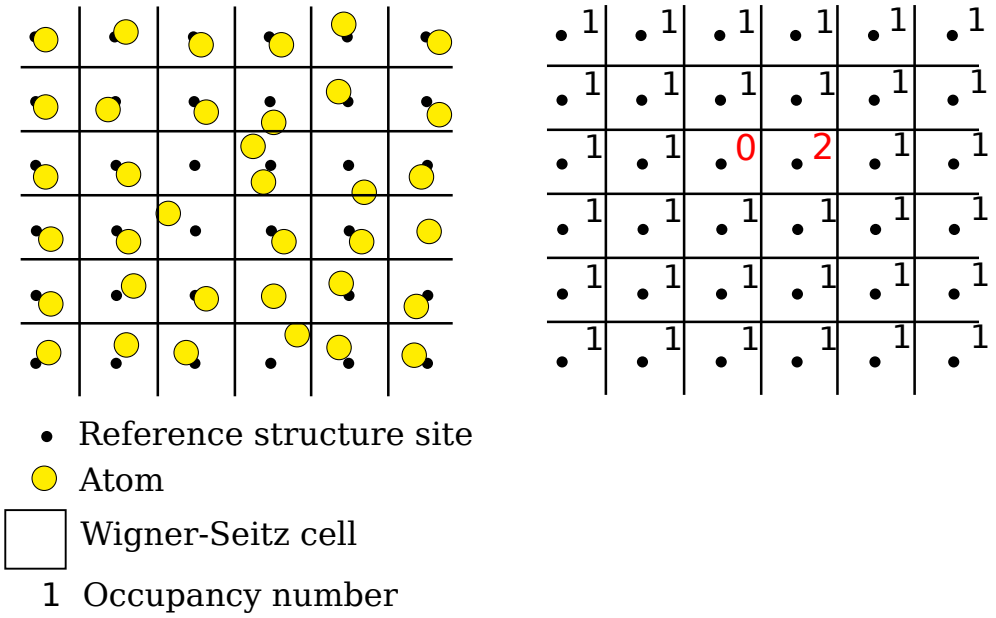

Figure 4.3: *2D illustration of the Wigner-Seitz cells method for counting defects in an atomic structure. When occupancy numbers are written in red, it means they are not equal to the reference value of 1.*

The Wigner-Seitz method directly allows to count the number of interstitials and vacancies via the occupancy numbers. It also directly identifies the vacancy sites. However, it does not explicitly labels which atoms are interstitial atoms and which ones are not. Indeed, if the Wigner-Seitz cell of a given site has an occupancy equal to two, one of the two atoms is an interstitial atom but the other may not be, the global rule we want to verify being that the number of vacancies is equal to the number of interstitial atoms. Simple rules for determining among those atoms which one is an interstitial and which one is not can be imagined. For example, the atom the further from the center of the cell could be labelled as the interstial one.

4.2.3 Application of the Lindemann and Wigtner-Seitz methods in Si and Ge

We apply both the Lindemann and Wigner-Seitz methods to sets of 100 collision cascades simulations each initiated in Si and Ge with 10 keV PKAs having distinct initial directions. For the analysis with the Lindemann method we use the defects and clusters analysis code developed in our research group by Antoine Jay, and for the analysis with the Wigner-Seitz method we employ the OVITO visualization and analysis software [6]. Table 4.1 shows the mean number of defects μ obtained in Si and Ge with both methods, as well as the 2^{nd} quartile value Q2 and the ratio of the standard deviation σ over the mean μ. In Table 4.2 are displayed, both for Si and Ge, the mean μ, standard deviation σ, minimum and maximum values of the ratio of the number of defects obtained with the Lindemann N_i^{lin} and Wigner-Seitz N_i^{wig} methods for each simulation i. The ratio of the Q2 and σ/μ values obtained with both methods in Si and Ge are also indicated.

The first striking observation one can make is the significant discrepancy of the mean μ and Q2 values obtained in Si and Ge with both methods. As indicated in Table 4.1, in Si, the mean number of defects is found to be 554 with the Lindemann method, compared to only 70 with the Wigner-Seitz one, yielding a ratio of 7.9 between the mean values. In Ge, the ratio is of 7.2 (2371 mean number of defects with Lindemann and 329 with Wigner-Seitz). Similar ratios are found for the Q2 values, as displayed in the $\text{Q2}^{\text{lin}}/\text{Q2}^{\text{wig}}$ column of Table 4.2. More

Table 4.1: *Mean (μ), Q2 and ratio of the standard deviation (σ) to the mean number of defects (μ) obtained on 100 cascades simulations in Si and 100 cascades simulations in Ge both initiated by 10 keV PKAs with the Lindemann and Wigner-Seitz method.*

		μ	Q2	$\frac{\sigma}{\mu}$
Si	Lindemann	554	517	0.27
	Wigner-Seitz	70	63	0.32
Ge	Lindemann	2371	2263	0.23
	Wigner-Seitz	329	322	0.28

important than the comparison of the mean number of defects obtained with each method, we can look at the distribution of the ratios cascade per cascade. The mean values of the ratios, displayed in the first column of Table 4.2, gives a value of 8.0 for Si and 7.2 for Ge. The second column of Table 4.2, showing the standard deviations σ of the ratio distributions, shows very small σ values of 0.55 for Si and 0.41 for Ge. It means that the ratio values are very centered around their mean value. It is even emphasized by the fact that 85% of the cascades yield a $N_i^{\text{lin}}/N_i^{\text{wig}}$ ratio between 7.1 and 8.9 in Si and between 6.6 and 7.4 in Ge. The minimum and maximum values of the ratios of the number of defects for each cascade also go in the sense of very little dispersion of the ratios around the mean ratio value. Indeed, a minimum of 6.8 (6.5) and a maximum of 9.7 (8.3), very close one from each other, are found for Si (Ge). Overall, the comparison of the mean, standard deviation, minimum and maximum values of the ratios of the number of defects indicate that the Lindemann and Wigner-Seitz methods are very consistent despite yielding very different number of defects: both methods scale really well one with each other. The same conclusion was already drawn from the cascades analysis of Nordlund *et al.* in [4] in Si. The value of 8.0 we obtain for the ratio of the number of defects in Si is exactly the one which was obtained by Nordlund *et al.*. The different, but very close, values we find for Si and Ge (8.0 and 7.2 respectively) for the mean of the number of defects ratios are probably due to the very different nature of the defects in Si and Ge. In the latter, most defects are part of very large amorphous pockets, which is by far less the case in Si, where defects are more dispersed in clusters of diverse sizes [7].

Table 4.2: *Comparison of the distributions of number of defects obtained with the Lindemann and Wigner-Seitz methods in Si and Ge.*

	$\mu\left(\frac{N_i^{\text{lin}}}{N_i^{\text{wig}}}\right)$	$\sigma\left(\frac{N_i^{\text{lin}}}{N_i^{\text{wig}}}\right)$	$\min_i\left(\frac{N_i^{\text{lin}}}{N_i^{\text{wig}}}\right)$	$\max_i\left(\frac{N_i^{\text{lin}}}{N_i^{\text{wig}}}\right)$	$\frac{\text{Q2}^{\text{lin}}}{\text{Q2}^{\text{wig}}}$	$\frac{\sigma^{\text{lin}}/\mu^{\text{lin}}}{\sigma^{\text{wig}}/\mu^{\text{wig}}}$
Si	8.0	0.55	6.8	9.7	8.2	0.8
Ge	7.2	0.41	6.5	8.3	7.0	0.9

The dispersion of the distribution of the number of defects for the cascades investigated obtained with each method are compared in the last columns of Table 4.1 and Table 4.2. We see that the dispersion of the number of defects is slightly decreased with the Lindemann method compared to the Wigner-Seitz one, both for Si and Ge.

The conclusion we can give of our comparison of the number of defects obtained with the Lindemann and Wigner-Seitz methods is that, although the number of defects they give are very different, the ratios of the number of defects obtained with both methods for each cascade studied show very little dispersion and thus are very much centered around a mean value. It could almost be considered that the ratio between the two methods, for a given material, is constant. Following this statement, the choice between one method or the other is mainly a matter of personal taste. The Wigner-Seitz method has the advantage of giving, for a given cluster, the net number of interstitials and vacancies, but in itself it does not explicitly label

atoms as interstitials or not like the Lindemann method does. In the end, we chose to employ in this manuscript the Lindemann method, because the very high number of defects it gives makes us confident in the fact it does not miss any, which is an important aspect for us considering we need complete catalogs of defects to study them with kART. Also, it is consistent with the analysis method we employed in the previous MD papers published in our group [8]. It can also be noted that the Wigner-Seitz method is the preferred one in the case of metals, where defects are mostly point-like, whereas the Lindemann spheres method was found to be especially well adapted for the study of defects under the form of disordered regions (amorphous pockets) we find in semiconductors [2]. It is difficult to identify interstitials and vacancies in amorphous pockets, we however choose to employ those terms to characterize atoms part of those regions. It could be replaced by the term of disordered atom, the notion of vacancies thus disappearing in the case of amorphous pockets in this case. Overall, what should be reminded is that, indifferently of the chosen method, the trends observed will be the same, and the excellent scaling between both methods allows to quite satisfactorily convert the number of defects obtained with one to the number of defects obtained with another.

The choice of a trustworthy method for counting defects is an important aspect of the cascades analysis. However, it does not address the issue of the stochasticity of the cascades. Indeed, meaningful conclusions can only be drawn from large enough sets of simulations. This statement is valid for every cascades properties, The purpose of the next section is to prove the necessity to resort to large sets of simulations, to treat the collision cascades results in a rigorous statistical way and to give rough values on the number of simulations to be performed in Si to have converged results.

4.3 Convergence study

Due to the high level of stochasticity of collision cascades, it is needed to run multiple cascades simulations with different initial directions for the PKAs for every case studied. The optimal number of simulations to perform cannot be known *a priori*, the commonly agreed rule of thumb being that the greater the number of simulations the more trustworthy the results. In this section, we perform a convergence study of cascades properties in Si with PKAs of 1 keV and 5 keV, with respect to the number of simulations performed. We look at the convergence of the number of defects, the number of clusters and the PKA penetration depth. The Lindemann criterion is employed for counting the defects in the damage structures. Two methods for choosing the initial directions of the PKAs are compared, and the influence of the initial site of the PKA is also investigated. This section is directly taken from our published article on the subject [9].

4.3.1 Methods

4.3.1.1 Computational details

The MD simulations of this chapter have been run using the LAMMPS code. The cascades are initiated with 1 keV or 5 keV PKAs in Si. Boxes of 1 000 000 atoms made of $50\times50\times50$ diamond-like unit cells are employed in both cases. The simulation boxes are divided into two areas, like explained in the previous chapter: in the outer cells the velocities are rescaled to maintain the temperature at a desired value (thus allowing energy excess to be evacuated), and the inner cells form an NVE ensemble in which the atoms evolve freely to simulate the collision cascades. The initialization of the simulations is made by scaling the velocities of all atoms, such that the overall temperature is the desired one (300 K in the current work). The system is equilibrated during 20 ps with a timestep of 1 fs. As the velocity of the atoms drastically changes throughout the cascade, the integration timestep has to be changed during the simulations. Calculations

initiated with both 1 keV and 5 keV PKAs are run for 200 ps. We imposed the condition that no atom moves more than 0.02 Å between two steps of the simulation, with a timestep varying between 0.01 fs and 1 fs. The potential employed is a combination of the SW [10] and ZBL [1] ones as described in the previous chapter. To account for the electronic effects, the TTM is used in combination with MD. The chosen parameters are the default ones presented in the previous chapter for Si and Ge.

4.3.1.2 Convergence study methodology

Some vocabulary needs to be defined for the proper understanding of this study. The term "simulation" refers to a single collision cascade simulation. The term "set" refers to a given number of simulations performed to calculate the statistical quantities of the set. In each simulation of a set, the initial direction of the PKA is different and its energy is the same. The size of the set is the number of simulations in the set.

Two distinct methods are employed to study the convergence: *(i)* in the first method, called **Random**, the initial directions of the PKAs are randomly chosen, *(ii)* in the second method, called **Symmetry**, a set of distinct unit vectors (*i.e.* directions) uniformly distributed on the surface of a sphere is defined. It corresponds to the method for coping with the stochasticity we presented in the previous chapter. As a reminder, only the directions which are in the minimal space domain inequivalent to the others by crystalline symmetries have been kept, as depicted in Fig. 4.4, which can also be found in the previous chapter, but which we also show here for practicity purposes.

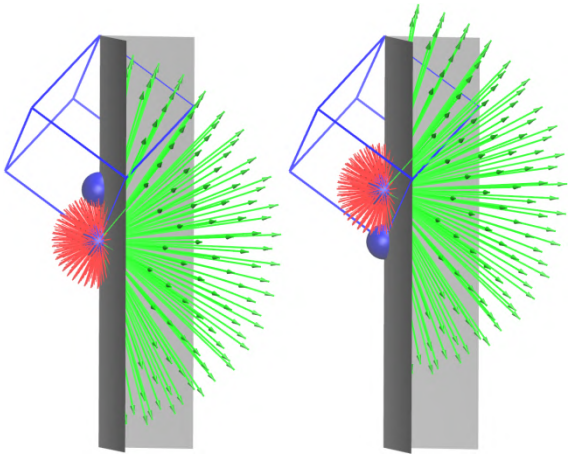

Figure 4.4: *Scheme of the minimal space domain in which 100 inequivalent directions are constructed. The two inequivalent atomic sites of the face-centered cubic diamond primitive unit cell are represented in blue. The inequivalent directions are depicted by long green arrows and the minimal space domain is delimited by the grey boundaries. The red small arrows represent the directions symmetrically equivalent to the green arrows of the minimal space domain. This figure was made by Antoine Jay.*

The unit sphere surrounding an atom is therefore divided into 6 symmetric parts. The minimal space domain is one of these parts. Thus, for each direction in the minimal space domain, there exists 5 others perfectly equivalent in the unit sphere. The weight of all the chosen directions is therefore the same.

The convergence is here considered as a combination of reproducibility and accuracy. To study the reproducibility of the simulations, statistical quantities for sets of different sizes are compared. Those quantities of interest are the mean value (μ), the minimum value (Min), the first

quartile value (Q1), the median or second quartile value (Q2), the third quartile (Q3) and the maximum value (Max). The accuracy is quantified through the standard error of the mean (SEM). Rather than the brute standard error of the mean we employ the ratio of the standard error of the mean to the mean value SEM/μ (called error coefficient).

4.3.2 Results and discussions

For both the Random and Symmetry methods, the distributions (*i.e.* box plots) and mean values of the number of defects, number of clusters and of the PKA penetration depth for Si PKAs of 1 keV in Si and sets of size 10, 20, 30, 40, 50, 60, 70, 80, 90 and 100 are presented in Section 4.3.2.1, Section 4.3.2.2 and Section 4.3.2.3. For the same set sizes, with the Symmetry method and with Si PKAs of 5 keV in Si, the distributions and mean values of the number of defects, number of clusters and of the PKA penetration depth are presented in Section 4.3.2.4. The influence of the lattice site initially chosen as the position of the PKA is investigated in Section 4.3.2.5.

4.3.2.1 Convergence of the number of defects for 1 keV PKAs in Si

Results provided in this section are obtained for PKAs of 1 keV in Si. The mean values of the number of defects in the Random and Symmetry cases for PKAs of 1 keV in Si are respectively shown in Fig. 4.5a and Fig. 4.5b. The box plots of the number of defects in the Random and Symmetry cases for PKAs of 1 keV in Si are respectively displayed in Fig. 4.5c and Fig. 4.5d.

Both the box plots and mean values of Fig. 4.5 are subject to strong variations for simulation sets of size inferior or equal to 30: the mean values range from 58 to 70 in the Random case and from 63 to 69 in the Symmetry case. Between 40 and 70 simulations in the sets, the discrepancies between the mean values are smaller, except in the Symmetry case (*i.e.* Fig. 4.5b) where a noticeable difference can be spotted between the sets of size 50 (67 defects) and 60 (61 defects). From 70 simulations in the sets, the mean values of the number of defects are well stabilized in the Symmetry case (*i.e.* Fig. 4.5b): the mean values range from 62 to 65 defects. It seems to be the case as well for the Random case of Fig. 4.5a but the mean value for the set size 100 suffers from a non negligible decrease compared to the previous value (change of 5 defects between the set of size 90 and the set of size 100). From sets of size 30, the distributions of Fig. 4.5c and Fig. 4.5d seem to be consistent one with each other. The distributions of the sets made of 80, 90 and 100 simulations for the Symmetry case have almost equal median (64.5, 64.5 and 65.0 respectively) and third quartile value (76.0, 75.0 and 75.0 respectively) whereas for the same set sizes for the Random case, the box plots still show some more important discrepancies.

Both in the Random and Symmetry case, the Min and Max values of the box plots are respectively smaller and greater for large sets than for small sets (see linear regressions *i.e.* dashed lines in Fig. 4.5c and Fig. 4.5d). The simulations having their Min and Max values far from the central box not being very frequent, it is more likely to observe such simulations with larger sets of simulations. Also, the extreme cases depicted by the Min and Max simulations corresponding to worst cases (PKA and SKAs channelling) scenarios or best cases (PKA and SKAs shock very close neighbor atoms) scenarios, they contain important physical information. Indeed, the worst case scenario corresponds to a cascade going deep into the material with defects distributed all along the trajectories of the PKA and SKAs and the best case scenario depicts a cascade with a small but dense region of defects. To correctly sample the Min and Max cases, it is needed to resort to large sets of simulations.

The evolution of the error coefficient (SEM/μ) of the number of defects of Fig. 4.6 gives valuable information regarding the convergence of the sets. The error coefficient is very similar for

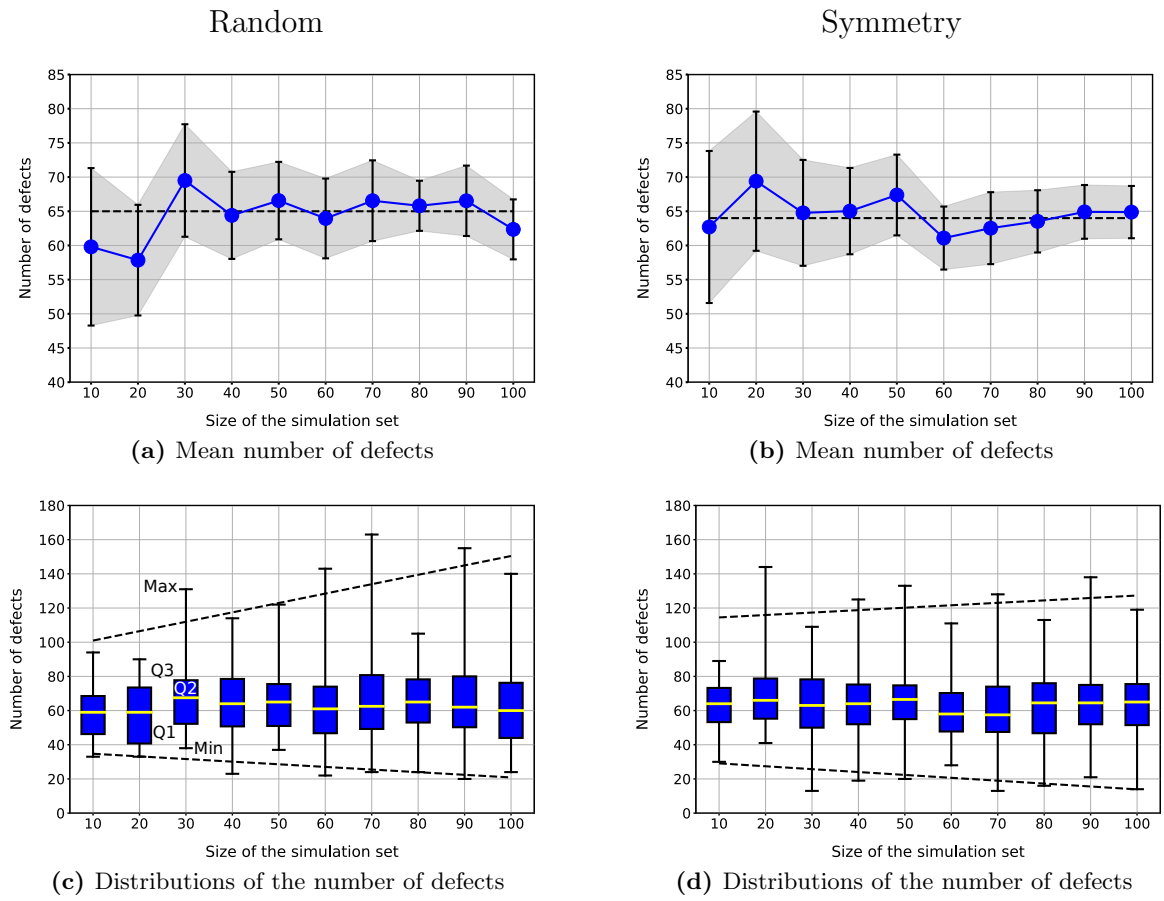

(a) Mean number of defects

(b) Mean number of defects

(c) Distributions of the number of defects

(d) Distributions of the number of defects

Figure 4.5: *Mean number of defects in the (a) Random and (b) Symmetry cases and box plots of the number of defects in the Random (c) and Symmetry (d) cases for 1 keV Si PKAs in Si with respect to the size of the simulation sets (i.e. the number of simulations in the sets). In (a) and (b), for each size of set, the error bars correspond to -1.96×SEM and 1.96×SEM. The probability that the real mean value sits within the error bars range is equal to 0.95. The region of the graphs delimited by the error bars of each set size is shaded. Solid blue lines are guides to the eye. In (a) and (b), dashed lines correspond to the mean values calculated with all the simulations performed, in each case (550). In (c) and (d), dashed lines represent linear regressions of the Min and Max values.*

both the Random and Symmetry cases and decreases from 0.09-0.10 to 0.03-0.04, with a faster decrease for smaller sets. Thus, the uncertainty in the calculation of the mean value decreases by a factor of about three when going from a set of size 10 to a set of size 100.

Considering the better stability of the box plots in the Symmetry case (Fig. 4.5d) than in the random case (Fig. 4.5c) and the good consistency of the mean values of Fig. 4.5b for large simulation sets, the Symmetry method appears to be more efficient than the Random one to make the number of defects converge for 1 keV cascades in Si. However, even with the Symmetry method, sets made of a minimum of 70 simulations need to be employed in order to stabilize both the mean values and distributions.

4.3.2.2 Convergence of the number of clusters for 1 keV PKAs in Si

Results provided in this section are obtained for PKAs of 1 keV in Si. The mean values of the number of clusters in the Random and Symmetry cases for PKAs of 1 keV in Si are respectively displayed in Fig. 4.7a and Fig. 4.7b. The box plots of the number of clusters in the Random

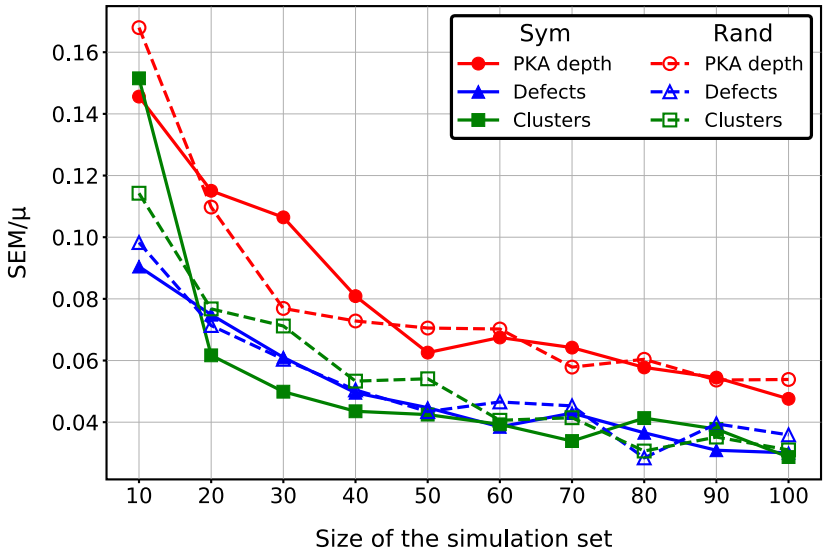

Figure 4.6: *Ratio of the Standard Error of the Mean SEM to the mean value μ of the number of defects, clusters and PKA penetration depth for collision cascades initiated by PKAs of 1 keV in Si in the Random (dashed lines) and Symmetry (full lines) cases with respect to the size of the simulation set. Lines are only guide to the eye.*

and Symmetry cases for PKAs of 1 keV in Si are respectively shown in Fig. 4.7c and Fig. 4.7d.

The variations in the mean number of clusters are more visible in the Random case (Fig. 4.7a) than in the Symmetry case (Fig. 4.7b): the mean number of clusters goes from 5.5 to 6.5 and from 6.0 to 6.5 respectively. The distributions of the Symmetry case of Fig. 4.7d show the striking feature of all having the same median value (6), eight out of ten sharing the same first quartile value (5) and the same third quartile value (7) for seven out of ten. In comparison the distributions of Fig. 4.7c show much less consistency, with median values ranging from 5 to 7 and only six out of ten showing the same median value of 6 for the Random case. Just like for the defects, the Min and Max value of the box plots are respectively smaller and greater for large sets than for small sets.

The evolution of the error coefficient for the number of clusters in Fig. 4.6 shows the same trend than for the previously commented error coefficient for the number of defects: it decreases quickly for low values of set size and slower and slower as the set size increases. It means that the accuracy in the calculation of the mean values of the number of clusters substantially increases with the size of the set increasing.

Considering the very consistent box plots for the number of clusters with the Symmetry method of Fig. 4.7d and the very small variations in the mean values of the number of clusters with the Symmetry method (Fig. 4.7b), this method eases the convergence, in terms of reproducibility, of the number of clusters compared to the Random one. The number of clusters appears to need a smaller set size to be already converged properly than the number of defects. From 60 simulations with the Symmetry method, for collision cascades of 1 keV in Si, the number of clusters already shows excellent stability in terms of distributions and mean values.

4.3.2.3 Convergence of the PKA depth for 1 keV PKAs in Si

Results provided within this section are obtained with 1 keV PKAs in Si. Fig. 4.8a and Fig. 4.8b respectively show the mean values of the penetration depth of 1 keV Si PKAs in Si in the Random

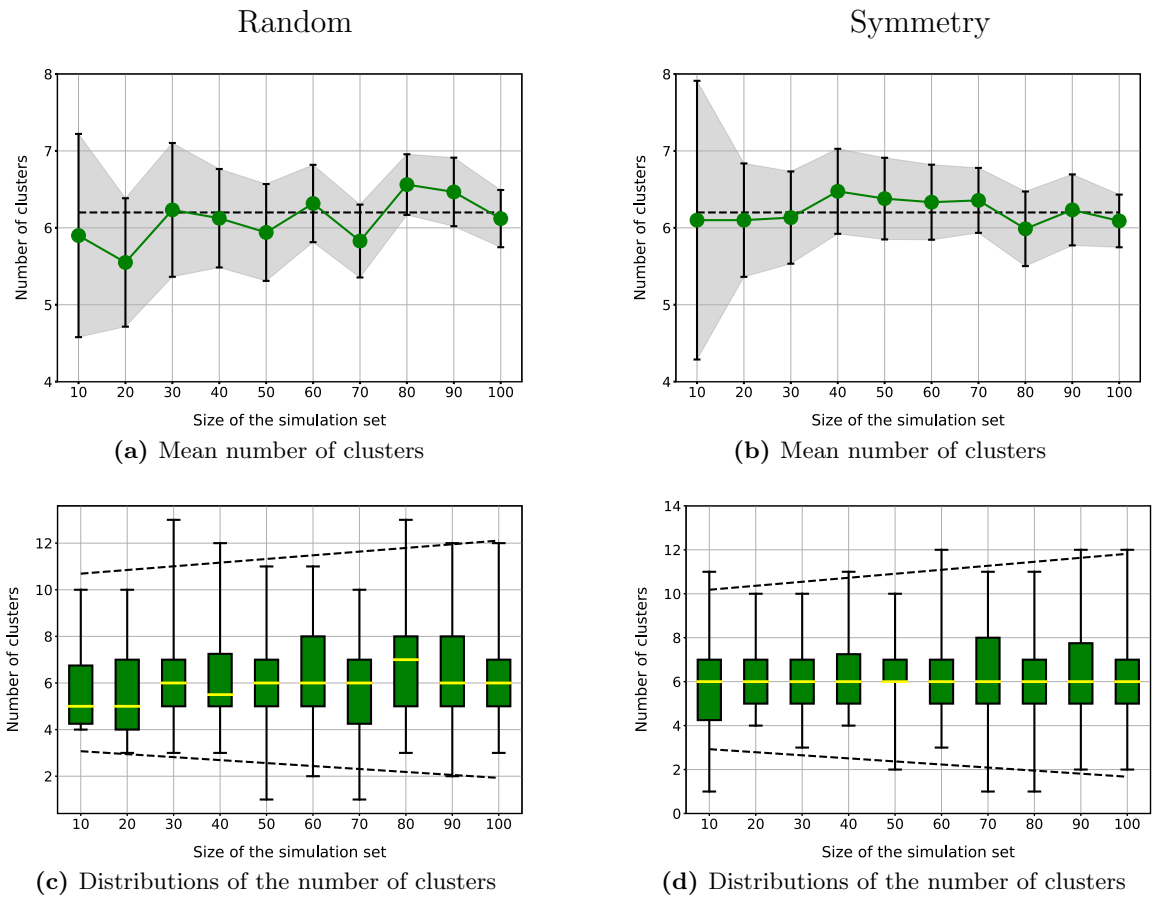

(a) Mean number of clusters

(b) Mean number of clusters

(c) Distributions of the number of clusters

(d) Distributions of the number of clusters

Figure 4.7: *Mean number of clusters in the (a) Random and (b) Symmetry cases and box plots of the number of defects in the Random (c) and Symmetry (d) cases for 1 keV Si PKAs in Si with respect to the size of the simulation sets (i.e. the number of simulations in the sets). In (a) and (b), for each size of set, the error bars correspond to -1.96×SEM and 1.96×SEM. The probability that the real mean value sits within the error bars range is equal to 0.95. The region of the graphs delimited by the error bars of each set size is shaded. Solid green lines are guides to the eye. In (a) and (b), dashed lines correspond to the mean values calculated with all the simulations performed, in each case (550). In (c) and (d), dashed lines represent linear regressions of the Min and Max values.*

and Symmetry cases with respect to the size of the simulation sets. Fig. 4.8c and Fig. 4.8d display the box plots of the PKA penetration depth in the Random and Symmetry cases respectively, with respect to the size of the simulation sets.

In the Random case, the mean values of Fig. 4.8a and distributions of Fig. 4.8c show significant variations up to set sizes of 50 simulations: mean values range from 22.6 Å to 33.4 Å. From 50 simulations, the mean values stabilize (but still show some discrepancies) between 24.1 Å and 28.5 Å and the distributions show a lot less variations.

In the Symmetry case, the mean values of Fig. 4.8b show great consistency for set sizes of 10 to 40. Within the same range the distributions of Fig. 4.8d also show remarkable stability for such small set sizes. However, this consistency in the results at small set sizes cannot be attributed to an early reproducibility of the results. Indeed, from 50 simulations, the mean values are all shifted up compared to the mean values obtained from smaller set sizes. The same happens for the distributions which are all shifted up. To us, this artifact of convergence observed for sets of 40 simulations and less results from the stochasticity of the cascades and is therefore

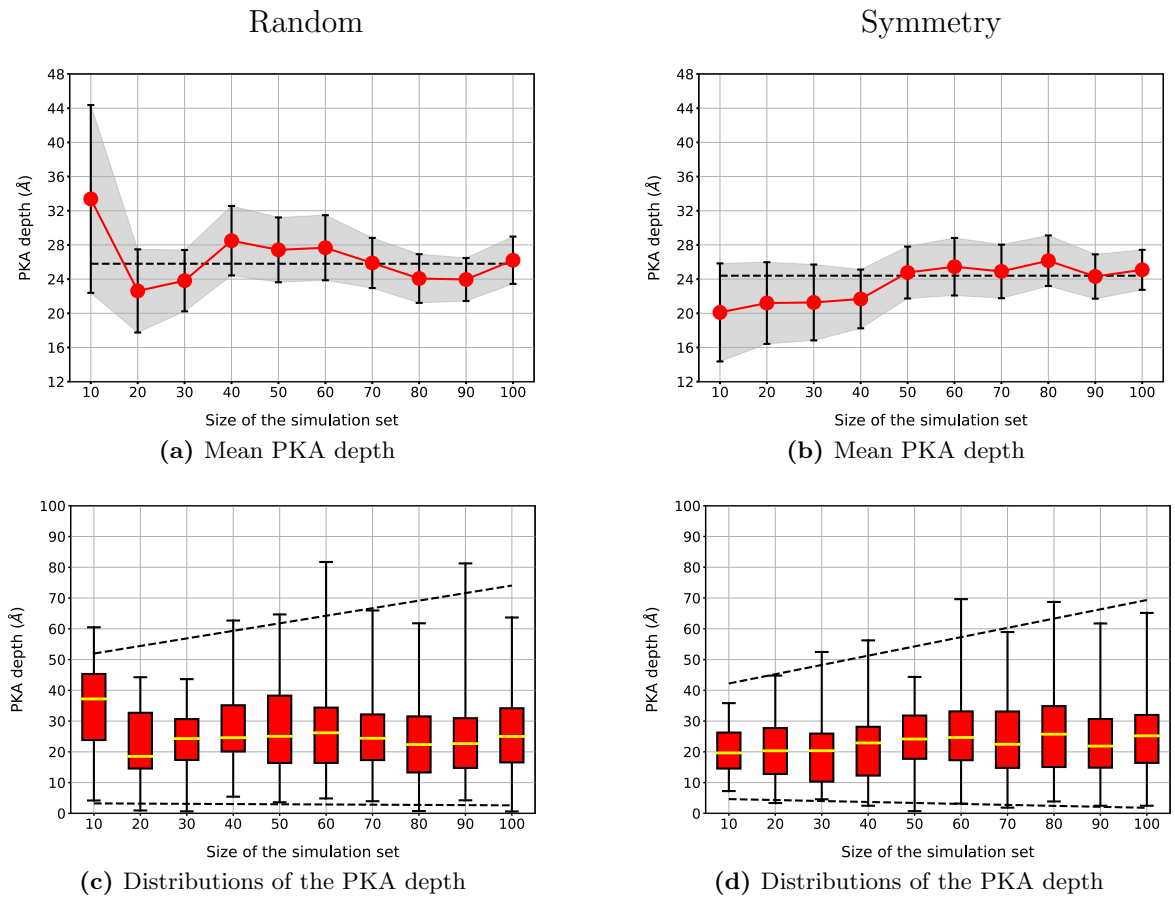

(a) Mean PKA depth

(b) Mean PKA depth

(c) Distributions of the PKA depth

(d) Distributions of the PKA depth

Figure 4.8: *Mean PKA depths in the (a) Random and (b) Symmetry cases and box plots of the number of defects in the Random (c) and Symmetry (d) cases for 1 keV Si PKAs in Si with respect to the size of the simulation sets (i.e. the number of simulations in the sets). In (a) and (b), for each size of set, the error bars correspond to -1.96×SEM and 1.96×SEM. The probability that the real mean value sits within the error bars range is equal to 0.95. The region of the graphs delimited by the error bars of each set size is shaded. Solid red lines are guides to the eye. In (a) and (b), dashed lines correspond to the mean values calculated with all the simulations performed, in each case (550). In (c) and (d), dashed lines represent linear regressions of the Min and Max values.*

coincidental. It also proves that assessing the reproducibility and thus the convergence of the results is not an easy task. From set sizes of 50 simulations, the mean values show excellent consistency: they are all comprised between 24.3 Å and 26.2 Å.

Concerning the box plots, the median values show some variations, but the overall shapes are consistent. This combined with the good stability of the mean values of Fig. 4.8b point towards the fact that reproducibility is attained. Also, once again, both in the Random and Symmetry case, the Min and Max value of the box plots are respectively smaller and greater for large sets than for small sets.

The analysis of Fig. 4.6, which displays the evolution of the error coefficient of all the properties of interest in the Random and Symmetry cases reveals that the error coefficient is comparable in the Symmetry and Random case. However, even if showing the same decrease rate, the error coefficient of the PKA depth (Fig. 4.6) is noticeably higher than the ones of the number of defects and clusters. It is approximately of 0.15 when the error coefficient for the other properties is around 0.10 (set size of 10) and of 0.05 when the error coefficient for the other

properties is around 0.03 (set size of 100). It reveals that the PKA penetration depth mean values are more subject to uncertainties and thus more difficult to converge than the number of clusters and defects: if one wants to reach an error coefficient of 0.06, about 30 simulations are needed for the number of clusters and defects whereas about 80 simulations are needed for the PKA penetration depth. Another argument in favor of this statement is the comparison of the mean values obtained with all the simulations performed in the Random and Symmetry cases (550 simulations in each case). To our knowledge, no collision cascades simulations mean values have ever been calculated on ensembles that large. For the number of defects we obtain 65 and 64 in the Random and Symmetry case respectively (see Fig. 4.5) and for the number of clusters 6.2 (see Fig. 4.7) in both cases. Those values, obtained with two completely independent sets of simulations, are very close and indicate excellent convergence for very large sets. In the case of the PKA depth, the mean values obtained are 25.8 Å and 24.4 Å in the Random and Symmetry case respectively (see Fig. 4.8). Even if close, the discrepancy between those two values is by far more important than for the number of defects and clusters. Even with sets as large as 550 simulations, the mean PKA depth values show some variations. Additionally to the reduced accuracy of the PKA depth property compared to the number of defects and of clusters observed in Fig. 4.6, PKA depth mean values are more difficult to reproduce even with very large sets.

Considering the box plots and mean values of Fig. 4.8, no method seems to provide with better convergence results than the other method. The mean values and distributions are stabilized from sets of size 70, even if the consistency is less obvious than with the number of defects or clusters. If the question of a compromise is not relevant for the number of clusters and defects as the error coefficient is already very low and the distributions and mean values stabilized for set sizes of 70 simulations and above for both properties, it is an interesting question for the PKA depth. Indeed, an error coefficient on the PKA depth of 0.04 is not even attainable with a set of 100 simulations. By choosing the number of simulations to be performed, one somehow chooses the accuracy of the mean values conclusions are built from.

On the whole, the analysis of the results of Fig. 4.5, Fig. 4.6, Fig. 4.7 and Fig. 4.8 allows us to draw some conclusions on the convergence of the outputs of cascades initiated with 1 keV PKAs in Si: *(i)* cascades results constructed from sets of made of less than 60 simulations show too much variations and too big error coefficients to draw conclusions, *(ii)* the results obtained with the Symmetry method are subject to less variations in both the mean values and distributions, especially for small set sizes, *(iii)* accuracy on the estimation of mean PKA depth values is reduced compared to the accuracy of estimated mean values of other properties. The production of defects and clusters being global effects, the distributions are well centered around their mean values (variation coefficient σ/μ about 0.3). As an illustration, a PKA in a channeling direction usually produces less defects than the mean (it loses more energy to the electrons through the TTM) but the production of the defects being global, *i.e.* also due to SKAs and other atoms, a large part of the cascade behaves "as usual". On the contrary, the PKA depth is drastically affected by a slight change in the PKA direction. The PKA depth distributions are therefore very dispersed (variation coefficient σ/μ about 0.5): the distributions tend to show more variations and the errors in the mean value (SEM/μ) greater than for the number of defects and clusters, *(iv)* Large sets are needed to correctly sample the Min and Max cases, *i.e.* the best and worst cases scenarios. Indeed, channeling and PKAs shocking very close atoms being "rare events", a large number of simulations are needed to observe a sufficient number of those events for the Min and Max values to be consistent between all the tested set sizes.

4.3.2.4 Convergence of collision cascades results with 5 keV PKAs in Si

Considering the results of sections Section 4.3.2.1, Section 4.3.2.2 and Section 4.3.2.3 which proved that the Symmetry method is more adequate, within this section, only the Symmetry method is employed. Fig. 4.9 shows the evolution of the error coefficient for all the properties studied in the Symmetry case for 1 keV and 5 keV PKAs. Fig. 4.10a, Fig. 4.10c and Fig. 4.10e respectively display the mean values of the number of defects, of the number of clusters and of the PKA penetration depth for cascades of 5 keV in Si. Fig. 4.10b, Fig. 4.10d and Fig. 4.10f respectively display the box plots of the number of defects, of the number of clusters and of the PKA penetration depth for cascades of 5 keV in Si.

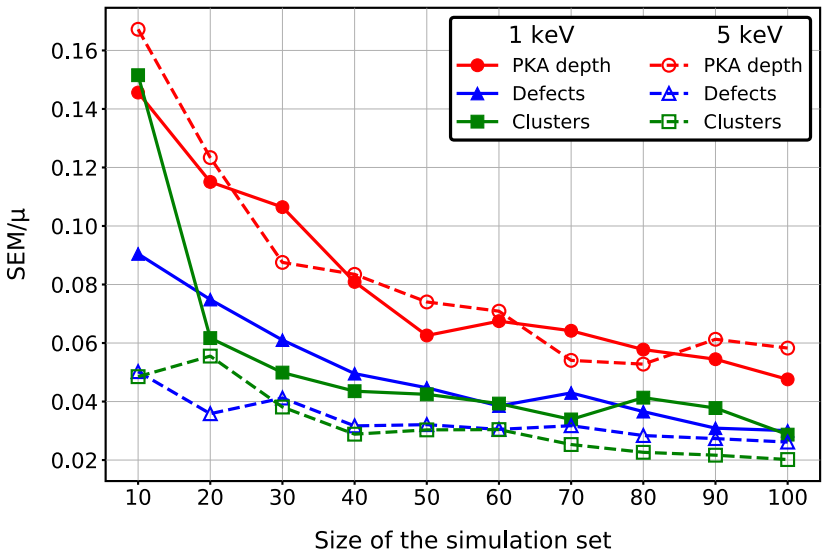

Figure 4.9: *Ratio of the Standard Error of the Mean (SEM) to the mean value μ of the number of defects, clusters and PKA penetration depth for collision cascades initiated by PKAs of 1 keV and 5 keV in Si with respect to the size of the simulation set. Lines are only guide to the eye.*

The mean numbers of defects of Fig. 4.10a show significant variations for set sizes up to 60: it ranges from 287 to 306 defects. For larger sets, the data still do not show clear sign of convergence: variations of about 3-5 defects between all adjacent mean values from 60 simulations in the sets to 100 simulations in the sets are observed. However, with respect to the number of defects at stake (around 300) the variations between each set size are in the order of 2% only: if no perfect consistency is reached, it does not jeopardize the interpretation of the results. The distributions of the defects in Fig. 4.10b show great consistency already from a set size of 60. It supports our thinking that the variations in the mean values of Fig. 4.10a are therefore not the result of a bad convergence but simply are due to slight variations in the distributions.

The evolution of the mean PKA penetration depth of Fig. 4.10e is very similar to the one of the mean number of defects commented above: strong variations for small set sizes, smaller variations but still no obvious convergence at larger set sizes. Just like in the case of the mean number of defects the variations are very small for set sizes above 70 (about 4% at most) and does not prejudice the interpretation of the results. Moreover, the range of the error bars is larger than the variations in the mean values, thus reducing the risk in the misinterpretation of the results. The distributions of the PKA depth of Fig. 4.10f show significant variations in the min, max, first quartile and third quartile values except for the sets of sizes 90 and 100 which are very similar. For all the set sizes the median values are very consistent and do not show large variations.

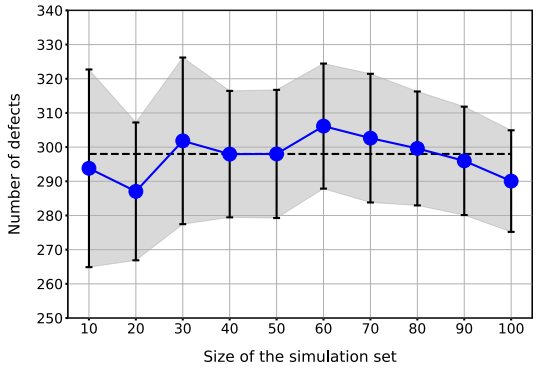

(a) Mean number of defects at the end of the collision cascades.

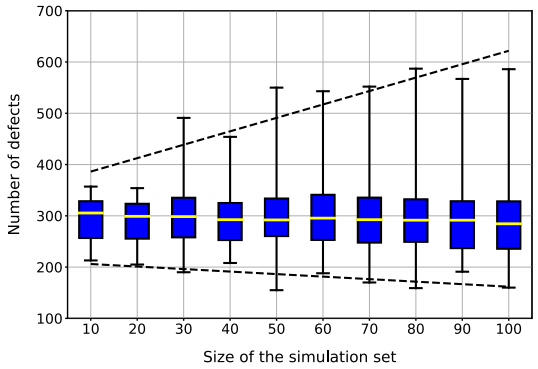

(b) Distributions of the number of defects at the end of the collision cascades.

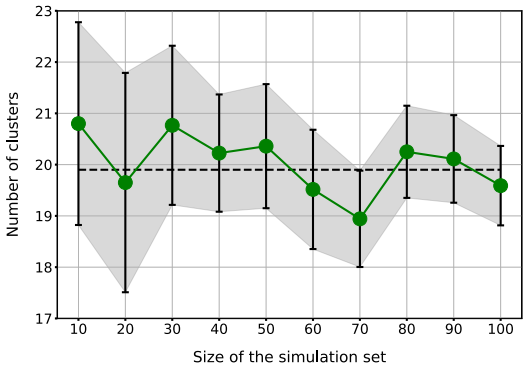

(c) Mean number of clusters at the end of the collision cascades.

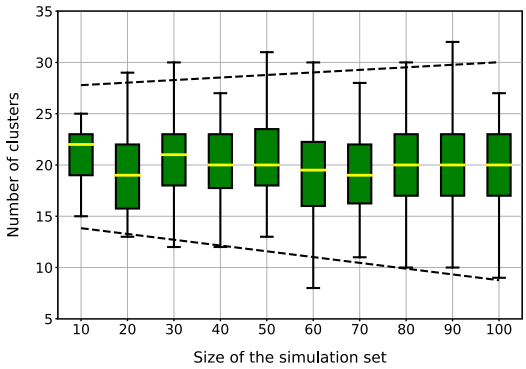

(d) Distributions of the number of clusters at the end of the collision cascades.

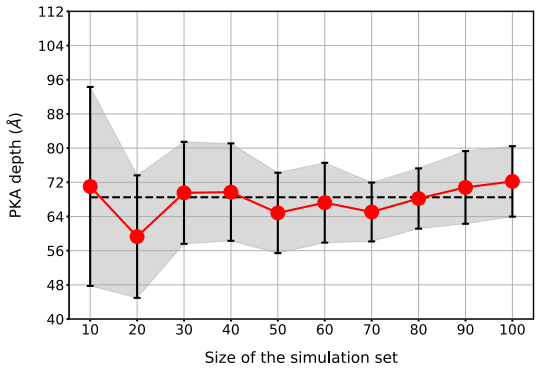

(e) Mean penetration depths attained during the cascades by the PKAs.

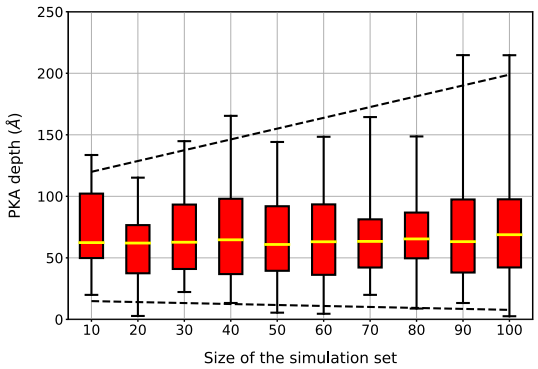

(f) Distributions of the penetration depths attained during the cascades by the PKAs.

Figure 4.10: *Mean (a) and box plots (b) of the number of defects, (c), (d) number of clusters and (e), (f) PKA penetration depth in collision cascades initiated by 5 keV Si PKAs in Si with respect to the size of the simulation set. For (a), (b) and (c), solid lines are guides to the eye. Dashed lines in (a), (c) and (e) correspond to the mean values obtained from all the simulations performed (550). Dashed lines in (b), (d) and (f) correspond to linear regressions of the Min and Max values.*

The evolution of the mean number of clusters of Fig. 4.10c shows small variations with mean values ranging from 19 to 21 clusters. The three last values (for set sizes of 80, 90 and 100) seem pretty well converged: the mean values are of 20.3, 20.0 and 19.6. The box plots of Fig. 4.10d show significant variations for small sizes of sets but great consistency for large set sizes (above 60 simulations per sets).

Table 4.3: *Mean values of the number of defects, number of clusters and PKA depth for 1 keV cascades in Si from sets of sizes 10 and 100. To asses the influence of the initial position of the PKA, both sites of the primitive diamond cell (see Fig. 4.4) are sampled twice: for each of the two sites, two initial positions are chosen in the simulation box. In parenthesis are given the SEM values.*

	PKA position	Mean defects	Mean clusters	Mean PKA depth (Å)
10 simulations	Site #1	63 (6)	6 (0.9)	20.1 (2.9)
	Site #1 bis	62 (5)	6 (0.6)	16.7 (2.0)
	Site #2	59 (5)	6 (0.6)	26.8 (4.4)
	Site #2 bis	60 (7)	5 (0.6)	28.7 (4.7)
100 simulations	Site #1	65 (2)	6 (0.2)	25.1 (1.2)
	Site #1 bis	63 (2)	6 (0.2)	25.9 (1.4)
	Site #2	64 (2)	6 (0.2)	24.4 (1.2)
	Site #2 bis	66 (2)	6 (0.2)	24.6 (1.2)

For all the properties investigated, the Min and Max values of the box plots (*i.e.* right column of Fig. 4.10) are respectively always smaller and greater with large sets of simulations than small sets of simulations. The Min and Max values appear to be consistent from 50 simulations for the number of defects, 60 simulations for the number of clusters and 90 simulations for the PKA depth. Again, it highlights that the PKA depth is harder to converge than the number of defects and number of clusters.

The error coefficient of the PKA depth of Fig. 4.9 are similar in the 1 keV and 5 keV cases: decrease from around 0.15 to approximately 0.05. However, the error coefficients of the number of defects and clusters in the 5 keV case are lower than in the 1 keV case.

On the whole, for 5 keV cascades in Si, it appears that: *(i)* stability in the distributions can be attained when no obvious stability in the mean values is reached, *(ii)* the mean values should always come with the SEM value in order not to misinterpret the results, *(iii)* reproducibility between the sets is harder to attain with 5 keV cascades than with 1 keV cascades.

4.3.2.5 Influence of the initial position of the PKA

After having studied the convergence of the number of defects and of clusters and of the PKA penetration depth for 1 keV and 5 keV PKAs in Si, one may ask if the initial position of the PKA has an influence. We seek to answer two questions in this section: *(i)* does the initial site of the PKA have an influence on the cascades outputs? *(ii)* do the two lattice sites of Fig. 4.4 need to be sampled with the Symmetry method? We highlight the fact that drawn conclusions of this part are only valid for mono-atomic materials in the diamond-like structure.

We ran four sets of 10 simulations and four sets of 100 simulations with 1 keV PKAs in Si with the Symmetry method. Four distinct initial PKA positions are sampled. The first two positions (named site #1 and site #1 bis) correspond to the first site of the primitive diamond cell (lower site of Fig. 4.4), the two other positions (named site #2 and site #2 bis) correspond to the second site of the primitive diamond cell (upper site of Fig. 4.4). Site #1 and Site #1 bis (respectively Site #2 and Site #2 bis) occupy the same site in their own primitive unit cell, but were chosen in the following simulation in different primitive cells. Table 4.3 displays the mean values of the number of defects, number of clusters and PKA depth for the sets of 10 and 100 simulations in the four sampled positions (Site #1, Site #1 bis, Site #2 and Site #2 bis).

Considering the four sets made of 10 simulations, the mean number of defects and clusters are coherent between all the sampled PKA positions: the mean number of defects ranges from 59 to 63 and the mean number of clusters from 5 to 6. However, the SEM values are quite large (expected knowing the error coefficient graph of Fig. 4.6) which reveals the mean values suffer from big uncertainties. The most striking feature is the significant variations in the mean PKA depth. It ranges from 16.7 Å to 28.7 Å. The initial PKA position has a drastic influence on the mean PKA depth. Moreover, it appears that the primitive cell site on which the PKA is initially located plays an important role: mean PKA depth of 16.7 Å and 20.1 Å for sites #1 and of 26.8 Å and 28.7 Å for sites #2.

Considering the four sets made of 100 simulations, the mean number of defects and clusters and, contrary to the sets of size 10, the mean PKA depth show excellent coherence between the four PKA positions sampled: the mean number of defects ranges from 63 to 66, the mean number of clusters is equal to 6 for all the simulations and the mean PKA depth ranges from 24.4 Å to 25.9 Å. The large variations observed with sets of size 10 disappear with sets of 100 simulations. The site of the primitive cell of the diamond structure does not influence the results as it does with sets of size 10. The SEM values are also a lot smaller than in the 10 simulations cases and show great consistency. Therefore, with sets of size 100, the influence of the initial position of the PKA is not an issue anymore.

4.3.3 Conclusions of the convergence study

The present study is the result of more than 2 000 MD simulations of collision cascades in Si. We find that a method based on symmetry considerations for the determination of the initial directions of the PKA improves the convergence and the consistency of the results in Si. It is also shown that in Si, it is harder to converge the PKA penetration depth than the number of defects and clusters. To obtain satisfactory convergence of the PKA depth and of the mean number of defects and clusters in Si, sets of simulations made of at least 70 simulations are needed even for PKA energies as low as 1 keV. At 5 keV, convergence as satisfactory as what is obtained at 1 keV is not yet obtained with sets of 100 simulations but the consistency of the results is enough to be able to draw meaningful conclusions on the data obtained with sets of around 80 simulations. It appears that the higher the energy of the PKAs, the bigger the sets must be. The simulations corresponding to best case and worst case scenarios being consistent between the size of sets starting from 60 simulations for 1 keV PKAs and 80 simulations for 5 keV PKAs in Si, large sets are also necessary to correctly sample the range of possible scenarios. Additionally, the initial position of the PKA is not found to have any influence on the results, at least at 1 keV, if the simulation sets are large enough. Finally, taking as example 1 keV and 5 keV PKAs in Si, more than only providing with a method to cope with the stochasticity of the cascades, this section proves the need to treat the data related to cascades in a statistically rigorous way: a convergence study is mandatory, even if only to assess the level of precision and trustworthiness of the study, the mean values should always come with the SEM value and the distributions be graphically represented. In the rest of the manuscript, we will always resort to graphical representations and rigorous statistical treatment of the data.

Conclusion

The properties of interest of the collision cascades as well as the statistical indicators we employ are now clearly defined. The Lindemann and Wigner-Seitz methods for counting defects have been presented and compared on two sets of 100 simulations, one in Si and one in Ge. Both methods have been found to scale really well in spite of very different absolute numbers of defects, in agreement with the published studies on the subject. In the rest of the manuscript, unless said otherwise, we will employ the Lindemann spheres method. In this chapter was also presented a

detailed convergence study of the number of defects, number of clusters and PKA penetration depth in Si, with respect to the number of simulations performed and to the method chosen for setting the initial directions of the PKAs. It was found that the convergence is improved with a method based on the Symmetry for defining the initial PKA directions, but that ensuring the convergence of the cascades properties, even at low energies, is far from being trivial. The most important conclusion of this study is that to avoid drawing conclusions from biased results, large number of simulations must be performed and an explicit and rigorous statistical treatment of the results has to be carried out.

References

[1] J. F. Ziegler, M. D. Ziegler, and J. P. Biersack, "SRIM - The stopping and range of ions in matter (2010)", Nucl. Instr. Meth. Phys. R. B **268**, 1818–1823 (2010).

[2] H. Hensel and H. M. Urbassek, "Implantation and damage under low-energy Si self-bombardment", Phys. Rev. B **57**, 4756 (1998).

[3] J. B. Gibson, A. N. Goland, M. Milgram, and G. H. Vineyard, "Dynamics of Radiation Damage", Phys. Rev. Jour. Arch. **120**, 1229–1253 (1960).

[4] K. Nordlund, M. Ghaly, R. S. Averback, M. Caturla, T. Diaz de la Rubia, and J. Tarus, "Defect production in collision cascades in elemental semiconductors and fcc metals", Phys. Rev. B **57**, 7556–7570 (1998).

[5] W. D. Luedtke and U. Landman, "Preparation, structure, dynamics, and energetics of amorphous silicon: A molecular-dynamics study", Phys. Rev. B **40**, 1164–1174 (1989).

[6] A. Stukowski, "Visualization and analysis of atomistic simulation data with OVITO - the Open Visualization Tool", Mod. Sim. Mat. Sci. Eng. **18**, 015012 (2010).

[7] P. Lopez, L. Pelaz, I. Santos, L. A. Marques, and M. Aboy, "Molecular dynamics simulations of damage production by thermal spikes in Ge", J. App. Phys. **111**, 033519 (2012).

[8] A. Jay, M. Raine, N. Richard, N. Mousseau, V. Goiffon, A. Hémeryck, and P. Magnan, "Simulation of Single Particle Displacement Damage in Silicon–Part II: Generation and Long-Time Relaxation of Damage Structure", IEEE Trans. Nucl. Sc. **64**, 141–148 (2017).

[9] T. Jarrin, A. Jay, N. Richard, and A. Hémeryck, "Coping with the stochasticity of collision cascades in Molecular Dynamics simulations", Nucl. Instr. Meth. Phys. R. B **500-501**, 1–9 (2021).

[10] F. H. Stillinger and T. A. Weber, "Computer simulation of local order in condensed phases of silicon", Phys. Rev. B **31**, 5262–5271 (1985).

Influence of electronic effects into collision cascades

5

Contents

Introduction

Among the improvements possibilities in the methodology of the simulation of collision cascades with MD, the inclusion of electronic effects is a very relevant aspect to be interested in. Indeed, the effects of the electrons in collision cascades are still not well understood, and the magnitude of the influence of the models employed on the results of collision cascades MD simulations are not very well known. The most widely employed model for the inclusion of electronic effects certainly is the TTM [1], which we present in detail in Chapter 3. However, very few studies have been entirely dedicated to a systematic study of the effects of the TTM parameters on collision cascades: Khara *et al.* studied in [2] the effects of the electronic specific heat C_e on SHI irradiation in Si, Zarkadoula *et al.* explored in [3] the effects of electron-phonon coupling in Ni and NiFe. Additionally, in W, Cui *et al.* studied in [4] the impact of electronic stopping power and Sand *et al.* explored in [5] and [6] the effects of the velocity threshold v_0 on the production of defects with models similar to the TTM. Those studies give interesting insights into the effects of some TTM parameters, but no extensive statistical study considering large enough number of simulations to overcome the high stochasticity of the cascades has been dedicated to the investigation of the impact of the TTM parameters on collision cascades, especially in semiconducting materials. Moreover, the physical accuracy of the TTM is being questioned by some published studies proposing to modify the basic equations of the TTM or to add parameters. For example, in [4], Cui *et al.* added a velocity threshold v_{th} parameter in addition to the already existing v_0 to switch off the effects of the γ_p parameter in the friction force above v_{th}. Also, Zarkadoula *et al.* demonstrated in [3] the need to add the t_{eph} parameter we present in Chapter 3, which is initially not present in the original version of the TTM by Duffy and Rutherford [1]. This last parameter is now widely employed in the community [**Darkins:2018**, 4, 7, 8]. Consequently to those uncertainties related to the TTM, some even choose not to include the effects of the electronic stopping power in their simulations as they do not judge the available models as being satisfactory enough [9]. A probable reason for this, as far as the TTM is concerned, may be the lack of reliable experimental or theoretical values and the uncertainty in the methods to determine some TTM parameters in even simple materials which can compel to make choices by default without always having a clear view on the implications. To clarify all this, a study on the effects of the different TTM parameters on the collision cascades results would be very valuable. This is what we intend to do in Section 5.1, where we investigate the effects of the parameters of the TTM in Si and Ge. Those two materials having very distinct responses to collision cascades [10, 11], the influence of the TTM on those two materials is expected to be different and thus to provide lots of information. We employ the version of the TTM we describe in Chapter 3, *i.e.* the original one of Duffy and Rutherford augmented with the t_{eph} parameter.

The EPH model [12–14], which we also present in detail in Chapter 3, was developed in 2019 to try to correct some of the issues related to the TTM. As a reminder, the main TTM limitations the EPH model circumvents are the constant density approximation and the electron-phonon coupling incorporation. Aiming at testing different state-of-the-art methods in this thesis, the present chapter also incorporates in Section 5.2.3 a comparative study of the influence of the EPH model and the TTM on collision cascades results in Si. The EPH model theoretically allows to incorporate electronic effects into MD calculations with the accuracy of *ab initio* methods. Consequently, the use of the EPH model requires to resort to TDDFT (ED to be more precise) calculations of electronic stopping in Si. The optimization process of the EPH model parameters thus compels to construct a solid methodology and to study the fundamental electronic mechanisms of the materials under investigation. With the purpose of being exhaustive on the subject of the EPH model for collision cascades simulations, and on top of that because this is the very first time the EPH model is employed on realistic cases to our knowledge, apart from the study part of the original paper of the TTM [14], we detail the procedure we followed

and the electronic stopping calculations results we obtain for the parametrization of the EPH model. Also, we want to emphasize the fact that, more than being used only to parametrize the EPH model, the TDDFT calculations we perform give interesting insights on the stopping power in semiconducting materials. Thus, Section 5.2.1 is entirely dedicated to the calculation of electronic stopping powers in Si using the TDDFT QB@LL code [15, 16] and Section 5.2.2 to the optimization of the EPH model parameters to reproduce TDDFT data and to an in depth comparison between the EPH model and the TTM with the purpose of highlighting the capabilities and limitations of each model.

5.1 Parametric study of the Two-Temperature Model

This section is taken with some adaptations from our published article on the subject [17].

5.1.1 Computational details

To initiate the collision cascade, the PKA is given a velocity corresponding to 10 keV and a certain direction. It collides other atoms on its path, creating SKAs, which displace other atoms from their equilibrium positions as well. 100 simulations per set of TTM parameters investigated are carried out. Each simulation is initiated by a distinct PKA direction, chosen following the method based on the symmetry of the structure presented in Chapter 4.

The TTM-MD simulations have been run using the LAMMPS code [18]. Boxes of 1 000 000 atoms made of 50×50×50 cubic diamond unit cells are employed in most directions, but for some channelling PKAs directions, boxes of 4 096 000 atoms made of 80×80×80 cubic diamond unit cells are necessary. The simulation box is divided into two areas: the outer cells (1 unit cell of width, *i.e* 5.431 Å) form an NVT ensemble in which the atomic displacements are controlled by a Langevin thermostat (damping time of 0.1 ps) to maintain the temperature at a desired value, and the inner cells form an NVE ensemble in which the atoms evolve freely to simulate the collision cascade.

The initialization of the simulation is made by scaling the velocities of all atoms, such that the overall temperature is the desired one, 100 K in the current work. The system is equilibrated during 20 ps with a timestep of 1 fs.

The maximum velocity of the atoms drastically changes between each step of the cascade: fast during the collision part, and slower during the thermal wave and recrystallization part [19]. Consequently, it is possible to decrease the precision of the integration timestep in parallel of the velocities, while maintaining a displacement lower than 0.025 Å between two steps. In the present work, running 10 keV simulations with Si and Ge on 300 ps, the typical timesteps are: 0.01 fs during 2 ps, then 0.1 fs from 2 ps to 20 ps, and finally 1 fs between 20 ps and 300 ps.

The SW [20] potentials augmented with the ZBL potential [21] presented in Chapter 3 are employed for the simulations both in Si and Ge. We recall that for Si, the SW potential employed is the one developed in [20], and for Ge the one parametrized in [22] with the slight modifications made in [10]. The fitting procedure and parameters of the SW and ZBL potentials are explained in Chapter 3.

Thermal properties both for the Si and the Ge potential, which are of prime importance in this study, are presented and compared to experimental values in Table 5.1. The values are the ones reported by Lopez *et al.* in [11]. The thermal properties of the SW potentials used for Si and Ge are not modified by the changes in the repulsive region. The melting temperatures show great consistency with experimental values. Simulated thermal conductivities are overestimated both

for Si and Ge, but the ratio, important for discussion, between κ_{Si} and κ_{Ge} in the experimental and simulated case is conserved. Thus, despite the discrepancies between the experimental and simulated values, the qualitative observations are not jeopardized.

Table 5.1: *Experimental (Expt.) and simulated (Simu.) values of the melting temperatures T_m and thermal conductivities κ (at 500 K) with the employed potentials for Si [20] and Ge [10, 22]. The values displayed are the ones reported in [11].*

	Si		Ge	
	Expt.	Simu.	Expt.	Simu.
T_m (K)	1685	1653	1211	1211
κ (W/cm/K)	0.78	1.74	0.33	0.72

5.1.2 Methodology

To investigate the effects of the TTM parameters on Si and Ge, 100 simulations are performed for each TTM parameterization. For a better understanding, each case is given a "scenario" name:

- The **Reference (Ref)** scenario refers to a case where the default γ settings defined in Chapter 3 are employed ($\gamma_p = 24.4$ g/mol/ps for Si and Ge, $\gamma_s = 39.4$ g/mol/ps for Si and $\gamma_s = 31.6$ g/mol/ps for Ge) with a C_e varying as shown in Fig. 3.12 of Chapter 3. The threshold v_0 is set to 79.8 Å/ps for Si and 45.2 Å/ps for Ge (*i.e.* the velocity corresponding to twice the cohesive energy of each material). We recall that in the TTM implementation of LAMMPS, C_e is left free for the user to be defined but not κ_e. However, it works internally with the relation $\kappa_e = \rho D_e C_e$ [23], with the electronic diffusivity D_e and the electronic density ρ compelled to be defined constant by the user. κ_e thus follows the same evolution than C_e. In the work we conduct, $D_e = 20000$ Å^2 and $\rho = 0.05$ e$^-$/Å^3 [23], which fully defines κ_e. This scenario is considered to be the baseline scenario to which all the others are compared.

- The **electronic friction (El-Fr)** scenario corresponds to a Ref scenario where γ_s is set to 100.0 g/mol/ps.

- The **electron-phonon (El-Ph)** scenario corresponds to a Ref scenario where γ_p is set to 100.0 g/mol/ps.

- The **High $\mathbf{C_e}/\boldsymbol{\kappa_e}$** scenario corresponds to a Ref scenario where C_e is set constant and equal to the high T asymptotic value of $3/2 k_B$. Following $\kappa_e = \rho D_e C_e$, it also corresponds to a scenario with a high T asymptotic value for κ_e, hence the name of the scenario.

- The **Low $\mathbf{C_e}/\boldsymbol{\kappa_e}$** scenario corresponds to a Ref scenario where C_e is set constant and equal to a low value of 10^{-6} eV/K. Following $\kappa_e = \rho D_e C_e$, it also corresponds to a scenario with a low value for κ_e, hence the name of the scenario.

- The **Low $\mathbf{v_0}$** scenario corresponds to a Reference scenario where v_0 is set to the velocity corresponding to once the cohesive energy, *i.e.* 56.4 Å/ps for Si and 32.1 Å/ps for Ge.

- The **phonon (PH)** keyword might be written next to the Ref (*i.e.* Ref (PH)), Low C_e/κ_e and High C_e/κ_e scenario names. It means the t_{eph} parameter is switched on to the value of 0.25 ps.

To rightfully compare the electron-phonon and electronic friction scenarios, the sum γ_i of γ_s and γ_p is kept constant between the two scenarios. Thus, when γ_p is equal to 100 g/mol/ps, γ_s is set to the default value of γ_p equal to 24.4 g/mol/ps. Therefore, $\gamma_i = \gamma_s + \gamma_p$ is always equal to 124.4 g/mol/ps for the El-Fr and El-Ph scenarios, for both Si and Ge materials. For the Ref, Ref (PH), El-Fr and El-Ph scenarios, the properties investigated in the cascade are the PKA penetration depth, the number of defects at the end of the cascade, the number of clusters, and the maximum electronic temperature. For the High C_e/κ_e, High C_e/κ_e (PH), Low C_e/κ_e, Low C_e/κ_e (PH) and Low v_0 scenarios, the number of defects at the end of the cascades and the maximum electronic temperature are investigated. Indeed, it was not judged relevant to compare the PKA depth observed in those scenarios because C_e, κ_e and v_0 have no friction effect on the moving ions. In this study, we employ the Lindemann criterion technique [24] for counting defects, as defined in the previous chapter.

5.1.3 Collision cascades results

The mean values of the investigated parameters for each simulation scenario are displayed in Table 5.2. This table also serves as a summary of the parameters employed in the different scenarios.

Table 5.2: *Mean values of the PKA depth, of the number of defects at the end of the cascade, and of the maximum electronic temperature attained. Average obtained over 100 simulations for all the scenarios considered. In parenthesis are given the standard errors of the mean. E_{coh} corresponds to the cohesive energy and m to the mass.*

		C_e as in Fig. 3.12		High γ_s	High γ_p	$C_e \approx 0$		$C_e = 3/2 k_B$		$v_0 = \sqrt{2 \times E_{coh}/m}$
	El-Ph coupling	Always	After 0.25 ps	Always	Always	Always	After 0.25 ps	Always	After 0.25 ps	Always
	Scenario name	Ref	Ref (PH)	El-Fr	El-Ph	Low C_e	Low C_e (PH)	High C_e	High C_e (PH)	Low v_0
Si	PKA depth (Å)	145 (8)		120 (5)	114 (5)					
	Defects	602 (10)	620 (11)	390 (9)	410 (8)	699 (14)	676 (14)	618 (12)	614 (9)	624 (13)
	Max T_{elec} (K)	7439	7525	11619	11152	121548	150594	4905	4812	7477
Ge	PKA depth (Å)	70 (5)		59 (3)	62 (3)					
	Defects	2361 (58)	2396 (61)	1569 (44)	1338 (33)	2625 (63)	2643 (61)	2191 (53)	2075 (49)	2372 (58)
	Max T_{elec} (K)	3875	3691	5584	5932	78121	83638	1768	1777	3690

5.1.3.1 Production of damage and PKA penetration depth in the El-Fr and El-Ph scenarios

In this section, the results of the El-Fr and El-Ph scenarios are compared to the Ref one in order to evaluate the impact of γ_s and γ_p. The mean numbers of defects observed at the end of the simulations are given in Table 5.2, and their distributions in Fig. 5.1a and Fig. 5.1b. According to Table 5.2, this number in Si (resp. in Ge) decreases from 602 (resp. 2361) for the Ref case, to 390 (resp. 1569) in the electronic friction scenario and 410 (resp. 1338) in the electron-phonon scenario. In the same way, Fig. 5.1a and Fig. 5.1b exhibit a drastic decrease of the number of defects when each of the two γ parameters increase. This implies that the γ parameters play a fundamental role in the reduction of the number of final defects. However, while γ_s and γ_p seem to have the same influence on the reduction of the number of defects in Si ($390 \approx 410$), this reduction is enhanced in the electron-phonon scenario in Ge ($1569 > 1338$).

The mean penetration depth of the PKAs is given in Table 5.2, and their distributions in Fig. 5.1c and Fig. 5.1d. A slight downward shift can be spotted in the PKA depths distributions of Fig. 5.1c and Fig. 5.1d. The mean PKA depth values of Table 5.2 are lower for the γ scenarios both in Si and Ge. The differences in the mean PKA depths of Table 5.2 are greater for Si (25 Å between the Ref and El-Fr scenarios and 31 Å between the Ref and El-Ph scenarios), compared to Ge (11 Å between the Ref and El-Fr scenarios and 8 Å between the Ref and El-Ph scenarios). Those results are physically sounded as the PKAs suffer more stopping in the γ scenarios than in the Ref scenario. However, as we have seen in Chapter 4, the PKA depth is a property harder

to converge than others, and the results presented should be considered with care even if they are consistent with what we expect.

More obvious than the change in the mean values, a clear reduction in the maximum PKA depth when moving to the electronic stopping and electron-phonon scenarios is observed in Fig. 5.1. The reason is that the maximum PKA penetration depths are observed when the PKA is in a channeling direction where very small amount of energy is lost through collisions. In these specific directions, the PKA is then more subject to the influence of the TTM. Trends in the PKA depth start to appear with 10 keV PKAs, but the γ parameters are expected to have an important role in the penetration depth at higher energies.

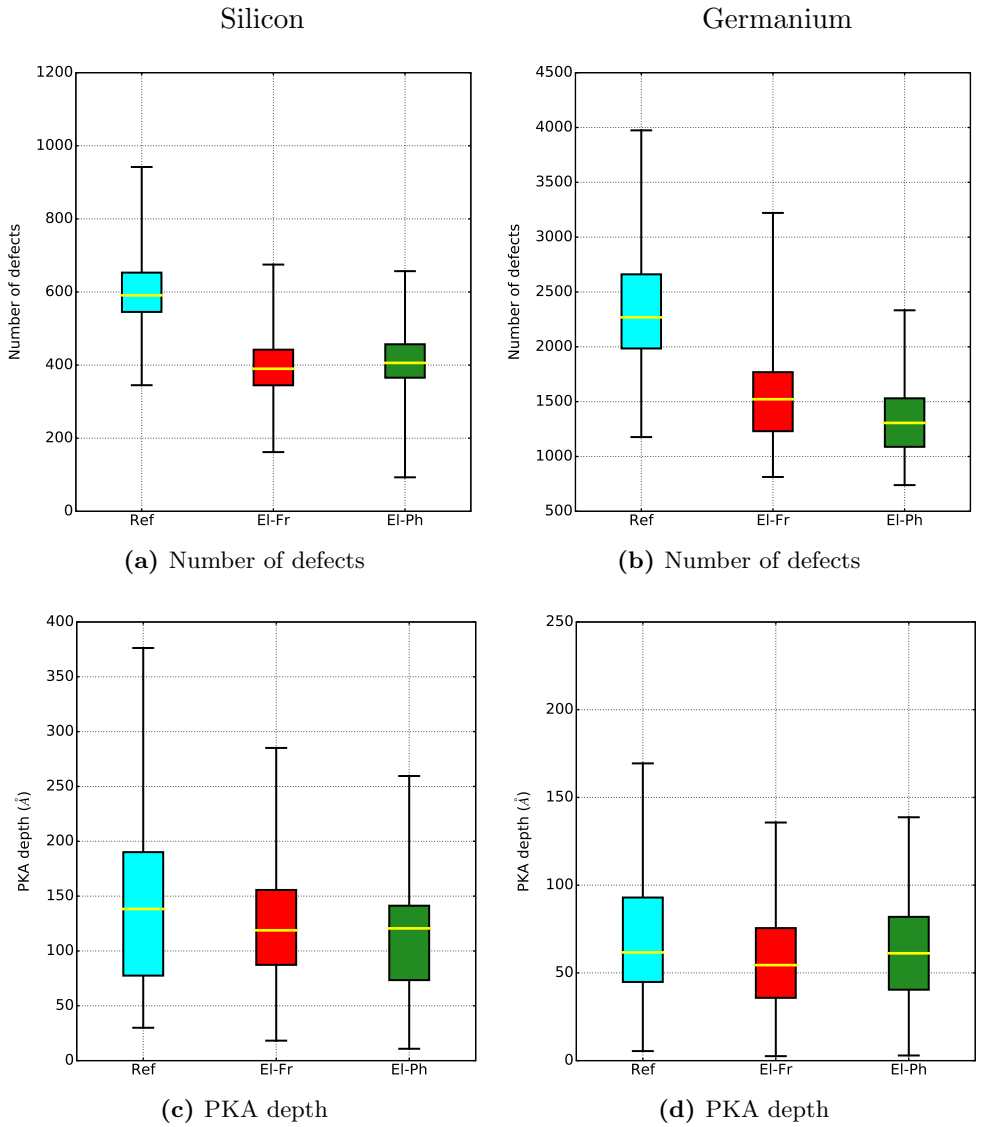

(a) Number of defects **(b)** Number of defects

(c) PKA depth **(d)** PKA depth

Figure 5.1: *Box plots of the number of defects after 300 ps of MD simulations time for the Ref and γ scenarios in Si (a) and Ge (b). Box plots of the PKA penetration depths for the Ref and γ scenarios in Si (c) and Ge (d). The lowest horizontal black bars correspond to the first quartile values (Q1), the middle ones to the median values (Q2) and the third ones to the third quartiles values (Q3). The two black vertical bars below and above each box represent the minimum (Min.) and maximum (Max.) values of the datasets. These box plots are constructed from 100 simulations per scenario.*

5.1.3.2 Damage production in the Ref, Low C_e/κ_e and High C_e/κ_e scenarios

The mean number of defects that were obtained with the Ref, Low and High C_e/κ_e scenarios are given in Table 5.2 and the associated distributions are displayed in Fig. 5.2a for Si and Fig. 5.2b for Ge. There is a clear downward shift of the entire defects distributions in Fig. 5.2a and Fig. 5.2b from the Low C_e/κ_e to Ref scenarios for Si and Ge. In Ge, the number of defects decreases again from the Ref to the High C_e/κ_e scenario. On the contrary in Si, no difference is visible between the Ref and High C_e/κ_e scenarios. Following Table 5.2, in Si (resp. Ge), the mean number of defects decreases from 699 (resp. 2625) in the Low C_e/κ_e scenario to 618 (resp. 2191) in the High C_e/κ_e scenario. The mean number of defects calculated in the Ref scenario lies exactly between the two extreme scenarios for Ge whereas it lies at the same level as the High C_e scenario in Si. The effects of C_e are therefore more important in Ge than in Si.

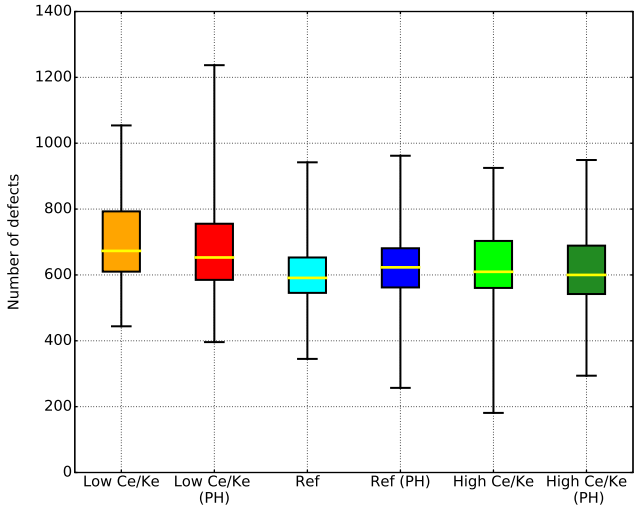

(a) Silicon

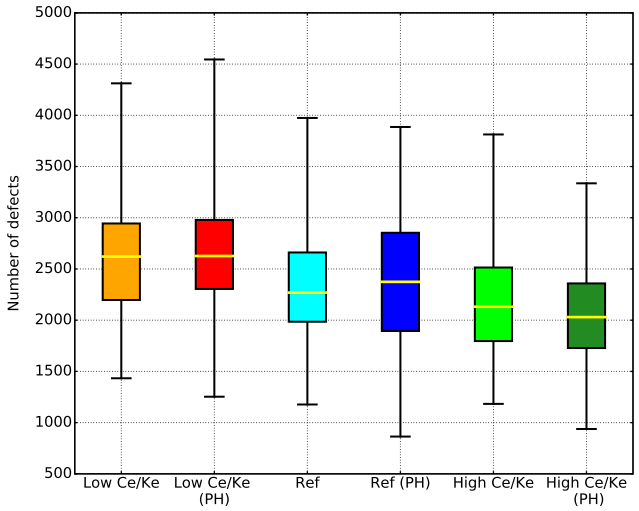

(b) Germanium

Figure 5.2: *Box plots of the number of defects in Si and Ge after 300 ps of MD simulations for different C_e/κ_e scenarios. Results are provided based on 100 simulations per scenario.*

5.1.3.3 Influence of v_0 on the number of defects

The impact of a change in v_0 between the two most recommended rules (*i.e.* one time the cohesive energy [8, 19] for the Low v_0 scenario or two times the cohesive energy [25] for the Ref scenario) to set it is investigated. The mean number of defects that were obtained with the Reference and Low v_0 scenarios are displayed in Table 5.2. In Si, there is only a discrepancy of 22 defects between the Ref (602) and Low v_0 (624) scenarios whereas the SEM is of 10 and 13 respectively. In Ge, the discrepancy is of 11 defects (2361 for the Ref scenario and 2372 for the Low v_0 scenario) and the SEM is of 58 in each case. Thus, there is not any difference between the Ref and the Low v_0 scenarios at the considered energies of 10 keV.

5.1.3.4 Influence of t_{eph} on the number of defects

The effect that t_{eph} has on the previously observed trends is investigated here. Table 5.2 gives the mean values of the number of defects for the C_e/κ_e scenarios with and without t_{eph} and Fig. 5.2a and Fig. 5.2b the global distributions. According to Table 5.2, the differences in the mean values of defects between the C_e/κ_e scenarios with or without t_{eph} are at most 25 defects in Si. In Ge, the differences are less than 50 defects for the Ref and Low C_e/κ_e scenarios whereas it is a bit higher, 120 defects, for the High C_e scenario. Considering the global distributions of Fig. 5.2a in Si for the same C_e scenarios with or without t_{eph}, the differences are too small to identify a trend. In Ge, no difference is visible with or without t_{eph} in the global distributions of Fig. 5.2b except for the High C_e/κ_e (phonon) scenario which seems to have undergone a slight decrease compared to the High C_e/κ_e (without t_{eph}) scenario. On the whole, the hierarchy between the C_e/κ_e scenarios in terms of number of defects is unchanged and the differences observed with the use of t_{eph} are so small that t_{eph} does not seem to play any role.

5.1.4 Discussions

Three main experimental trends are confirmed by the TTM-MD simulations:

- Experimental studies show that a lot more defects are observed in Ge than in Si [26, 27]. Those trends are confirmed by our own simulations in which in the Ref scenario there are in average about 300% more defects in Ge (Fig. 5.1b) than in Si (Fig. 5.1a).
- Experiments have shown that the penetration depth of various ions is higher in Si than in Ge [28]. Our simulations confirm that self PKAs penetrate always deeper in Si (Fig. 5.1c) than in Ge (Fig. 5.1d).
- It was also shown experimentally that amorphous regions are preferentially formed in Si-Ge alloys and in pure Ge than in pure Si [27]. Our simulations tend to confirm this phenomenon. In Table 5.3 is displayed the distribution of the defects inside the clusters depending on the cluster sizes for both Si and Ge in the Ref scenarios. It is found that there are less clusters of defects in Ge (mean value of 21 in Ge compared to 34 in Si) and that the vast majority of defects in Ge are contained within very large amorphous pockets of defects. On the contrary, in Si, the clusters formed are of much smaller size which indicates they are not part of large amorphous pockets.

Heat spikes, or thermal spikes, image the local melting of a material under the effect of elastic and inelastic interactions between an incoming energetic particle and the atoms of the target material. The hot liquid zones which are formed during a thermal spike may form amorphous regions when they cool down. MD simulations have helped understanding that the heat spike mechanism is the leading mechanism in the formation of large amorphous pockets in Ge. On

Table 5.3: *Average number of clusters created by a 10 keV PKA after 300 ps of TTM-MD simulations in Si and Ge materials for Ref scenario, and the distribution of the defects inside these clusters as a function of their size. Results are obtained from sets of 100 simulations*

	Si	Ge
Mean number of clusters	34	21
% of defects in clusters of size ≤ 5	11%	3%
% of defects in clusters of size > 5 and ≤ 100	56%	5%
% of defects in clusters of size > 100 and ≤ 1000	33%	15%
% of defects in clusters of size > 1000	0%	77%

the contrary, in Si, even if some heat spikes can lead to amorphous pockets, a much larger portion of single interstitials and vacancies and small clusters remains [10, 11, 19]. The lower melting point of Ge compared to Si as well as its lower thermal conductivity, which makes the dissipation of heat slower, were cited as the two main reasons for the enhanced melting of Ge in response to particle irradiation [11]. The melting point and the thermal conductivity are both determined by the interatomic potential. Therefore, the fine tuning of the thermal properties of the interatomic potential is of prime importance.

5.1.4.1 Si versus Ge: different mechanisms in response to particle irradiation

To finely understand the effects of the TTM in Si and Ge, we plotted in Fig. 5.3 the average evolution of the number of TTM ionic cells that have an atomic temperature higher than the melting temperature of the material (melting temperature of 1687 K for Si and 1211 K for Ge) over 100 simulated cascades. Very quickly, the curves reach their peak value (collision phase), then, rapidly decrease for a very short time before continuing to slowly decrease. The fact that a cell has a temperature higher than the melting one does not mean it is melted. To be melted, cells must necessary have a temperature higher than the melting point, for a sufficient amount of time. In the following, we refer to hot cells as the ones having a temperature higher than the melting temperature. The number of hot cells combined with the time for the relaxation of the hot cells are relevant indicators of the presence of molten regions in the material.

We observe a clear difference in Fig. 5.3(a) and Fig. 5.3(b) between Si and Ge: the number of hot cells is always higher in Ge and the relaxation time required for the number of hot cells to reach zero is longer. However, as explained in Chapter 3 on the use of t_{eph}, during the early stages of a cascade the calculated temperature does not represent an accurate evaluation of the temperature of the cell. In fact, the temperature is an average over a high number of atomic velocities, whereas the early stages of the cascade only involve the displacement of a small number of SKAs. Thus, one may ask if the number of melted cells is not biased during the collision part. Generally, after $t_{eph} \sim 0.25$ ps, the collision part of the cascade is over and the fast-moving atoms have lost all their energy through collisions. This implies that about all the atoms in a same cell have the same averaged velocity and that a temperature can be well defined in this cell. Thus, only after t_{eph}, Fig. 5.3 really shows the number of hot cells inside the materials.

The larger peak values and relaxation times for Ge scenarios in Fig. 5.3(a) and Fig. 5.3(b) explain why steady amorphous pockets (hot cells becoming molten cells) are preferentially formed in Ge and not in Si. According to the mean PKA penetration depth of Si and Ge (Table 5.2), Ge PKAs deposit their energy in smaller regions and therefore create denser cascades and melted zones. This together with the lower thermal conductivity of Ge compared to Si (Table 5.1) could explain the long relaxation time needed for the hot cells to lower their energy. Hence, it

confirms that melting of the material is indeed far more important in Ge than in Si. However, it is impossible to conclude yet on the influence of the TTM on this melting behavior.

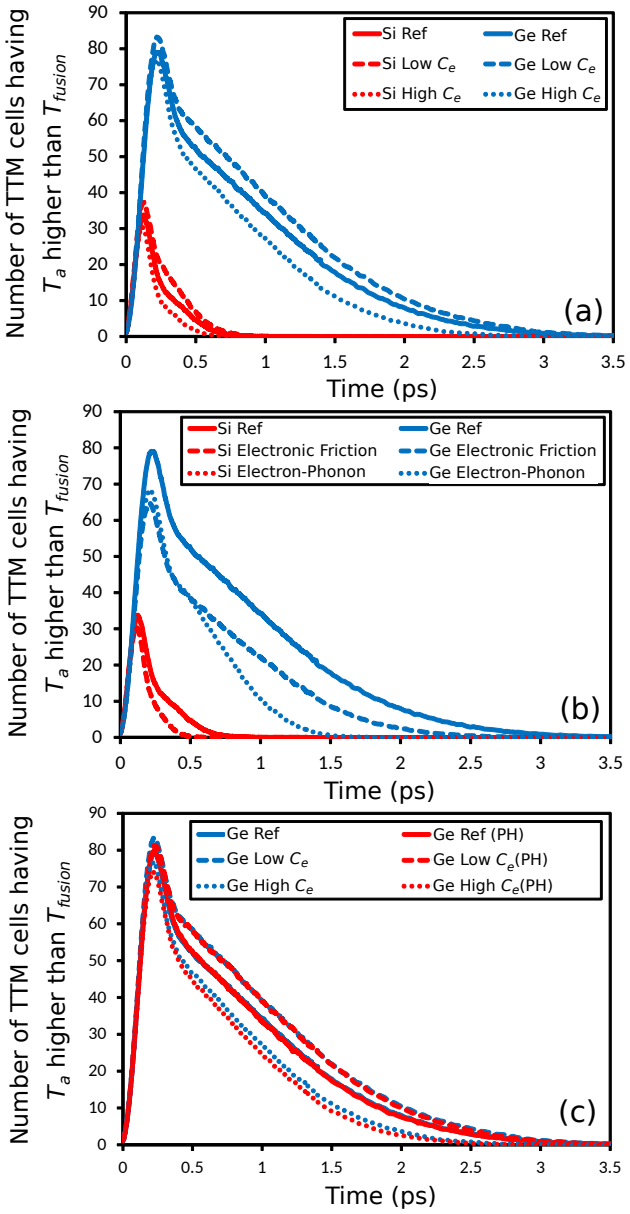

Figure 5.3: *Evolution of the number of TTM cells having a temperature higher than the melting temperature (a) in Si and Ge for the three different C_e scenarios (b) in Si and Ge for all the γ parameters scenarios (c) in Ge for the C_e scenarios with and without the t_{eph} option. Each curve is the result of an average over 100 simulations.*

5.1.4.2 C_e scenarios reveal electron-phonon coupling participates to melting within the TTM

The hot cells are defined after the collision phase when the velocities are below v_0. In this case, the energy ΔU exchanged between the ionic subsystem and the electronic subsystem at each timestep writes [1]:

$$\Delta U = \frac{\Delta t N 3 k_b \gamma_p}{m}(T_{elec} - T_{ionic}) \tag{5.1}$$

where N is the number of atoms in the cell, k_b is the Boltzmann constant, Δt is the MD timestep, m is the mass of an atom, T_{elec} is the electronic temperature and T_{ionic} the atomic (or ionic) temperature.

Thus, the more T_{elec} is higher than T_{ionic}, the more the energy transfer is in favor of the ionic subsystem. Moreover, in Table 5.2, the maximum electronic temperatures increase with C_e decreasing. Hence, according to (5.1) the amount of energy gained by the ionic subsystem increases with C_e decreasing. More accurately, the amount of energy gained by the ionic subsystem at each timestep increases with C_e. However, the total amount of energy exchanged is not controlled by C_e but by the γ parameters. Thus, a decrease in C_e actually increases the rate of energy transfer, but not the total amount of energy transferred, *i.e.* the energy is transferred back to the ions faster. In addition to C_e, κ_e also has an influence on the transferred energy from the electrons to the ions. Indeed, a decrease in the electronic thermal conductivity κ_e reduces the rate of temperature (heat) diffusion of a cell to nearby cells. In other words, for a same timestep, less energy is transferred from a given cell to the nearby cells. Thus, hot electronic cells stay hot for a longer time, and locally transmit more energy to the ions according to (5.1). Again, on the whole, the amount of energy transferred stays the same no matter the value of κ_e, but the energy transferred is more localized with a lower κ_e.

It is observed in Fig. 5.3(a) that for both Si and Ge, the number of hot cells is higher for the scenarios with a lower C_e/κ_e. However, C_e or κ_e do not have any effects in the rate of energy loss of the moving ions: the only mean by which a change in C_e or κ_e can induce a change in the number of hot cells is from the energy transfer from the electrons to the ions through electron-phonon coupling and following the mechanisms described in the previous paragraph. The evolution of the number of hot cells in Fig. 5.3(a) is linked to the evolution of the mean number of defects in Table 5.2. It means that, with the TTM, the electron-phonon coupling is sufficient to induce partial melting of the material. The effects of C_e and κ_e are more visible in Ge than they are in Si because the formation of thermal spikes preferentially occurs due to interatomic potential related properties: a lower melting temperature and a lower thermal conductivity compared to Si. The hypothesis of the mechanism we just presented is also supported by the work of Santos *et al.* in [29], which showed that an ensemble of ions having energies of a few eV (thus well below the threshold displacement energy of about 21 eV on average in Si) could lead to the formation of amorphous pockets.

However, the influence of C_e and κ_e we report may seem surprising in light of already published studies on the subject. Indeed, Khara *et al.* proved in [2] that a lower C_e reduces the radius of the amorphous track formed during SHI irradiations in Si, which could indicate that less defects are created with a lower C_e. The rightfully employed argument in [2] to explain their results is that with a lower C_e, the electronic energy is transferred very quickly to the ions and thus there is no time for the energy to diffuse between the electronic cells and thus induce a larger amorphous zone around the ion trajectory. The question is, how come this argument is not applicable to our case ? The answer lies in the fact that the energies we employ (10 keV) and the ones they have employed in [2] (MeV range) are not comparable. At the energies employed by Khara *et al.*, there is no doubt amorphization of the material will occur. Indeed, about 25 keV/nm^{-1} is lost to the electrons in their simulations. The major question in their case is not if defects are going to be created due to electron-phonon coupling, but what will be the extent of the created amorphous track. In our case, the energy lost to the electrons is a lot smaller (about 15 eV/Å at 10 keV in Si). There is thus far less energy available to induce melting of the material via energy transfer due to electron-phonon coupling. The little amount of energy available thus has to be transferred very quickly and locally to have a chance of inducing melting of the material. This is the reason why we observe enhanced melting with low values of C_e and κ_e in our study : a low C_e favors the quick transfer of energy from electrons to ions and a low κ_e ensures a very local spatial extent of this transfer.

Additionally, one may ask if noticeable discrepancies would be observed if a DFT calculated C_e was used (like in the work of Khara *et al.* [2]) instead of the C_e of the Ref scenario. The

differences between the C_e parameters in the Low C_e/κ_e, High C_e/κ_e and Ref scenarios being much more significant than what would be the differences between a DFT calculated C_e (κ_e) and the C_e (κ_e) of the Ref scenario, the hypothetical observed discrepancies would be small. Also, we have seen in Section 5.1.3 that the number of defects is more sensitive to changes in C_e and κ_e in Ge than it is in Si. Thus, we expect no change for Si and only a slight change for Ge.

5.1.4.3 Competition between γ_p thermal and mechanistic effects

We have discussed how the C_e scenarios reveal that melting is possible by energy transfer through γ_p. However, the role of γ_p is dual: on the one hand, increasing γ_p increases the energy transfer from the electrons to the ions but on the other hand, increasing γ_p increases the energy loss of the moving atoms by electronic friction. Thus, there is a competition between the mechanistic effects that reduce the number of defects, and the thermal effects that increase the number of defects. The drastic reduction in the number of defects observed in Table 5.2 when increasing γ_p (El-Ph scenario) reveals that the mechanistic effects are dominating over the thermal effects.

5.1.4.4 γ_p enhanced effect in Ge due to the presence of large thermal spikes

For Si, the mean numbers of defects that appear in Table 5.2 and the global distributions shown in Fig. 5.1a reveal that the reduction of the number of defects in the El-Ph and El-Fr scenarios is very similar. This is correlated with the number of hot cells presented in Fig. 5.3(b): in the case of Si, the curves of the two γ parameters scenarios overlap perfectly. This means that the two γ parameters contribute equally to the melting of the material.

On the contrary, for Ge, the mean values of Table 5.2 and the global distributions of Fig. 5.1d reveal that the reduction of the number of defects is enhanced in the El-Ph scenario compared to the El-Fr one. This is correlated with the number of hot cells presented in Fig. 5.3(b): the electron-phonon and electronic friction curves have about the same peak value but the decrease in the electron-phonon curve case is sharper and the curve quickly goes below the electronic-friction one. This means that in the TTM, γ_p reduces more the melting in Ge than γ_s does and consequently induces a lower number of defects.

The only difference between γ_p and γ_s in the way they contribute to the ionic subsystem energy loss is that γ_p is always activated whereas γ_s is not activated when the velocity of the atom is smaller than v_0. If this difference induces no remarkable effects in Si, it does in Ge. In fact, in Ge, the vast majority of defects is produced in liquid-like regions cooling down to become amorphous pockets, and the atoms in these regions have a velocity lower than v_0. In this case, the γ_p parameter permanently acts to reduce the energies of the atoms in those amorphous pockets and γ_s does not. Therefore, the sizes of the liquid-like zones shrink quicker in the El-Ph scenario compared to the El-Fr scenario. Consequently, less and smaller amorphous pockets are formed and fewer defects are obtained.

The fact that there are more liquid-like regions in Ge than in Si is mainly due to two of their basic properties defined by the interatomic potential. First, Ge atoms are heavier and have a larger radius than Si ones. Consequently, the Ge PKAs and SKAs deposit their energies quickly and in smaller regions, inducing a localized melting. Second, the melting temperature of Ge is much lower than the one of Si. Consequently, a PKA with the same energy leads to obtain more melted cells in Ge than in Si. The effects of the TTM is then drastically correlated to the interatomic potential.

5.1.4.5 v_0 has no influence

The v_0 scenarios considered show no change in the mean number of defects at the end of the cascade. At the considered energies of 10 keV, the setting of v_0 to either one time the cohesive energy or two times the cohesive energy (*i.e.* the rules the most employed) has no influence. However, it can be expected that it has an influence at higher PKA energies.

5.1.4.6 t_{eph} has no influence

The use of t_{eph} induces no changes in the global trends for the C_e and γ scenarios, at the considered energy of 10 keV. It is confirmed by Fig. 5.3(c) which shows the evolution of the number of TTM cells having their temperature greater than the fusion temperature. The parameter t_{eph} is however expected to influence the results in simulations where the electronic temperatures attained are greater (due to higher PKA energies for example). We still recommend to use it even in 10 keV simulations in order to overcome the bias induced by the badly defined ionic temperature at the beginning of the cascade.

5.1.5 Partial conclusion

An extensive statistical study aiming at assessing the impact of the main TTM parameters and truly understanding their physical role within the TTM is performed. Due to the stochasticity of the cascades, carrying out a high number of simulations is of prime importance to analyze global trends of their impact. The data presented in this study are the results of more than 2 000 TTM-MD collision cascades simulations initiated with 10 keV PKAs. The comparisons between simulations with various TTM parameter values allows us to draw five main conclusions:

(i) The electronic stopping parameter and the electron-phonon coupling parameter have the larger impact on the production of defects.

(ii) The influences of the electron-phonon coupling parameter, of the electronic specific heat and of the electronic thermal conductivity on the number of defects are greater for materials more subject to thermal spikes.

(iii) Changes in the threshold velocity for the electronic stopping power between the two most recommended rules to set it induces no difference in the mean number of defects.

(iv) The use of a parameter to set the time of activation of the electron-phonon coupling implies no change in the trends, at the considered energies.

(v) The electron-phonon coupling contributes to increase the number of defects in materials for which the irradiation leads to molten regions.

Those conclusions depend on the type of the PKA and on the melting temperature of the material under investigation, which are crucial to predict the appearance of molten regions and thus the influence of the TTM. The goal of this work is to bring very valuable quantitative data for the TTM users, as well as precious qualitative data on the role the electrons have in a collision cascade simulated with MD-TTM depending on the material under investigation and therefore the cascade behaviors at stake. It also highlights the significant influence of badly known parameters on collision cascades results, and the non-negligible influence of thermal parameters on the results. Those two aspects can be envisioned as limitations or uncertainties related to the use of the TTM, which more recent models aim at further investigating and correcting.

5.2 Electronic effects into collision cascades from *ab initio* calculations with the EPH model

This section is a detailed version of an article we have submitted for publication. In this section, we employ the acronym TDDFT to designate ED calculations as it is better known and carries more information on the nature of the technique in itself. As stated in the introduction, we first aim at parametrizing the EPH model with TDDFT calculations of electronic stopping power. Consequently, we detail the computational details and methodology we follow for electronic stopping calculations with TDDFT in Section 5.2.1.1, the electronic stopping results in Section 5.2.1.2 and we parametrize the EPH model for Si in Section 5.2.2. Then, we apply the EPH model to collision cascades in Si in Section 5.2.3.

5.2.1 Electronic stopping power in Si

5.2.1.1 Computational details and methodology

TDDFT calculations are performed using the QB@LL code [15, 16]. All our simulations are performed in 3×3×3 simulation boxes of bulk diamond Si with the experimental lattice constant of 5.431 Å [30]. Periodic boundary conditions are employed to accurately model a bulk system. Calculations are carried out with the PBE approximation for the exchange and correlation functional and a norm conserving pseudopotential explicitly considering the $3s^2 3p^2$ electrons as valence electrons is used. The number of electrons considered within the pseudopotential was found to have a drastic influence on the electronic stopping calculations in [31] and [32], where different pseudopotentials are tested. Both studies proved that core electrons of the target atoms and of the projectile could become excited, at least at high projectile energies. Thus, the results obtained with the $3s^2 3p^2$ pseudopotential are compared in Section 5.2.1.2 with results we obtained with another pseudopotential with 12 valence electrons adapted from the one generated by Lee *et al.* in [33] to work with PBE functionals and generated with the OPIUM code [34]. We use a plane-wave cutoff of 100 Ry with the 4 valence electrons pseudopotential and a cutoff of 220 Ry with the 12 valence electrons pseudopotential.

The initial condition required for the real time propagation is obtained by first performing a self consistent calculation of the system made of the supercell and the projectile. Then, the electronic wavefunctions are propagated in time from the wavefunctions obtained from the static calculation, and the nuclei classical equations of motions are integrated in time, with force calculations deriving from the electronic Hamiltonian and the electronic wavefunctions. Fig. 5.4 depicts the situation at the very first step of the TDDFT simulation: a simulation box is constructed, a Si projectile is placed within the box and given a velocity in a certain direction.

In our simulations, we want to record only the effects of the electronic stopping, not of the nuclear stopping. To ensure this, the forces on all the atoms are set to zero all along the simulations, *i.e.* host atoms are held fixed during the simulations, and the projectile moves at constant velocity. Consequently, there are no slowing down of the projectile due to host atoms, and no friction force originating from the electrons acting on the projectile. The only physical process recorded during the simulations is the excitation of the electrons of the projectile and of the target material. The effect of the electronic stopping cannot be calculated from the velocity or energy loss of the projectile as it moves at constant velocity. However, this forced constant velocity of the projectile conducts to a system that is not isolated anymore. In a way, it can be viewed as the effect of an energy source. The total energy of the system is therefore not conserved, and globally increases all along the simulations. This total energy increase corresponds to the energy acquired by the electrons of the system for their excitation, and the slope of the curve of the total energy with respect to the distance traveled by the projectile gives the electronic

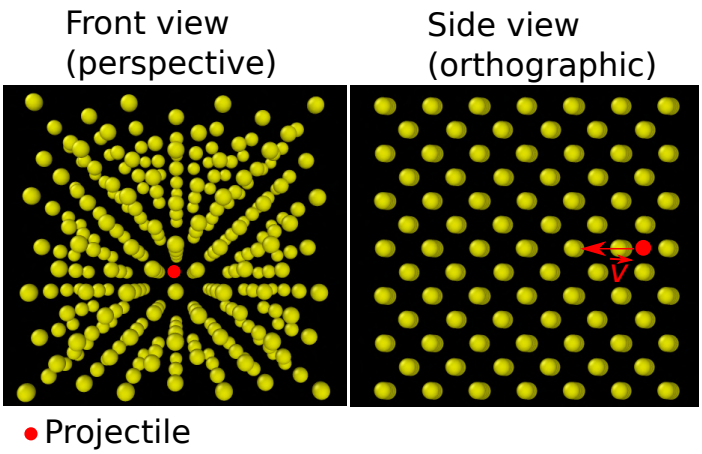

Figure 5.4: *Construction of a TDDFT simulation. The example given is for a <001> channel trajectory. Atomic snapshots have been obtained with OVITO [35].*

stopping power of the projectile at the constant velocity chosen. Fig. 5.5 shows the total energy evolution obtained with Si projectiles having energies ranging from 10 keV to 200 keV in Si, with respect to the distance traveled by the projectiles. For the energy range considered, the greater the energy of the projectile, the greater the slope of the total energy.

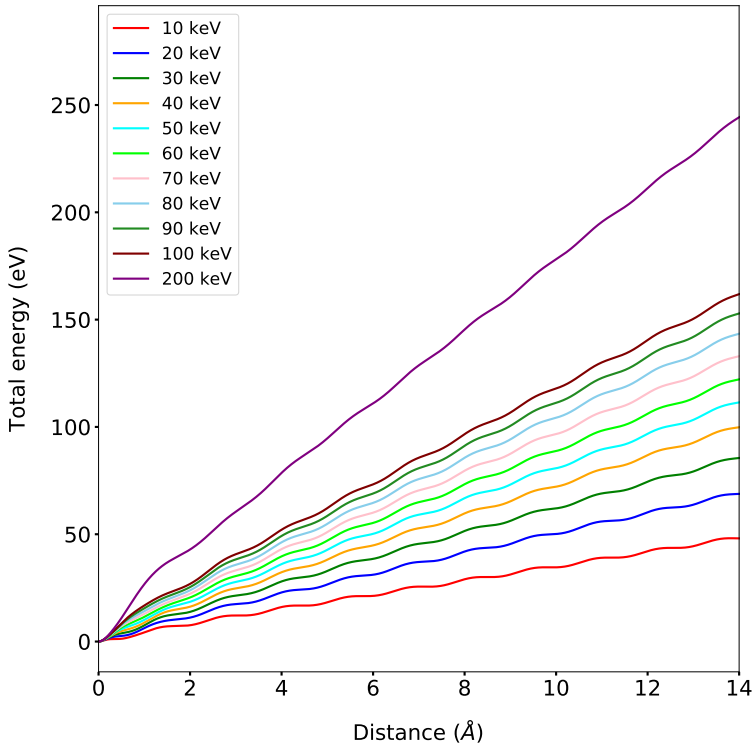

Figure 5.5: *Total energy change of the studied systems with respect to the distance traveled by the Si projectile in the <001> channel, for various energies.*

The timestep is a very important parameter of the simulations which should be chosen carefully. The remarks made in Chapter 3 on the relation between energy conservation and timestep for MD simulations are also valid for ED calculations. For projectiles of energy below 50 keV, we use a timestep of 1 as, and from 50 keV and above we employ a timestep of 0.5 as. The computational cost associated with ED calculations being very important, it is therefore important not to employ too small timesteps, which would make the simulations very long, especially at

the relatively low velocities we consider here. The timesteps are chosen to ensure energy conservation, minor unsignificant changes in the calculated electronic stopping powers and reasonable computational cost.

We simulated the ions and electrons dynamics in the <001> , <110> and <111> center and off-center channel trajectories as well as in directions incommensurate to the crystal lattice. Fig. 5.6 shows the front orthographic views of the <001> , <110> and <111> channels in Si. Incommensurate directions are chosen following the indications of [36], such that they avoid channeling directions and head-on collisions. To extract the stopping power from the simulations in the channels, we calculated the slope of the linear regression of the total energy versus the distance x traveled by the projectile, but only between $x = 1/2 \times a_{lat}$ and $x = 5/2 \times a_{lat}$ for the <001> direction, $x = \sqrt{2}/2 \times a_{lat}$ and $x = 5\sqrt{2}/2 \times a_{lat}$ for the <110> direction, and $x = \sqrt{3}/2 \times a_{lat}$ and $x = 5\sqrt{3}/2 \times a_{lat}$ for the <111> direction. There are diverse explanations for those lower and upper limits for the electronic stopping calculations. Firstly, as can be seen on Fig. 5.5 showing the total energy of the simulation box for Si projectiles within the <001> channel in Si at various energies, the very first moments of the projectile trajectory are characterized by a short transient state one should not consider in the calculation of the electronic stopping power [36]. Secondly, the calculation of the stopping power is more accurate if performed on the symmetrical segments of trajectories given above. Indeed, the contribution of the lattice to the total energy should be totally removed. Calculating the electronic stopping power on the given paths ensures the mean contribution of the lattice is null, as we calculate the electronic stopping on exactly two unit cells in each case [37]. Another solution would be to launch Born Oppenheimer Approximation-MD (BOA-MD) simulations on the same trajectories, to only take into account the contribution of the lattice, subtract the total energy obtained with the BOA-MD runs to the total energy obtained with TDDFT calculations and calculate the slope of this energy difference. However, this second method is longer and requires to launch twice the number of simulations, for the same level of precision.

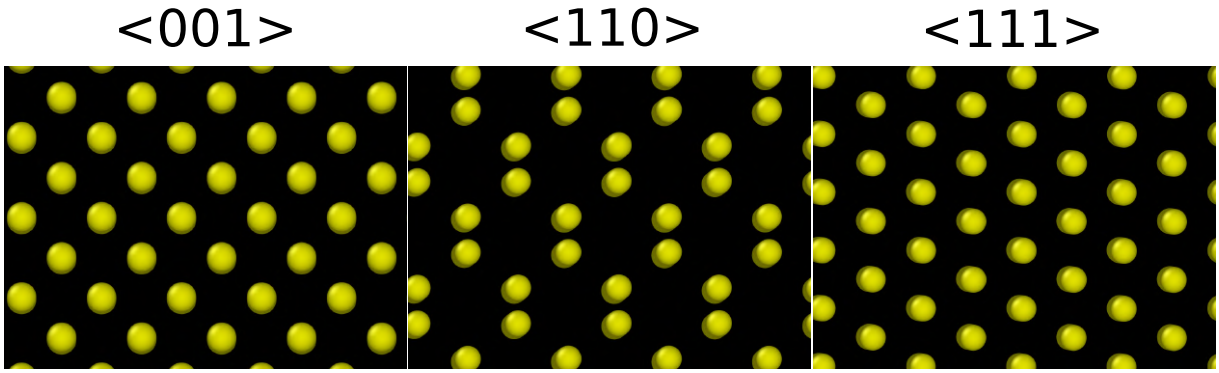

Figure 5.6: *Front orthographic views of the <001> , <110> and <111> channels in diamond Si. Atomic snapshots have been obtained with OVITO [35].*

5.2.1.2 Electronic stopping results and discussions in Si

In this section, we are interested in the extraction of the electronic stopping power from the evolution of the total energy with respect to the distance traveled by the projectile in TDDFT calculations, in center and off-center (1/2) <001> channel trajectories for energies ranging from 10 keV to 200 keV. By off-center (1/2), we mean that the projectile position initially is $(1.125 \times a_{lat}, 1.5 \times a_{lat}, 0.0)$, *i.e.* one half of the x-axis distance to another atom for a projectile in the center position. Trajectories along the <110> and <111> channels have been investigated only with 100 keV projectiles.

The purpose of our TDDFT calculations is to allow parameterizing the EPH model for MD simulations of collision cascades. Thus, we are interested in projectiles of low energies, which explains why we restrict ourselves to Si projectiles of 10 keV to 200 keV. While for higher energies it has been proven to be mandatory, at least in Ni [31], to employ pseudopotentials with semicore electrons in the valence, no pseudopotential-dedicated study was performed for the low energies of interest for us. A detailed study with a 12 valence electrons pseudopotential was performed for Si in [33]. Here, we ran a few simulations to determine if it is necessary to employ a pseudopotential with semicore electrons in the valence, which would be of considerably higher computational cost. For the sake of comparison, we performed a simulation in the <001> center channel with a projectile of 700 keV with both a 4 valence electrons pseudopotential and a 12 valence electrons pseudopotential. The pseudopotential with 4 valence electrons gives a stopping power of 33.9 eV/Å, compared to 53.6 eV/Å with the pseudopotential with 12 valence electrons. The reported value with the pseudopotential with semicore electrons in the valence is of very good agreement with the calculations performed with a similar pseudopotential in [33]. Doing the same comparison for a 200 keV projectile along the same trajectory, we find an electronic stopping of 16.7 eV/Å with the 4 valence electrons pseudopotential and of 16.0 eV/Å with the 12 valence electrons pseudopotential. The lower value found with the pseudopotential explicitly integrating semicore electrons is counter-intuitive. It can be explained by the fact that the 12 valence electrons pseudopotential generated with OPIUM supports only one projector per angular moment, meaning it had to be generated for the $2s^2 2p^6 3s^0 3p^0$ reference configuration and not the neutral $2s^2 2p^6 3s^2 3p^2$ one. Therefore, it suffers from transferability issues which could easily explain uncertainties in the electronic stopping calculations. However, results are similar enough to state that below 200 keV *a minima*, a pseudopotential with more than 4 valence electrons is of no use. All the results presented in the following were obtained with the 4 valence electrons pseudopotential.

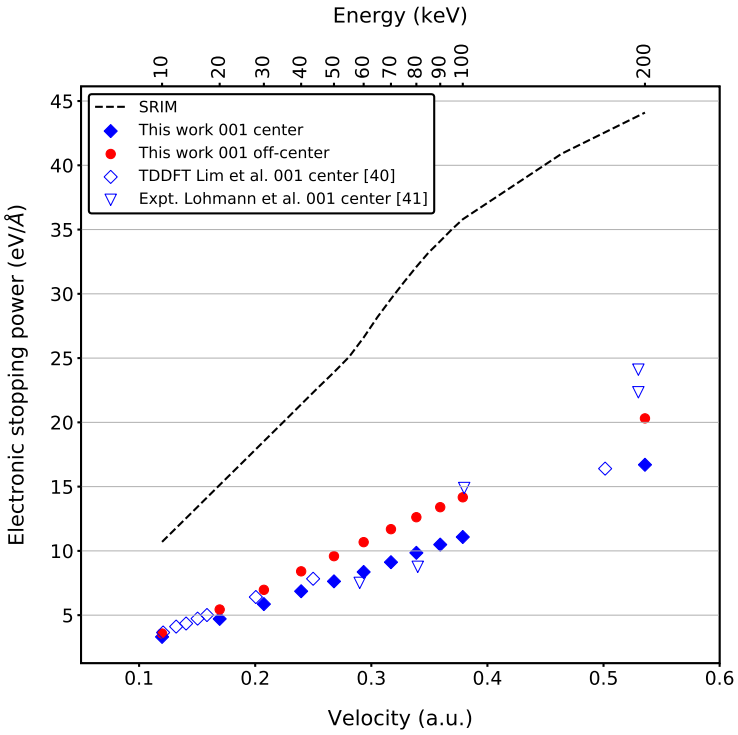

Figure 5.7: *Electronic stopping powers with respect to the velocity of the projectile in a.u. calculated for projectiles of energies ranging from 10 keV to 200 keV (solid markers) and compared to stoppings from other computational (empty diamond markers) and experimental (empty triangle markers) references and calculated with SRIM [38] (dashed line).*

In Fig. 5.7, the electronic stopping powers of initially neutral Si projectiles into bulk Si along the center <001> channel and the off-center <001> channel (1/2) are shown with respect to the velocity of the projectile. TDDFT calculations results from [39], experimental results from [40] and SRIM [38] results are also shown for comparison. According to Fig. 5.7, the electronic stopping power increase in Si for projectiles between 10 keV and 200 keV in the <001> channel is clearly linear with the projectile velocity. Our calculations compare really well with the results presented in [39], even if a slight discrepancy can be noticed, which could not be explained neither by the use of LDA vs PBE, nor by the different lattice parameters employed, according to additional calculations we performed. The stopping powers found for the off-center <001> trajectories are a bit higher than the center ones, and this discrepancy increases with the projectile velocity. Our results for the center channel and the ones of [39] are in good agreement with the state of the art experimental results of [40] for the <001> center channel. This gives us confidence in the reliability of the electronic stopping powers calculated from TDDFT despite the fact that our stoppings are 2 to 3 times smaller than SRIM stopping powers. This last point is of course partly due to the fact that we only look at results for the <001> channels, whereas the electronic stopping in SRIM is some sort of average over all possible directions. Some of the stoppings reported for the various trajectories sampled for the 100 keV projectile in Table 5.4 already are closer to the SRIM value, even if always lower.

Table 5.4: *Electronic stopping powers calculated with TDDFT for various directions for a neutral Si projectile of 100 keV.*

	Elec. stop. (eV/Å)
<001> center channel	11.09
<110> center channel	9.79
<111> center channel	13.76
<001> off-center channel (1/2)	14.17
<001> off-center channel (1/4)	19.47
<110> off-center channel	12.15
SRIM	35.76

The disagreement between SRIM and TDDFT stoppings for Si into Si at low energies was already pointed out in [39]. The more recent work of Lee *et al.* at higher energies in [33] reports TDDFT electronic stoppings for initially charged Si^{+12} projectiles up to two times greater than SRIM stoppings, compared to TDDFT stoppings up to two times lower for neutral Si^{+0} projectiles, thus agreeing with our results obtained with neutral Si projectiles.

Trying to reproduce SRIM values of electronic stopping power requires to run very long TDDFT simulations on various random trajectories (see [37]) and with different projectile initial charge state to obtain converged values of the stopping. However, this is not in the scope of this study whose purpose is to use TDDFT calculations of electronic stopping to parameterize the EPH model for MD simulations of collision cascades.

5.2.2 Parametrization of the EPH model

After having investigated the electronic stopping power in Si and proved the trustfulness of our simulations by comparing our results to other numerical and experimental studies, we can begin the parametrization of the EPH model with confidence.

This section is dedicated to the parameterization of the $\alpha(\rho)$ parameter of the EPH model. Following the equations of the EPH model exposed in Chapter 3, α is expressed in $(\text{eV.ps/Å}^2)^{1/2}$ (default units of the model). The parameter we actually have to fit, following [13], is homogeneous to (eV.ps/Å^2), thus the square of α. It is sometimes called β in [13] and [14], has the

same role in B_{IJ} that α has in W_{IJ}, as can be understood from Chapter 3, and can be seen as the electronic stopping power of the projectile divided by its velocity. The original papers of the EPH model do not explicitly mention β in the equations though they actually name it in the text and optimize it. Although we actually do optimize the β parameter and not the α one, as α appears in the equations, in the following the α parameter is the discussed parameter.

Prior to diving into the parametrization of the $\alpha(\rho)$ parameters, we can say a few words about the electronic density within the EPH model. As it is advised in [13], we use for the electronic densities of a single atom of the simulation the atomic electronic densities calculated with the OPIUM code. The electronic density at a given point of the simulation box is therefore the sum of the contributions of the atomic electronic densities of all the atoms of the simulation box. In Fig. 5.8 is displayed the atomic electronic density we calculated.

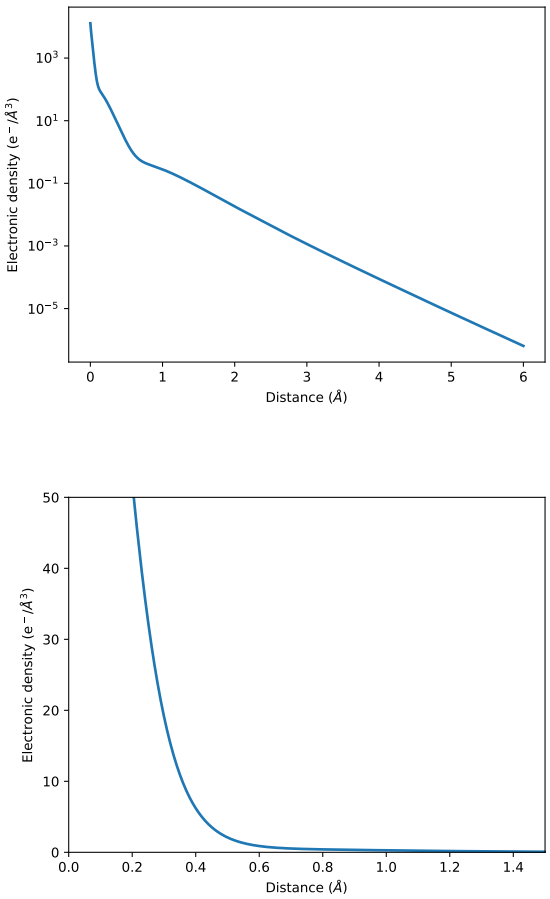

Figure 5.8: *Atomic electronic density calculated with OPIUM and employed in the EPH model. The lower figure is a zoom of the first one, focusing on low distance values and restricting electronic density between 0 and 50* $e^-/Å^3$.

The best parameterization is the one that gives, for an ensemble of different projectile trajectories, an evolution of the energy lost to the electrons with respect to the distance that is the closest to what was obtained with TDDFT calculations. The energy lost to the electrons is a direct output of the EPH model, whereas it requires an extra step to be obtained from TDDFT calculations. To end up with only the energy transmitted to the electrons by the projectile ion, the contribution of the lattice to the total energy must be subtracted. If employing integer numbers of the unit cells is enough to get rid of the contribution of the lattice to the total energy for the calculation of electronic stopping powers (see Section 5.2.1.1), it cannot be sufficient for

the parametrization of the EPH model. Indeed, we need the real values of the energy given to the electrons, and we work with incommensurate projectile trajectories for which the technique employed for the calculation of electronic stopping powers does not work. Practically speaking, it means that the energy with respect to distance obtained with a BOA-MD run on a given trajectory (E_{BOA}) must be subtracted to the energy with respect to distance obtained with TDDFT on the same trajectory (E_{TDDFT}). At a given distance r on the projectile path, the energy $E_{elec}(r)$ lost to electrons in a TDDFT run thus is:

$$E_{elec}(r) = E_{TDDFT}(r) - E_{BOA}(r) \tag{5.2}$$

In this section, when an energy loss to electrons obtained with TDDFT is mentioned, it was calculated with (5.2). Fig. 5.9 shows the total energy with respect to the distance traveled by the projectile during a TDDFT and a BOA simulation, as well as the difference $E_{elec}(r)$ between the two, for various projectile trajectories. The peaks appearing in the BOA and TDDFT curves of Fig. 5.9 corresponds to short interatomic distances between the projectile and an host atom, and then regions of high electronic densities. Thus, the slope of the E_{elec} curve, *i.e.* electronic stopping power, increases with the electronic density on the plotted trajectories.

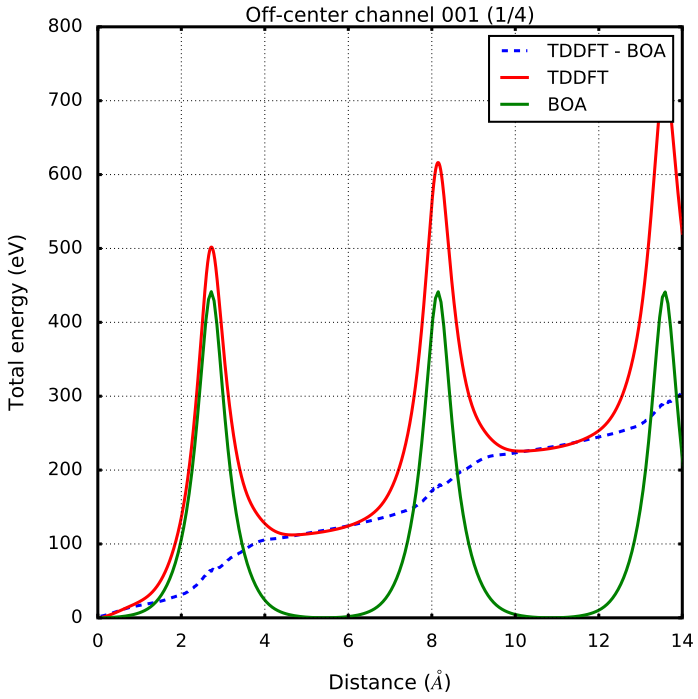

Figure 5.9: *Total energy evolution during a TDDFT and a MD-BOA run for an (1/4) off-center channel <001> direction. By off-center (1/2) we mean that the projectile position initially is (*$1.0625 \times a_{lat}$, $1.5 \times a_{lat}$, 0.0*), i.e. 1/4 of the x-axis distance to another atom for a projectile in the center position. The difference between the two is depicted by the dashed blue line. The total energy scale is set so that the total energy of the TDDFT and MD-BOA simulations at the very first step is strictly equal to zero.*

The subtraction of BOA to TDDFT doubles the number of simulations to perform as for one single trajectory, one TDDFT and one BOA-MD simulations are needed. The parameterization of the EPH model requiring to run many TDDFT calculations in various trajectories, it is computationally prohibitive to fit the model with simulations launched with too low velocities. Indeed, the smaller the initial energy (velocity) of the projectile, the longer time takes the simulation. Thus, we fit the EPH model with TDDFT calculations initiated with a projectile of 100 keV, even if we will then perform our MD simulations of collision cascades with lower

initial energies. Doing this, we reach an affordable computational cost. This approximation is reasonable knowing that the EPH model assumes that the electronic stopping is linear with the projectile velocity, as this is always the case for metals, for which the EPH model has been developed for. In Si, Lim *et al.* demonstrated in [39] that the electronic stopping is metal-like above 3 keV, meaning it is linear with the velocity. Our calculations in the <001> channel confirmed this observation (see Fig. 5.5) for 10 keV to 200 keV projectiles. Still following Lim *et al.* work, below 3 keV and above 60 eV, the bandgap induces changes as electronic stopping power still increases with velocity but faster than above 3 keV. Below 60 eV, the stopping was found to be non-zero. However, at low energies (velocities) the contribution of electronic effects is less important than at high energies and the initial energies we employ for MD simulations of collision cascades are a lot greater than 3 keV. Consequently, the errors coming from this linear stopping approximation are expected to be small.

In the following, we compare the EPH and TTM models to reference TDDFT calculations. To rank the different MD-EPH (MD-TTM) parameterizations, an appropriate distance measure between the energy loss to electrons along a given projectile trajectory during the reference TDDFT simulations and the MD-EPH (MD-TTM) simulations must be defined. We choose to employ the Mean Absolute Error (MAE):

$$MAE = \frac{1}{n}\sum_{i}^{n} |E_{MD}(r_i) - E_{TDDFT}(r_i)| \tag{5.3}$$

where n is the number of points sampled along the trajectory and r_i is the distance traveled by the projectile associated to point i. E_{MD} in this equation describes either the energy loss to electrons during a MD-EPH or a MD-TTM simulation.

An optimization scheme for the $\alpha(\rho)$ parameter of the EPH model can now be established. This scheme is presented in Fig. 5.10.

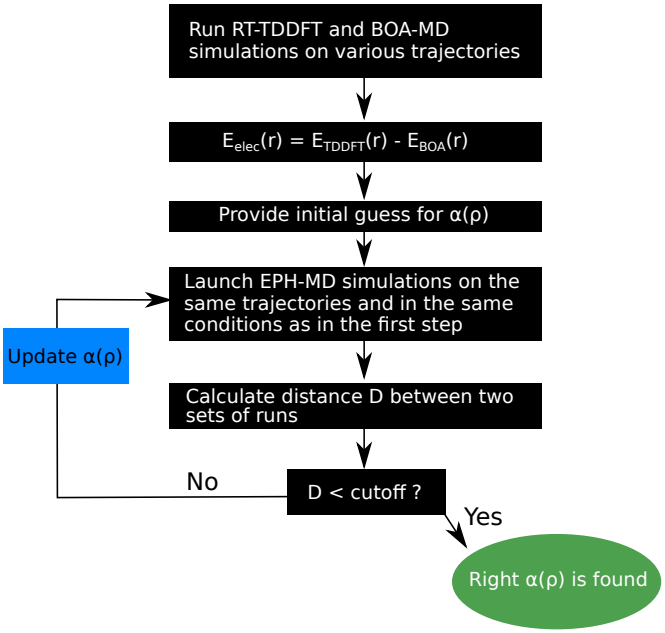

Figure 5.10: *Optimization scheme of the $\alpha(\rho)$ parameter.*

We fit the EPH model using ten different trajectories: <001> center channel and two off-center trajectories, <110> center channel and one off-center channel trajectory, <111> center channel and also four incommensurate directions, one having a vacancy on the projectile path. Table 5.5 summarizes the characteristics of all sampled directions, and Fig. 5.11 illustrates the sampled channeling directions.

	Initial projectile position	Velocity unit vector
Center channel <001>	$(1.25 \times a_{lat},\ 1.5 \times a_{lat},\ 0.0)$	$(0.0,\ 0.0,\ 1.0)$
Center channel <110>	$(0.0,\ 0.0,\ 1.625 \times a_{lat}\ )$	$(1/\sqrt{2},\ 1/\sqrt{2},\ 0.0)$
Center channel <111>	$(1.25 \times a_{lat},\ 1.25 \times a_{lat},\ 0.0)$	$(1/\sqrt{3},\ 1/\sqrt{3},\ 1/\sqrt{3})$
Off-center channel <001> (1/2)	$(1.125 \times a_{lat},\ 1.5 \times a_{lat},\ 0.0)$	$(0.0,\ 0.0,\ 1.0)$
Off-center channel <001> (1/4)	$(1.0625 \times a_{lat},\ 1.5 \times a_{lat},\ 0.0)$	$(0.0,\ 0.0,\ 1.0)$
Off-center channel <110>	$(0.0,\ 0.0,\ 1.81 \times a_{lat}\ )$	$(1/\sqrt{2},\ 1/\sqrt{2},\ 0.0)$
Incommensurate 1	$1.25 \times a_{lat},\ 1.5 \times a_{lat},\ 0.0)$	$(0.3620,\ 0.0.1134,\ 0.9252)$
Incommensurate 1 + vacancy	$(1.25 \times a_{lat},\ 1.5 \times a_{lat},\ 0.0)$	$(0.3620,\ 0.0.1134,\ 0.9252)$
Incommensurate 2	$(1.25 \times a_{lat},\ 1.5 \times a_{lat},\ 0.0)$	$(0.4017,\ 0.1867,\ 0.8965)$
Incommensurate 3	$(1.25 \times a_{lat},\ 1.25 \times a_{lat},\ 0.0)$	$(0.1922,\ 0.4364,\ 0.8790)$

Table 5.5: *Main characteristics of the trajectories sampled for fitting the EPH model.*

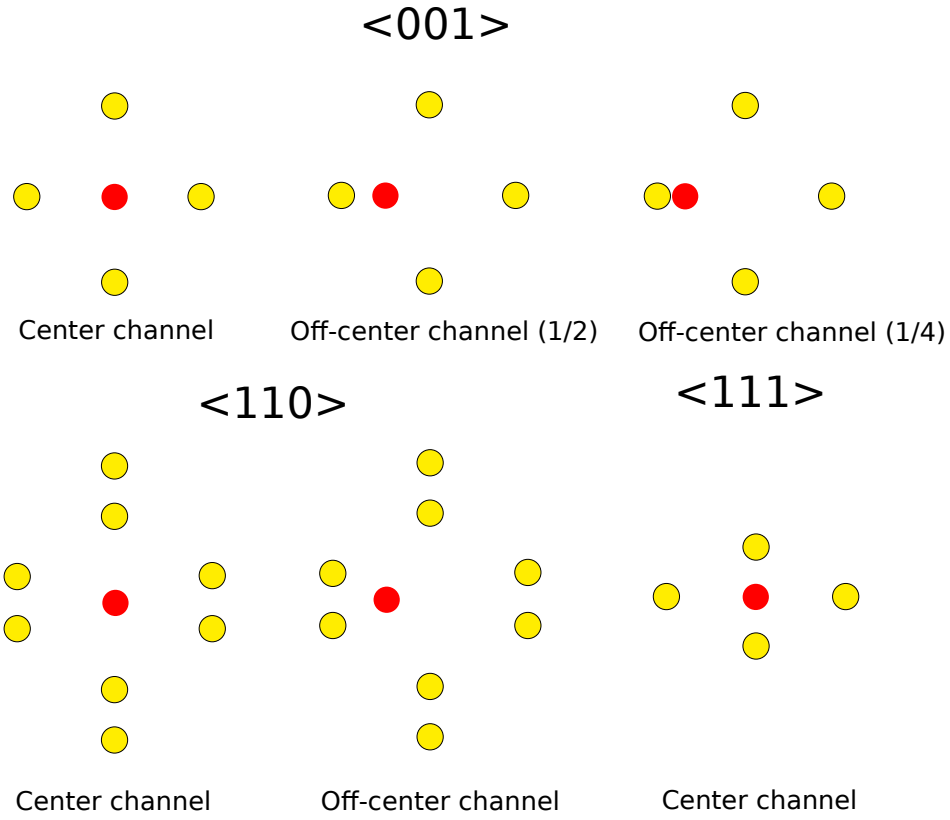

Figure 5.11: *Illustration of the sampled channeling directions. Host atoms are in yellow, the projectile is in red. Relative distances between atoms are not exact. The purpose of this figure is only illustrative.*

The conditions of the MD-EPH runs are the same as for the TDDFT runs: the forces on all the atoms are set to zero and the projectile moves with a constant velocity. For comparison, MD-TTM simulations in the same conditions are also launched. Within the TTM and EPH runs of this section, electron-phonon coupling is switched off, so we only report electronic stopping power. Within the TTM, where the total friction coefficient actually is the sum of the electronic stopping γ_s parameter and the electron-phonon coupling γ_p parameter [1], it means we neglect

energy exchanges between ions and electrons via the stochastic force term (electron-phonon coupling) and we only consider the γ_s parameter in the friction term. Switching the electron-phonon coupling on would not change the outcomes, but would make necessary an extra smoothing step of the energy loss to electrons curves.

It was found in [41] that the electronic stopping power is a multivalued function of the electronic density, *i.e.* for a single value of the electronic density there exists multiple values of stopping. The $\alpha(\rho)$ parameters that are to be given as input to the EPH model cannot be multivalued with the density, for obvious reasons. Thus, the stopping retrieved from the EPH model can only approximate the reference TDDFT stopping. We want to make it as true as possible to the TDDFT data using a single-valued function for the α parameter. In [13], Caro *et al.* have used a complex optimization algorithm procedure with spline and knot points for $\alpha(\rho)$. In this study, we do not want to engage in complex optimization processes, and we want to employ simple expressions for $\alpha(\rho)$. We are going to see two approaches: one where α is kept constant, and another one where $\alpha(\rho)$ has a quadratic expression of the form $(a\rho+b\rho^2)\times(1+e^{c(\rho-\rho_f)})^{-1}$. The exponential decay term in the quadratic expression must be added to the quadratic expression otherwise the stopping at high ρ would be drastically overestimated. This is also motivated by the observations made in [13] that the electronic stopping tends to saturate at very high values of the electronic density. The quadratic expression has no constant term as we wanted it to be equal to 0 at $\rho = 0$: a stopping equal to 0 in the absence of electrons is more satisfactory physically speaking.

In the following, we show data corresponding to the already optimized α parameters of the constant and quadratic cases studied. We define the best optimization as the one for which the total MAE, which is the MAE calculated from the sampled positions of all the studied trajectories, is the smallest. Fig. 5.12 represents the optimized $\alpha(\rho)$ parameters with respect to density in those two cases. The optimized expressions of the α parameter in the constant and quadratic cases respectively give:

- $\alpha(\rho)^2 = 0.0037$ eV/ps/Å^2
- $\alpha(\rho)^2 = (0.041\times\rho + 0.0\times\rho^2)\times\frac{1}{1+e^{10(\rho-0.3)}}$ eV/ps/Å^2

Starting from a quadratic expression of $\alpha(\rho)$, we obtained a linear one in the end with the b parameter strictly equal to 0. As the final linear expression we obtain originates from the optimization of an initially quadratic expression, the term quadratic will be kept in the following.

Fig. 5.13 and Fig. 5.14 respectively show the energy loss to the electrons in channeling and incommensurate trajectories obtained with TDDFT, the EPH model and the TTM. Table 5.6 displays the MAE in the EPH constant and quadratic scenarios and the TTM fitted to TDDFT case only, for all the trajectories studied. Note that the TTM electronic stopping parameter in the TTM curves below named "TTM fitted" (see Fig. 5.13 and Fig. 5.14) has been optimized as well to minimize their MAE with respect to the TDDFT data. Contrarily, the TTM parameters of the simulations whose corresponding curves are entitled "TTM SRIM" are not fitted to TDDFT data. In this case, the electronic stopping power parameter γ_s is obtained from SRIM calculations of electronic stopping power.

The most blatant feature, common to all the graphs of Fig. 5.13, is the fact that the TTM in its SRIM-derived parametrization largely overestimates the energy lost to the electrons compared to TDDFT. This is not a surprise considering the existing discrepancy between our TDDFT electronic stopping results and SRIM stopping calculations we highlighted in Section 5.2.1.2.

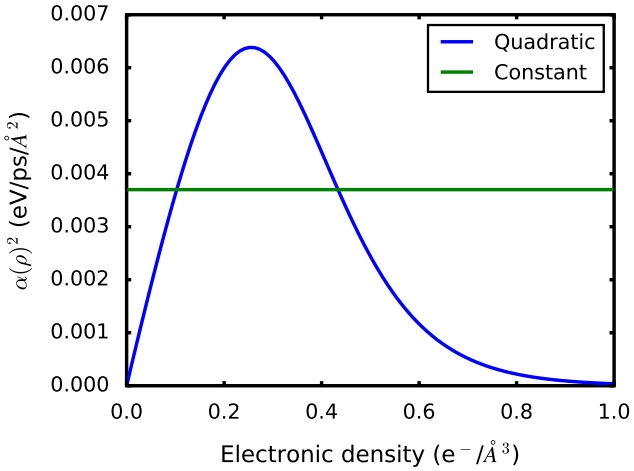

Figure 5.12: *Constant and quadratic optimized $\beta(\rho) = \alpha(\rho)^2$ functions.*

We also clearly see an increase in the slope of the energy lost to electrons when regions of higher densities are sampled. This is especially clear in Fig. 5.13e and all the incommensurate directions of Fig. 5.14, in which the projectile encounters high values of electronic density on its path. However, at high values of electronic density, the slope of the energy loss to electrons stops increasing and stabilizes. The increase in electronic stopping thus seems to saturate when high values of electronic density are reached. Visually from the just cited figures, the EPH model also provides an increase of the stopping power when the electronic density increases, just like in the TDDFT results. This can be observed in Fig. 5.13d, Fig. 5.13e, Fig. 5.13f as well as all the graphs of Fig. 5.14, in which the changes in the slopes of the energy loss to electrons with changes in the electronic density are obvious. This consists in a first qualitative satisfactory aspect of the EPH model.

We now focus on the channel trajectories of Fig. 5.13. The <001> off-center channel (1/2), <110> off-center channel and <111> center channel TDDFT trajectories of Fig. 5.13 are very well reproduced by the constant parameterization of the EPH model, the density dependence of the energy loss to electrons being followed very closely by MD-EPH simulations. This is confirmed by Table 5.6 and the low MAE associated to these trajectories. The quadratic parameterization also reproduces quite well the <110> off-center channel and <111> center channel, but does not perform as good as the constant case for the <001> off-center channel (1/2) (MAE of 4.2 eV for the constant case compared to 11.3 eV for the quadratic case).

The <001> center channel and <001> off-center channel (1/4) do not follow the TDDFT data curves as close as the previously cited trajectory does but still are satisfactory. The constant α function provides better results for the <001> center channel (MAE of 14.6 eV compared to 20.9 eV) and for the <001> off-center channel (1/4) (MAE of 9.2 eV compared to 29.2 eV).

Following the good results obtained with the EPH model for the 5 trajectories already cited, it is surprising that for the <110> center channel trajectory, the MD-EPH simulations are far below the reference TDDFT data (Fig. 5.13b). We suspected that the electronic density approximated by the EPH model for this trajectory to be very low compared to the real electronic density that the projectile sees in the TDDFT simulation, thus explaining this important discrepancy. However, we compared the EPH electronic densities and *ab initio* ones calculated with Quantum Espresso [42, 43] for various trajectories including the center <110> one, and we found that in every cases densities are similar. It thus cannot explain the discrepancies we observe for the center <110> channel between EPH and TDDFT. This point should be further studied.

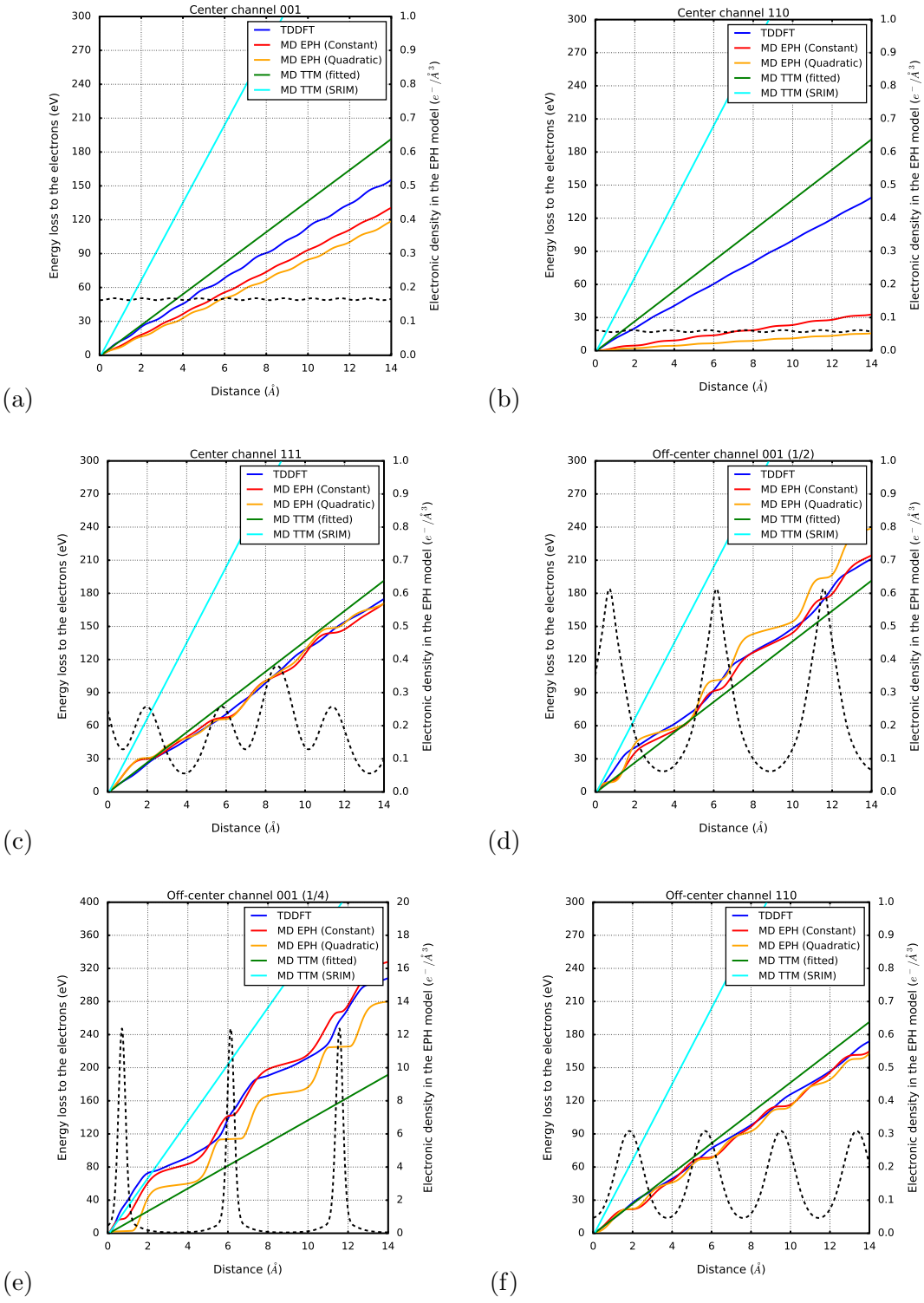

Figure 5.13: *Energies lost to the electrons for all the channel trajectories studied with 100 keV Si projectiles in Si calculated with TDDFT, the EPH model and the TTM (solid lines). The electronic density seen by the projectile in the EPH model is represented in each case with a dashed black line. Beware that the y-axis scales are not the same in each graph.*

In Fig. 5.13e can be noticed a step-like behavior of the energy loss to electrons in the EPH model. This behavior is intrinsic to the model, but arises for lower values of the electronic density in the quadratic parametrization of the EPH model compared to the constant one. Indeed, the $\alpha(\rho)$ parameter in the quadratic parametrization smoothly decays to zero, meaning when ρ exceeds the value for which $\alpha(\rho) = 0$, no energy is transferred between ions and electrons, the energy lost to electrons levels off until the projectile reaches a lower value of ρ.

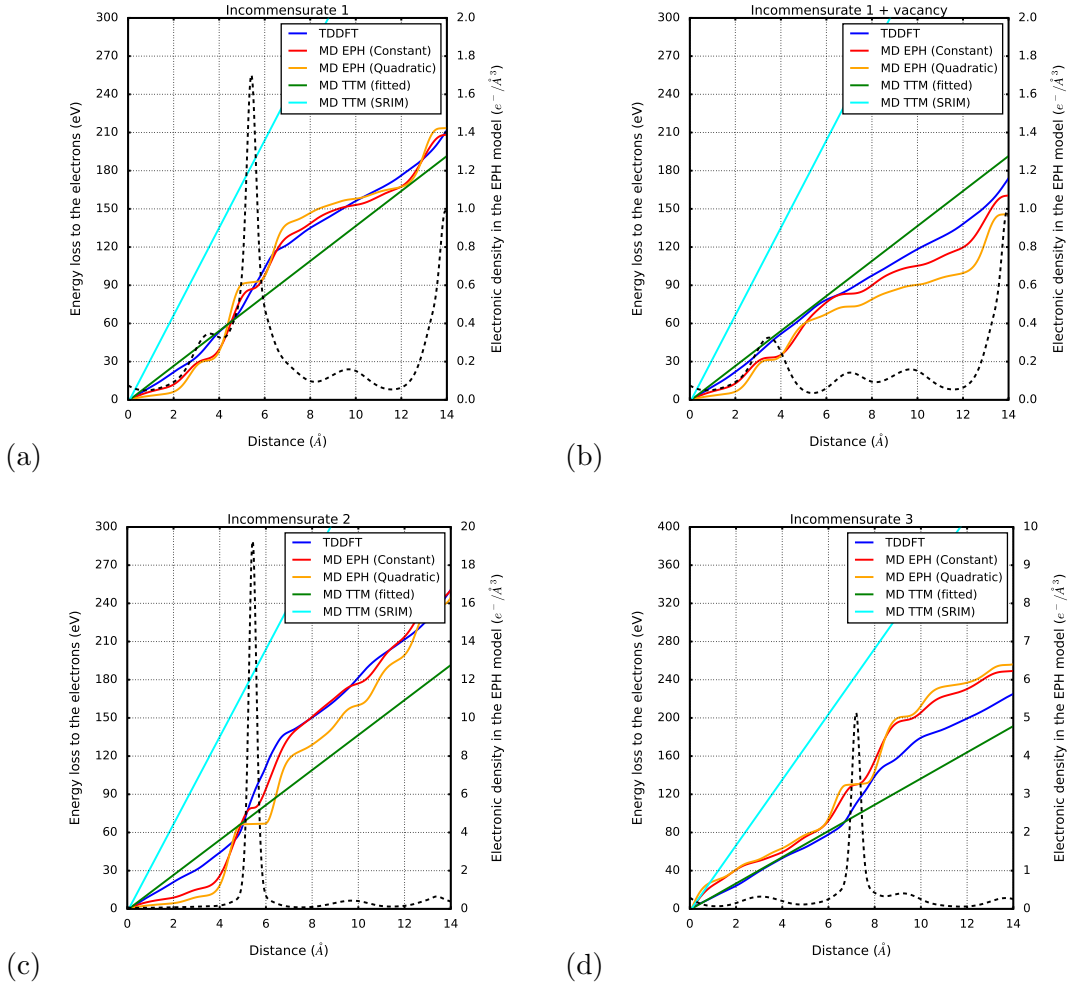

Figure 5.14: *Energies lost to the electrons for all the incommensurate trajectories studied with 100 keV Si projectiles in Si calculated with TDDFT, the EPH model and the TTM (solid lines). The electronic density seen by the projectile in the EPH model is represented in each case with a dashed black line. Beware that the y-axis scales are not the same in each graph.*

The TTM fitted energy loss curves in the channel cases of Fig. 5.13, although they are completely linear, gives good overall trends in many cases, as can be observed in Fig. 5.13. According to Table 5.6, the MAE is even smaller in the TTM fitted case than in both the constant and quadratic MD-EPH scenarios for the <110> center channel, and smaller than the quadratic MAE for the <001> center channel (MAE of 16.4 eV with the TTM fitted compared to 20.9 eV in the quadratic case). However, the TTM fitted performs clearly worse than the constant and quadratic EPH cases for the <111> center channel, <001> off-center channel (1/4) and <110> off-center channel trajectories.

From Fig. 5.13e it is blatant that this is for the <001> off-center channel (1/4) that the TTM fitted performs the worst compared to the EPH model. The electronic density reaching very

high values in this case, the TTM fitted largely underestimates the value of the stopping as it cannot vary with the electronic density contrary to the stopping in the EPH model.

Table 5.6: *Distance (MAE) of the EPH and TTM fitted energy losses curves with respect to the reference TDDFT data.*

	EPH Constant (eV)	EPH Quadratic (eV)	TTM fitted (eV)
Center channel <001>	14.6	20.9	16.4
Center channel <110>	75.3	87.7	36.8
Center channel <111>	6.2	3.8	14.6
Off-center channel <001> (1/2)	4.2	11.3	13.5
Off-center channel <001> (1/4)	9.2	29.2	67.2
Off-center channel <110>	3.6	4.6	8.7
Incommensurate 1	5.6	9.6	16.6
Incommensurate 1 + vacancy	8.2	17.3	10.0
Incommensurate 2	6.8	14.3	36.6
Incommensurate 3	21.5	25.2	20.8
Total	15.1	22.5	27.3

Now focusing on the incommensurate directions of Fig. 5.14, the TTM curves in their SRIM-derived parametrizations show again very large discrepancies with the reference TDDFT data.

We also observe with the incommensurate directions that during close encounters (collisions) between the projectile and an atom of the lattice, the energy loss to electrons in the EPH model in the graphs of Fig. 5.14 is step-like. It degrades a bit the similarities between the TDDFT and the EPH data. Due to this step-like behavior, rather than searching for point by point correspondence between the TDDFT data and our EPH curves during those close encounters, we aim at obtaining on average during the shock a good fit between EPH and TDDFT data. In other words, we aim at having the value of energy loss to electrons with the EPH model the closest possible to the TDDFT data, after the shock.

In spite of this step-like behavior, visually from Fig. 5.14, the comparison of different incommensurate trajectories seems to be in favor of the EPH model compared to the TTM fitted. Indeed, for all the directions sampled, the EPH model, especially in its constant $\alpha(\rho)$ formulation, follows quite closely the reference TDDFT curves, except in the Incommensurate 3 direction (Fig. 5.14d) where the energy lost during the collision (the electronic density peak) is overestimated. The low density regions and in most cases the high density ones seem to be well reproduced by the EPH model, and the density dependence of the energy loss to electrons globally well followed. It can be easily noticed visually from Fig. 5.14b and Fig. 5.14c that the constant MD-EPH performs better than the quadratic one. Table 5.6 actually indicates that for incommensurate directions, the constant EPH always performs better than the quadratic one.

Following Table 5.6, the TTM fitted performs worse than the EPH constant case for all incommensurate directions but the incommensurate 3 case. It is for the incommensurate 2 direction that the MAE difference is the greatest, the EPH constant case having a MAE of 6.8 eV and the TTM fitted a MAE of 36.6 eV. Just like in the case of channeling trajectories, the case in which the TTM fitted performs the worst is the case in which the highest electronic density is sampled. The quadratic EPH reproduces the TDDFT data better than the TTM fitted for the incommensurate 1 (MAE of 9.6 eV compared to 16.6 eV), the incommensurate 2 (MAE of 14.3 eV compared to 36.6 eV) directions, but worse for the incommensurate 1 + vacancy (MAE of 17.3 eV compared to 10.0 eV) and incommensurate 3 (MAE of 25.2 eV compared to 20.8 eV).

On the whole, the EPH constant and quadratic cases performs better than the TTM fitted, the total MAE of the constant EPH case being of 15.1 eV, the one of the quadratic EPH of 22.5 eV and the one of the TTM fitted of 27.3 eV. Visually, from Fig. 5.13 and Fig. 5.14, the EPH model also allows to reproduce in many cases very closely the density dependence of the stopping observed in TDDFT simulations, which is, on top of the quantitatively better MAE, more satisfactory from a physical standpoint than the always constant stopping given by the TTM fitted.

Also, on the whole, the constant EPH performs better than the quadratic one (Total MAE of 15.1 eV compared to 22.5 eV), which can be surprising considering the relative complexity of both functions, and the fact that an $\alpha(\rho)$ parameter shape in many ways similar to our quadratic expression was employed in [13]. This means that, the density terms appearing as weighting factors in (3.60) are sufficient to guarantee a rich density dependent behavior of the stopping in the EPH model. An important reason for the less satisfactory performance of the quadratic EPH regarding TDDFT data lies in the decay to zero we have chosen for the quadratic expression. Indeed, in light of the graphs of Fig. 5.13 and Fig. 5.14, it is questionable as no step-like behavior of the stopping is observed in our TDDFT data like it was in [13]. However, a decay is necessary otherwise the energy loss to electrons would diverge in regions of high electronic densities. As a compromise, it could be a wise choice to set this decay to a non-zero value instead of strictly zero, or to make the $\alpha(\rho)$ function reach an asymptote which could be adequate to reproduce the stopping at high densities as we observed it seems to reach a plateau in regions of high electronic densities. However, in this study we wanted to keep our $\alpha(\rho)$ expression simple and as easy as possible to optimize and to follow the advice of the original articles of the EPH model [13, 14] for the shape of $\alpha(\rho)$.

Regarding the constant parametrization of the EPH model, in spite of the good results it provides, the fact that α is non-zero when $\rho = 0$ ought to be discussed. Indeed, as we said earlier, it is more satisfactory physically to have $\alpha(\rho) \approx 0$ at low ρ. A consequence of this might be an overestimation of the electron-phonon coupling strength as the part of the $\alpha(\rho)$ function governing the magnitude of electron-phonon coupling in the low ρ one. This is an aspect we can only assess by performing MD-EPH simulations of collision cascades with different thermal parameters of the EPH model, like we did in [17] with the TTM. To provide an answer to this question, among other objectives, the next section is dedicated to simulations of collision cascades with the EPH model and with the TTM for comparison. Cascades results in terms of number of defects, number of clusters or PKA penetration depth are compared and discussed, and the effects of the thermal parameters of both the EPH model and the TTM are investigated.

5.2.3 Collision cascades with the EPH model

5.2.3.1 Computational details

We use the LAMMPS code for MD simulations [18]. The cascades are initiated with 10 keV PKAs in Si. Boxes of 1 000 000 atoms made of 50×50×50 diamond-like unit cells and 4 096 000 atoms made of 80×80×80 diamond-like unit cells are employed. The simulation boxes are divided into two areas: in the outer cells the velocities are rescaled to maintain the temperature at a desired value, and the inner cells form an NVE ensemble in which the atoms evolve freely to simulate the collision cascade.

The initialization of the simulation is made by scaling the velocities of all atoms, such that the overall temperature is the desired one (300 K in the current work). For calculations carried out with the TTM, the system is equilibrated for at least 20 ps with a timestep of 1 fs. With the EPH, we found that this equilibration time needed to be increased to 100 ps. As the velocity

of the atoms drastically changes throughout the cascade, the integration timestep has to be changed during the simulations. We imposed the condition that no atom moves more than 0.02 Å between two steps of the simulation, with a timestep varying between 0.001 fs and 1 fs. The potential employed is the SW one developed in [20], combined to the ZBL [21] as described in Chapter 3.

To correctly account for the stochasticity of the cascades, distributions and statistical quantities are based on 75 simulations in distinct independent directions. We usually employ sets of 100 simulations but the high computational cost of simulations with the EPH model compelled us to reduce this number to the already satisfactory one of 75. The method employed for choosing the directions is detailed in Chapter 4.

5.2.3.2 Methodology

To assess the influence of the thermal parameters of the EPH model and of the TTM, *i.e.* the electronic specific heat C_e and the electronic thermal conductivity κ_e, simulations with different values of those parameters are carried out. In all the simulations launched, C_e and κ_e are considered to be constant. We employ this approximation so that the effects of C_e and κ_e are easier to observe and discuss. In reality, C_e and κ_e are electronic temperature T_{elec}-dependent.

The scenario we label 1 refers to a case where C_e and κ_e are purposely set to low values compared to what could be considered as the reference electronic temperature T_{elec} dependent ones. In scenario 1, $C_e = 5 \times 10^{-6}$ eV/K and $\kappa_e = 5 \times 10^{-3}$ eV/K/Å/ps. It corresponds to realistic values of C_e and κ_e at low T_{elec}, but not on the entire range of T_{elec} spanned in the simulations (see Fig. 3.12).

The scenario we label 2 refers to a case where C_e and κ_e are purposely set to high values compared to what could be considered as the reference electronic temperature T_{elec} dependent ones. In scenario 2, $C_e = 3/2k_B = 1.29 \times 10^{-4}$ eV/K and $\kappa_e = 1.29 \times 10^{-1}$ eV/K/Å/ps. It corresponds to realistic values of C_e and κ_e at high T_{elec}, but not in the entire range of T_{elec} spanned in the simulations (see Fig. 3.12).

The scenario we label 3 refers to a mix between scenario 1 and scenario 2: C_e takes the high value it has in scenario 1 and κ_e the low value it has in scenario 2. In scenario 3, $C_e = 1.29 \times 10^{-4}$ eV/K and $\kappa_e = 5 \times 10^{-3}$ eV/K/Å/ps.

Those three scenarios are employed with the TTM and with the constant parametrization of the EPH model. Only scenario 3 is used with the EPH quadratic parametrization, as our results with the constant parametrization of the TTM show, as we will see later, it is not necessary to perform simulations with all the thermal parameters scenarios in the quadratic EPH case.

5.2.3.3 Results and discussions

Table 5.7 summarizes the parameters employed in the various collision cascades scenarios we simulated, and gives the mean values of the number of defects, the number of clusters and the mean PKA penetration depth for each of those scenarios. Fig. 5.15 and Fig. 5.16 respectively show the distribution of the number of defects and of the PKA penetration depth under the form of box plots for all the studied simulation scenarios.

Table 5.7: *Summary of the parameters employed in the different sets of cascades simulations carried out and mean values of the number of defects, number of clusters and of the PKA penetration depth for all the simulation sets. The value in brackets next to the mean values correspond to the SEM values. Each mean value is calculated from a set of 75 simulations initiated with distinct PKA directions. This table only gives a summary of the parameters employed, more details can be found in the text.*

Model employed	EPH				TTM (SRIM)		
α function (for EPH)	Quadratic	Constant					
Thermal scenario name	3	1	2	3	1	2	3
C_e	High	Low	High	High	Low	High	High
κ_e	Low	Low	High	Low	Low	High	Low
Elec. stopp. + el-ph	Fitted	Fitted	Fitted	Fitted	SRIM + [44]	SRIM + [44]	SRIM + [44]
Mean number of defects	767 (21)	730 (17)	763 (21)	719 (16)	1299 (47)	473 (10)	555 (17)
Mean number of clusters	46 (1)	47 (1)	46 (1)	46 (1)	21 (1)	38 (1)	33 (1)
Mean PKA depth (Å)	156 (7)	160 (7)	151 (7)	150 (8)	151 (6)	150 (7)	144 (7)

5.2.3.3.1 Defects and clusters evolution

From Fig. 5.15, the similarity between all the EPH scenarios is immediately striking. The different thermal parameters employed in the constant case as well as the switch between quadratic or constant parametrizations do not seem to lead to visible effects on the number of defects. The first, second and third quartile values are comparable between each studied scenario. The minimum and maximum values show larger discrepancies but this cannot be attributed to changes in the thermal parameters or in the α function employed. The high degree of stochasticity of the cascades makes it very difficult to have converged minimum and maximum values for a given set of simulations. Consequently, it is very hard to draw conclusions from the minimum and maximum values only. The similar values in the number of defects between all the scenarios studied with the EPH model can also be observed in the mean values displayed in Table 5.7, differing by at most 48 defects and having SEM values of about 20 each time. The mean number of clusters displayed in Table 5.7 are even more similar, with mean values differing at most by 1 cluster only.

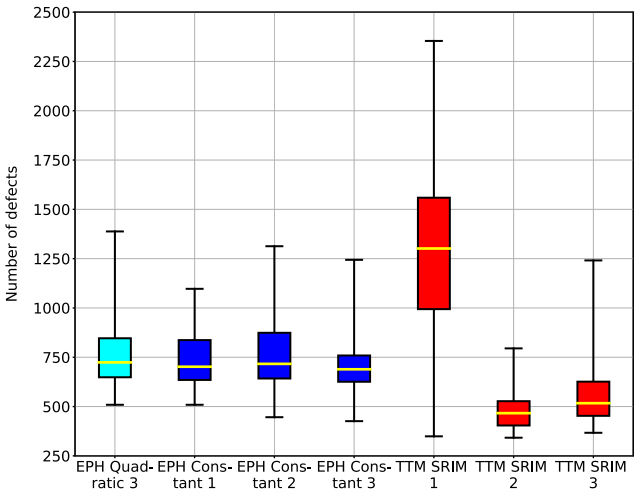

Figure 5.15: *Box plots of the number of defects obtained after 300 ps of simulations for all the studied sets of parameters with the TTM and EPH models. From lowest to highest, the horizontal lines of a box plot represent the minimum value of the set, the first quartile value, the median (or second quartile value, in yellow), the third quartile and the maximum value of the set. Box plots are constructed from 75 simulations in each case.*

The fact that the constant and quadratic parametrizations of the EPH model give similar defects number is not surprising considering both parameters have been fitted to reproduce the same reference TDDFT data. More interestingly and less expected, the fact that the different thermal scenarios used in the constant α case (which as we said earlier is expected to overestimate the electron-phonon coupling magnitude), show no conclusive variations in the number of defects reveals that the electron-phonon coupling has no effect on the defects formation. Indeed, the thermal parameters C_e and κ_e of the EPH model (and of the TTM), do not act on the friction force acting on the moving projectile. They only control the electronic energy loss temporal rate (C_e) to the ions and the electronic energy diffusion to nearby electrons (κ_e). Thus, it means that in Si at 10 keV, no defects are created due to the energy fed back from the electrons to the ions via electron-phonon coupling. In the standard SRIM parametrization of the TTM, with the electron-phonon coupling parameter taken from [44], we found in Section 5.1 that electron-phonon coupling had an effect on the creation of defects in Si and Ge. In Section 5.1, the simulations were carried out at the lower temperature of 100 K. To be able to compare our simulations, we launch new collision cascades simulations with the TTM in this section at 300 K, like it is done for the EPH model.

Looking at the box plots of the TTM scenarios in Fig. 5.15, it can be observed that the distributions of the number of defects between the studied thermal scenarios show impressive discrepancies. The entire distribution of scenario 1 is obviously shifted upwards compared to scenarios 2 and 3. Quantitatively, the median values in scenarios 2 and 3 are respectively of 467 and 517, whereas it is of 1308 for scenario 1. The first quartile values in scenarios 2 and 3 are respectively 404 and 453, whereas it is of 994 for scenario 1. The third quartile values in scenarios 2 and 3 are respectively 527 and 626, whereas it is of 1559 for scenario 1. This trend is confirmed by the mean values of the number of defects of Table 5.7, which are similar for scenarios 2 and 3 (473 and 555 respectively) and about 3 times greater for scenario 1 (1383). This goes in the sense of the parametric study of the TTM we performed in Section 5.1, where we observed that more defects were created with low values of C_e and κ_e. However, in the previous parametric study we performed on the TTM, the discrepancies between similar scenarios for the thermal parameters were much smaller. We checked the calculation of our number of defects with the Weigner-Seitz method of the OVITO software [35], and found the same factor of about 3 between the mean values. The fact that the present calculation are carried out at 300 K instead of 100 K like we did in Section 5.1 could explain those enhanced discrepancies. As it is clearly explained in Section 5.1.4 and above in this section, the only way the thermal parameters C_e and κ_e can influence the number of defects is via the electron-phonon coupling. If the energy fed back from the electrons to the ions via electron-phonon coupling is enough to induce melting of the material, the number of observed defects increases. Carrying out simulations at 300 K may favor this melting behavior. The comparison of the number of clusters also gives valuable information regarding the melting of the material in scenario 1 with the TTM. Indeed, according to Table 5.7, we find on average 38 and 33 clusters in the TTM scenarios 2 and 3, and only 21 for the scenario 1. Thus, with the scenario 1, more defects are contained within a smaller number of clusters, meaning that the clusters are bigger. Looking at the size and shape of the clusters of defects, in the case of scenario 1, for nearly all the cascades, defects are almost all contained in very large amorphous pockets (which we trivially define to be clusters containing more than 100 defects), which is by far less frequent in cascades of scenarios 2 and 3: 76% of defects are contained in amorphous clusters in scenario 1 whereas only 10% and 25% in scenario 2 and 3 respectively. The low values of C_e and κ_e indeed induced melting via electron-phonon coupling, which led to those large amorphous pockets. From the basic heat diffusion equation of the TTM [1], a low value of C_e results in a high rate of energy exchange between electrons and ions [2], and a low value of κ_e gives a poor distribution of electronic heat in the material. As a result, the electronic energy is contained in very specific regions of the material and is very quickly fed back to the ions of the same regions, thus inducing melting. From the figures mentioned above,

it also appears that a bit more defects are observed in scenario 3 compared to scenario 2, as well as less clusters. It also indicates an increase melting of the material due to the low value of κ_e employed in scenario 3. However, this melting is by far less important than in scenario 1, meaning that this is the combined effects of C_e and κ_e which led to the large melting in scenario 1. Note than with the SW potential, the lattice thermal parameters of Si (melting point and lattice thermal conductivity) are well reproduced [11], the melting behavior of the material is therefore realistic. The important point to remember from those MD-TTM cascades calculations in Si is that with the TTM, electron-phonon coupling can have very large effects on the number of defects in collision cascades in Si, whereas with the EPH model, the electron-phonon coupling was not found to have any effect. Despite the fact the parameters chosen for κ_e and C_e in scenario 1 are unrealistic, this is a first hint pointing towards the fact that the TTM in its original form [1], and parametrized with SRIM for γ_s and a literature search for γ_p, might overestimate the effects of the electron-phonon coupling in collision cascades. Another argument that supports this point is that experimentally, amorphization of Si via electronic mechanisms occur with swift heavy ion irradiation of considerably greater energy compared to our 10 keV collision cascades, *i.e.* tens of MeV [45, 46]. Thus, melting (amorphization) of the material via electron-phonon coupling as important as the one we observe with the TTM in scenario 1 is highly unrealistic. To counterbalance what we just said, one could argue that the overall lower electronic stopping power at stake in the EPH model compared to the TTM makes the amount of energy lost to electrons smaller than with the TTM and thus reduces the possibility to observe electron-phonon coupling effects as there is less energy to give back to the ions. MD-EPH simulations with various values of constant α and performed on a system where thermal effects are more obvious than in Si, like Ge for example [11, 17], would help to set light on this specific point.

We now focus on scenarios 2 and 3 of the TTM and 1, 2 and 3 for the EPH model, for which energy transfer via electron-phonon coupling has very few effects on the number of defects. The comparison of the distributions for the number of defects showed in Fig. 5.15 with the EPH model and the TTM immediately reveals that a lot more defects are created with the EPH model than with the SRIM parametrization of the TTM. The median of the number of defects for all the EPH model scenarios is comprised between 719 and 763, whereas with the scenario 2 and 3 of the TTM we respectively have a median of 467 and 517. The mean values of Table 5.7 displays about the same discrepancy, with mean values ranging from 719 to 767 with the EPH model and mean values of 473 (scenario 2) and 555 (scenario 3) with the TTM in its SRIM parametrization. This can be easily explained by the fact that the amount of energy loss to the electrons obtained with the EPH model fitted to the reference TDDFT data is by far smaller than the amount of energy loss to the electrons with the SRIM parametrization of the TTM, as displayed in Fig. 5.13 and Fig. 5.14. Consequently, as less energy is lost to electrons, more energy is available to create defects via collisions between ions or local melting of the matter as it occurs in semiconducting materials [10, 47]. This highlights the significance of the existing controversy between SRIM and TDDFT electronic stopping calculations, as we prove here it has an important impact on the number of defects created during collision cascades. To be complete on this point, note that in the TTM, the electron-phonon coupling parameter γ_p also contributes to the friction force, the total friction coefficient being the sum of the electronic stopping parameter γ_s and γ_p. The discrepancies between the number of defects observed with the EPH and the TTM scenarios are therefore enhanced by this aspect of the TTM.

To conclude on the defects analysis, the results obtained with the EPH model and with the TTM would be much more similar if we had employed the TTM parameters we fitted to the TDDFT data in Section 5.2.2. However, a TTM parametrization with TDDFT data is not representative of the use that is made of the TTM. Here, we wanted to compare the results obtained following the default guidelines for the parametrization of both models [1, 13].

5.2.3.3.2 PKA penetration depth

The analysis of the PKA penetration depth is more straightforward than the number of defects and clusters. The mean values of Table 5.7 reveals that the mean PKA penetration depth for the EPH scenarios are all comprised between 151 Å and 160 Å. The SEM values (about 8) accompanying those mean values conduct to consider the PKA penetration depth in all the EPH scenarios as being similar: no evolution or trends in the mean PKA depth can be observed. The fact that the thermal scenarios of the constant parametrization of the EPH model do not yield different values of the PKA penetration depth is expected, as both C_e and κ_e do not act on the friction force the moving ions are subject to. Considering the similarities in the electronic stopping between the constant and quadratic parametrization of the EPH model for all the directions studied in Section 5.2.2, the very similar mean values of the PKA penetration depth for the EPH constant and quadratic cases are coherent as well.

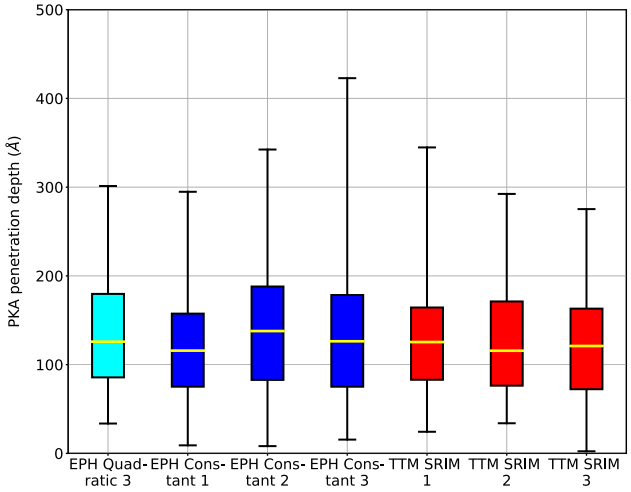

Figure 5.16: *Box plots of the PKA penetration depth for all the studied sets of parameters with the TTM and EPH models. From lowest to highest, the horizontal lines of a box plot represent the minimum value of the set, the first quartile value, the median (or second quartile value, in yellow), the third quartile and the maximum value of the set. Box plots are constructed from 75 simulations in each case.*

The mean values of the PKA penetration depth for the TTM scenarios are also very consistent one with another (151 Å, 150 Å and 144 Å for scenarios 1, 2 and 3 respectively), for the same reasons than the ones just exposed for the EPH thermal scenarios. However, it seems that the mean values of the PKA penetration depth of the EPH model are slightly greater than the ones obtained with the SRIM parametrization of the TTM. The uncertainties (SEM values) coming with those mean values do not allow to be completely conclusive on this point. The analysis of the box plots of Fig. 5.16 do not give much more information on this aspect as all the distributions seem to be fairly similar: no clear trend or behavior can be observed.

An increase in the PKA penetration depth with the EPH model would be physically sound. Indeed, the electronic stopping with the EPH model is overall smaller than with the SRIM parametrization of the TTM we adopted. Moreover, with the EPH model, the electronic stopping is specifically low for channelling directions (see Fig. 5.13), allowing for an increased depth of the PKAs if they find themselves in a channelling direction. The slight increase in the mean PKA penetration depth for the EPH model goes in this sense, even if it is less blatant one could expect it to be. Interestingly, the discrepancies are even smaller than what we observed in our parametric study of the TTM in Section 5.1.3. The conclusion of those observations, similarly to what we observed for the PKA penetration depth in Chapter 4, is that, in low

energy collision cascades, the PKA depth is a quantity it is hard to draw conclusions on, even with 75 simulations. However, if it is very difficult to be conclusive on the PKA penetration depth, the electronic stopping impact on the creation of defects, especially in semiconducting materials where the formation of amorphous pockets of defects can be observed, is obvious.

5.2.4 Partial conclusion

First principles TDDFT calculations of electronic stopping were combined with the EPH model for the inclusion of non-adiabatic electronic effects into MD simulations of collision cascades. A simple parametrization of the EPH model with a constant α function already gives very satisfactory results in terms of electronic density (or crystal direction) dependence of the electronic stopping obtained with MD-EPH simulations in Si, considering TDDFT results as the reference. If the TTM in its SRIM parametrization obviously does not allow reproduction of the TDDFT data, when parameters of the TTM are fitted to the TDDFT data, although the energy loss to electrons is independent of the electronic density and the friction parameter is scalar, the results obtained do not differ as much as one could expect from the TDDFT data. However, the EPH model allows to better reproduce the electronic stopping calculated with TDDFT in Si than the TTM, whose incorporation of electronic stopping is not tensorial and density-dependent like in the EPH model. Indeed, quantitatively the agreement between the EPH model and TDDFT is better, and qualitatively it makes more sense physically speaking for the electronic stopping to be dependent on the electronic density. By refining the $\alpha(\rho)$ expressions employed for the fitting, we believe even better reproduction of the TDDFT data can be achieved with the EPH model.

Collision cascades carried out in Si at 10 keV have revealed that the choice of the model employed for the inclusion of the electronic effects and the parametrization of the chosen model have a significant influence on the number of defects created. Our collision cascades simulations performed with the EPH model fitted on TDDFT data gives a lot more defects than cascades carried out with the TTM parametrized with SRIM calculations. Fundamental discussions comparing SRIM and TDDFT electronic stopping calculations are then of prime importance as it has visible effects on collision cascades even at the relatively low energy of 10 keV. The impact of the electron-phonon coupling on the creation of defects is found to be significant with the TTM and highly dependent on the C_e and κ_e parameters chosen, whereas no influence of the electron-phonon coupling on the creation of defects was observed with the EPH model in Si. This last aspect points towards a probable overestimation of the significance of electron-phonon coupling in the naive but widespread parametrization method we employed for the TTM. Additional calculations with the EPH model at different energies, with different parameters and on different systems would considerably help to be totally conclusive on the significance of electron-phonon coupling in collision cascades.

On the whole, we believe this study gives solid proofs in favor of the necessity of pursuing the studies comparing SRIM-derived and TDDFT-derived electronic stopping (actually on the understanding and quantification of electronic stopping in general), as well as trustworthy arguments defending the significant impact the finer incorporation of electron-phonon coupling within the EPH model has on collision cascades results.

Conclusion

The first part of this chapter is dedicated to the extensive study of the effects of the most used model for the inclusion of electronic effects into MD simulations of collision cascades, *i.e.* the TTM. The quantitative study performed is very valuable for anybody using or interested in the use of the TTM, as it contributes to identify the most important parameters and their effects.

Interesting effects of some parameters of the TTM were identified and interpreted in light of the properties of the studied materials. However, the study performed also highlights the limitations of the TTM, in terms of uncertainties in the choice of the parameters, and implementation of some physical features, for instance electron-phonon coupling. The EPH model, which we employ in the second part of this chapter, seems to correct some issues and limitations regarding the use of the TTM. Even if the intrinsically greater computational cost of the EPH model compared to the TTM and the need to resort to TDDFT for its parametrization make its use much more complicated than the TTM, this is the price to pay for the greatly enhanced physical description it offers compared to the TTM. However, in the case of Si, the differences in electronic stopping powers obtained with TDDFT (and consequently with the EPH model) and with SRIM we observed is a major question which should be answered for future users to be confident in the EPH model. Future works on the subject of TDDFT calculations of electronic stopping should try to answer to this question.

In the next and final chapter, we employ the TTM in our MD simulations as the simulations conducting to the results showed were even started before the EPH model was developed and used in collision cascades simulations.

References

[1] D. M. Duffy and A. M. Rutherford, "Including the effects of electronic stopping and electron-ion interactions in radiation damage simulations", J. Phys.: Cond. Matter. **19**, 1–11 (2007).

[2] G. Khara, S. T. Murphy, S. L. Daraszewicz, and D. M. Duffy, "The influence of the electronic specific heat on swift heavy ion irradiation simulations in silicon", J. Phys.: Cond. Matter. **28**, 395201 (2016).

[3] E. Zarkadoula, G. Samolyuk, and W. J. Weber, "Effects of the two-temperature model on cascade evolution in Ni and NiFe", J. Nucl. Mat. **490**, 317–322 (2017).

[4] J. Cui, Z. Zhou, B. Fu, and Q. Hou, "Assessing the influence of electronic effects on molecular dynamics simulations of primary radiation damage in tungsten", Nucl. Instr. Meth. Phys. R. B **471**, 90–99 (2020).

[5] A. E. Sand, S. L. Dudarev, and K. Nordlund, "High-energy collision cascades in tungsten: Dislocation loops structure and clustering scaling laws", Europhys. Lett. **103**, 46003 (2013).

[6] A. E. Sand, K. Nordlund, and S. L. Dudarev, "Radiation damage production in massive cascades initiated by fusion neutrons in tungsten", Nucl. Instr. Meth. Phys. R. B, 207–211 (2014).

[7] E. Zarkadoula, D. D. M., N. K., S. M. A., T. I. T., W. J. Weber, and K. Trachenko, "Electronic effects in high-energy radiation damage in tungsten", J. Phys.: Cond. Matter. **27**, 135401 (2015).

[8] E. Zarkadoula, G. Samolyuk, H. Xuen, H. Bei, and W. J. Weberab, "Effects of the two-temperature model on cascade evolution in Ni and NiFe", Scr. Mat. **124**, 6–10 (2016).

[9] N. Chen, E. Rasch, D. Huang, E. R. Heller, and F. Gao, "Atomic-Scale Simulation for Pseudometallic Defect-Generation Kinetics and Effective NIEL in GaN", IEEE Trans. Nucl. Sc. **65**, 1108–1118 (2018).

[10] K. Nordlund, M. Ghaly, R. S. Averback, M. Caturla, T. Diaz de la Rubia, and J. Tarus, "Defect production in collision cascades in elemental semiconductors and fcc metals", Phys. Rev. B **57**, 7556–7570 (1998).

[11] P. Lopez, L. Pelaz, I. Santos, L. A. Marques, and M. Aboy, "Molecular dynamics simulations of damage production by thermal spikes in Ge", J. App. Phys. **111**, 033519 (2012).

[12] A. Tamm, M. Caro, A. Caro, G. Samolyuk, M. Klintenberg, and A. A. Correa, "Langevin Dynamics with Spatial Correlations as a Model for Electron-Phonon Coupling", Phys. Rev. Lett. **120**, 185501 (2018).

[13] M. Caro, A. Tamm, A. A. Correa, and A. Caro, "Role of electrons in collisions cascades in solids. 1. Dissipative model", Phys. Rev. B **99**, 174301 (2019).

[14] A. Tamm, M. Caro, A. Caro, and A. A. Correa, "Role of electrons in collision cascades in solids. 2. Molecular dynamics", Phys. Rev. B **99**, 174302 (2019).

[15] F. Gygi, "Architecture of Qbox: A scalable first-principles molecular dynamics code", IBM Jour. Res. Dev. **52**, 137–144 (2008).

[16] E. W. Draeger, X. Andrade, J. A. Gunnels, A. Bhatele, A. Schleife, and A. A. Correa, "Massively parallel first-principles simulation of electron dynamics in materials", J. Par. Dist. Comp. **106**, 205–214 (2017).

[17] T. Jarrin, A. Jay, A. Hémeryck, and N. Richard, "Parametric study of the Two-Temperature Model for Molecular Dynamics simulations of collision cascades in Si and Ge", Nucl. Instr. Meth. Phys. R. B **485**, 1–9 (2020).

[18] S. Plimton, "Fast Parallel Algorithms for Short-Range Molecular Dynamics", J. Comput. Phys. **117**, 1–19 (1995).

[19] A. Jay, M. Raine, N. Richard, N. Mousseau, V. Goiffon, A. Hémeryck, and P. Magnan, "Simulation of Single Particle Displacement Damage in Silicon–Part II: Generation and Long-Time Relaxation of Damage Structure", IEEE Trans. Nucl. Sc. **64**, 141–148 (2017).

[20] F. H. Stillinger and T. A. Weber, "Computer simulation of local order in condensed phases of silicon", Phys. Rev. B **31**, 5262–5271 (1985).

[21] J. F. Ziegler, J. P. Biersack, and U. Littmark, *The Stopping Range of Ions in Solids*, 1st ed. (Pergamon Press, N. Y, 1983).

[22] K. Ding and H. C. Andersen, "Molecular-dynamics simulation of amorphous germanium", Phys. Rev. B **34**, 6987–6991 (1986).

[23] M. Toulemonde, C. Dufour, A. Meftah, and E. Paumier, "Transient thermal processes in heavy ion irradiation of crystalline inorganic insulators", Nucl. Instr. Meth. Phys. R. B **166-167**, 903–912 (2000).

[24] H. Hensel and H. M. Urbassek, "Implantation and damage under low-energy Si self-bombardment", Phys. Rev. B **57**, 4756 (1998).

[25] C. Bjorkas and K. Nordlund, "Assessment of the relation between ion beam mixing electron-phonon coupling and damage production in Fe", Nucl. Instr. Meth. Phys. R. B **267**, 1830–1836 (2009).

[26] T. E. Haynes and H. O. W., "Damage accumulation during ion implantation of unstrained Si1-xGex alloy layers", Appl. Phys. Lett. **61**, 10.1063/1.107669 (1992).

[27] A. N. Larsen, "MeV ion implantation induced damage in relaxed Si1-xGex", J. App. Phys. **81**, 2208 (1997).

[28] Y. Kayser, P. Hönicke, D. Banas, J. Dousse, J. Hoszowska, P. Jagodzinski, A. Kubala-Kukus, S. H. Nowak, and M. Pajek, "Depth profiling of low energy ion implantations in Si and Ge by means of micro-focused grazing emission X-ray fluorescence and grazing incidence X-ray fluorescence", J. An. At. S. **30**, 1086–1099 (2015).

[29] I. Santos, L. A. Marques, L. Pelaz, and P. Lopez, "Molecular dynamics study of damage generation mechanisms in silicon at the low energy regime", in 2007 spanish conference on electron devices (2007), pp. 37–40.

[30] C. Kittel, *Introduction to Solid State Physics*, 8th ed. (John Wiley and Sons, 2004).

[31] R. Ullah, E. Artacho, and A. A. Correa, "Core Electrons in the Electronic Stopping of Heavy Ions", Phys. Rev. Lett. **121**, 116401 (2018).

[32] D. C. Yost, Y. Yao, and Y. Kanai, "Examining real-time time-dependent density functional theory nonequilibrium simulations for the calculation of electronic stopping power", Phys. Rev. B **96**, 115134 (2017).

[33] C. Lee, J. A. Stewart, R. Dingreville, S. M. Foiles, and A. Schleife, "Multiscale simulations of electron and ion dynamics in self-irradiated silicon", Phys. Rev. B **102**, 024107 (2020).

[34] J. Yang, "Opium-Pseudopotential Generation Project", http://opium.sourceforge.net (2018).

[35] A. Stukowski, "Visualization and analysis of atomistic simulation data with OVITO - the Open Visualization Tool", Mod. Sim. Mat. Sci. Eng. **18**, 015012 (2010).

[36] A. A. Correa, "Calculating electronic stopping power in materials from first principles", Comp. Mat. Sci. **150**, 291–303 (2018).

[37] A. Schleife, Y. Kanai, and A. A. Correa, "Accurate atomistic first-principles calculations of electronic stopping", Phys. Rev. B **91**, 014306 (2015).

[38] J. F. Ziegler, M. D. Ziegler, and J. P. Biersack, "SRIM - The stopping and range of ions in matter (2010)", Nucl. Instr. Meth. Phys. R. B **268**, 1818–1823 (2010).

[39] A. Lim, W. M. C. Foulkes, A. P. Horsfield, D. R. Mason, A. Schleife, E. W. Draeger, and A. A. Correa, "Electron Elevator: Excitations across the Band Gap via a Dynamical Gap State", Phys. Rev. Lett. **116**, 043201 (2016).

[40] S. Lohmann, R. Hole ňák, and D. Primetzhofer, "Trajectory-dependent electronic excitations by light and heavy ions around and below the bohr velocity", Phys. Rev. A **102**, 062803 (2020).

[41] M. Caro, A. Tamm, A. A. Correa, and A. Caro, "On the local density dependence of electronic stopping of ions in solids", J. Nucl. Mat. **507**, 258–266 (2018).

[42] P. Giannozzi et al., "QUANTUM ESPRESSO: a modular and open-source software project for quantum simulations of materials", J. Phys.: Cond. Matter. **21**, 395502 (2009).

[43] P. Giannozzi, O. Baseggio, P. Bonfà, D. Brunato, R. Car, I. Carnimeo, C. Cavazzoni, S. de Gironcoli, P. Delugas, F. Ferrari Ruffino, A. Ferretti, N. Marzari, I. Timrov, A. Urru, and S. Baroni, "Quantum ESPRESSO toward the exascale", J. Chem. Phys. **152**, 154105 (2020).

[44] A. Chettah, H. Kucal, Z. G. Wang, M. Kac, A. Meftah, and M. Toulemonde, "Behavior of crystalline silicon under huge electronic excitations: A transient thermal spike description", Nucl. Instr. Meth. Phys. R. B **267**, 2719–2724 (2009).

[45] A. Kamarou, W. Wesch, E. Wendler, A. Undisz, and M. Rettenmayr, "Radiation damage formation in InP, InSb, GaAs, GaP, Ge, and Si due to fast ions", Phys. Rev. B **78**, 054111 (2008).

[46] H. Amekura, M. Toulemonde, K. Narumi, R. Li, A. Chiba, Y. Hirano, K. Yamada, S. Yamamoto, N. Ishikawa, N. Okubo, and Y. Saitoh, "Ion track in silicon formed by much lower energy deposition than the track formation threshold", Nat. Sci. Rep. **11**, 185 (2021).

[47] K. Nordlund, S. J. Zinkle, S. A. E., F. Granberg, A. R. S., R. E. Stoller, T. Suzudo, L. Malerba, F. Banhart, W. J. Weber, F. Willaime, S. L. Dudarev, and D. Simeone, "Primary radiation damage: A review of current understanding and models", Phys. Rev. B **512**, 450–479 (2018).

Application of the multiscale approach to Si, Ge and Si-Ge alloys

6

Contents

Introduction

This last chapter is dedicated to the study of Si, Ge and Si-Ge alloys in the context of our multiscale approach. Firstly, we use Geant4 [1–3] to identify the PKA characteristics in order to be able to initiate the collision cascades in the MD step that follows (Section 6.1). Then, in Section 6.2, collision cascades simulations in Si, Ge and Si-Ge alloys are carried out. To our knowledge, collision cascades in Si and Ge have already been studied using MD in [4] and [5], but not in Si-Ge alloys. Aiming at being complete on the subject and providing interesting comparisons, we present MD results obtained on the three materials. Finally, clusters relaxation and damage healing are studied with kART.

6.1 Particle-matter interactions

6.1.1 Computational details

The Geant4 toolkit is employed for the simulations. The applications constructed are based on the Geant4 "Hadr04" example provided with the toolkit. As we are interested in neutron interactions with matter, the physics list employed for the simulations is the neutronHP one. The same simulations with protons would require another physics list, for example the QGSP_BIC one [6]. Cubic boxes of Si, Ge and $Si_{0.8}Ge_{0.2}$ are constructed, with a width of several tens of cm so that all particles interact within the box. The particles created following neutron irradiation are not followed (*i.e.* the simulation stops). Only their type and energy is stored. For each case studied, 10^6 simulations are launched, ensuring good statistics.

6.1.2 Results and discussions

We have investigated the effects of incident energetic neutrons ranging from 200 keV to 18 MeV on the production of PKAs in Si, Ge and Si-Ge alloys. For this section, we restrict our investigation of Si-Ge alloys to $Si_{0.8}Ge_{0.2}$. Indeed, this alloy composition is a widely employed one in the microelectronic industry, and is therefore of interest for us. In Section 6.1.2.1 we present and discuss the results obtained in Si, in Section 6.1.2.2 the ones obtained in Ge and in Section 6.1.2.3 the ones obtained in $Si_{0.8}Ge_{0.2}$.

6.1.2.1 Si

Fig. 6.1 shows the relative occurrence of the created PKAs in Si following an interaction with a neutron, depending on the energies of the PKAs, for neutron energies ranging from 200 keV to 18 MeV. The nearly flat shapes of the curves of Fig. 6.1 corresponding to neutrons of 200 keV and 700 keV reveal that, at those neutron energies, the energy distribution of the created PKAs is uniform. In other words, with 700 keV neutrons for example, there are about the same number of PKAs created with an energy of 500 eV and an energy of 80 keV. It also reveals that 200 keV neutrons can create PKAs in Si of at most about 40 keV, whereas 700 keV neutrons are able to create PKAs in Si of at most about 100 keV. As the energy of the neutrons increases, higher energy PKAs are being created. However, for low PKA energies (below about 50 keV), the curves still are more or less flat. At higher energies, the relative occurrence of relative PKAs decreases with the PKA energy. For all the neutrons energies considered, there are more low energy PKAs created than high energy ones. With 10 MeV neutrons, about 10 times more neutrons are created with an energy of 10 keV than with an energy of 10^3 keV. From 200 keV to 10 MeV neutrons, the maximum created PKA energy keeps increasing, whereas it stays constant from 10 MeV to 18 MeV. Indeed, the 10 MeV, 14 MeV and 18 MeV curves more or less overlap between 10^3 keV and 10^4 keV, and plunge at the same maximum value of about 10^4 keV. It probably means that inelastic nuclear reactions dominate at those high energies, otherwise the energy of the created PKAs would keep increasing with the neutron energy.

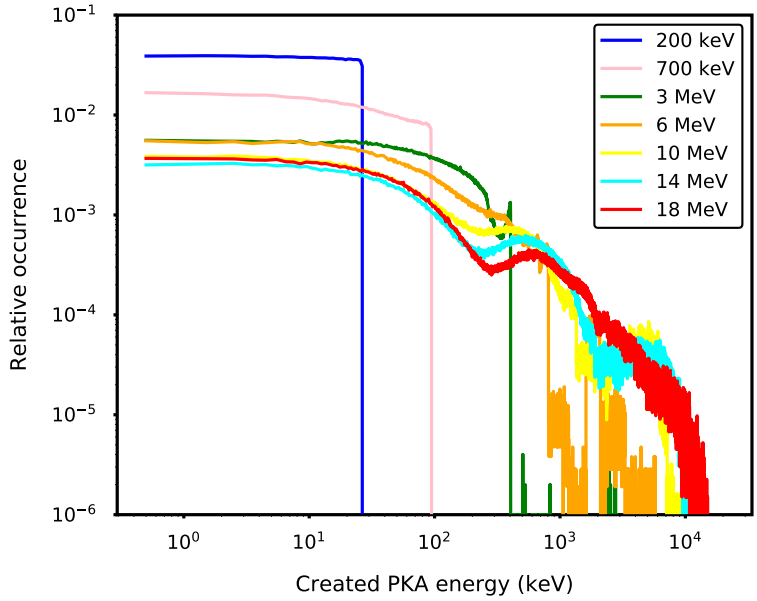

Figure 6.1: *Relative occurrence of PKAs created in Si as a function of their energy following a collision with a neutron, for neutrons energy ranging from 200 keV to 18 MeV. For each neutron energy, 10^6 simulations have been launched.*

Fig. 6.2 displays the ratio of created PKAs following interactions with neutrons having energies ranging from 200 keV to 18 MeV in Si, as a function of their type (Z number). In other words, it depicts the occurrence of spallation reactions depending on the neutrons energy. At 200 keV, 700 keV and 3 MeV, no or nearly no spallation reactions occur and 100% of the created PKAs are Si atoms. Then, as the energy increases, Al and Mg ions are being created. Protons and alpha particles, which are spallation products of the reaction leading to the formation of Al and Mg ions, are also created, but are not shown in Fig. 6.2. The ratio of Si ions among the created PKAs therefore decreases with the neutron energy. With neutrons of 18 MeV, about 55% of the created PKAs are Si ions, the rest is composed of Al, Mg, H (proton) and He (alpha particle) ions.

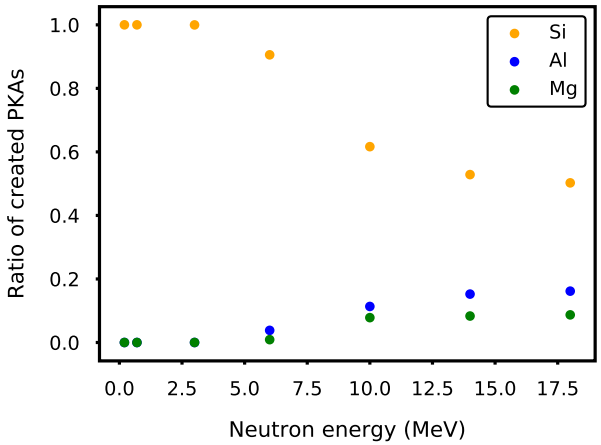

Figure 6.2: *Ratio of PKAs created in Si as a function of their type after collisions with neutrons of energies ranging from 200 keV to 18 MeV. For each neutron energy, 10^6 simulations have been launched. Only the heavy ($Z > 10$) spallation products are shown here. The data points of the created protons following spallation reactions would follow the one the Al PKAs, and the one of the alpha particles the one of the Mg PKAs.*

Fig. 6.3 shows the relative occurrence of the created protons and alpha particles (low Z PKAs) in Si following an interaction with a neutron, depending on the energies of the PKAs, for neutron energies ranging from 200 keV to 18 MeV. Coherently to what has been just said concerning Fig. 6.2, no or nearly no spallation reactions occur for 200 keV, 700 keV and 3 MeV neutrons. What is striking in the energy distribution of those light spallation products is that the high energy ones are found in greater quantities, which is the inverse of what was observed for all the PKAs indistinctly from their type in Fig. 6.1. Although they can be of high energy, those light particles actually lose the most part of their energy in ionization of the material and electronic excitations, and thus induce very little displacement damage compared to heavy PKAs. Moreover, they can travel over long distances in the material, and will presumably not have the occasion to induce any collisions in the sensitive region of a microelectronic device before exiting the material. Therefore, they are not of great interest for us.

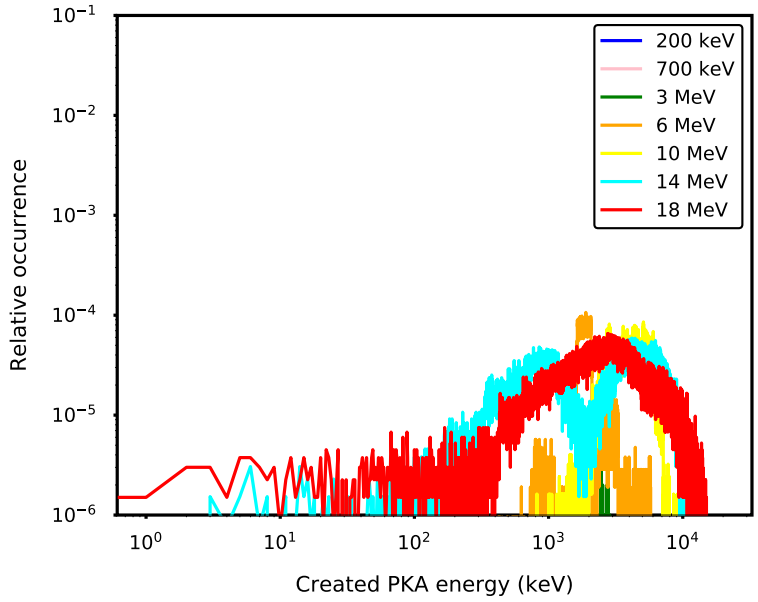

Figure 6.3: *Relative occurrence of light spallation products ($Z < 5$) created in Si as a function of their energy following the reaction with a neutron, for neutrons energy ranging from 200 keV to 18 MeV. For each neutron energy, 10^6 simulations have been launched.*

Fig. 6.4 shows the relative occurrence of the created Mg, Al and Si PKAs in Si following an interaction with a neutron, depending on the energies of the PKAs, for neutron energies ranging from 200 keV to 18 MeV. For all neutron energies, the curves are very similar to the ones of Fig. 6.1. The 200 keV, 700 keV and 3 MeV neutron curves are even identical in Fig. 6.1 and in Fig. 6.4 as no spallation reaction occurs for those neutron energies. The main differences lie in the high created PKAs energy region. Indeed, according to Fig. 6.4, there are less high energy PKAs created if we focus only on Mg, Al and Si ions rather than if we include all PKAs. It can be easily explained with the help of what we said about Fig. 6.3 and light PKAs: the high PKAs energy parts of the curves of Fig. 6.1 are actually made of protons and alpha particles, which are not considered in Fig. 6.4.

Fig. 6.5 displays the relative occurrence of only the created Si PKAs in Si following an interaction with a neutron, depending on the energies of the PKAs, for neutron energies ranging from 200 keV to 18 MeV. The global trends follow the ones of Fig. 6.1 and Fig. 6.4 which incorporate all PKAs and only $Z > 10$ PKAs respectively. However, we notice that the created Si PKAs reach a lower energy maximum for 6 MeV to 18 MeV incident neutrons than the $Z > 10$ PKAs of Fig. 6.4. It means that among the heavy PKAs, the most energetic ones are the spallation

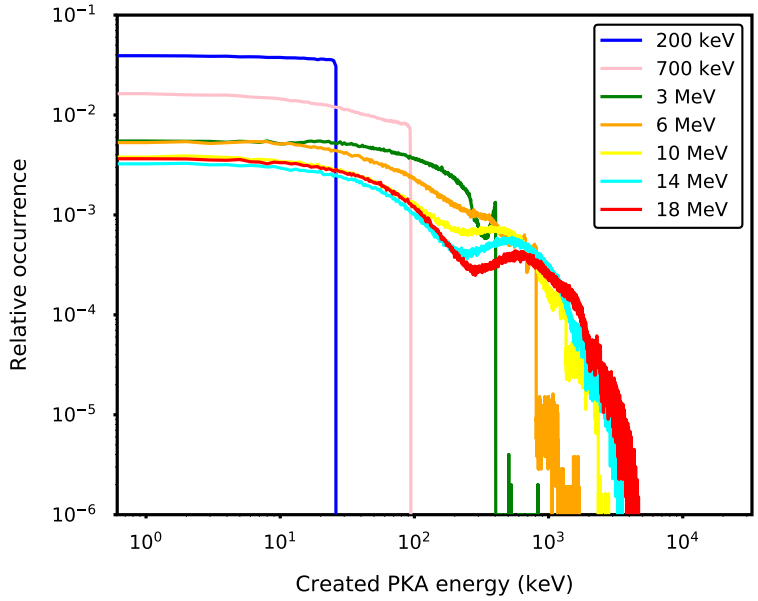

Figure 6.4: *Relative occurrence of heavy PKAs ($Z > 10$) created in Si as a function of their energy following the reaction with a neutron, for neutrons energy ranging from 200 keV to 18 MeV. For each neutron energy, 10^6 simulations have been launched.*

products Al and Mg. Moreover, we notice that contrary to Fig. 6.1 and Fig. 6.4, the greater the energy of the neutron, the greater the energy of the most energetic PKAs created. Indeed, as the interactions leading to the creation of Si PKAs are elastic, the maximum energy transmitted to the PKAs tends to increase with the incident neutrons energy.

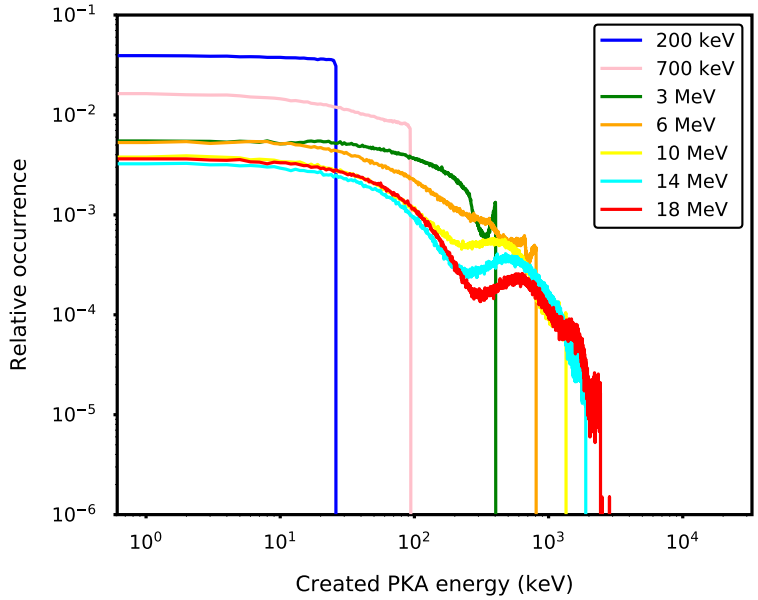

Figure 6.5: *Relative occurrence of strictly Si PKAs ($Z = 10$) created in Si as a function of their energy following collision with a neutron, for neutrons energy ranging from 200 keV to 18 MeV. For each neutron energy, 10^6 simulations have been launched.*

The series of graph discussed above provides important information for the choice of the energies and of the nature of the PKAs to employ for the MD simulations of collision cascades in Si. We found that the majority of created PKAs ($Z > 10$) have a relatively low energy (below 100 keV).

Moreover, it was shown in [6] with Geant4 that collision cascades initiated by high energy PKAs (above 100 keV) tend to split into subcascades, too far apart to overlap. This numerical result is supported by ion implantation experiments showing Transmission Electron Microscope (TEM) evidences of subcascade splitting [7–9]. It seems therefore sufficient to study the lower energy subcascades instead of the complete cascade, as the latter simply is an addition of subcascades. Moreover, in MD simulations of collision cascades, the initial energy of the PKA dictates the size of the simulation box to employ, and consequently the computational time. Considering we need to perform large number of simulations to cope with the stochasticity of the cascades, focusing on lower energy subcascades rather than on complete high energy cascades is thus of high interest. This is therefore what we do in the MD simulations of Section 6.2. We use 10 keV PKAs into Si, and from time to time 1 keV ones, thus ensuring to be below the subcascade splitting energy, and to employ the most frequently created PKA energies. We also saw that light spallation products contribute very little to atomic displacements. Thus, they will not be taken into account for MD simulations in Si. However, the question of the type of the PKAs to employ is not completely answered, as if we can eliminate protons and alpha particles, a non-negligible amount of Al and Mg ions are created, which are able to induce atomic displacements. The similar masses and atomic radius of Si, Al and Mg ions indicates their respective effect certainly are similar, in terms of clusters of defects created and displaced atoms. However, a cluster of defects having an Al or Mg impurity may have different electronic properties than "pure" clusters, only made of vacancies and Si interstitials. This could be a motivation to include the spallation PKAs in our MD study. Nonetheless, among all the defects created during a collision cascade, only one, the PKA which underwent a nuclear reaction with a neutron, is an impurity ion. Therefore, only one cluster of defects among all the created ones incorporates an impurity ion. We can thus consider the effects of the impurity ion can be neglected compared to the effects of all the other defects created. Moreover, thinking ahead to our next MD step, the MD interatomic potentials for pure Si are more trustworthy than the ones for mixed Si-Al and Si-Mg systems. Finally, in Si, we restrict ourselves to Si PKAs of about 10 keV.

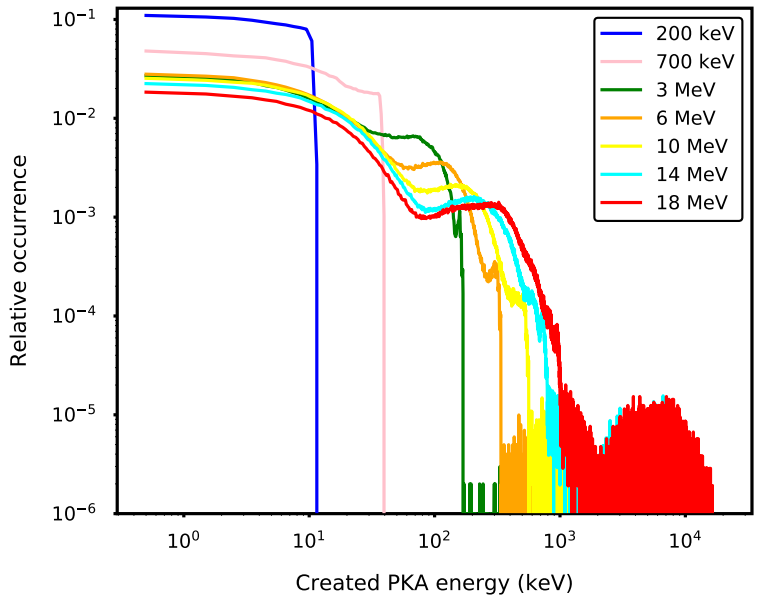

Figure 6.6: *Relative occurrence of PKAs created in Ge as a function of their energy following a collision with a neutron, for neutrons energy ranging from 200 keV to 18 MeV. For each neutron energy, 10^6 simulations have been launched.*

6.1.2.2 Ge

Fig. 6.6 shows the relative occurrence of the created PKAs in Ge following an interaction with a neutron, depending on the energies of the PKAs, for neutron energies ranging from 200 keV to 18 MeV. The overall shapes of the curves are very similar to the Si ones (see Fig. 6.1), the created PKAs being globally lower in energy. The main difference resides in the high energy part of the curves. In Si, the PKAs created following an interaction with 10 MeV, 14 MeV and 18 MeV neutrons have the same maximum energy, which is not the case in Ge where the higher the neutron energy, the higher the maximum PKA energy (a bit less than 10^3 keV for 10 MeV neutrons, a bit more than 10^3 keV for 14 MeV neutrons and about 10^4 keV for 18 MeV neutrons). It probably means that the majority of the interactions, even at those high neutron energies, are elastic.

Fig. 6.7 displays the ratio of created PKAs following interactions with neutrons having energies ranging from 200 keV to 18 MeV in Ge, as a function of their type (Z number). In other words, it depicts the occurrence of spallation reactions depending on the neutrons energy. The situation in Ge is very different from the situation in Si (see Fig. 6.2). Indeed, in Ge (Fig. 6.7), almost no spallation reaction occurs even with high neutron energies. With 18 MeV neutrons, only about 1% of the PKAs are Ga or Zn ions. This confirms what we said above concerning the high energy part of Fig. 6.6: spallation reactions are very rare.

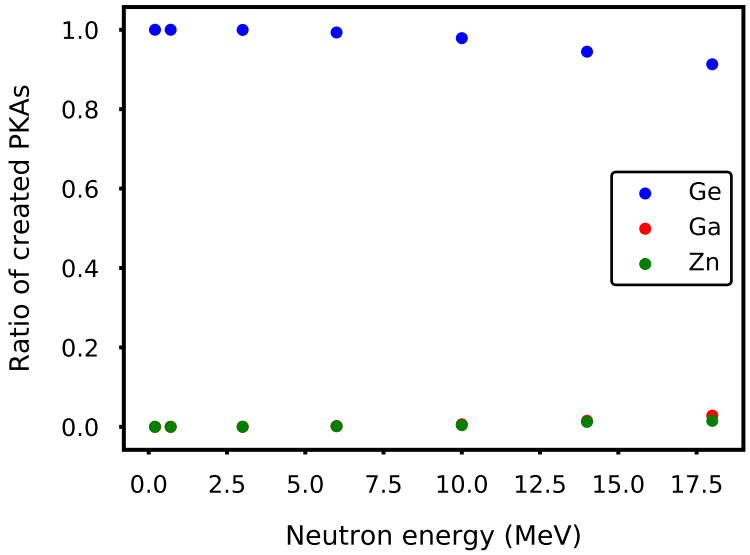

Figure 6.7: *Ratio of PKAs created in Ge as a function of their type after collisions with neutrons of energies ranging from 200 keV to 18 MeV. For each neutron energy, 10^6 simulations have been launched. Only the heavy ($Z > 10$) spallation products are shown here. The data points of the created protons following spallation reactions would follow the one the Ga PKAs, and the one of the alpha particles the one of the Zn PKAs.*

In Ge, it seems obvious that the PKAs employed for the MD simulation of collisions cascades should be Ge PKAs. The energy we should choose for those PKAs is subject to discussion, as we did not study subcascades splitting with Geant4. However, subcascade splitting was observed experimentally from ion implantation experiments carried out in Ge [9]. Moreover, as we want to be able to compare our results with Si, we employ PKAs of 10 keV in Ge as well.

6.1.2.3 Si-Ge alloys

We present the results obtained for the $Si_{0.8}Ge_{0.2}$ composition of the alloy only.

Fig. 6.8 shows the relative occurrence of the created PKAs in $Si_{0.8}Ge_{0.2}$ following an interaction with a neutron, depending on the energies of the PKAs, for neutron energies ranging from 200 keV to 18 MeV. We retrieve the nearly flat shapes of the 200 keV and 700 keV curves of Fig. 6.1 and Fig. 6.6. However, a small step can be noticed for those two neutron energies in Fig. 6.8, corresponding to the maximum energies of the PKAs created in Ge identified in Fig. 6.6, which are a bit lower than the ones created in Si (about 10 keV in Ge for 200 keV neutrons compared to about 50 keV in Si). Fig. 6.8 then seems to be a mix of Fig. 6.1 and Fig. 6.6. Higher energy curves follow the overall trends of the created PKA energies already observed in Si and Ge, with a relative occurrence of the created PKAs decreasing with the energy of the PKAs increasing.

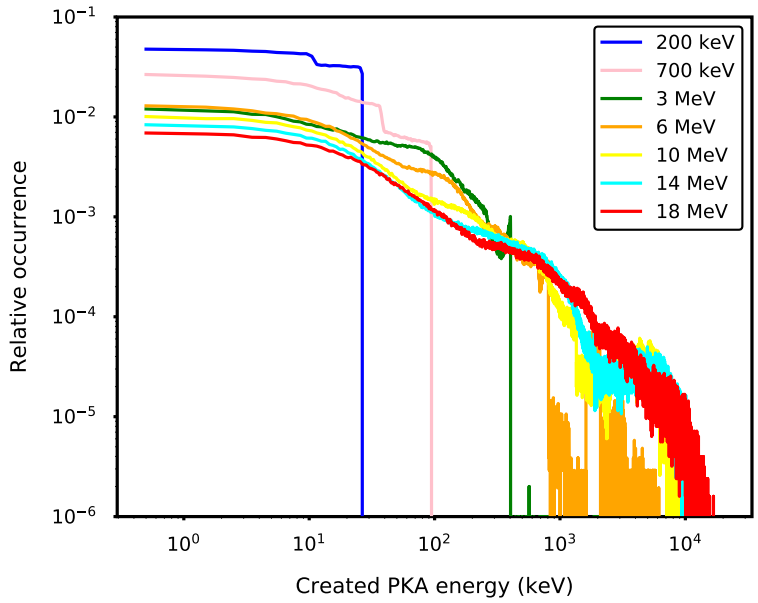

Figure 6.8: *Relative occurrence of PKAs created in $Si_{0.8}Ge_{0.2}$ as a function of their energy following a collision with a neutron, for neutrons energy ranging from 200 keV to 18 MeV. For each neutron energy, 10^6 simulations have been launched.*

Fig. 6.9 displays the ratio of created PKAs following interactions with neutrons having energies ranging from 200 keV to 18 MeV in $Si_{0.8}Ge_{0.2}$, as a function of their type (Z number). With a neutron energy of 200 keV, a great majority of Si PKAs are created (about 90%). The proportion of Si PKAs is thus greater than the initial percentage of Si atoms in the material (80%). However, already with 700 keV neutrons, the ratio of Ge PKAs formed (about 35%) overcomes the initial alloy composition (20% of Ge atoms). The ratio of created Si PKAs and Ge PKAs stays stable between 700 keV and 3 MeV, before slowly decreasing for both. For Si PKAs, spallation reactions inducing the formation of Al and Mg ions are responsible for this decrease. For Ge PKAs, as almost no spallation reaction occurs at the considered energies (we do not even show on the graph the Ga and Zn ions created as they count for less than 1% of the total), this decrease cannot be completely explained by spallation reactions. With 18 MeV neutrons, about 20% of the created PKAs are Ge PKAs, which corresponds to the initial alloy composition, and about 45% of the created PKAs are Si PKAs. The rest is made of Al and Mg ions (about 10% each), as well as traces of Ga and Zn ions. The majority of the created PKAs thus are either Si and Ge ions, and for a wide range of neutron energies, the ratio of created Ge PKAs overcomes the initial Ge alloy proportion.

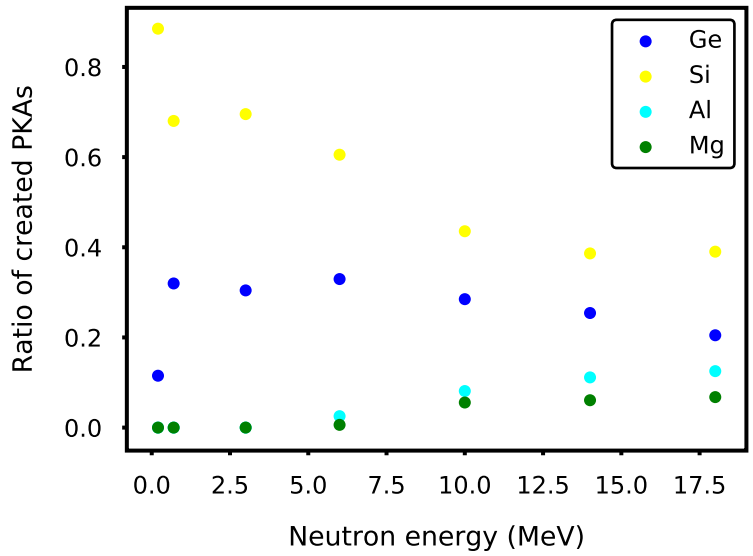

Figure 6.9: *Ratio of PKAs created in $Si_{0.8}Ge_{0.2}$ as a function of their type after collisions with neutrons of energies ranging from 200 keV to 18 MeV. For each neutron energy, 10^6 simulations have been launched. Only the heavy ($Z > 10$) spallation products are shown here. The data points of the created protons following spallation reactions would follow the one the Al PKAs, and the one of the alpha particles the one of the Mg PKAs.*

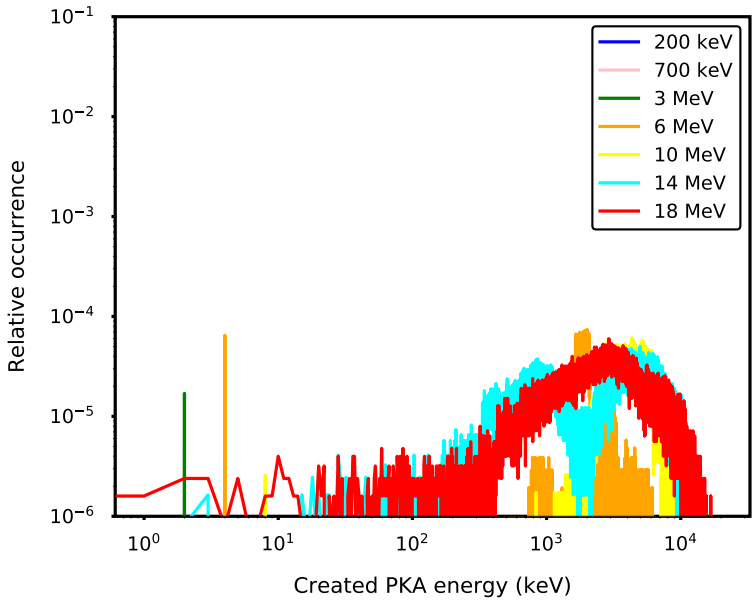

Figure 6.10: *Relative occurrence of light spallation products ($Z < 5$) created in $Si_{0.8}Ge_{0.2}$ as a function of their energy following an interaction with a neutron, for neutrons energy ranging from 200 keV to 18 MeV. For each neutron energy, 10^6 simulations have been launched.*

Fig. 6.10 shows the relative occurrence of the created protons and alpha particles PKAs in $Si_{0.8}Ge_{0.2}$ following an interaction with a neutron, depending on the energies of the PKAs, for neutron energies ranging from 200 keV to 18 MeV. Coherently to what has been just said concerning Fig. 6.2, no spallation reactions occur for 200 keV, 700 keV and 3 MeV neutrons. Indeed, no light Z PKAs are formed at those low energies. All the protons and alpha particles formed whose energy distribution is displayed in Fig. 6.10 originate from neutron collisions with Si atoms as we have seen in Fig. 6.9 that nearly no spallation reactions originate from Ge atoms

(very few Ga or Zn ions formed). Consequently, Fig. 6.10 is very similar to Fig. 6.3, with light particles being very high in energy. The same conclusions can be drawn from Fig. 6.3 and from Fig. 6.10, *i.e.* light PKAs will presumably not have the occasion to induce any collisions in the sensitive region of a microelectronic device before exiting the material. However, they are of great interest for anyone interested in devices degradation by ionization.

Fig. 6.11 shows the relative occurrence of the created heavy PKAs in $Si_{0.8}Ge_{0.2}$ ($Z > 10$) following an interaction with a neutron, depending on the energies of the PKAs, for neutron energies ranging from 200 keV to 18 MeV. The curves globally follow the same trends as the ones in pure Si (see Fig. 6.4). It again appears that the high energy parts of the curves of Fig. 6.8 are due to the light Z PKAs as the maximum PKAs energies reached with heavy PKAs in Fig. 6.11 are lower than the ones reached considering all the possible PKAs in Fig. 6.8.

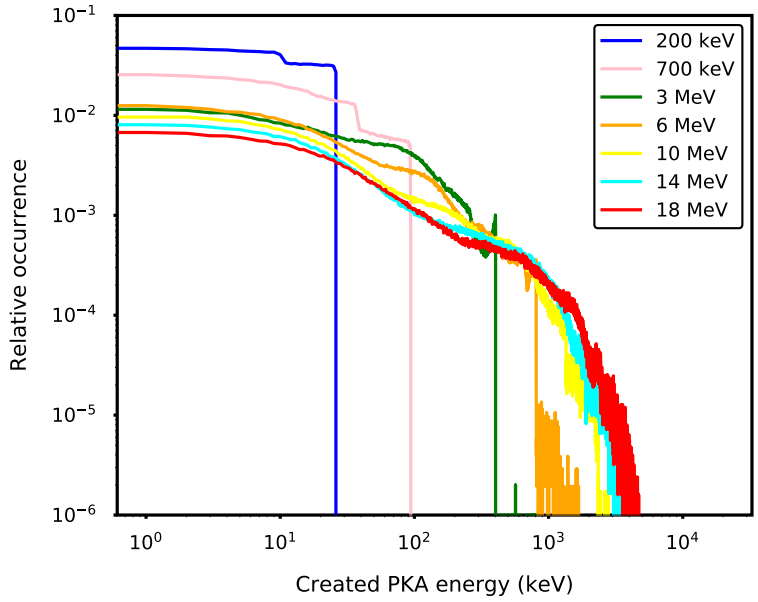

Figure 6.11: *Relative occurrence of heavy PKAs ($Z > 10$) created in $Si_{0.8}Ge_{0.2}$ as a function of their energy following an interaction with a neutron, for neutrons energy ranging from 200 keV to 18 MeV. For each neutron energy, 10^6 simulations have been launched.*

Fig. 6.12 and Fig. 6.13 displays the relative occurrence of the created Si and Ge PKAs only (respectively) in $Si_{0.8}Ge_{0.2}$ following a collision with a neutron, depending on the energies of the PKAs, for neutron energies ranging from 200 keV to 18 MeV. The overall shapes of the curves are alike the curves of Fig. 6.11, but the maximum energies reached are lower. For example, with 18 MeV neutrons, we reach a maximum PKA energy of about 6×10^3 keV considering all the heavy PKAs, compared to 4×10^3 keV with the Si PKAs only and 10^3 keV with Ge PKAs only. Moreover, the energies of the Si PKAs are overall greater than the energies of the Ge ones.

In $Si_{0.8}Ge_{0.2}$, the majority of created PKAs are either Si or Ge ions (65% of the total with a neutron energy of 18 MeV). Moreover, the proportion of Ge ions in the total corresponds at least to the initial percentage of Ge into the alloy. Therefore, both Si and Ge PKAs have to be investigated in the MD step to follow this one. Other PKA species (Al, Mg, Ga or Zn) will not be studied, as they are found in less important quantities, and are not expected to lead to different cascades outputs compared to the initial atom (Si or Ge) from which they were created via spallation reactions. Moreover, following the same arguments than for Si and Ge concerning the predominance of low energy PKAs and subcascades division [6], we employ 10 keV Si and Ge PKAs (sometimes 1 keV) to study collision cascades in Si-Ge alloys in the following.

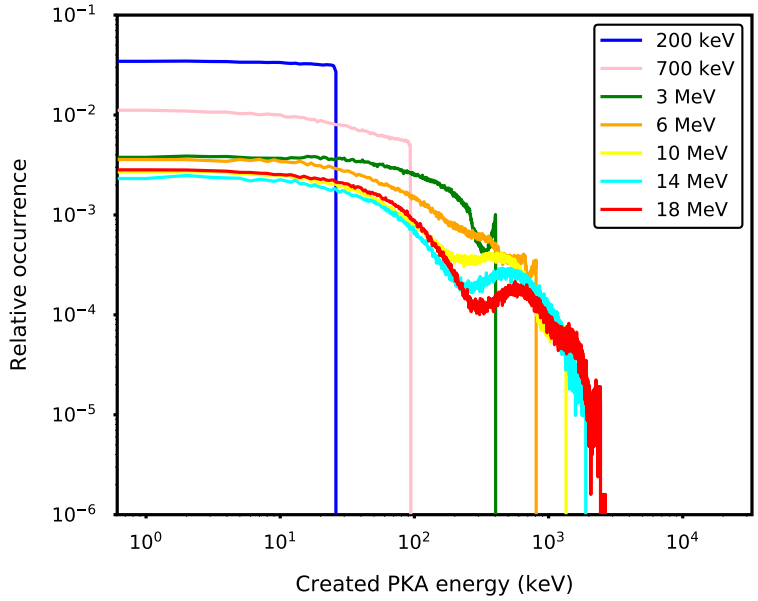

Figure 6.12: *Relative occurrence of strictly Si PKAs (Z = 10) created in $Si_{0.8}Ge_{0.2}$ as a function of their energy following collision with a neutron, for neutrons energy ranging from 200 keV to 18 MeV. For each neutron energy, 10^6 simulations have been launched.*

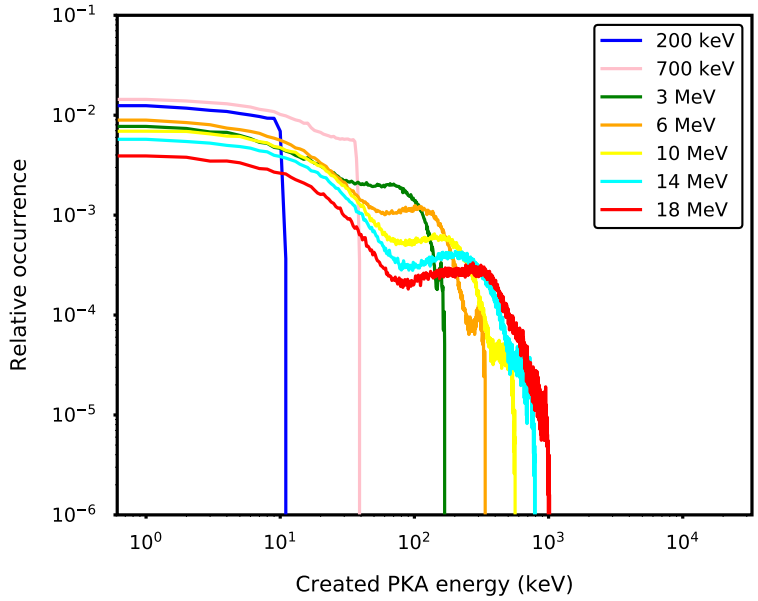

Figure 6.13: *Relative occurrence of strictly Ge PKAs (Z = 32) created in $Si_{0.8}Ge_{0.2}$ as a function of their energy following collision with a neutron, for neutrons energy ranging from 200 keV to 18 MeV. For each neutron energy, 10^6 simulations have been launched.*

6.2 Collision cascades in Si, Ge and Si-Ge alloys

6.2.1 Computational details

The LAMMPS [10] code is employed. To initiate the collision cascade, the PKA is attributed a velocity vector corresponding to the desired energy and direction. It collides other atoms on its path, creating SKAs, which displace other atoms from their equilibrium positions as well. In pure Si and pure Ge we employ Si and Ge PKAs respectively, of 1 keV and 10 keV. In Si-Ge

alloys, we employ both Si and Ge PKAs of 1 keV and 10 keV. 100 simulations per cases (PKA energy, PKA type) investigated are carried out. Each simulation is initiated by a distinct PKA direction, chosen following the method based on the symmetry of the structure presented in Chapter 4.

With 1 keV PKAs, boxes of 216 000 atoms made of 30×30×30 cubic diamond unit cells are employed for Si, Ge and Si-Ge alloys. With 10 keV PKAs, boxes of 1 000 000 atoms made of 50×50×50 cubic diamond unit cells are employed for Ge and Ge PKAs in Si-Ge alloys, whereas for Si and Si PKAs in Si-Ge alloys, boxes of 4 096 000 atoms made of 80×80×80 cubic diamond unit cells are necessary. Indeed, Si PKAs travel on longer distances, and larger boxes are therefore needed. Si-Ge alloys are diamond random alloys. In other words, the structure is the one of diamond and each diamond lattice site can be occupied by either a Si atom or a Ge atom, without any short or long-range order. To reproduce this aspect in the MD simulations, the types of the atoms of the Si-Ge MD simulations are randomly attributed, while staying true to the desired overall element concentrations.

The simulation boxes are divided into two areas: the outer cells (1 unit cell of width) form an NVT ensemble in which the atomic displacements are controlled by a Langevin thermostat (damping time of 0.1 ps) to maintain the temperature at a desired value, and the inner cells form an NVE ensemble in which the atoms evolve freely to simulate the collision cascade. The initialization of the simulation is made by maintaining the temperature at 300 keV for 20 ps (timestep of 1 fs) by integrating the equations of motion in the NVT ensemble.

The maximum velocity of the atoms drastically changes between each step of the cascade: fast during the collision part, and slower during the thermal wave and recrystallization part [11]. Consequently, it is possible to decrease the precision of the integration timestep in parallel of the velocities, while maintaining a constant maximum atomic displacement between two steps. In the present work, we use the *fix* implemented in LAMMPS to update the timestep so that the maximum distance traveled by an atom between two steps is 0.02 Å. Employed timesteps typically go from 10^{-3} fs at the lowest to 1 fs at the greatest.

The SW potentials [12] augmented with the ZBL potential [13] presented in Chapter 3 are employed for the simulations both in Si and Ge. We recall that for Si, the SW potential employed is the one developed in [12], and for Ge the one parametrized in [14] with the slight modifications made in [4]. The SW potential employed for Si-Ge alloys follows the advice of [15] to combine the one we use for Si and the one we use for Ge. Combination rules of the SW pseudopotential for Si and Ge were compared in [16], and it was concluded that the most satisfactory combination rules are the ones of [15]. The fitting procedure and parameters of the SW and ZBL potentials are explained in Chapter 3.

The TTM is employed in the simulations. We do not employ the EPH model as we have not parametrized it for Ge. Moreover, calculations carried out for this section were begun even before we started working on the EPH model for Si. For pure Si and pure Ge, the TTM parameters employed are the ones detailed in Chapter 3. All the parameters common to pure Si and pure Ge also are for Si-Ge alloys (γ_p, D_e, ρ). For Si-Ge alloys, we chose γ_s as the mean value between the pure Si and the pure Ge γ_s parameters, *i.e.* 35.5 g/mol/ps (LAMMPS metal units). The velocity threshold v_0 and electronic specific heat C_e are chosen depending on the alloy composition. In a $Si_{1-x}Ge_x$ alloy, $v_0 = (1-x) \times v_0^{Si} + x \times v_0^{Ge}$. Similarly, the fitting parameters of the $C_e(T_{elec})$ expression we present in Chapter 3 are calculated based on the same combination rules. We do not use the t_{eph} parameter.

6.2.2 Results and discussions

6.2.2.1 Si and Ge

In the study we presented in the last chapter focusing on the effects of the TTM in Si and Ge, we already showed that the response of Si and Ge materials to irradiation (PKAs) is drastically different. We introduce this section with results on pure Si and pure Ge, obtained with a thermostat temperature of 300 K compared to 100 K in Chapter 5. Fig. 6.14 displays the histogram distributions of the number of defects obtained at the end of cascades initiated with 10 keV PKAs in Si and in Ge. A drastic discrepancy in the number of defects can be observed, the Ge distribution of Fig. 6.14 being blatantly shifted on the right compared to the Si one. The mean number of defects in Si is of 471 (10), whereas it is of 2130 (80) in Ge. Numbers in brackets accompanying mean values are SEM values. Moreover, in Fig. 6.14, the Si defects distribution appears to be very narrow (minimum of about 200 defects and maximum of about 800 defects) and thus displays a sharp peak, compared to the Ge one which spreads from about 600 defects to nearly 4000 defects, with a peak, if existing, which is a lot less pronounced.

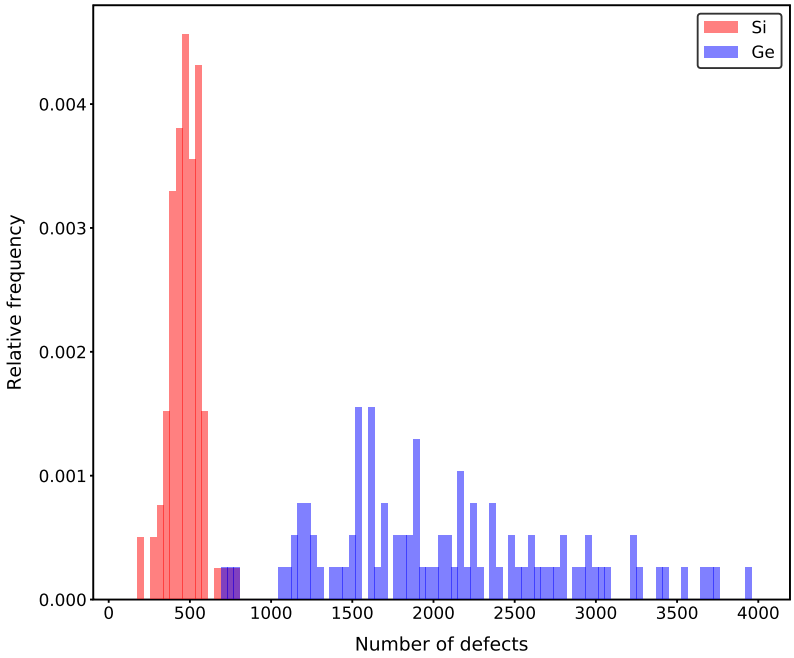

Figure 6.14: *Distributions of the number of defects obtained in Si and Ge, at the end of collision cascades (300 ps) initiated with 10 keV Si PKAs and Ge PKAs respectively. The histograms are constructed from sets of 100 simulations for each material.*

On average, for 10 keV collision cascades, defects are distributed within 37 (1) clusters in Si, compared to 30 (1) in Ge. Overall, more defects are formed in Ge, and they are dispersed into a smaller number of clusters, meaning that the clusters of defects are bigger. Looking with more attention to the distribution of defects inside the clusters, based on our data we calculated that in Ge about 3% only of the interstitial atoms actually are isolated SIAs, and that about 65% of the interstitial atoms are contained in clusters of more than 1000 defects, which can be considered amorphous. In Si, about 15% of the interstitial atoms are isolated SIAs, and about 63% of them are contained of clusters of relatively small sizes, *i.e.* up to 100 defects. Actually, among the 100 cascades simulations in Ge we have performed, 66 display 1 big amorphous cluster containing more than 1000 defects. The reasons behind the formation of those big amorphous clusters in Ge and not in Si have been identified to lie in the thermal characteristics of the materials [5]. The melting temperature of Ge (1211 K) being smaller than the one of Si (1687 K) by nearly 500 K, it is easier to form liquid regions which will turn into amorphous zones. Moreover, the

thermal conductivity of Ge is smaller than the one of Si, favoring local melting as the material cools down slowly as heat does not diffuse fast enough. On the whole, defects formation in Ge mainly is the fact of the heat spike phenomenon described in the previous chapter, whereas this mechanism is more rare and restricted in Si at 10 keV. Note that the interatomic potentials we employ reproduce quite well the thermal properties mentioned (see Chapter 3 and Chapter 5).

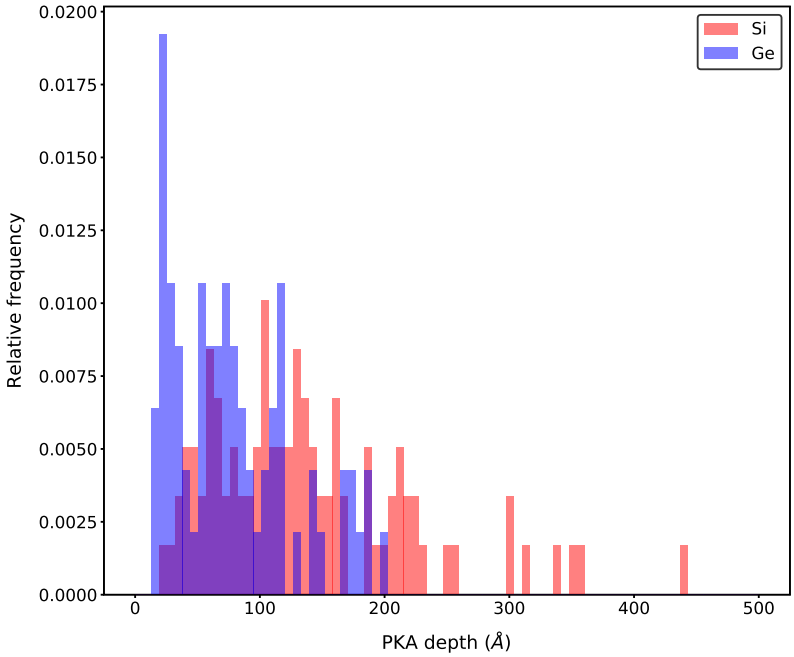

Figure 6.15: *Distributions of the PKA penetration depth obtained in Si and Ge, at the end of collision cascades initiated with 10 keV Si PKAs and Ge PKAs respectively. The histograms are constructed from sets of 100 simulations for each material.*

Fig. 6.15 shows the histogram distributions of the maximum PKA penetration depth attained during 10 keV collision cascades in Si and Ge. The PKAs penetrate deeper in Si than in Ge, as attests the left-shift of the Ge distribution compared to the Si one. The mean PKA penetration depth in Si is of 148 Å whereas it is of 79 Å in Ge. It indicates that the cascades in Ge are denser than in Si, where PKAs or SKAs can travel on longer distances. The PKAs depth distribution is narrower in Ge than it is in Si. Indeed, in Ge the PKA depth ranges from about 15 Å to about 200 Å, whereas it ranges from about 20 Å to nearly 450 Å in Si. Supporting the idea of the denser cascades in Ge, Fig. 6.16 shows the distribution of the distance to the initial position of the PKA of the interstitials created in Si and in Ge. The interstitial atoms are clearly further from the initial PKA position in Si than in Ge, showing a greater spatial extent of the collision cascades in Si. The distribution of the Ge interstitials of Fig. 6.16 shows a taller and narrower peak than the Si distribution.

On the whole, two very distinct average cascades behavior can be identified in Si and Ge. Fig. 6.17 shows two cascades initiated with self PKAs of 10 keV, one in Si and one in Ge, whose characteristics correspond to the mean one for Si and Ge respectively. The differences between the two are immediately visible, especially the large amorphous pocket in Ge.

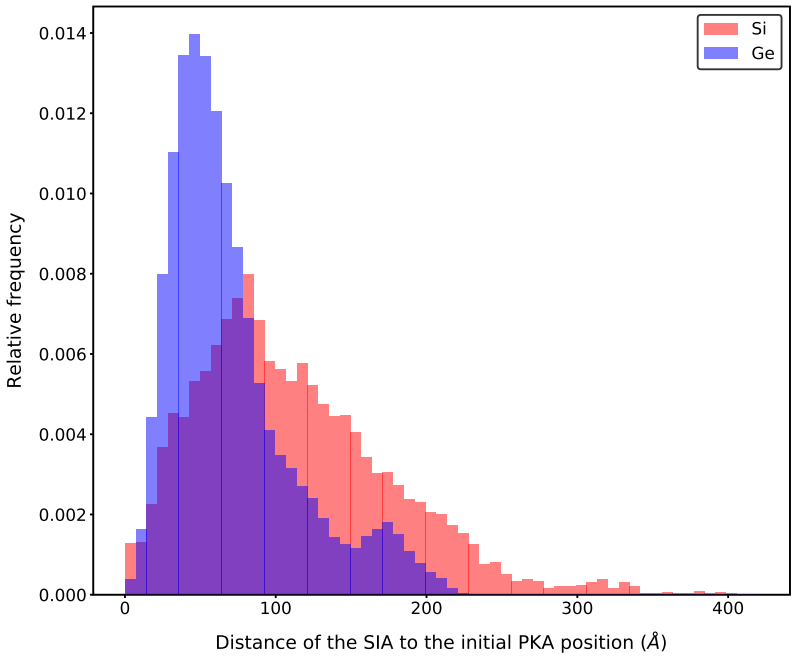

Figure 6.16: *Distribution of the distance to the initial position of the PKAs of interstitial atoms created in Si and Ge following 10 keV collision cascades. Each histogram serie is constructed based on 100 simulations.*

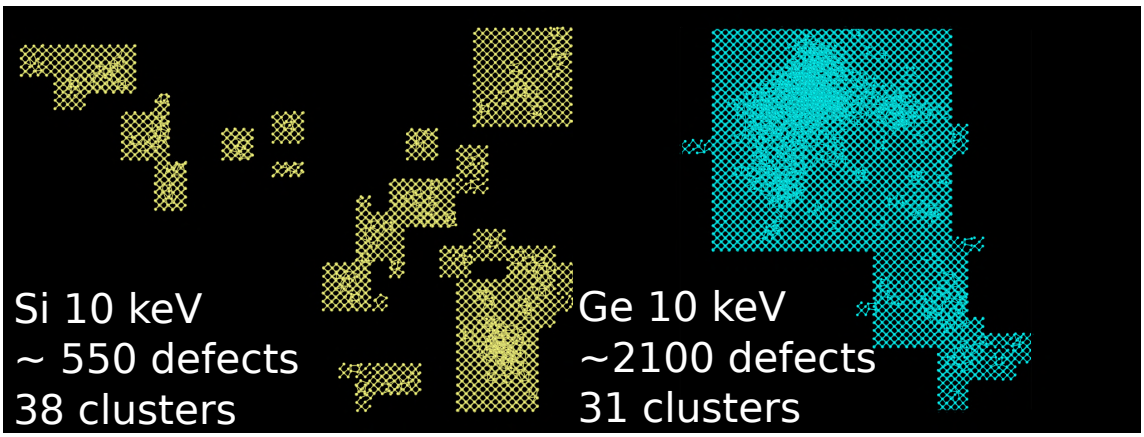

Figure 6.17: *Snapshots of two collision cascades initiated with self PKAs of 10 keV in Si (left, yellow) and Ge (right, cyan) after 300 ps.*

6.2.2.2 Si-Ge alloys

If an extensive body of work has been carried out aiming at understanding DD effects in Si and Ge, the underlying atomistic mechanisms at work in Si-Ge alloys are still not very well understood. During the 1990s, the growing interest for the fabrication of Si–Ge devices (same fabrication techniques as the pre-existing ones for Si, tunable bandgap, high carrier mobility) motivated many experimental research groups to investigate DD-related effects, mainly the behavior of Si-Ge alloys under ion implantation. The common point they all agree on is the increase in the damage caused by ion implantation due to the Ge content increase in the alloy [17–19]. The amount of damage reported for Si-Ge alloys is far greater than the linear interpolation of the damage created in two pure compounds [20]. It was also observed that for a Ge fraction of 50% or more in the alloy, the amount of damage observed was the same as in pure Ge. In the following, we wish to compare our simulation results to those experimental trends.

Fig. 6.18 shows the mean number of defects obtained with 1 keV Si and Ge PKAs in $Si_{1-x}Ge_x$ depending on the alloys composition (x value). Firstly, it can be seen that for a same alloy composition, Ge PKAs create more defects than Si PKAs. For example, with the $Si_{0.5}Ge_{0.5}$ alloy, we obtain on average 105 (3) defects with Si and 127 (4) defects with Ge. Secondly, both for Si PKAs and Ge PKAs, the greater the amount of Ge in the alloy, the greater the number of defects created. This last aspect follows the experimental trends identified in [19] via ion implantation experiments. However, we do not observe a saturation of the level of defects created at $x = 0.5$ like it was noticed experimentally. Higher energy calculations would give us more information on the subject by confirming or invalidating the trends observed at 1 keV.

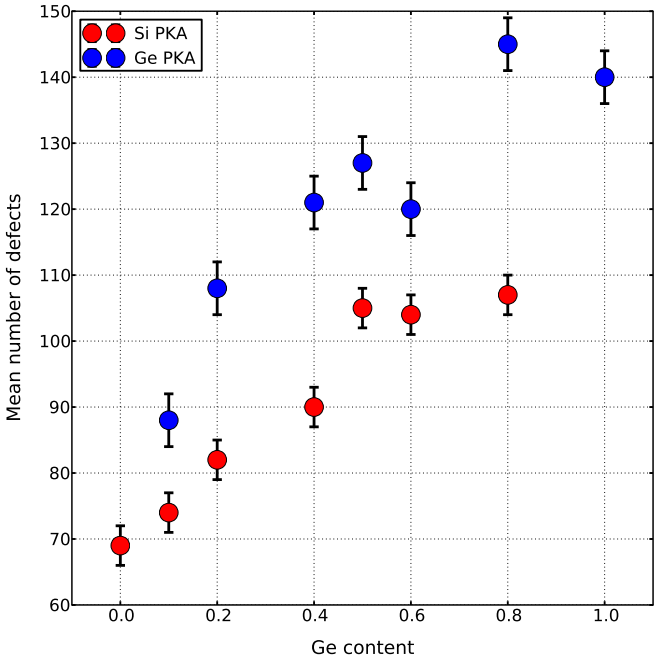

Figure 6.18: *Mean number of defects obtained for various x Ge content of $Si_{1-x}Ge_x$, both for 1-keV Si and Ge PKAs. The error bars are defined as $\pm 1.96 \times SEM$. Mean values are calculated from 100 simulations.*

Table 6.1 displays the PKA penetration depth, distance and deviation of 1 keV Si and Ge PKAs in Si-Ge alloys of various composition. The SRIM [21] projected range values (which should be compared to the PKA penetration depth) are also shown for comparison. For each alloy composition, the distance and penetration depth values are greater for Si PKAs than for Ge PKAs. The deviation of the PKAs is also greater for Si PKAs than Ge PKAs. The penetration depth or distance of the PKAs do not seem to be influenced by the alloy composition, all penetration depth of Si PKAs being between 26.2 Å and 27.5 Å. The SRIM projected range values compare quite well with the penetration depth values we obtained with MD, and highlight the fact that the penetration depth do not vary a lot with the alloy composition at an energy of 1 keV. For Si PKAs, the discrepancy ranges from 4 Å to 9 Å, and from 3 Å to 9 Å for Ge PKAs. The existing discrepancy can of course be explained by the different nature of the SRIM and MD techniques, but also by the fact that SRIM simulates ion implantation whereas we are interested in PKAs into matter. However, on the whole, the same trends are observed with SRIM and with our MD simulations, *i.e.* Si PKAs penetrate deeper than Ge PKAs. Note that SRIM values at 1 keV should be considered with care, as there are important and frequent interrogations on the adequacy of the code at those low energies.

The discrepancies observed in the penetration depth and distance of Si and Ge PKAs as well as the higher number of defects with Ge PKAs than with Si PKAs reveal that the nature of the

Table 6.1: *Deviation, distance and depth of 1-keV Si and Ge PKAs in Si-Ge alloys, as defined in Chapter 4. The SRIM projected range values are also given for comparison with the PKA depth. Between parenthesis are given the SEM values, rounded to the upper unit.*

		Deviation (Å)	Distance (Å)	Depth (Å)	SRIM projected range (Å)
Pure Si		11.8 (1)	29.8 (1)	27.2 (1)	36
Pure Ge		11.1 (1)	23.5 (1)	20.5 (1)	23
$Si_{0.8}Ge_{0.2}$	Si PKA	14.1 (1)	30.5 (1)	26.6 (1)	35
	Ge PKA	10.6 (1)	28.0 (1)	25.5 (1)	34
$Si_{0.7}Ge_{0.3}$	Si PKA	15.0 (1)	31.2 (1)	27.5 (1)	34
	Ge PKA	12.2 (1)	29.5 (1)	26.5 (1)	33
$Si_{0.5}Ge_{0.5}$	Si PKA	15.8 (1)	31.0 (1)	26.2 (1)	30
	Ge PKA	11.5 (1)	28.0 (1)	25.3 (1)	29

PKAs has a very important role. Cascades initiated with Si PKAs tend to be more dispersed and to produce less defects than cascades initiated with Ge PKAs, even if the material is the same. It has to do with the way PKAs transmit their energy. Ge PKAs having a wider atomic radius than Si PKAs, which is illustrated by the more stringent short range interatomic potential of the Ge-Ge or Si-Ge pair interactions compared to the Si-Si one (see Chapter 3), they tend to transmit their energy quicker, resulting in denser region of defects and shorter penetration depth. It could also provide another explanation on the significant differences in the number of defects observed in Si and in Ge. The material and its thermal properties of course has its significance, but the nature (mass, atomic radius) of the PKAs also has an important role.

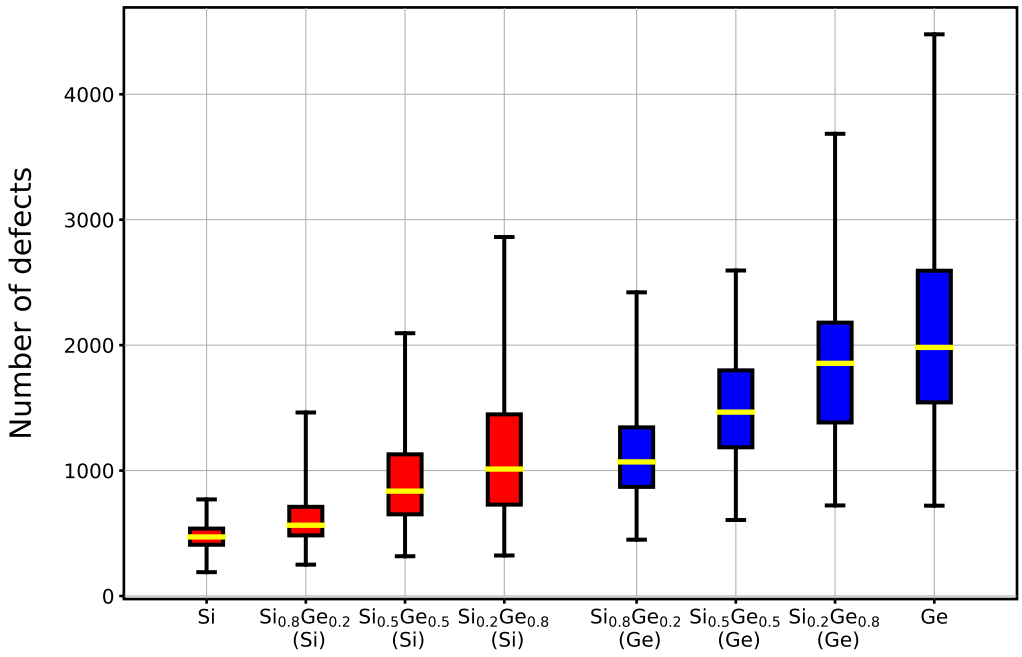

Figure 6.19: *Box plots distributions of the number of defects obtained in Si-Ge alloys at the end of 10 keV collision cascades simulations (300 ps) initiated with Si and Ge PKAs. Box plots are constructed from 100 simulations in each case.*

Fig. 6.19 shows the box plots distribution of the number of defects obtained at the end of cascades initiated with 10 keV PKAs in Si-Ge alloys, with 10 keV Si and Ge PKAs. Fig. 6.20

displays the mean number of defects obtained at the end of cascades initiated with 10 keV PKAs in Si-Ge alloys, with 10 keV Si and Ge PKAs. Just like we observed with cascades initiated with 1 keV PKAs, Si PKAs create less defects in Si-Ge alloys than Ge PKAs. Indeed, visually from Fig. 6.19 and Fig. 6.20, the number of defects created with Si PKAs is always lower than the one created with Ge PKAs. The discrepancy in the mean values is of about 500 defects for $Si_{0.8}Ge_{0.2}$, and goes up to about 750 defects for $Si_{0.2}Ge_{0.8}$. Also, the content of Ge atoms in the alloys has an important influence on the results. Just like with 1 keV PKAs, the number of defects created increases with the alloys Ge content. Both for Si and Ge PKAs, it appears clearly in Fig. 6.20 that the increase in the mean number of defects with the content of Ge in the alloys seems to be linear. Also, the entire box plots distributions of Fig. 6.19 are shifted upward when the content of Ge increases. This observation is valid both for Si and Ge PKAs.

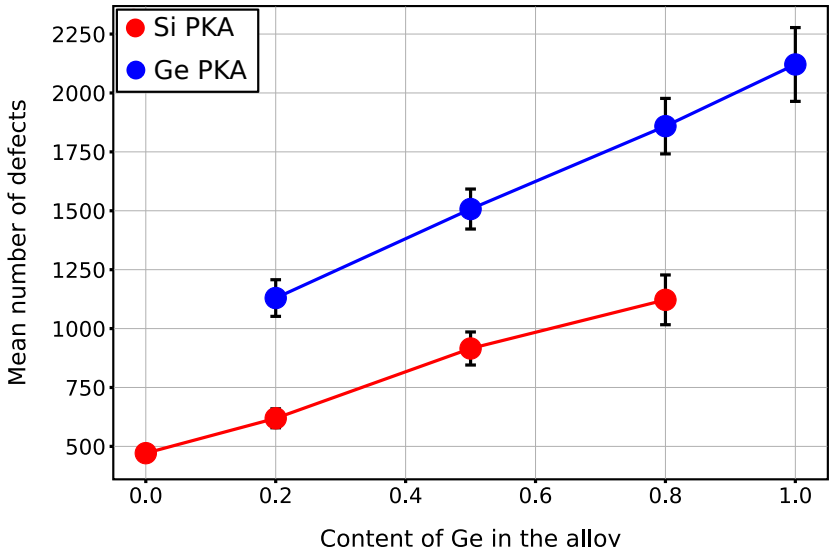

Figure 6.20: *Mean number of defects obtained for various Ge content (x) of $Si_{1-x}Ge_x$ at the end of collision cascades simulations (300 ps) both for 10 keV Si and Ge PKAs. The error bars are defined as $\pm 1.96 \times SEM$. Lines are guide to the eye. Mean values are calculated based on 100 simulations in each case.*

From Fig. 6.19 can also be seen that the width of the box plots drastically increases with the content of Ge in the alloys. Quantitatively, this is confirmed by the increase in the standard deviation of the number of defects. For Si PKAs, the standard deviation is of 101 in Si, 204 in $Si_{0.8}Ge_{0.2}$, 356 in $Si_{0.5}Ge_{0.5}$ and 536 in $Si_{0.2}Ge_{0.8}$. For Ge PKAs, it is of 395 in $Si_{0.8}Ge_{0.2}$, 431 in $Si_{0.5}Ge_{0.5}$, 598 in $Si_{0.2}Ge_{0.8}$ and 795 in Ge. The richer in Ge the alloy is, the more diverse seem to be the possible scenarios in the defects distribution. It is interesting to see that pure Si and pure Ge behave as extreme cases of what can be obtained with Si-Ge alloys. The greater the Ge content, the closer to pure Ge will behave the cascades in terms of number of defects. This is confirmed by the distributions of the defects into clusters, summed up in Table 6.2. Indeed, as the content of Ge increases in the alloys, the percentage of defects contained into big amorphous clusters (more than 1000 defects according to the Lindemann method) increases, both for Si and Ge PKAs: for Ge PKAs, 25% in $Si_{0.8}Ge_{0.2}$, 42% in $Si_{0.5}Ge_{0.5}$, 60% in $Si_{0.2}Ge_{0.8}$ and 65% in pure Ge. This increase is of course related to the overall increase in the number of defects but also testimonies of an enhanced amorphization of the material with the Ge content.

Table 6.2: *Mean number of defects, clusters, percentages of the defects contained into the clusters depending on the size of the clusters and SRIM number of defects ("full cascade" mode), for collision cascades initiated with PKAs of 10 keV in various Si-Ge alloys.*

	Si	Ge	$Si_{0.8}Ge_{0.2}$		$Si_{0.5}Ge_{0.5}$		$Si_{0.2}Ge_{0.8}$	
			Si PKA	Ge PKA	Si PKA	Ge PKA	Si PKA	Ge PKA
Mean number of defects (MD)	471 (10)	2120 (80)	619 (21)	1129 (40)	915 (36)	1507 (43)	1121 (54)	1859 (60)
SRIM defects	239	378	242	286	247	308	287	342
Mean number of clusters	37 (1)	30 (1)	29 (1)	24 (1)	31 (1)	23 (1)	32 (1)	27 (1)
% of defects into very small clusters ($\leq$ 5 defects)	18	4	12	6	7	4	7	3
% of defects into small clusters ($>$ 5 and $\leq$ 100 defects)	62	8	42	18	27	13	21	10
% of defects into medium clusters ($>$ 100 and $\leq$ 1000 defects)	20	23	51	52	55	41	48	27
% of defects into big clusters ($>$ 1000 defects)	0	65	5	25	11	42	23	60

The second important conclusion we can draw from Fig. 6.19, Fig. 6.20 and Table 6.2 is that the nature of the PKA is very significant. Two very distinct cascades scenarios in terms of number of defects and clusters creation are observed depending on the nature of the PKA. We have already mentioned the increased number of defects obtained with Ge PKAs, but from Table 6.2 can also be observed that more clusters are obtained with Si PKAs than with Ge PKAs, the exception being the case of pure Ge for which we surprisingly obtained 30 clusters on average. Overall, with Si PKAs, the cascades are more dispersed in terms of clusters than with Ge PKAs.

An interesting property of the state of damage at the end of the cascades is the atomic type of the interstitials. The Lindemann method we employ reveals that for every cascade studied, the interstitials are composed of the same percentages of Si or Ge atoms as in the alloy global composition. The initial PKA type is not found to influence this aspect either. We checked those conclusions stays true with the Wigner-Seitz method for counting defects presented in Chapter 4. Our results indicate it does with the Wigner-Seitz method as well. On the whole, we can conclude nor Si neither Ge interstitial atoms are preferentially formed.

Fig. 6.19 and Fig. 6.20 confirm the experimental statement concerning the increase of the damage with the content of Ge in the alloy, but still do not report a saturation of the number of defects at about $x = 0.5$, like observed experimentally. This can have various explanations. Firstly, our calculations are carried out at 10 keV, whereas the experimental studies we compare our results with employ ions of about 100 keV. Secondly, the situation we simulate and the experiments carried out in [19] are not completely comparable. Indeed, the experiments studied the implantation of ions in Si-Ge alloys, and the level of damage is measured in terms of amorphization following ion implantation, whereas we directly measure the defects created by Si and Ge PKAs acquiring their energy inside the materials. Finally, concerning the comparison of our MD-obtained number of defects with SRIM, displayed in Table 6.2, we see the given numbers show large discrepancies. The first and main reason is the difference in the way defects are counted within SRIM and with the Lindemann method we employ (see Chapter 4). Both simulation methods and counting methods are so far apart it is not surprising to observe such large discrepancies. More interestingly, the trends in the evolution of the number of defects observed with MD and with SRIM are globally the same, but are greatly enhanced in our MD calculations compared to SRIM. Firstly, with SRIM, Si or Ge PKAs do not give very different number of defects. Indeed, from the numbers of Table 6.2, the increase in the number of defects switching from Si to Ge PKAs is only of 20% with SRIM for all the investigated Si-Ge alloys, whereas it is of 80% for $Si_{0.8}Ge_{0.2}$ and 65% for $Si_{0.5}Ge_{0.5}$ and $Si_{0.8}Ge_{0.2}$ with MD. Secondly, the impact of the content of Ge in the alloy is not as significant as it is with MD. Between pure Si and pure Ge, the number of defects increases of about 60% with SRIM, whereas the increase is of about 300% with MD. The increase between $Si_{0.8}Ge_{0.2}$ and $Si_{0.5}Ge_{0.5}$ with Si PKAs in SRIM is of 6% only, whereas it is of 47% with MD. A strong hypothesis to explain this aspect is that SRIM does not consider manybody effects like melting (and thus formation of amorphous pockets), which is a significant aspect of defects production in Si-Ge alloys. To us, it is a vibrant proof of the superiority of MD compared to SRIM in the prediction of the level of damage.

Fig. 6.21 shows the box plots distribution of the PKA penetration depth in cascades initiated with 10 keV PKAs in pure Si, pure Ge and Si-Ge alloys of various compositions (initiated with both Si and Ge PKAs). Table 6.3 displays the mean PKA penetration depth calculated on the same materials, as well as the SRIM projected range values for comparison.

What is immediately striking in Fig. 6.21 is the discrepancy between the Si PKAs box plots and the Ge PKAs ones. Cascades initiated with Si PKAs always penetrate deeper in the material than the ones initiated with Ge PKAs. It confirms what we have observed with PKAs of 1 keV. The mean values of Table 6.3 goes in the same sense. Indeed, for a same alloy composition,

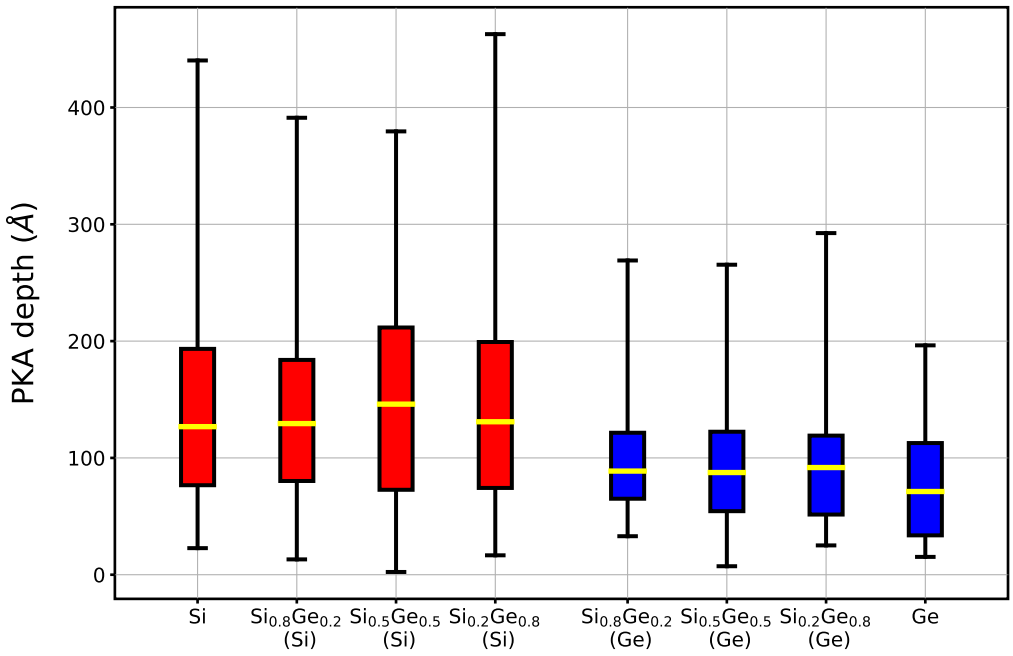

Figure 6.21: *Box plots distributions of the maximum PKA penetration depth attained in Si-Ge alloys for 10 keV collision cascades initiated with Si and Ge PKAs. Notations (Si) or (Ge) indicate the PKA type employed. Box plots are constructed from sets of 100 simulations in each case.*

the mean penetration depth of Si PKAs is always greater than the Ge PKAs one. For example, in $Si_{0.5}Ge_{0.5}$, the mean penetration depth of Si PKAs is of 150 Å, whereas it is of 92 Å with Ge PKAs. Apart from the comparison between Si and Ge PKAs penetration depth, it is not possible to conclude on any other observable trend based on Fig. 6.21. All the cascades initiated with Si PKAs seem to yield the same mean PKA penetration depth. The same observation can be made for the cascades initiated with Ge PKAs, except that the entire box plots distribution of pure Ge seems to be shifted downwards compared to the box plots distribution of Ge PKAs in $Si_{0.8}Ge_{0.2}$, $Si_{0.5}Ge_{0.5}$ and $Si_{0.2}Ge_{0.8}$. The mean values of Table 6.3 do not give us much more information, all the mean penetration depth of Si PKAs being comprised between 142 Å and 151 Å, the ones of Ge PKAs in $Si_{0.8}Ge_{0.2}$, $Si_{0.5}Ge_{0.5}$ and $Si_{0.2}Ge_{0.8}$ between 92 Å and 100 Å, and the one of pure Ge indeed being lower and equal to 79 Å.

Table 6.3: *Mean PKA penetration depth and SRIM projected range ("full cascade" mode), for collision cascades initiated with PKAs of 10 keV in various Si-Ge alloys.*

	Si	Ge	$Si_{0.8}Ge_{0.2}$		$Si_{0.5}Ge_{0.5}$		$Si_{0.2}Ge_{0.8}$	
			Si PKA	Ge PKA	Si PKA	Ge PKA	Si PKA	Ge PKA
Mean PKA depth (MD) (Å)	148 (10)	79 (6)	142 (8)	100 (5)	150 (9)	92 (5)	151 (10)	94 (6)
SRIM projected range (Å)	180	86	173	119	158	104	146	90

On Table 6.3 is also displayed the penetration depth (projected range actually) obtained with SRIM in "full cascade" mode. The penetration depths reported for pure Si and pure Ge with MD are in relatively good agreement with the SRIM ones, the discrepancy being of 32 Å for Si and 7 Å for Ge. SRIM also predicts a greater penetration depth of the Si PKAs than the Ge PKAs. However, SRIM also predicts that the penetration depth of the PKAs decreases with the amount of Ge in the alloy, which seems to be physically sounded. Indeed, as the material gets

denser, ion trajectories are shorter. Our MD calculated values do not predict the same behavior, except in the case of pure Ge. The discrepancies between the penetration depth depending on the content of Ge in the alloy obtained with SRIM not being very large (34 Å between pure Si and Si PKAs into $Si_{0.2}Ge_{0.8}$), it is possible that 100 MD simulations are not enough to clearly be able to observe this behavior. Indeed, we have seen in Chapter 4, in Chapter 5 and when studying 1 keV PKAs that the PKA penetration depth is a value which is hard to reproduce and difficult to converge. Finally, the main point concerning the PKA penetration depth on which our MD calculations and SRIM calculations agrees on is the greater depth of Si PKAs compared to Ge ones. This aspect can be further confirmed and enriched by Fig. 6.22, which displays the histogram distributions of the Si and Ge PKAs penetration depth in $Si_{0.5}Ge_{0.5}$. The right-shift of the Si PKAs is not as obvious compared to what we have observed in Fig. 6.15 for pure Si and pure Ge, but it can still be clearly seen that Si PKAs tend to penetrate deeper than Ge ones.

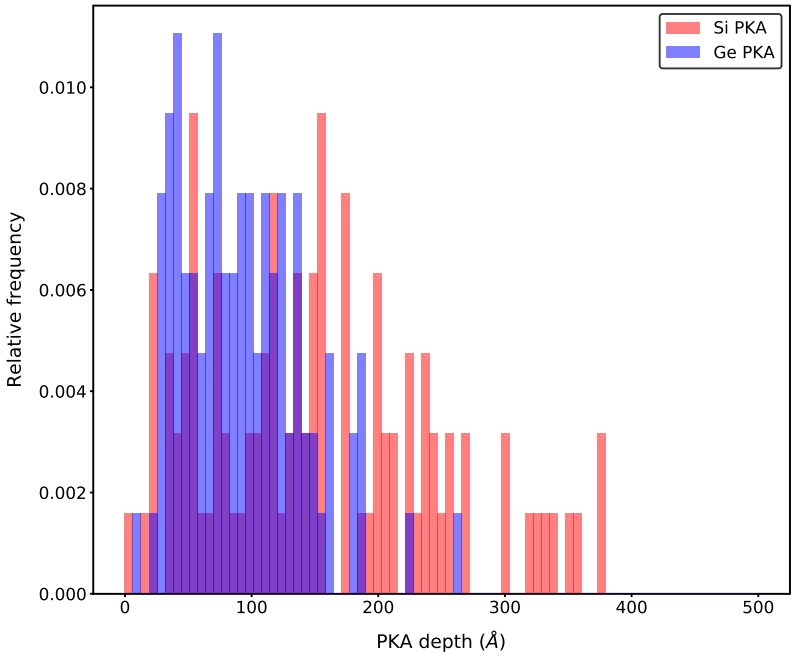

Figure 6.22: *Histogram distributions of 10 keV Si and Ge PKAs penetration depth in* $Si_{0.5}Ge_{0.5}$.

Our analysis of the PKAs and defects depth in Si-Ge alloys for 10 keV collision cascades confirms the two distinct average cascades scenarios depending on the PKA type already predicted from the analysis of the defects and clusters. Ge PKAs deposit their energy on shorter paths than Si PKAs, and create more defects, preferentially contained in big clusters. In Si-Ge devices undergoing irradiation, amorphous clusters as well as smaller interstitial or vacancy clusters of defects coexist. The greater the content of Ge in the alloys, the more the average structures morphologies will be close to pure Ge, *i.e.* large amorphous clusters. The effects of the PKA type directly have to do with the way PKAs transmit their energy, and therefore their intrinsic properties (mass, atomic radius). However, the influence of the content of Ge in the alloys reveals the thermal properties of the alloys are important. Indeed, we believe, just like for pure Si and pure Ge, that the melting temperature and thermal conductivities are responsible for the different damage states between the different alloys composition. Indeed, the lower the amount of Ge in the alloy is, the greater are the melting temperature and thermal conductivity, and thus the harder it is to induce melting of the material and consequently create amorphous defects, as the melting temperature is more difficult to attain and heat is quickly conducted away. Those thermal aspects are coupled to the simple fact that the greater the amount of Ge in an alloy,

the more likely it is for a PKA to create Ge SKAs, which we know induce more defects than Si PKAs. The increase of the number of defects and of the size of amorphous clusters with the increase in the alloy Ge content is a combination of the thermal and PKAs aspects mentioned.

The conclusions we draw from the MD collision cascades simulations are not definitive. Indeed, healing of the clusters of defects and damaged structures are necessary to be able to be completely conclusive on the nature of the created defects in Si, Ge and Si-Ge alloys. However, already interesting and meaningful trends on the creation of defects have been observed with MD. In the next section, we quickly review the main results obtained with kART in Si in the article of Jay *et al.* [11], before getting interested in the results obtained in Ge by Juan Esteban Montoya Cardona, a 6-month intern I participated in the supervision of.

6.3 Healing of the damaged structures in Si and Ge

6.3.1 Computational details

We use the Tersoff potential [22] for the forces calculations in Ge. This potential is known to better reproduce the defects configurations and diffusion barriers than the SW potential. For large clusters, the local force option is adopted as it speeds up the calculations. The simulation parameters adopted are derived from the "vacancy in Si" example of kART. The search frequency has been increased to 20 in order to span more possible events, and the different radius appearing in the parameters (topological for example) have been adapted to the Ge lattice parameter. All calculations in Ge were performed by Juan Esteban Montoya Cardona.

For the few calculations in Si we have carried out for this thesis, the SW potential is employed, with the parameters of the "vacancy in Si" example. The calculations we performed in Si are mainly for illustrative purposes, as the kART step was already applied to Si by Antoine Jay in [11]. This is the reason why we use the SW potential and not the Tersoff one just like we do for Ge. Indeed, we wanted to use the same potential as the one employed in [11].

6.3.2 Results and discussions

The main results reported here for Si are the ones obtained by Jay *et al.* in [11]. The kART calculations carried out in Si during this thesis were only for verification or illustrative purposes. In Si, several important trends concerning the recrystallization and diffusion of defects were identified.

The healing of each clusters of defects individually leads to recrystallization of the clusters, when possible. For example, vacancies and interstitials inside a cluster recombines and thus reduce the size of the cluster. This is for example what can be seen in Fig. 6.23. Starting from an initial cluster made of 4 interstitials and 3 vacancies, we end up with a mono-interstitial. Generally, the final state of the cluster corresponds to the initial net difference between the number of interstitials and the number of vacancies. Consequently, among the relaxed clusters we find lots of small clusters made of only one type of defects, *i.e.* monointerstitials, diinterstitials, triinterstitials, monovacancies, divacancies and trivacancies.

This is valid for the clusters which are initially of relatively small size. Indeed, bigger clusters will also partly recrystallize but they hardly reach sizes that small. Also, after having partly recrystallized the clusters of defects, it is possible to observe their diffusion. Monointerstitials and monovacancies can diffuse to recombine, when they meet each other, or agglomerate to form clusters of defects. For example, a monointerstitial which diffuses and finds itself in the vicinity of another monointerstitial is going to aggregate with it and form a diinterstitial. This

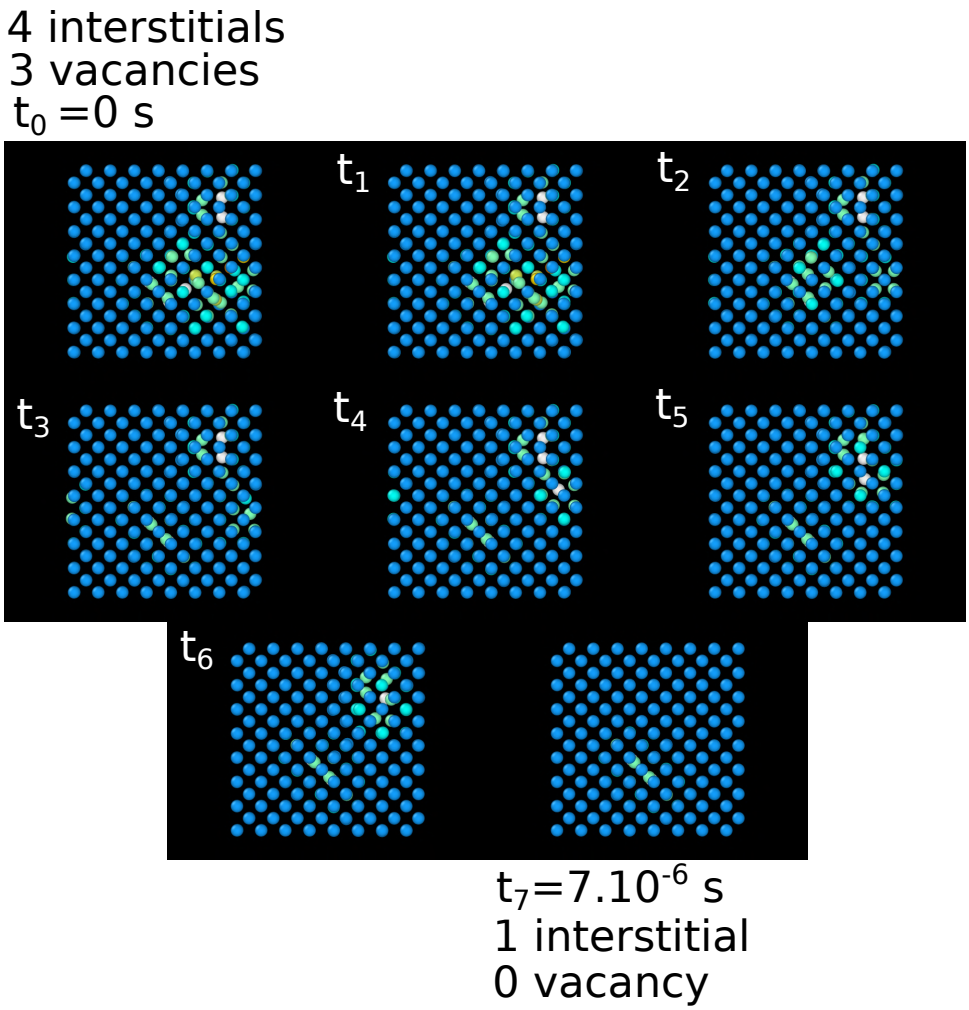

Figure 6.23: *Different steps of a cluster recrystallization in Si with kART. Snapshots are obtained with OVITO [23]. Blue atoms are perfectly diamond Si one, others are disordered atoms which are not in a diamond structure.*

mechanism contributes to an overall reduction of the number of defects by decreasing the number of monointerstials and monovacancies. It also increases the percentage of small clusters of defects in the material. Overall, a drastic reduction of the total number of defects is observed, the big clusters shrink in size, small clusters recombine as much as they can and thus shrink in size as well, and monointerstitials and monovacancies either recombines are form small clusters of defects. In the end, we therefore have lots of small clusters like di-tri interstitials or vacancies, very few monointerstitials or monovacancies and some big pockets of defects depending on the cascades.

Going further into the physics of the clusters with kART, in Si it was found in [11] that a same cluster can have various metastable states. For example, a trinterstitial can oscillate between different configurations. We suspect this kind of mechanism, as stated in the first chapter, to be responsible for the DC-RTS phenomenon in image sensors. In [11], the SW potential of [12] is employed for the kART simulations, and diffusion barriers between the different clusters metastable states are calculated based on this interatomic potential. However, although this interatomic potential is very efficient and adequate for a wide range of properties, it is not suited to correctly reproduce defects geometries and diffusion barrier. To circumvent this issue, one can resort to Nudged Elastic Band (NEB) DFT calculations to calculate diffusion paths, like it was done in [24], or employ the recently developed ARTn + DFT method [25]. As the

time imparted to this thesis did not allow to resort to such demanding techniques, for the kART calculations performed in Ge by Juan Esteban Montoya Cardona under my supervision, we choose to employ a Tersoff potential [22] as it is more adequate than SW to calculate defects configurations and diffusion barriers. Clusters of defects in Si-Ge alloys were not studied in this thesis.

In total, 4 collision cascades initiated with 10 keV PKAs in Ge were healed with kART. Two of those cascades were chosen because they correspond to the mean characteristics of the collision cascades we found in Section 6.2, *i.e.* around 2000 defects and 30 clusters, and the other 2 correspond to cascades where very few defects are created (around 1000) and lots of defects are created (around 3500). For each of those cascades, the clusters were relaxed independently. The diffusion of the vacancies and interstitials which was already studied in [11] in the case of Si was not investigated for Ge as results are expected to be the same.

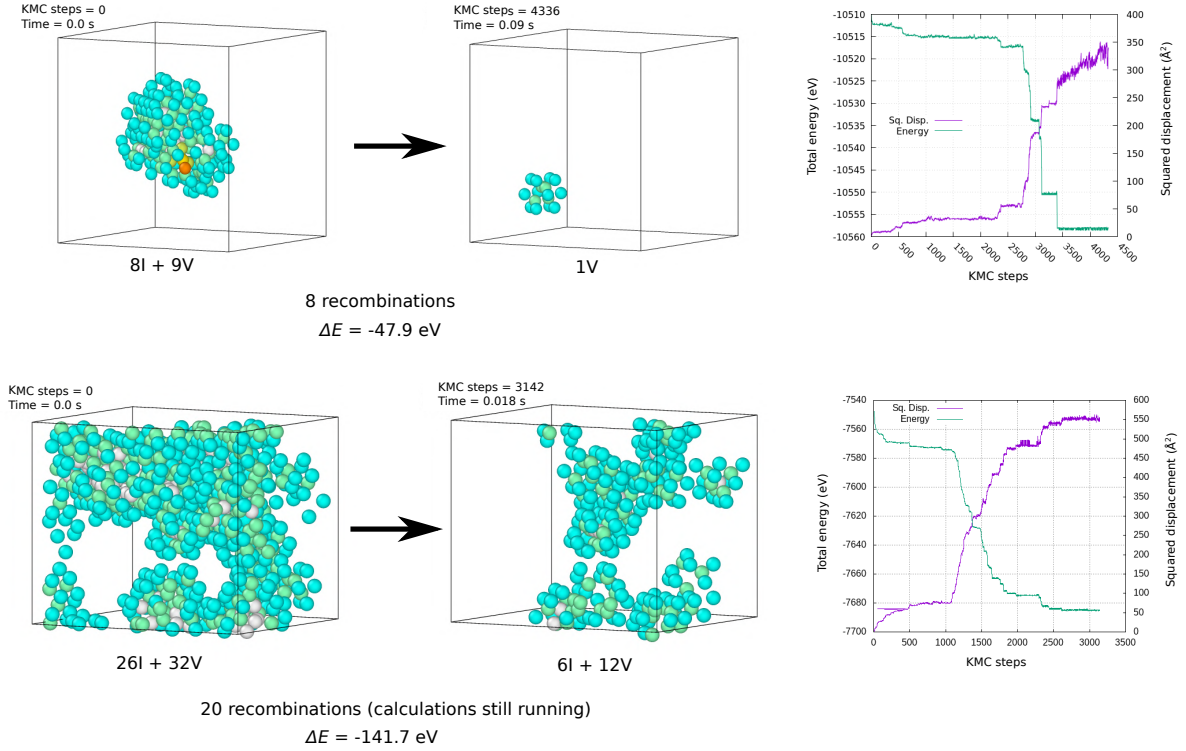

Figure 6.24: *Initial and final states of two recrystallized clusters in Ge with kART. The graphs display the energy changes along the recrystallization processes and the sqaured displacement of the atoms of the simulation boxes. Atomic snapshots were obtained withy OVITO [23]. Only the atoms which are not found by OVITO to be in a perfect diamond structure are displayed. The different colors correspond to the different structures identified by OVITO. This figure was made by Juan Esteban Montoya Cardona.*

The results obtained are very similar to the ones observed in Si. Indeed, the calculations highlighted a recrystallization of the clusters of defects, leading to an overall reduction of the number of defects in the structure, and a reduction of the total energy. Fig. 6.24 shows two examples of the initial and final state of the recrystallized clusters, as well as the energy changes and squared displacement of the atoms along the simulation. We clearly see a decrease in the energy of the clusters, and a reduction in the number of defects. At the time this section was written, the calculation for the largest of the two clusters was not finished, meaning an even more important reduction could be observed. In some cases, just like in the first example of Fig. 6.24, a complete recrystallization is observed (there are no defects left or only a single type of defects), whereas in others, some interstitials and vacancies remain. The big amorphous

clusters of defects characterizing the state of defects in Ge could not be recrystallized due to technical issues regarding the usage of kART. Therefore, we do not know how those big clusters behave. Many studies identify those big clusters as very stable, they are therefore not expected to undergo a drastic recrystallization like the smaller ones. It is thus very likely the major part of the defects in Ge is still contained in large amorphous pockets, whereas other smaller clusters recrystallized or diffused to aggregate to the amorphous pockets.

The results we obtained with kART, in addition to unraveling interesting recrystallization mechanisms and quantifying this phenomenon, gives interesting insights into the interatomic potentials approach and kART itself. A first observation is that with kART, we are very dependent on the accuracy of the interatomic potentials employed, as we are looking at fine atomic diffusive events involving only few atoms, for which the potentials can be badly suited. Even for simple events, the diffusion barriers found with kART and interatomic potentials are questionable in light of experimental and *ab initio* results. For example, we find with kART and the Tersoff potential [22] that the uncharged monovacancy in Ge has a diffusion barrier of 0.7 eV, which is in agreement with some experimental [26] and DFT studies [27], but in disagreement with the diffusion barrier of 0.14 eV we obtain employing the ARTn + DFT [25] technique as well as in disagreement with the values reported by other studies: 0.36 eV in [27], 0.14 eV in [28] and 0.13 eV in [29]. This aspect highlights the difficulties in the study of diffusion mechanisms even for simple systems, already highlighted in Si by Gabriela Herrero Saboya [24], and therefore the uncertainties in the diffusion events predicted by the Tersoff and SW potentials.

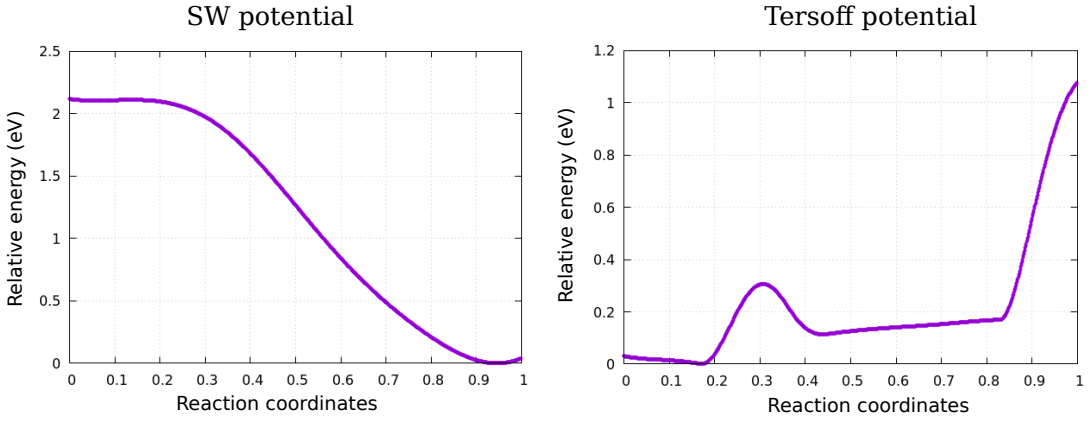

Figure 6.25: *Energy change with respect to the grand state for two identical fictitious diffusion pathways for a monointerstitial in Ge initially in a tetrahedral configuration and ending in a dumbbell configuration, with the SW [14] and the Tersoff [22] potentials. This figure was made by Juan Esteban Montoya Cardona.*

Another major difficulty we faced is the so called "rugosity" of the Tersoff potential. SW is known to be a "smooth" pseudopotential, meaning the potential energy surface obtained with SW is continuous and smooth, even when far from minimums. The reason for this lies in the smooth exponential cutoffs we mentioned in Chapter 3. However, it is also known to badly reproduce diffusion barriers and defects configurations. The Tersoff potential is recognized to be more accurate for the calculation of those properties, but it is not "smooth", meaning its potential energy surface displays local minimums of purely numerical origin with no physical meaning. The Tersoff potential is said to to be "rugous". Consequently, the fine sampling of the potential energy surface by kART can induce the algorithm to get lost in such local minimums, and thus to find unrealistic events or on the contrary not to find the realistic events which should be carried out. Fig. 6.25 illustrates this, where we see the energy curve of the diffusion of a monointerstitial in Ge along a random direction we forced the system to follow, with the SW and with the Tersoff potential. Fig. 6.25 does not display realistic migration

barriers or minimum energy pathways, but fictitious energy curves along a straight diffusion path, and should therefore only be considered for illustrative purposes. It can be seen that the curve of the SW potential is smooth, whereas the one of the Tersoff potential shows some local minimums and sudden slope variations. It is thus not surprising that the Tersoff potential can lead the algorithm to dead-ends. This is the reason which explains why the great majority of kART articles [11, 30–33] employ the SW potential, in spite of it being unadequate for the calculation of diffusion barriers and defects configurations, and the results reported being valid in the context of the SW potential only. To circumvent those issues and benefit from the efficiency and smartness of the ARTn algorithm for finding events on the fly, resorting to ARTn + DFT [25] is a very interesting choice as with DFT the potential energy surface is perfectly smooth.

Conclusion

In this chapter has been applied the three first steps of the multiscale approach to Si, Ge and Si-Ge alloys. The first MC step allowed to study the creation of PKAs both by elastic and inelastic (nuclear) neutron interactions with matter. At the considered energies, spallation reactions are favored in Si compared to Ge. Coherently, in Si-Ge alloys, Si atoms are more subject to spallation reactions. We concluded that the PKAs types of interest for us are Si and Ge only. Considering the energies, we choose to restrict ourselves to 10 keV collision cascades. This value is motivated by physical reasons of subcascades splitting exposed in [6]. With MD, collision cascades simulations are carried out in Si, Ge and Si-Ge alloys. A lot more defects are observed in Ge compared to Si. Moreover, the formation of amorphous pockets is favored in Ge, leading to very large clusters of defects of an extent we rarely find in Si. The heat spike mechanism is responsible for this, and it is made more efficient in Ge due to the nature of the Ge PKAs (mass, atomic radius) and the thermal properties of Ge. In Si-Ge alloys, interesting features have been observed based on the Ge content of the alloy and the PKA type employed. It was found that the number of defects obtained increases with the content of Ge in the alloy. The maximum number of defects being obtained in pure Ge, and the minimum one in pure Si. This observation follows experimental observations on the subject. The nature of the damage is also modified with the content of Ge. Indeed, the greater the content of Ge is, the bigger the clusters of defects are. Concerning the types of PKAs employed, two distinct average cascades scenarios are observed. More defects are obtained with Ge PKAs than Si PKAs, for every alloy composition studied. The average cascades scenarios observed are very distinct depending on the nature of the PKA. The trajectories of Ge PKAs are shorter than the ones of Si PKAs, and tend to create defects contained in bigger clusters. Evolution in the thermal properties of the materials with the Ge content partly explains the Ge content related effects. However, the nature of the PKA employed also has a very important role. Some collision cascades obtained in Ge were relaxed with kART, and results compared to the ones already obtained in Si in [11]. The basic mechanisms are similar, *i.e.* we observe healing of the clusters and diffusion of single interstitials and vacancies to recombine or form small clusters. Clusters of medium size also partly recrystallize. Overall, the trends observed in the MD calculations about the nature of the defects hold true. We expect it to stay valid for Si-Ge alloys as well.

References

[1] S. Agostinelli et al., "Geant4 a simulation toolkit", Nucl. Instr. Meth. Phys. R. A **506**, 250–303 (2003).

[2] J. Allison et al., "Geant4 developments and applications", IEEE Trans. Nucl. Sc. **53**, 270–278 (2006).

[3] J. Allison et al., "Recent developments in Geant4", Nucl. Instr. Meth. Phys. R. A **835**, 186–225 (2016).

[4] K. Nordlund, M. Ghaly, R. S. Averback, M. Caturla, T. Diaz de la Rubia, and J. Tarus, "Defect production in collision cascades in elemental semiconductors and fcc metals", Phys. Rev. B **57**, 7556–7570 (1998).

[5] P. Lopez, L. Pelaz, I. Santos, L. A. Marques, and M. Aboy, "Molecular dynamics simulations of damage production by thermal spikes in Ge", J. App. Phys. **111**, 033519 (2012).

[6] M. Raine, A. Jay, N. Richard, V. Goiffon, S. Girard, M. Gaillardin, and P. Paillet, "Simulation of Single Particle Displacement Damage in Silicon – Part I: Global Approach and Primary Interaction Simulation", IEEE Trans. Nucl. Sc. **64**, 133–140 (2017).

[7] L. Howe and M. Rainville, "Features of collision cascades in silicon as determined by transmission electron microscopy", Nucl. Instr. Meth. **182-183**, 143–151 (1981).

[8] J. Narayan, O. Oen, D. Fathy, and O. Holland, "Atomic structure of collision cascades in ion-implanted silicon and channeling effects", Mat. Lett. **3**, 67–72 (1985).

[9] L. Howe and M. Rainville, "Heavy ion damage in silicon and germanium", Nucl. Instr. Meth. Phys. R. B **19-20**, Ion Beam Modification of Materials, 61–66 (1987).

[10] S. Plimton, "Fast Parallel Algorithms for Short-Range Molecular Dynamics", J. Comput. Phys. **117**, 1–19 (1995).

[11] A. Jay, M. Raine, N. Richard, N. Mousseau, V. Goiffon, A. Hémeryck, and P. Magnan, "Simulation of Single Particle Displacement Damage in Silicon–Part II: Generation and Long-Time Relaxation of Damage Structure", IEEE Trans. Nucl. Sc. **64**, 141–148 (2017).

[12] F. H. Stillinger and T. A. Weber, "Computer simulation of local order in condensed phases of silicon", Phys. Rev. B **31**, 5262–5271 (1985).

[13] J. F. Ziegler, J. P. Biersack, and U. Littmark, *The Stopping Range of Ions in Solids*, 1st ed. (Pergamon Press, N. Y, 1983).

[14] K. Ding and H. C. Andersen, "Molecular-dynamics simulation of amorphous germanium", Phys. Rev. B **34**, 6987–6991 (1986).

[15] S. Ethier and L. J. Lewis, "Epitaxial growth of Si1-xGex on Si(100)2 x 1: A molecular-dynamics study", J. Mat. Res. **7**, 2817–2827 (1992).

[16] L. Martín, I. Santos, P. López, L. A. Marqués, M. Aboy, and L. Pelaz, "Modeling sige through classical molecular dynamics simulations: chasing an appropriate empirical potential", in 2018 spanish conference on electron devices (cde) (2018), pp. 1–4.

[17] T. E. Haynes and H. O. W., "Damage accumulation during ion implantation of unstrained Si1-xGex alloy layers", Appl. Phys. Lett. **61**, 10.1063/1.107669 (1992).

[18] C. O'Raifeartaigh, R. C. Barklie, A. N. Larsen, F. Priolo, G. Franzó, G. Lulli, M. Bianconi, J. K. N. Lindner, F. Cristiano, and P. L. F. Hemment, "2 mev si ion implantation damage in relaxed si1-xgex", Nucl. Instr. Meth. Phys. R. B **120**, Proceedings of the E-MRS 1996 Spring Meeting Symp. I on New Trends in Ion Beam Processing of Materials, 165–168 (1996).

[19] A. N. Larsen, "MeV ion implantation induced damage in relaxed Si1-xGex", J. App. Phys. **81**, 2208 (1997).

[20] D. Y. C. Lie, "Doping and processing epitaxial gexsi1-x films on si(100) by ion implantation for si-based heterojuntion devices applications", J. Elec. Mat. **27**, 377–401 (1998).

[21] J. F. Ziegler, M. D. Ziegler, and J. P. Biersack, "SRIM - The stopping and range of ions in matter (2010)", Nucl. Instr. Meth. Phys. R. B **268**, 1818–1823 (2010).

[22] J. Tersoff, "Modeling solid-state chemistry: Interatomic potentials for multicomponent systems", Phys. Rev. B **39**, 5566–5568 (1989).

[23] A. Stukowski, "Visualization and analysis of atomistic simulation data with OVITO - the Open Visualization Tool", Mod. Sim. Mat. Sci. Eng. **18**, 015012 (2010).

[24] G. H. Saboya, "Defects in silicon: revisiting theoretical frameworks to guide ab initio characterization", Université Toulouse 3 Paul Sabatier, (2020) `https://tel.archives-ouvertes.fr/tel-03158564/`.

[25] A. Jay, C. Huet, N. Salles, M. Gunde, L. Martin-Samos, N. Richard, G. Landa, V. Goiffon, S. De Gironcoli, A. Hémeryck, and N. Mousseau, "Finding Reaction Pathways and Transition States: r-ARTn and d-ARTn as an Efficient and Versatile Alternative to String Approaches", J. Chem. Theory Comput. **16**, 6726–6734 (2020).

[26] D. Shaw, "Self- and impurity diffusion in ge and si", Phys. Status Solidi B **72**, 11–39 (1975).

[27] H. Pinto, J. Coutinho, V. Torres, S. Öberg, and P. Briddon, "Formation energy and migration barrier of a Ge vacancy from ab initio studies", Mat. Sci. Sem. Proc. **9**, 498–502 (2006).

[28] J. Lee, K. Duk Na, S.-C. Lee, C. S. Hwang, and J.-H. Choi, "Effects of magnitude and direction of the biaxial compressive strain on the formation and migration of a vacancy in Ge by using density functional theory", J. App. Phys. **110**, 033504 (2011).

[29] P. Ramanarayanan, K. Cho, and B. M. Clemens, "Effect of composition on vacancy mediated diffusion in random binary alloys: First principles study of the Si1-xGex system", J. App. Phys. **94**, 174–185 (2003).

[30] L. K. Béland, P. Brommer, F. El-Mellouhi, J. F. Joly, and N. Mousseau, "Kinetic activation-relaxation technique", Phys. Rev. E **84**, 046704 (2011).

[31] L. K. Béland and N. Mousseau, "Long-time relaxation of ion-bombarded silicon studied with the kinetic activation-relaxation technique: Microscopic description of slow aging in a disordered system", Phys. Rev. B **88**, 214201 (2013).

[32] N. Mousseau, L. K. Béland, P. Brommer, J. F. Joly, F. El-Mellouhi, E. Machado-Charry, M. C. Marinica, and P. Pochet, "The Activation-Relaxation Technique: ART Nouveau and Kinetic ART", J. At. Mol Opt. Phys. **2012**, 925278 (2012).

[33] F. El-Mellouhi, N. Mousseau, and L. J. Lewis, "Kinetic activation-relaxation technique: An off-lattice self-learning kinetic Monte Carlo algorithm", Phys. Rev. B **78**, 153202 (2008).

General conclusion and perspectives

The original ambition of the present thesis is the development and application of a multiscale simulation approach for the prediction of DD effects into semiconducting materials for opto and microelectronic applications. For this simulation approach to be successful, the methods, models and methodologies must be questioned, tested and adapted to the newest and most relevant developments, and this for every step of the multiscale approach.

The second MD step of the simulation approach is a crucial one as it dictates the propagation of the collision cascades and therefore the creation of damage into the materials. An accurate and trustworthy modelling of the physical phenomena at stake during this step is then of prime significance. However, the basic MD framework is not suited to model the theoretically demanding physical phenomena occurring within a collision cascade. Indeed, high energy collisions between atoms are not correctly taken into account into general-purpose interatomic potentials, the degree of stochasticity of the collision requires to perform large sets of simulations and electronic stopping and electron-phonon coupling must be incorporated into the simulations. The basic MD framework has therefore to be adapted. In this thesis, we focus on the stochasticity and electronic effects aspects.

The statistical study we perform in Chapter 4 gives valuable insights into the degree of uncertainties related to collision cascades simulations in Si. It demonstrates that even with collision cascades initiated with 1 keV PKAs, a relatively high number of 60 simulations *a minima* must be performed for the results to be considered converged. A more general conclusion of this study is that the level of convergence of MD simulations of collision cascades results is not trivial and should be, at best, verified by performing a convergence study of the results, or at least made clear and unambiguous in the results by being transparent in the reported data in terms of statistical quantities employed, uncertainties on the mean values and visual representation of the data sets. This statistical study can also be envisioned in the wider context of the issue related to results reproduction in science. A careful and transparent statistical study guarantees unambiguous interpretation and evaluation of the results by the community.

In Chapter 5 are tested two methods for the inclusion of electronic effects, the well known TTM and the very recent EPH model. With the TTM, both in Si and in Ge, the inclusion of electronic stopping into the simulations was found to decrease the level of damage created. However, electron-phonon coupling was also found to induce local melting of the material, thus favoring the creation of defects. This effect is enhanced in Ge compared to Si. Thus, the parametric study we perform with the TTM in Si and Ge reveals the effects of the electrons depend on

the nature of the material. In Ge, which is subject to heat spikes of greater intensities than Si due its lower melting point and thermal conductivity, energy transfer by electron-phonon coupling from electrons to ions is unambiguously able to enhance the formation of amorphous pockets. It reveals the main trends of a material response to irradiation are still dictated by the general material properties (*i.e.* melting temperature, thermal conductivity, density ...), but that depending on the nature of those material properties, electronic effects can also have a major influence on the collision cascades. This has implication on the number of defects and the structure of the clusters of defects created, in terms of size for example, and therefore possibly on the devices electronic responses. However, those results are obtained in the context of the TTM, which, although being the most widely employed model for the inclusion of electronic effects into MD simulations, is intrinsically subject to limitations related to the basis of its physical model (constant electronic density in the model for example), but also to its parametrization. Indeed, uncertainties, and even sometimes arbitrariness, in the choice of some parameters we identified as having major impact on the results, even for simple materials like Si and Ge, forces us to restrict the interpretation of the results obtained with the TTM to the TTM itself, instead of presenting them as general conclusions on the effects of electrons into collision cascades. Truly understanding the role of electrons in collision cascades may thus require to resort to models finer than the TTM. This is why we also employ the EPH model, which can be envisioned as a sophisticated version of the TTM, incorporating non-constant electronic density and finer electron-phonon coupling implementation. We show that this model is able to incorporate electronic stopping and electron-phonon coupling into MD simulations of collision cascades with the accuracy of first principles calculations. Indeed, we successfully reproduced with MD-EPH simulations the complex density-dependent energy loss to electrons obtained with TDDFT calculations. In terms of use for collision cascades simulations, this model shows no enhanced melting in Si due to electron-phonon coupling, contrary to the TTM. According to us, this could be the proof of the finer understanding of the electron-phonon coupling into the EPH model than into the TTM, as experimentally, formation of amorphous pockets due to energy fed back from electrons to ions only occurs with ion irradiation in the MeV order. We also found very different number of defects when using the EPH model, whose parameters are fitted to reproduce TDDFT data, and the TTM with parameters derived from SRIM. This highlights the significance of the controversy in electronic stopping calculations with TDDFT codes and with SRIM.

Finally, the multiscale approach was applied in Chapter 6 to Si, Ge and Si-Ge alloys. Energies and types of the PKAs to employ with MD were chosen based on neutron-matter interaction simulations with Geant4, which identified low energy PKAs as the dominant and most important ones, and that spallation products need not to be taken into account into MD simulations. The MD simulations performed in Si and Ge confirmed the distinct behavior already observed in the response to irradiation of the two materials, and eased the analysis of the results obtained in Si-Ge alloys. The simulations carried out in Si-Ge alloys also followed some of the experimental trends observed in the 90s in the context of ion implantation into Si-Ge alloys. For instance, our simulations confirmed that the greater the content of Ge into the alloy, the greater the number of defects will be and the bigger will be the clusters. Also, the nature of the PKA was found to have a significant influence on the results, Ge PKAs leading to denser and more defective collision cascades. Those aspects are very relevant in the context of the development of Ge and Si-Ge based devices, as the different damage structures observed might lead to different levels or mechanisms of devices degradation. The healing of the clusters of defects and damage structures with kART revealed that SIA and SV tend to diffuse in order to recombine, or to form small clusters of defects, whereas small clusters of defects recrystallize to form smaller clusters. The large amorphous pockets observed in Ge and sometimes in Si could not be studied. They are expected to shrink in size but stay amorphous. On the whole, the final picture of the damage structures in Si and Ge after the kART step is pretty similar to the final picture at the end of the

MD run, with overall less defects in the material, less SIA and SV and more small clusters in Si and slightly smaller amorphous pockets in Ge. Those results are important for various reasons. Firstly, it validates the efforts undertook for the accurate simulation of the propagation of the collision cascades with MD, the final overall state of defects at the end of kART being closely related to the one at the end of the MD run. The question of the stochasticity and of the inclusion of electronic effects thus becomes fundamental even from a technological standpoint. Indeed, we have seen it can have significant implications on the number of created defects, on the types of clusters found in the materials and therefore on the prediction of the sensitivity of a material to irradiation. Secondly, it should dictate the systems of interest to be studied in the fourth and last *ab initio* step of our multiscale approach, which we do not treat in this thesis. Indeed, if small clusters of defects have already been investigated in the context of our multiscale approach[1,2], larger ones have never been. However, recent results suggest that small clusters like E-centers would not be responsible for the DC-RTS behavior observed in image sensors[2], whereas bigger clusters of defects are more and more suspected to be responsible for DC and DC-RTS, considering, among other arguments, that their enhanced electronic cross sections compared to point defects allows to explain the experimental measurements showing high DC-RTS levels. The problem is that such big clusters can be hardly studied with *ab initio* techniques, due to their size and the infinity of possible configurations. To me, it is a strong motivation to construct an experimental campaign comparing the level of DC and DC-RTS in Si, Ge and Si-Ge image sensors. The trends observed depending on the material would give valuable insights on the kind of clusters responsible for DC and DC-RTS, as we know from our simulations the expected average shape of the clusters in each material. Now that we have gained knowledge and enhanced control on the capabilities, limitations and uncertainties related to the different steps and transitions of the multiscale approach, I believe comparisons with experimental data is a key aspect of the future success of our multiscale approach for the fundamental understanding and prediction of DD.

To conclude this manuscript, in addition to the hypothetical experimental studies mentioned just above, works should keep being conducted on the multiscale simulation approach itself. Already based on the work presented in this thesis, interesting perspectives could be envisioned. According to me, the weakest point of our global simulation approach lies in the transition between the first MC step and the second MD step. Indeed, switching from a continuous description of matter designed for particle and high energy physics to an atomic one initially conceived for the simulation of systems at or near equilibrium conducts to important information loss. Simulation methodologies combining the atomic BCA code MARLOWE to MD simulations have already been proposed[3]. We could employ such techniques to be able to launch simulations with PKAs of higher energies, or try to inspire ourselves from this simulation scheme to combine our Geant4 simulations to MD ones.

Other interesting perspectives concern the interatomic potentials employed in the MD simulations. More and more machine learned potentials are being developed, and one was even designed to study collision cascades simulations within Si[4]. The accuracy of those potentials certainly is greater than the SW + ZBL one we employed, but their computational cost remains

[1] A. Jay, A. Hémeryck, N. Richard, L. Martin-Samos, M. Raine, A. Le Roch, N. Mousseau, V. Goiffon, P. Paillet, M. Gaillardin, and P. Magnan, "Simulation of Single Particle Displacement Damage in Silicon-Part III: First Principle Characterization of Defect Properties", 65, 724-731 (2018).

[2] G. H. Saboya, "Defects in silicon: revisiting theoretical frameworks to guide ab initio characterization", Université Toulouse 3 Paul Sabatier, (2020) https://tel.archives-ouvertes.fr/tel-03158645.

[3] C. J. Ortiz, "A combined bca-md method with adaptive volume to simulate high-energy atomic-collision cascades in solids under irradiation", Computational Materials Science 154, 325–334 (2018).

[4] A. Hamedani, J. Byggmästar, F. Djurabekova, G. Alahyarizadeh, R. Ghaderi, A. Minuchehr, and K. Nordlund, "Insights into the primary radiation damage of silicon by a machine learning interatomic potential", Mat. Res. Lett. 8, 364–372 (2020).

an issue. However, machine learned potentials are an interesting and dynamic field of study for the improvement of our multiscale approach. Accurate and "smooth" machine learning potentials could also be of great use for kART, for which the results of course depend on the accuracy of the potentials but also on their "smoothness" for the exploration of the potential energy surface.

The analysis of the cascade could also be improved. An increasing number of published papers show interest in the search of relevant descriptors to classify collision cascades[5]. The large datasets of cascades we have built could be employed to work on those aspects of cascades analysis.

Still concerning MD simulations of collision cascades, the EPH model should be further studied and employed and theoretical works could be conducted to adapt this model to semiconducting materials. Indeed, the EPH model and the TTM are both developed for metals, and although many arguments support their accuracy for simulations with semiconducting materials, the errors related to the use of those models to semiconductors should be evaluated. On the same subject, the discrepancies observed in collision cascades results with TDDFT-derived and SRIM-derived MD stopping consists in a strong motivation to explain or correct the existing gap between TDDFT and SRIM stopping power calculations, at least in Si.

[5] A. De Backer, C. S. Becquart, P. Olsson, C. Domain, "Modelling the primary damage in Fe and W: influence of the short-range interactions on the cascade properties: Part 2 – multivariate multiple linear regression analysis of displacement cascades", J. Nucl. Mater. 459, 152887 (2021).